Study of Bismuth-based Perovskite-like Materials for Solar Cell and Supercapacitor Applications

Tianyue Li

Thesis submitted for the degree of Ph. D.

The University of Edinburgh

January 2019

Declaration

I hereby declare that this thesis has been composed solely by myself. Except where states otherwise by reference or acknowledgment, the work presented is entirely my own. This work has not been submitted, in whole or in part, in any previous application for a degree.

Tianyue Li

January 2019

Acknowledgement

I would like to express my sincere gratitude to many people who have generously contributed to the work presented in this thesis and helped me through my PhD study.

Firstly, I am extremely grateful to my enthusiastic supervisor Professor Neil Robertson for his guidance and support throughout my PhD study. I thank Professor Robertson not only for his tremendous academic support, but also for his constant encouragement and valuable suggestions throughout the research work. Professor Robertson has always made himself available to help me clarify my doubts, correct my manuscripts and provide support despite his busy schedules. On top of that, Professor Robertson's international horizons, collaborative research spirit and highly motivated working attitude will profoundly influence my future personal development in a positive manner.

The journey of PhD study was not easy. Thanks to the help received from everyone in (or formerly in) Robertson's group, I have been making obvious progress over my research study. I would like to thank Dr. Michal Maciejczyk and Dr. Helen Benjamin for their help on chemical synthesis, crystal growth and electrochemistry; Dr. Aruna Ivaturi for her help on film preparation and device fabrication; Dr. Wenjun Wu for his always help on device fabrications and theoretical guidance; Dr. John Mallows for guiding me making the first dye-sensitized solar cell in my life, and his collaboration on supercapacitor studies during his post-doc period; I would also thank Dr. Andrew McMahon, Georgia Tsagkaropoulou, Rebecca Nicolson and Dr. Rosinda Fuentes for their generous help on my computational studies; Dr. Gylen Odling for his help on optical measurements and his patience on answering my thousands of stupid questions; Ying, German and Artit for their academic support and lively vibes; my project students Stephan Monfront, Alba Franco Gozalenze, and Keir Adams for their passion and hard works; and everyone who had offered me help during my PhD study.

I would like to express my gratitude to Prof. Hongwei Han and Prof. Yue Hu for allowing me to carry out research in Huazhong University of Science and Technology, where I have learned a lot and received warm-hearted helps from every group member, made me feel welcome. I would also like to acknowledge Qifei Wang who offered me kind help and carried out further collaboration with us on the device studies.

I would like to thank so many people in the University of Edinburgh and University of St. Andrews for offering me help in different aspects of my research work. Special mention needs to go to Dr. Carole Morrison and Dr. David Rogers for their tireless discussions and help on solving my puzzles on computational chemistry. Also, Dr. Morrison's online lectures on Moodle were extremely helpful for my research topic. Thanks to Dr. Nichol S. Gary for his guidance on solving crystal structures; Dr. Ronald Brown for his guidance and help on performing XPS measurement; Dr. Andrei Gromov for his time on helping me with the Raman measurement; Dr. Andrew Schofield for his guidance on using the SEM; Dr. Dimitrios Kampouris for his tireless discussion and guidance on the supercapacitor studies; Dr. Julia Payne for the discussions on doping studies and her help on performing TEM measurement; and of course all the staff in the school of Chemistry for making here such a great place for research and study.

Besides research study, I would like to thank so many people for offering me help over my different roles in the university. Dr. Chris Mowat and Dr. Anna-Maria Maciejuk must be thanked for their help on the school Internationalization and Public engagement event organization; Dr. Caroline Kirk and Dr. Murray Low for their guidance and trust of me working as an undergraduate lab demonstrator; Dominic Lewis, Geraldine Harvey and everyone in Reslife for their help over my resident assistant (RA) role, and taught me about the working attitude; Elizabeth Harris and Hasa Reddy for being my RA partner in Ratcliffe Terrace accommodation; and all of the lovely residents who made Ratcliffe Terrace into a big and warm family for everyone.

I would like to thank EPSRC SuperSolar Hub and Solar Fuels Network for offering me opportunities to attend international conferences, from where I broadened my research horizons and built my network.

The supercapacitor studies in our group were initiated in April 2018, and Dr. John Mallows was focusing on the initial experimental set up and Bi-based electrode materials screening during his three-month project funding period here. This work was followed up by Keir Adams, who was a project student working with the author, with more in-depth studies on the supercapacitor mechanisms and device optimizations. Therefore, the supercapacitor electrode material studies based on both $Bi_{13}S_{18}I_2$ and TBI are included in this thesis, since the author directly supervised and assisted Alba and Keir during their project time, carried out the material characterization and supercapacitor study for TBI independently, and drafted the paper for both $Bi_{13}S_{18}I_2$ and TBI study.

Finally, I would like to thank all my friends in Edinburgh and across the world for your support and love. Most importantly, I would express my deepest gratitude to my parents who have been consistently offering me support over my PhD study, both morally and financially. Even though they are thousands of miles away from me, their unconditional love and support are always the most powerful and precious motivation for me over my PhD study, and for my future life journey.

Lay Summary

Low-cost, stable and solution-processable materials have attracted significant research interest for their green and economical applications in solar energy harvesting and energy storage. The rapid emergence of lead-halide perovskites solar cells along with their ever-increasing efficiency has led to a new era of solar energy research. Lead-based perovskite solar cells are central to the efficiency rise, however, the toxicity of lead and its adverse effects on the environment have raised lots of concern. At the same time, research into supercapacitor electrode materials with desirable properties are crucial, as supercapacitors featuring high power density, quick charge-discharge rates and long cycle life are ideal for future energy storage.

In this thesis, different non-toxic bismuth-based materials have been synthesised and studied in order to investigate their potential as solar absorbers and supercapacitor electrode materials. Experimental investigations into their crystal structures, optical properties and electrochemical properties were carried out, together with device studies based on solar cells and supercapacitors to further probe their light harvesting and energy storage performances.

To sum up, the initial work in this thesis expands the material types available for developing the lead-free solar absorbers and supercapacitor electrode materials. This work also sheds light on the material design and device optimization of bismuth-based perovskite-like materials for solar cell and supercapacitor applications.

Abstract

Low-cost, stable and solution-processable materials have attracted significant research interest for their green and economical applications in solar energy harvesting and energy storage. The rapid emergence of lead-halide perovskites solar cells along with their ever-increasing efficiency has led to a new era of solar energy research. Lead-based perovskite solar cells are central to the efficiency rise, however, the toxicity of lead and its adverse effects on the environment have raised lots of concern. At the same time, research on supercapacitors electrode materials with desirable properties are crucial, as supercapacitors possess high power density, quick charge-discharge rates and long cycle life.

In the first chapter, background knowledge about solar technology will be discussed, with emphasis on perovskite solar cells within the third generation of photovoltaic technology. Moreover, studies on bismuth-halide complexes will be discussed in detail to pave the road for explanation and discussion of the main research topic. In the first two chapters of the results and discussion section, hybrid iodobismuthates with heterocyclic cations have been synthesized and studied, including $[C_5H_6N][BiI_4]$ (**$[PY][BiI_4]$**), $[C_6H_8N][BiI_4]$ (**$[MEPY][BiI_4]$**), $C_3H_5N_2SBiI_4$ (**$[AT][BiI_4]$**) with 1D structure, together with 0D $[C_3H_5NS]_3Bi_2I_9$ (**$[TH]_3[Bi_2I_9]$**) and $[C_4H_6N_2]_3Bi_2I_9$ (**$[PZ]_3[Bi_2I_9]$**). Their structures have been investigated by single crystal X-ray diffraction, and one-dimensional $[BiI_4]^-$ anionic chains built by edge-sharing $[BiI_6]^{3-}$ octahedra were found in all the 1D materials; alongside short I…I, I…C contacts and hydrogen bonding of **$[PY][BiI_4]$** and **$[AT][BiI_4]$**, giving rise to three-dimensional intermolecular interactions. All the compounds are semiconductors, with band gap values around 2.0 eV. Larger band edge dispersions of electronic band structures for 1D materials were calculated compared to 0D materials, and the contributions from the organic moieties to the conduction band minimum has been derived by density functional theory. Solid-state optical and electrochemical studies performed on materials as thin films were carried out, and their stabilities under ambient environment have been demonstrated. **$[PY][BiI_4]$** and **$[AT][BiI_4]$** were used as the absorber layer in printable mesoscopic solar cells without hole-transport material, leading to efficiencies up to 0.9% (0.47% for **$[AT][BiI_4]$**), showing a promising new approach towards the development of lead-free third-generation photovoltaic materials. Additionally, solar cells with carbon counter electrode and **$[AT][BiI_4]$** as light harvester have shown interesting results as lead-free solar energy generator/storage integration devices.

In chapter 5, band gap engineering of 0D $Cs_3[Bi_2I_9]$ and 1D **[PY][BiI$_4$]** has been studied and achieved by incorporating 2^- anions (including S^{2-}, SiF_6^{2-}, and TiF_6^{2-}) into the crystal lattice, by the drop-casting and bismuth xanthate thermal decomposition method. In both cases, about 0.3-0.4 eV decrease in band gap values can be found. Powder XRD data collected on the dianion-treated thin films shows no structural change to the original samples, suggesting the crystal structure of **[PY][BiI$_4$]** and $Cs_3[Bi_2I_9]$ remained unchanged after the dianionic treatment. The existence of sulfur in S-treated **[PY][BiI$_4$]** as thin films has been confirmed by EDS and SEM, and HRTEM images showed good crystallinity of the doped **[PY][BiI$_4$]** thin films. Raman Spectroscopy on 2^- treated thin films showed the existence of Bi-S bonds in both cases, suggesting that some S atoms are partially substituting iodine atoms in the crystal lattice.

In Chapter 6 of this thesis, eco-friendly, solution-processable and stable Bi-based materials are studied for energy storage applications in electric double-layer capacitors (EDLCs). Firstly, we demonstrated a novel synthetic route for films of an underexplored 3-D hexagonal bismuth chalcohalide, $Bi_{13}S_{18}I_2$, and investigated its potential as the active electrode material in EDLC-type supercapacitors. The synthetic procedure has been optimised and comprises of the lowest annealing temperature (150°C) and the shortest processing time (1 h) currently reported. When integrated in a symmetrical EDLC with an aqueous $NaClO_4$ electrolyte, the $Bi_{13}S_{18}I_2$-based device achieves a remarkable areal capacitance of 210.68 mF cm^{-2} with 99.7% capacitance retention after 5000 cycles. Both the $Bi_{13}S_{18}I_2$ powder and thin-film electrodes have been characterized through XRD, XPS, Raman spectroscopy, and SEM. Secondly, organic-inorganic $[CN_2SH_5]_3[BiI_6]$ (TBI) was synthesized and characterized. Single crystal X-ray diffraction study reveals that TBI crystallizes in monoclinic system, with discrete $[BiI_6]^{3-}$ octahedra as the inorganic motif. Utilizing TBI as the active supercapacitor electrode material, together with carbon cloth current collector and neutral $NaClO_4$ water solution as the electrolyte, we have achieved an electrode areal capacitance over 3.22 F cm^{-2} and specific capacitance over 1030 F g^{-1} when the device operates as an EDLC. The supercapacitor device shows superior capacitance retention after 5,000 charge-discharge cycles. The superior stability, low-cost, and facile synthesis of both $Bi_{13}S_{18}I_2$ and TBI prove the promising potential of Bi-based materials for supercapacitor applications.

To sum up, the initial work in this thesis expands the material types available for developing lead-free Bi-based solar absorbers and supercapacitor electrode materials. This work also sheds light on the material design and device optimization of Bi-based perovskite-like materials for solar cell and supercapacitor applications.

Abbreviations

^{1}H NMR	Proton Nuclear Magnetic Resonance
AM1.5G	Air Mass 1.5 Global
AT	2-aminothiazolium
B3LYP	Becke's three parameter exchange functional with the Lee-Yang-Parr
CBI	Cesium bismuth iodide
CPE	Constant phase element
CV	cyclic voltammetry
DCM	Dichloromethane
DFT	Density Functional Theory
DMF	Dimethylformamide
DMSO	Dimethylsulfoxide
DSSC	Dye-Sensitized Solar Cells
EDLC	Electric double-layer capacitor
EIS	Electrochemical impedance spectroscopy
ESR	Equivalent series resistance
FF	Fill Factor
FTO	Fluorine Doped Tin Oxide
HOMO	Highest Occupied Molecular Orbital
HRTEM	High resolution transmission electron microscopy
IM	Imidazolium
IPCE	Incident Photon-to-current Conversion Efficiency
J_{sc}	Short Circuit Current Density
J-V	Photocurrent density-Voltage
LUMO	Lowest Unoccupied Molecular Orbital

MEPY	2-Methylpyridinium
PCE	Power conversion efficiency
PTFE	Polytetrafluoroethylene
PY	Pyridinium
PYZ	Pyrazinium
SEM	Scanning electron microscopy
TBI	Thiourea bismuth iodide
TEM	Transmission electron microscopy
TH	Thiazolium
TD-DFT	Time-dependent DFT calculations
V_{OC}	Open Circuit Voltage
W	Warburg impedance element
XRD	X-ray diffraction
XPS	X-ray photoelectron spectroscopy
Y_0	Numerical value of admittance at $\omega = 1$ rad/s
Z	Complex Impedance

Contents

Chapter 1: Introduction

1.1 World Energy Consumption and Challenge

The ever-increasing global energy demand has been urgently challenging human beings. The latest data from the BP Statistical Review 2018 of World Energy, points out that fossil fuels (oil, natural gas and coal) continue to dominate, suppling 85% of global energy consumption (**Figure 1.1**).[1]

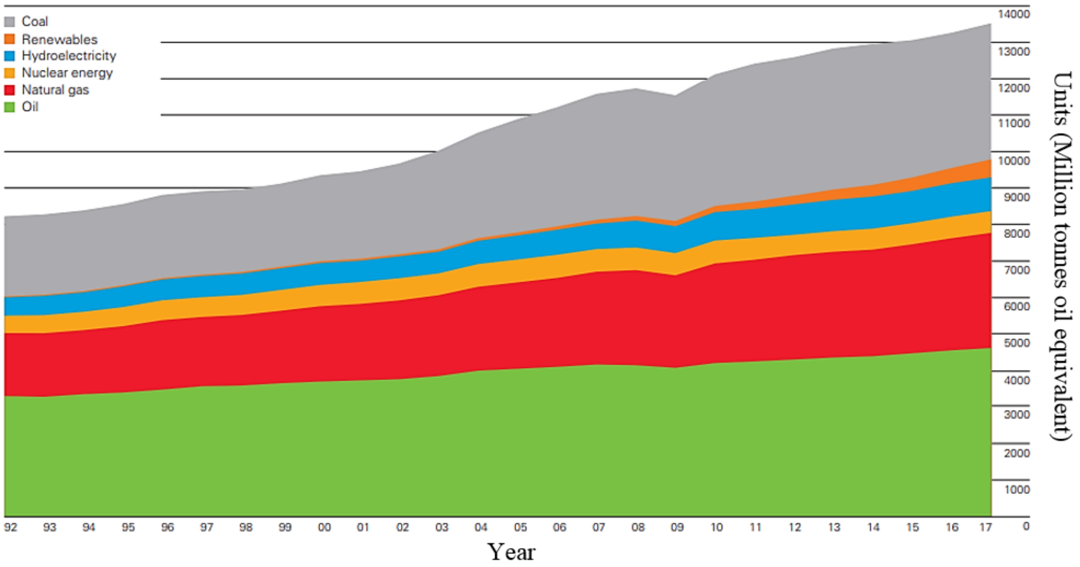

Figure 1.1 World primary energy consumption by source from 1992 to 2017. Figure is reproduced from Ref. 1.

There are three main aspects of the energy challenge. First is the problem of energy demand and supply. The ever-increasing population, economics and other social factors is leading to the continuous increase of energy demand.[2] Secondly, the overall energy infrastructure largely depends on the burning of fossil fuels, and the depletion of the fossil fuels is much faster than their regeneration rate. In this case, natural resources including natural gas, petroleum and coal are depleting, which raise concerns over possible energy shortage issues. The third aspect is the environmental challenge brought by excessive consumption of fossil fuels, which adversely affects the environment and causes acid rain, air pollution and global warming.[2]

1.2 Renewable Energy

The ever-increasing demand for the provision of energy and the environmental issues from burning fossil fuel call for the development of sustainable and renewable energy, which can be obtained from wind, sunlight, rain, tides, waves, and geothermal heat.[3] Switching to the renewable energy not only brings about benefit to the economy, but also addresses the requirement for environmental protection.[4] Solar energy has a good reputation as the most promising candidate for future energy, as it is inexhaustible, clean, renewable, and widely distributed on the planet. Solar energy can be harnessed by using solar water heating, which directly turns the solar energy into heat or stores it in energy storage materials; or by photovoltaic systems, which transform solar energy into electricity. The latter scheme forms the subject of this thesis.

1.3 Solar Cells

1.3.1 Basic concepts in photovoltaic technologies

1.3.1.1 Properties of Sunlight

Sunlight is a form of electromagnetic radiation, originated from nuclear fusion reactions at the centre of the sun. The radiation from the interior is then absorbed by H ions at the surface and re-emitted from the outer surface of the sun, which gives rise to the approximation radiation with the temperature of 5777 K.[5] The most intense irradiance from the sunlight is at the visible light region (**Figure 1.2**), with a wavelength range of 400-700 nm. The pathway for the sunlight to travel to the earth is referred as Air Mass (AM), which can be approximated by $1/\cos\theta$, where θ is the angle between the sun and the direct overhead point. Air Mass Zero (AM0) is defined as the spectral irradiance from the sun without any atmospheric absorption (**Figure 1.2**, yellow part), which is determined to be a constant value of 1.3661 kW/m^2. However, owing to the difference of atmosphere thickness and the angle of incident sunlight, as well as the partial absorption caused by the H_2O, CO_2, O_2 and O_3 in the atmosphere, the solar spectral power density on the earth's surface is much less than AM0 (**Figure 1.2**, red part). For photovoltaic work, AM1.5 is used as the standard radiation, normalised to an integrated power of 1 kW/m^2. [6]

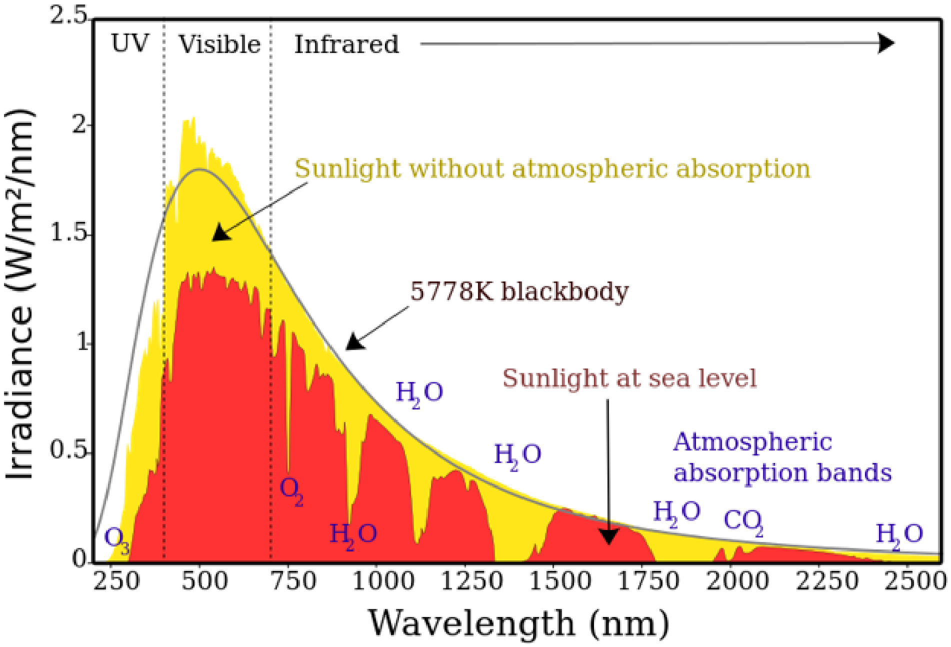

Figure 1.2 Solar irradiance spectrum before (yellow) and after (red) atmospheric absorption by different atmospheric absorption bands. Figure is reproduced and reformatted from Wikipedia.

1.3.1.2 Photovoltaic Effect

The photovoltaic (PV) effect is the generation of voltage by photovoltaic materials under light illumination, discovered by Alexandre Edmond Becquerel in 1839.[7] Photons carry energy, and when the photons with suitable energy (higher than the bandgap value of PV materials) are incident onto the PV materials, energy from the light can be absorbed and transferred to electrons, which leads to the photoexcitation of electrons. Excitation of electrons causes the generation of excitons, which subsequently undergoes charge separation and forms charge carriers - electrons and holes.[6] The electrons jump onto higher energy levels, namely the conduction band (CB), while leaving an empty vacant hole in the valence band (VB).[8] The energy difference (ΔE) of the initial and final states can be calculated by $\Delta E = h\nu$. Different from the photoelectric effect that photoelectron is emitted into vacuum level, here light-generated carriers stay within the semiconductor material. The photovoltaic effect at a P-N junction with an external load is illustrated schematically in **Figure 1.3**. In this case, electrons are accumulated at the n-type side while holes gather at p-type side, preventing them from recombining with each other. The extra energy from the excited electrons leads to the generation of a potential difference, which drives the electrons to travel through the load in the external circuit.[9]

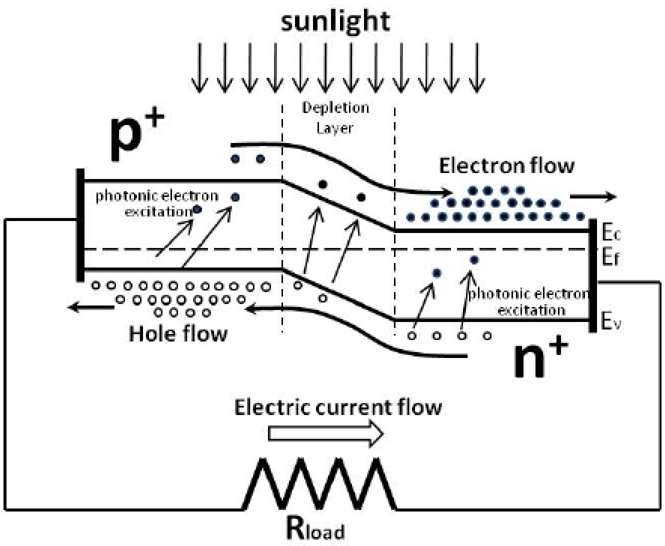

Figure 1.3 Schematic diagram of photovoltaic effect at a P-N junction with an external load. The photo-generated electrons flow through the conduction band of n-part diode while the photo-generated holes flow through the p-part diode. Figure reformatted from ref. 9

1.3.1.3 Solar cell parameters

I-V curves

A p-n junction is widely found in solar cell devices, where electrons and holes can be extracted selectively into two difference terminals to generate current. Due to the semi-conducting feature and photovoltaic properties, the solar cell performs as a diode in the dark while generating photovoltage when exposed under light. I-V curve measurement of solar cells characterizes the solar cell performance. As shown in **Figure 1.4**, the light-generated I-V curve of a solar cell under illumination is superimposed upon the rectifying I-V curve of a diode when the solar cell is in the dark. Due to the PV effect, I-V curve has been shifted down to the fourth quadrant and thus power can be extracted from the diode.[10]

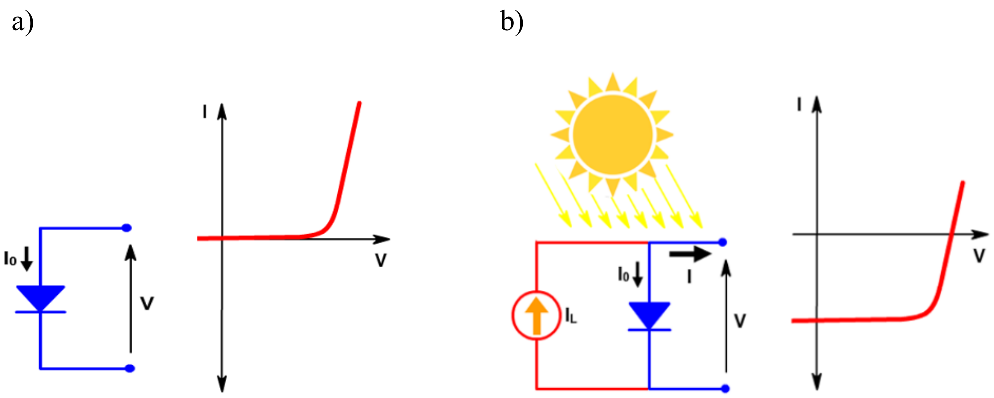

Figure 1.4 The effect of light on the I-V curve from a photovoltaic diode in the dark (a) and under sun illumination (b). Figures are reproduced from PVeducation.org website

When testing the solar cell performance, external electrical bias is added to dictate the potential drop due to the load in the external circuit. The Shockley diode equation describes the calculation of diode current (I) under forward or reverse applied bias.[11]

$$I = I_0[\exp\left(\frac{V_D}{nV_T}\right) - 1] \quad \text{(Equation 1.1)}$$

Where

I_D is the diode current,

I_0 is the reverse bias situation current,

V_D is the voltage across the diode,

V_T is the thermal voltage,

n is the ideality factor or emission coefficient.

Under light illumination, photo-generated current (I_L) is added and thus the diode current can be revised as:

$$I = I_0\left[\exp\left(\frac{V_D}{nV_T}\right) - 1\right] - I_L \text{ (Equation 1.2)}$$

For convenience, the I-V curve is commonly flipped to the first quadrant. A typical I-V curve of a solar cell is shown in **Figure 1.5**, where

I_{sc}: short-circuit current

V_{oc}: open-circuit voltage

I_{mp}: maximum power current

V_{mp}: maximum power voltage

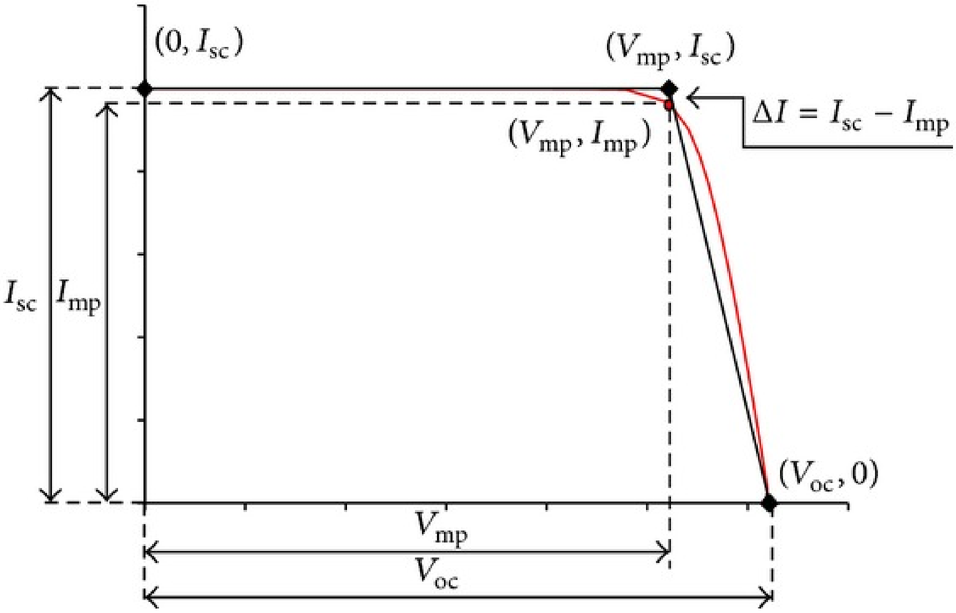

Figure 1.5 A typical I-V curve of a solar cell. Figure is reproduced from ref. 10.

Short-circuit current (I_{sc})

Short-circuit current (I_{sc}) describes the maximum current flows over the solar cell device when the voltage across the cell is zero, i.e., when the cell is short-circuited. Ideally, I_{sc} is the maximum current a solar cell can achieve assuming there is no energy loss. Short-circuit current can be influenced by other parameters, including incident light spectrum and intensity, the area of solar cell active area, the solar absorber light-harvesting properties, recombination rate of charge carriers and so on. In standard solar cell testing, a mask is used to quantify the incident area so that current density (J_{sc}) can be calculated. Standard light source (AM=1.5) is used to control the incident light intensity and spectrum.

Open-circuit voltage (V_{oc})

Accordingly, V_{oc} refers to the maximum voltage that can be achieved by a solar cell device when there is no current flowing through. This is largely determined by the energy levels of the PV materials, either the HOMO-LUMO gap of the organic light absorbers or the bandgap value for inorganic and hybrid PV materials. Other characteristics can also influence the V_{oc} value, including the recombination rate of charge carries, charge carrier concentration and the light source intensity.

Fill factor (FF)

FF describes the ‘squareness’ of the I-V curve, and it is defined as the ratio of the maximum power from the solar cell over the product of V_{oc} and I_{sc}. It can also be graphically described as the area ratio of the largest square that can fit into the I-V curve over the square defined by V_{oc} and I_{sc}. Aspects that play an important role in determining the fill factor includes the recombination rate, series resistance of the solar cell device, the shunt resistance, all of which are also linked to the grain boundary of the crystalline solar absorber material.

Power conversion efficiency (PCE)

PCE (η) manifests the solar cell performance in a direct way, which is defined as the ratio of output energy/power by the solar cell to the input energy/power from the sun. Since the solar testing condition for a solar cell has been standardized, the value for input power from the solar simulator is 1 kW/m^2. The maximum output power can be calculated from the I-V curve, where $P_{max} = V_{oc} \cdot I_{sc} \cdot FF$ (Equation 1.3).

1.3.1.4 Quantum Efficiency

Quantum efficiency (QE) indicates the amount of current that a solar cell can produce under illumination at different wavelengths. There are two types of quantum efficiency – internal (IQE) and external (EQE). EQE is defined as the ratio of the number of charge carriers collected by the solar cell (*Ne*) over the number of photons from the incident light onto the solar cell (*Np*), while IQE is the fraction of absorbed photons that are being converted into electrons. The equation for calculating EQE and IQE are shown below

$$EQE = \frac{N_e}{N_p} \cdot 100\% = \frac{1240\, J_{sc}}{\lambda \cdot P_m} \text{ (Equation 1.4)}$$

$$IQE = \frac{EQE}{1-R} \text{ (Equation 1.5)}$$

Where J_{sc} is the short circuit current density (unit: A·cm^{-2}), λ is the wavelength (unit: nm), P_m is the luminous flux (unit: W·cm^{-2}), and R is the reflectivity. Since 1-R is always less than 1, the IQE measured is always higher than the EQE for a given device.

A typical QE graph is shown in **Figure 1.6**, where the efficiency is plotted against the wavelength. Ideally, the QE curve is a square, where 100% of incident light are absorbed and converted into electrons. However, there are many factors that can affect the QE of a solar cell device. For EQE, optical loss is one of the most important factors, where transmission and reflection of the incident light happens at the incident surface. The bandgap value of a PV material decides the ability to absorb photons with different wavelengths. At the same time, charge collection ability also significantly affect the EQE value, where the photo-generated excitons can separate and be collected at the interfaces and junctions. IQE losses occur due to recombination of photo-generated charge carriers in the PV material, with reasons including defects in the semiconductors, limited charge carrier diffusion length, material interface properties, energy level mismatches, etc.[11] In solar cell studies, EQE is also quoted as incident photon-to-current efficiency (IPCE), while IQE is quoted as absorbed photo-to-current efficiency (APCE). The integration of EQE curve over all the wavelength range gives rise to the J_{sc} of the solar cell device.

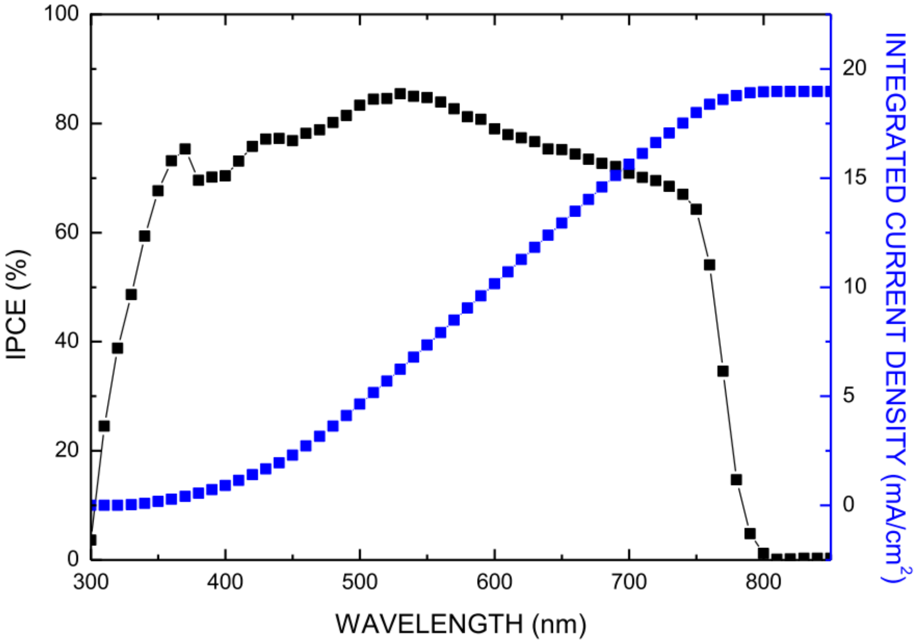

Figure 1.6 A typical IPCE curve of a perovskite solar cell (black) with the integrated product of the IPCE curve under AM 1.5 photon flux (integrated current density, blue). Figure was reproduced from the literature.[13]

1.3.1.5 Shockley-Queisser limit and ideal band gap for solar cells

Shockley-Queisser limit, also known as detailed-balance limit, was discovered by William Shockley and Hans-Joachim Queisser in 1961, refers to the maximum theoretical efficiency of a single-P-N junction solar cell under AM 1.5 solar spectrum, which is around 33.7% at band gap value of 1.34 eV.[14] This theoretical value was calculated based on the amount of electrical energy that can be extracted from the incoming photon.[15] There are three main reasons that leads to the energy loss from the photons:

- Blackbody radiation

The blackbody radiation effect refers that any object that is at a temperature above 0 K will emit electromagnetic radiation. In the case of solar cells, about 7% of the energy loss is caused by this blackbody radiation effect when the solar cell is operating at room temperature.

- Spectrum losses

  The photo-generated electron-hole pair generation requires the incident photon carries larger energy than the energy difference between valence band and conduction band of the semiconductor, namely the band gap value. Therefore, photons with energy that are less than the band gap energy value will not contribute to power production, which lead to the spectrum loss. The theoretical study shows that for silicon-based solar cells with a band gap value about 1.1 eV has a spectrum loss of about 20% under 1.5 AM illumination.

- Electron-hole recombination

  The generation of electron-hole pair under illumination is desirable for photovoltaic applications; however, the recombination of photo-generated electrons and holes happens at the same time, especially common to be found at the crystal grain boundaries, interfaces and defect points.

The maximum efficiency of a single-junction solar cell versus the band gap value of solar absorber is illustrated in **Figure 1.7**.

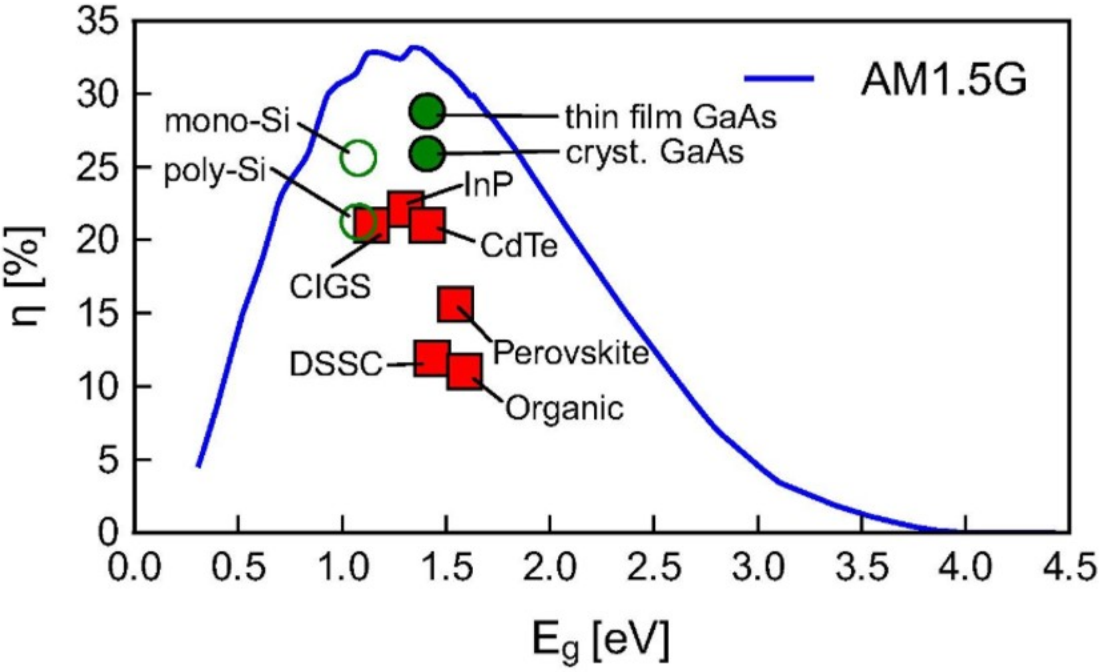

Figure 1.7 The maximum light to electric power conversion efficiency (Shockley-Queisser limit) for a solar cell operated at 298.15 K and illuminated with the AM 1.5G spectral irradiance in accordance with standard solar test conditions as a function of the band gap energy. Figure regenerated from ref 15.

1.3.1.5 A brief history

Solar cells are devices generating electricity from sunlight by using the photovoltaic mechanism, and Charles Fritts made the first photovoltaic cell by using selenium on a thin layer of gold in 1883.[16] In 1905, Albert Einstein explained the photoelectric effect, recognizing that the energy of light is carried in a discrete quantized manner, which led energy into the new quantum era.[17] After the first practical solar cell made by Daryl Chapin, Calvin Souther Fuller and Gerald Pearson in 1954, improvements and optimizations have been made to reduce the cost of cell fabrication and enhance the efficiency.[18]

1.3.2 First generation: Silicon-based solar cells

The most prevalent commercialized solar cell today is the silicon-based solar cell, which dominates more than 90% of the PV market, including forms of crystalline, multi-crystalline, and micro-crystalline silicon.[19] This is known as the first generation of photovoltaics, which shows high power conversion efficiency (up to 25%) and long-term durability (more than 25 years). However, silicon-based PV materials have an indirect band gap, which leads to inefficiency of light absorption. To achieve the best absorption for the solar cell, a thick and bulky solar absorber layer is needed, which increases the cost and also limits the flexibility.[20] Moreover, costs of fabrication and purification of the absorber layer are hard to reduce even after decades of developments, and the manufacture of silicon also adversely affects the environment to some extent. New technologies that employ low-cost and effective light absorbing materials and with more versatile applications are under investigation.

1.3.3 Second generation: Thin-film solar cells

In the 1970s, the second generation of solar cells, known as thin-film solar cells, was first studied and is now widely commercialized. Cadmium telluride (CdTe), copper indium gallium diselenide (CIGS) and amorphous silicon (a-Si) are three thin-film technologies that nowadays have often been used for outdoor photovoltaic applications.[21] Compared to the crystalline silicon solar cell, thin-film photovoltaics are materials with a direct band-gap (of about 1.45 eV for CdTe),[22] which have higher absorbance coefficients and thus a thinner layer of the material is required. However, as the natural abundance of indium, tellurium and selenium is quite low, and also the toxicity of cadmium is of concern, whether the current thin-film solar cells can be extensively applied is questioned.

1.3.4 Third generation: OPV, DSSC, QD and perovskite solar cells

The third generation of photovoltaic technology includes organic solar cells (OPV), dye-sensitized solar cells (DSSC), quantum-dot solar cells and perovskite solar cells.[23-24] The first high-efficiency DSSC was studied and reported by Michael Grätzel and Brian O'Regan in 1991, which opened a new era for the study of photovoltaics. This was a milestone for DSSC, which may have potential merits ranging from ease of manufacture to low cost. Recently these new technologies are opening up broader applications, including multi-coloured, flexible, semi-transparent and portable solar cells. However, problems like poor stability for long-term applications and relatively low efficiency compared to silicon-based solar cells call for further improvements to DSSCs.[25] Instead of using bulk semiconductor materials, quantum-dot solar cells utilize semiconducting particles with reduced size to nanoscale. In this case, the nanoparticle radius is below the exciton Bohr radius, and therefore the electron energy levels within the quantum particles become finite, so that their energy levels and band gaps can be tuned by changing the particle sizes.[26] Another family of third generation photovoltaics is the perovskite solar cell. In the last few years, the rise of metal halide perovskites as solar absorbers has stunned the community of photovoltaics.[27] Since 2009 when methylammonium lead iodide/bromide was first used in a liquid-electrolyte DSSC with efficiency of 3.8%,[28] the efficiency race has continued, reaching up to 22.7% power conversion efficiency (PCE) as of Dec. 2018.[29] Due to the inexpensive materials, and also the printing methods which brings about low-cost manufacturing, perovskite solar cells may offer a bright future in the development of photovoltaics.[27] The best research cell efficiencies for different types of PV technologies are indicated in **Figure 1.8** for comparison.

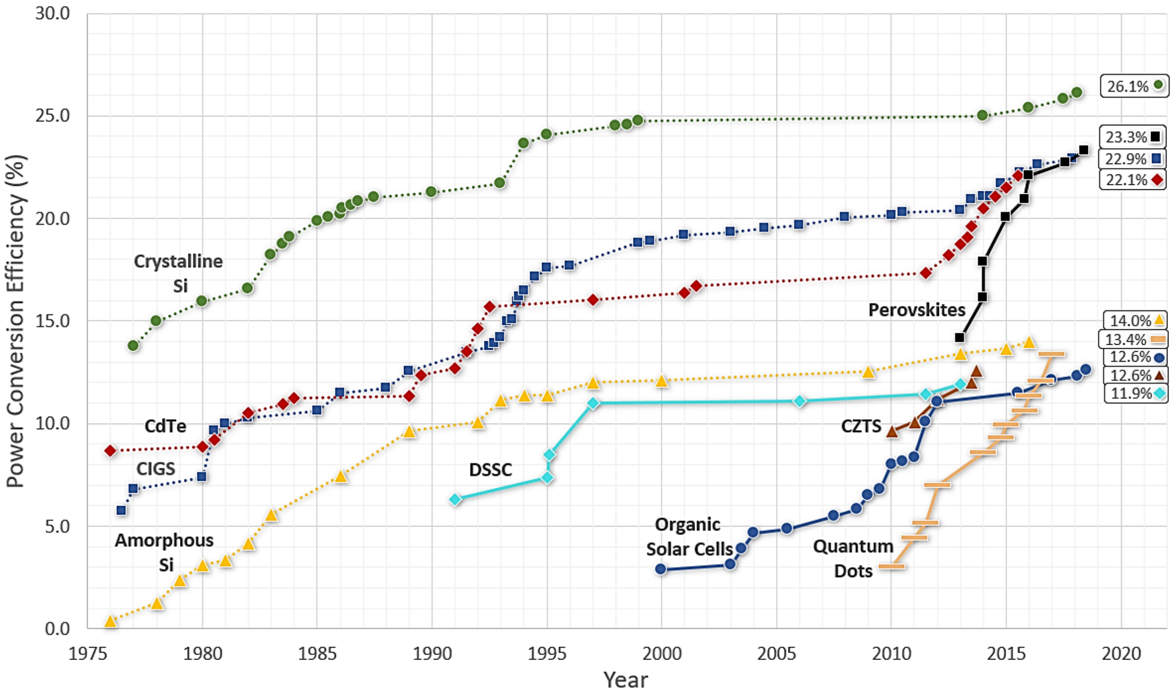

Figure 1.8 Research cell efficiencies of different types of photovoltaic technologies. This graph uses data taken from the NREL solar cell efficiency chart [29]

1.4 Perovskite Solar Cells

1.4.1 The crystal structure of perovskite

Perovskite is the mineral calcium titanate (chemical formula: $CaTiO_3$), and nowadays any material with the same crystal structure as $CaTiO_3$ belongs to the perovskite family. Generally, compounds adopting the formula of ABX_3 are classed as perovskites, where A and B are two cations and X is an anion. Ideally, the larger A anion is in a 12-fold cuboctahedral coordination sphere with twelve X anions, while the smaller B cation occupies the octahedral site surrounded in an octahedron manner by six anions.[30] Applications for the thousands of different materials with this structure have been investigated, including thermoelectric, semiconducting and superconducting materials.[31] The most-studied perovskite material, methylammonium lead iodide perovskite, $CH_3NH_3PbI_3$, is used as a light absorber, whereby Pb (II) occupies the octahedral site while the methylammonium cation is on the cube-octahedral site (**Figure 1.9**).[32] The symmetry of a particular perovskite is dependent on the relative ion sizes, and the three-dimensional structure results from the stoichiometry of organic cations and metal halides. It is observed that with increased dimensionality from 2D (A_2BX_4) to 3D (ABX_3), a narrower band gap is observed, which is beneficial for solar cell applications.

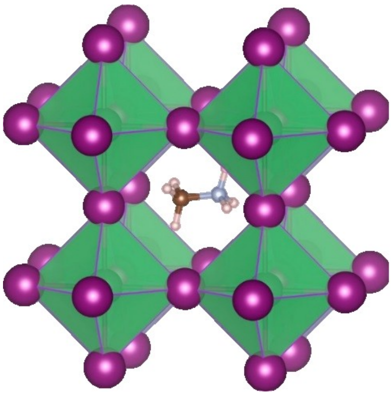

Figure 1.9 Unit cell of cubic Methylammonium lead iodide perovskite. Purple sphere: I; green octahedra: PbI_6 ; methylammonium is illustrated in brown (C); blue (N) and pink (H). Figure reproduced from ref. 32.

1.4.2 Recent Development of Perovskite solar cells

Three-dimensional $[CH_3NH_3][PbX_3]$ (X=Cl, Br, I) perovskite were incorporated as light harvesters in the liquid state DSSC in 2009 by Kojima *et al*, with 3.1% PCE for X=Br and 3.8% for X=I.[28] This relatively low efficiency compared to the best DSSCs at that time did not draw too much attention, and also fast degradation when contacting with oxygen and humid was observed at that time. Two years later, Park *et al* deposited $CH_3NH_3PbI_3$ perovskite on TiO_2 to produce a thin film. He has also demonstrated that the absorption of lead iodide perovskite was much greater than the ruthenium-based dyes typically used in DSSCs. The poor stability problem in the liquid-state solar cell was not solved until solid-state hole transport material (spiro-MeOTAD) was applied by Park *et al*, which led to cells with PCE of 9.7%.[33] Another key alternative was made by Lee *et al*, whereby the electron transport material TiO_2 was substituted by a mesoporous Al_2O_3 scaffold. This also led to the discovery that lead-halide perovskite itself could transport electrons as the large bandgap of Al_2O_3 does not assist in electron extraction.[34] Almost at the same time, Etgar *et al* observed that $CH_3NH_3PbX_3$ (X=Cl, I) could also work as a hole-transport material in addition to its functionality as a light absorber, and the PCE of the HTM-free perovskite solar cells has increased from 5% to 12.8% during the last few years.[35] The multi-functionality of perovskite as an ambipolar semiconductor material prompted the possibility of planer geometry with even thinner devices and potentially lower cost.[27] The ever-increasing PCE of perovskite solar cells has been realized by enhanced deposition methods or by composition engineering of perovskite materials,[33,34] and hit 21.7% efficiency with record-level reproducibility.[29]

1.4.3 Perovskite solar cell architectures, mechanisms and fabrication

The general device architecture for solid-state organic-inorganic perovskite solar cells is shown in **Figure 1.9A**.[38] In this type of structure, the light absorber (perovskite) is sandwiched between an HTM (p-type material, e.g., spiro-MeOTAD) and a mesoporous scaffold (n-type material such as TiO_2) The whole solar cell device is completed with FTO-coated glass as working electrode and a thin layer of gold as the counter electrode.

A)

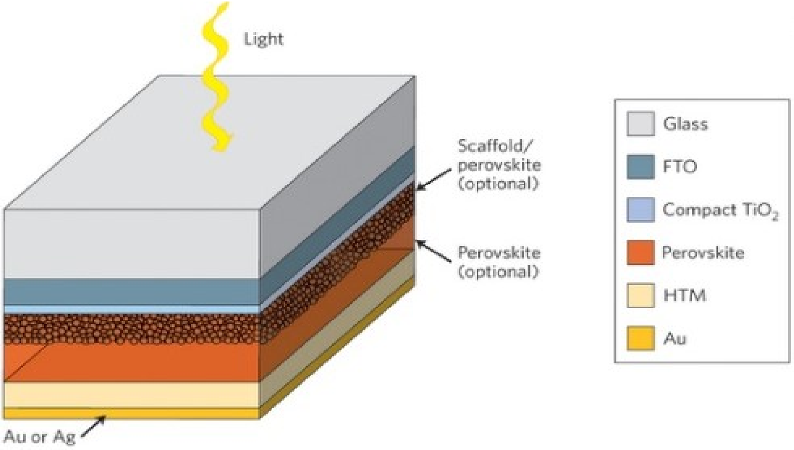

B)

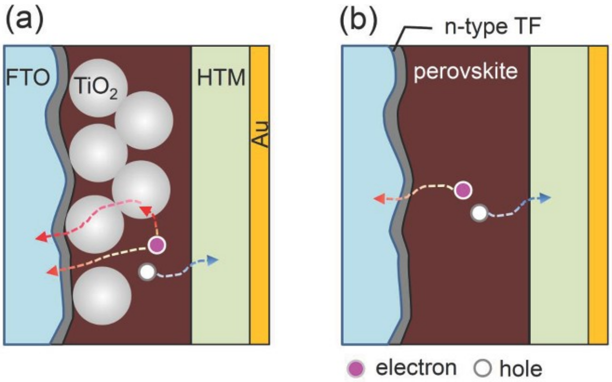

Figure 1.10 (A) General solid-state perovskite solar cell device structure, reproduced from reference; (B) Charge generation and excitation in mesoscopic (a) planar structure (b) perovskite solar cell, reproduced from reference.[39]

Figure **1.10 B** presents the excitation and charge generation process in mesoscopic perovskite solar cells (with mesoporous TiO_2 layer) (a) and in the planar-structured perovskite solar cell (b). When the incoming photon is absorbed by perovskite, electrons will be excited from ground state to excited state (typically from valence band to conduction band), leaving a hole with positive charge behind. This is followed by the emergence of free charge carriers, and the contacts of an electron transport material (typically TiO_2) and hole transport material (HTM) lead to the extraction of these free charge carriers due to the difference of energy levels. Specifically, injection of photo-generated electrons into TiO_2 and injection of photo-generated holes into HTM (as shown in **Figure 1.10 Aa**) occurs, giving a photovoltage that can generate current in the circuit. In the planar-structured perovskite solar cell, the mesoporous layer of TiO_2 is missing, as lead-halide perovskite itself can conduct both holes and electrons. Compared with mesoscopic perovskite solar cells, less recombination of photo-generated charge carriers was found in the planar solar cells due to a smaller interface area.[38] It also has been experimentally proven that the solar cells still show high efficiency even when the mesoporous TiO_2 was replaced with an insulating alumina framework.[34]

Energy levels of perovskite materials and charge-extracting materials should be carefully considered, as the selective extraction of electrons and holes is driven by energy level differences. Therefore, it is essential to consider the energy levels of different components in a solar cell, and the rate of charge separation and injection must be faster than the rate of recombination or annihilation. The electron transfer processes (green arrows) within the HTM/perovskite/TiO_2 cell and undesired electron-hole recombination processes (orange arrows) are shown in the scheme illustrated in **Figure 1.11**. [40]

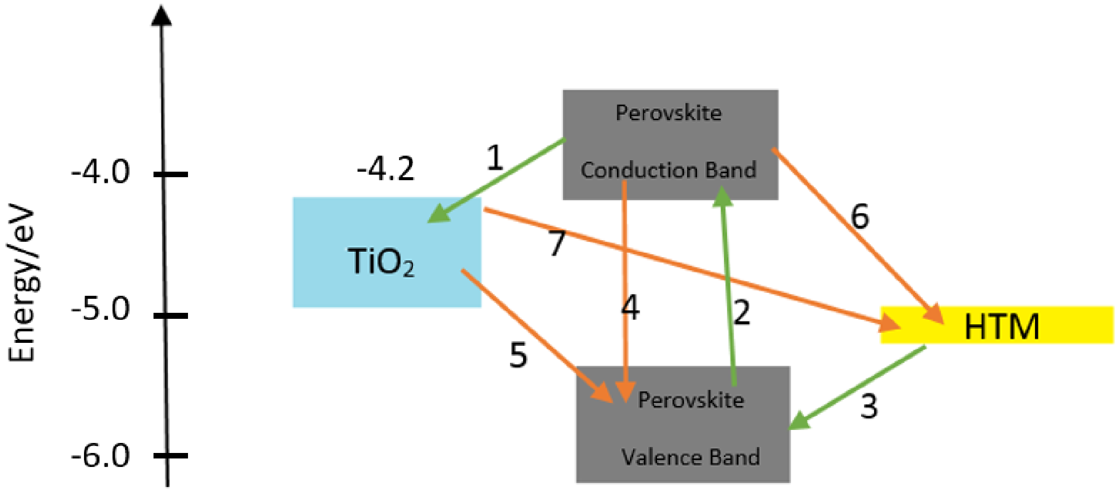

Figure 1.11 Schematic diagram of energy levels and electron transfer processes in a perovskite solar cell. Green arrows: desirable photo-generated electron transfer process; red arrows: possible electron-hole recombination process. Figure regenerated from ref 40.

1. Electron excitation from valence band to conduction band of the perovskite.
2. Electron injection into TiO_2
3. Hole injection into the HTM.
4. Radiative or non-radiative decay of the excited state.
5. Back transfer of electron at the surface of TiO_2
6. Back transfer of electron at the surface of the HTM
7. Recombination process on the interface of TiO_2 and HTM

1.5 Studies on lead-free perovskite solar absorbers

Lead halide perovskite solar cells have many advantages including high efficiency approaching that of silicon cells and low-cost fabrication. Nevertheless, lead is a heavy metal, which is toxic to human beings and harmful to the ecosystem. Once the lead-halide perovskite solar cells have been widely commercialized, there will be constant concerns over the leakage of lead and the improper disposal of waste cells. To address the toxicity issue, there has been research on lead-free metal-halide photovoltaics, and recently potential substitutes including tin, antimony and bismuth have been studied.

1.5.1 Tin-based solar absorbers

The most obvious candidate for substituting lead is tin (Sn), which is also a group 14 element with similar atomic radius to lead. Noel *et al* reported that substituting lead with tin forming perovskite as $CH_3NH_3SnX_3$, led to PCE over 6%.[41] Inorganic and mixed halide tin-based perovskite solar cells were studied with efficiency around 6%, made by $CsSnI_3$ and $CH_3NH_3SnI_{3-x}Br_x$ perovskites, respectively.[42-43] However, when moving up group 14 elements in the periodic table, the stability of the 2^+ oxidation state is much poorer. This disappointing point was shown in the works mentioned above, as none of these Sn-based perovskite solar cells could survive under ambient environment. Therefore, the poor stability of tin perovskites will largely hinder their future development. Recent study on developing 2D/3D formamidium tin iodide perovskite solar cells has shown enhanced PCE up to 9% with good reproducibility. However, decomposition of Sn-perovskite happens rapidly without encapsulation with only 59% of PCE remaining after only 3 days in air. This raises the need to explore other substitutes of lead for perovskite solar cells with better stability and less toxicity.

1.5.2 Antimony-based solar absorbers

Antimony is located in the next group neighbouring to lead and tin, and is widely used in therapeutics acting as a potential non-toxic alternative to lead. Strong lone pair effect can be observed for antimony especially in hybrid complexes, which commonly adopts a +3 oxidation state. Due to the difference in oxidation state, a perovskite structure is precluded from direct formation. Studies on inorganic Sb_2S_3 and SbSI have been carried out to explore their photovoltaic properties.[44-45] By using Sb_2S_3 as photo-sensitizer in a mesoscopic solar cell structure, nearly 5.2% PCE has been achieved by Moon *et al.*[46] Se-doped Sb_2S_3 has been studied by Yuan *et al*, achieving 4.17% PCE by adopting a HTM-free planar solar cell structure with post surface selenization doping method.[47]

Direct substitution of lead in $[CH_3NH_3][PbI_3]$ with antimony gives $Cs_3Sb_2I_9$ with an indirect bandgap of 2.05 eV, but only 0.5% PCE has been achieved in a solar cell device. By mixing sulfur and iodide in the anionic part of $MA_3Sb_2I_9$, a perovskite-like structure has been achieved with chemical formula of MASbSI, This material has created a new record for hybrid antimony-based solar cells with efficiency of 3.08%. Band gap value of 2.03 eV has been experimentally measured, with superior stability manifested in the device study. [48]

1.5.3 Bismuth-based solar absorbers

As the least toxic heavy metal with desirable chemical properties, bismuth is playing an important role especially in non-toxic green chemistry. Recently research on bismuth-based hybrids for photovoltaic applications has attracted lots of attention, together with rapid development of bismuth-based solar cell studies. The potential to be a PV material have been proven by bismuth sulfide,[49] bismuth iodide,[50-51] bismuth chalcohalides,[52-53] hybrid bismuth iodide,[54] silver bismuth iodide[55-56] and bismuth-based double perovskites.[57-58] So far, efficiency of 4.3% has been achieved by inorganic Ag_3BiI_6,[56] 2.5% has been achieved by $Cs_2AgBiBr_6$ double perovskite,[58] and 1.64% has been achieved by hybrid $[CH_3NH_3][Bi_2I_9]$.[59] The above mentioned bismuth-based solar absorbers also demonstrated good air-stability, illustrating the promising potential to develop bismuth-based lead-free photovoltaics.

1.6 Studies on bismuth-halide complexes

1.6.1 Electronic properties, crystal dimensionality and structural diversity of bismuth complexes

Bi^{3+}, similar to Pb^{2+} has large atomic number and radius, and falls in group 15 at the bottom of the periodic table. As a member with the heaviest nucleus of this group, the relativistic contraction tends to draw the s-electrons closer to the nucleus. This gives rise to the great difference of the energy for outermost s and p orbitals, and typically bismuth only loses 6p electrons, leaving the s electron lone pair to yield stable Bi^{3+} during reactions. The outermost s electrons of bismuth are stereochemically inactive, i.e., behaving more like core electrons. This is known as the inert pair effect, which is in contravention to the VSEPR theory but prevalent in heavy elements in groups 12 to 16.[60] Another advantage brought about by the stable 6s lone pair of bismuth is the high Born effective charges in bismuth halides. Since the s-states of bismuth are fully occupied, unusual p character in the conduction band can be found, which is responsible for the hybridization between bismuth p bands and halide p bands. This hybridization increases the Born effective charges significantly, and also leads to effective defect screening, which has been computationally proven.[61] This determines that octahedrally-coordinated bismuth halides may have longer charge-carrier lifetime and improved carrier mobility, thus potentially elevating photovoltaic performance. Therefore, the electronic structure, especially the 6s lone-pair-bearing electron of Bi^{3+}, plays an important role in geometry determination and optoelectronic behaviour optimization.

The dimensionality of a crystal structure is defined by the translational symmetry relationships, and thus the lattice dimensionality coincides with the total number of independent translational elements that are required to describe the crystal structure. Kitaigorodskii's definition of the molecular geometrical concept can be applied. For zero-dimensional objects, there are no propagations in any crystallographic direction. For a one-dimensional structure, an infinite linear bridged structure can be found that extends along one direction to extend the molecularity. For two-dimensional crystal structures, the molecularity extends over two dimensions that lead to sheet-like connections. A lattice that has the dimensionality of three is periodic in all the independent crystallographic directions.

One of the most obvious structural properties of iodobismuthates is the great diversity of the anionic structure motif. For the organic-inorganic framework of iodobismuthates, structure and dimensionality are largely determined by the organic or inorganic counter-ion, including their sizes, shapes, and chemical properties. Studies from 0-dimentional mono- or poly-nuclear compounds to infinite structure with 1D or

2D dimensionalities give rise to an extensive family of iodobismuthate anions ($[BiX_4]^-$, $[BiX_5]^{2-}$, $[BiX_6]^{3-}$, $[Bi_2X_9]^{3-}$, $[Bi_2X_{10}]^{4-}$, $[Bi_2X_{11}]^{5-}$, $[Bi_3X_{12}]^{3-}$, $[Bi_4X_{18}]^{6-}$ and $[Bi_6X_{22}]^{4-}$).[62] Examples and details will be discussed in the following sections.

1.6.2 Mononuclear complexes of $[BiI_6]^{3-}$

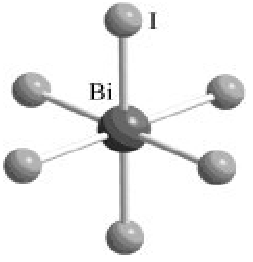

Figure 1.12 $[BiI_6]^{3-}$ octahedral complex

$[BiI_6]^{3-}$ is regarded as the simplest iodobismuthate with the structure shown in **Figure 1.12**. The central Bi atom is octahedrally coordinated by six iodides, at a distance of 3.073 Å.[57] The octahedral structure of $[BiI6]^{3-}$ is caused by the inert pair effect, which leads the lone-pair to be distributed on the central atom spherically and thus stereochemically inactive. Although deviations from an ideal octahedral structure in $[BiI_6]^{3-}$ can be found in some cases,[63] the distortion is negligible when compared to what is expected according to VSEPR with the lone pair directed to the triangular face of the octahedron. More in-depth studies indicate that whether or not the structural distortion (i.e., stereochemical activity or inactivity of the lone-pair) exists among $[BiX_6]^{3-}$ (X=Cl, Br, I) depends on the attractive and repulsive relationships of frontier orbitals of bismuth and the halides.[64]

1.6.3 Binuclear complexes $[Bi_2I_8]^{2-}$, $[Bi_2I_9]^{3-}$, $[Bi_2I_{10}]^{4-}$

Three different motifs for the octahedral building blocks for iodobismuthate dimerization have been studied extensively so far, specifically, 5-coordinate bismuth dimers (**Figure 1.13a**), face-sharing BiI_6 octahedral dimers (**Figure 1.13b**) and edge-sharing BiI_6 octahedral dimers (**Figure 1.13c**).

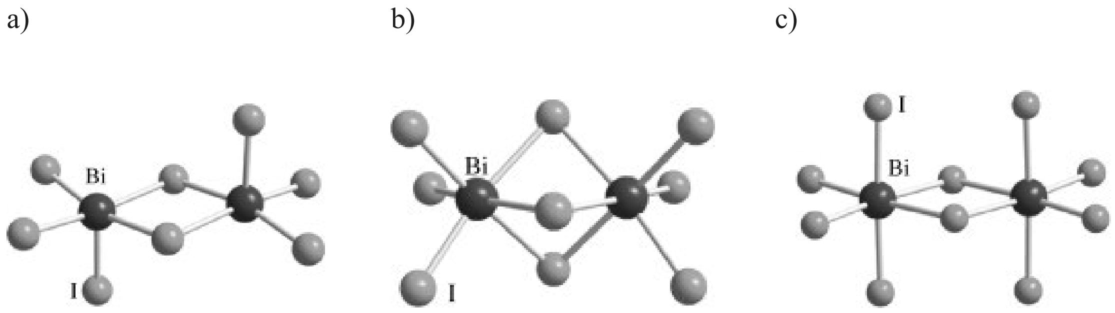

Figure 1.13 Zero-dimensional Bi-I motifs including 5-coordinate bismuth dimer (a), face-sharing BiI_6 dimer (b) and edge-sharing BiI_6 dimer (c). Figures are reproduced from ref [65]

Compared to **Figure 1.13b** and **c**, the Bi-I motif in **Figure 1.13a** indicates that it is possible to have an axial vacancy for I^-, which makes the structure somewhat unique. Studies on this type of 5-coordinated Bi-I dimers can be found in the literature.[66] $[Bi_2I_9]^{3-}$ complexes have been extensively investigated including the crystal structures, optical properties and quantum physical properties, and different cations including $CH_3NH_3^+$,[67-68] Cs^+,[69] Rb^+ and K^+[70] have been studied which may be used to aid the rational design of photovoltaics. $[CH_3NH_3]_3Bi_2I_9$ (MBI) has attracted attention as an analogue of methylammonium lead iodide by replacing lead with bismuth (III). Although it does not adopt a perovskite structure due to the different chemical valence to lead, merits including non-toxicity, solution-processability and stability in humid environment making the study of iodobismuthates as photovoltaics quite promising.[69,71] Moreover, tunable electrochemical and optical properties were found when changing the temperature[72] or changing the ratio of I and Cl in $[CH_3NH_3]_3Bi_2I_{9-x}Cl_x$.[69]

1.6.4 One-dimensional iodobismuthates with chain structures

Compared with the various isolated zero-dimensional Bi/I anions with different geometries, iodobismuthates featuring infinite chain structures or layered structures are rarely studied. 1D chains composed of bismuth and iodine are usually built from the basic $[BiI_6]^{3-}$ octahedral moiety or from larger units. The linear chain can be formed by infinite connections of $[BiI_6]^{3-}$ octahedra via an edge-, face-, or corner-sharing manner, which leads to an extensive family of iodobismuthates (**Figure 1.14 a, b, c**).[62 73-76] Studies have shown that it is also possible for poly-nuclear species to build up a chain structure, e.g., tetranuclear $[Bi_4I_{14}]^{2-}$ units.[77]

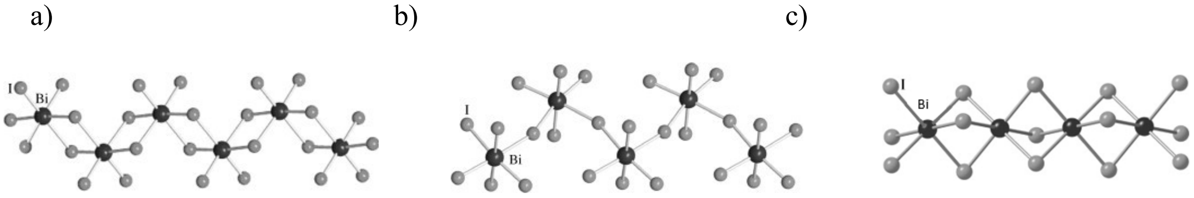

Figure 1.14 Edge-sharing 1D chain structure with edge-sharing $[BiI_4^-]_n$ (a), corner-sharing $[BiI_5^-]_n$ (b), and face-sharing $[BiI_3^{3-}]$ (c), reproduced from ref. 65.

Inorganic iodobismuthates containing one-dimensional BiI_4^- anionic chain-structure built by BiI_6 octahedra have been recently studied by Natalie A. Yelovik *et al*, specifically $LiBiI_4 \cdot 5H_2O$, $KBiI_4 \cdot H_2O$, $MgBi_2I_8 \cdot 8H_2O$, and $MnBi_2I_8 \cdot 8H_2O$. Direct band gaps for these compounds were determined and fall into the range of 1.70 -1.76 eV; also their thermal stability in air up to 120 degrees was observed.[78] As for hybrid iodobismuthates featuring 1D BiI_4^- chain structure, Dennington et al has synthesized piperazinium-cation based bismuth iodide materials, with band gap values ranging from 1.9 eV to 2 eV.[79] These studies indicate that iodobismuthates with extended anionic part of the structure may emerge as promising light-absorbing materials with high stability and non-toxicity.

1.6.5 Two- and three- dimensional iodobismuthates structures

Higher dimensional networks of hybrids refer to the extension of metal-ligand bond directions, which can correspond to higher dimensionality of charge transport. It has been shown that the electronic band gaps of metal-halide hybrids increase in a monotonic manner with the decrease of the coordination network's dimensionality, however, in the case of lead, the compounds show higher stability to oxygen and humidity in most cases.[80] Previous studies on two/three dimensional organic-inorganic hybrid networks composed of bismuth and halogen are rarely available. This is probably because the chemical valence of bismuth makes it impossible to form 3D perovskite structure with only halogen and organic moieties. However, for zero- and one-dimensional iodobismuthates, higher dimension of charge transport can also be achieved by considering non-covalent interactions (i.e., intermolecular interactions) between organic ligands and inorganic frameworks. This gives rise to pseudo-2D or -3D frameworks that may allow enhanced charge transport, at the same time maintaining the advantage of air-stability brought by substituting lead with bismuth.

1.6.6 Bismuth double perovskite

Since the chemical valence of bismuth is different from lead, bismuth cannot adopt the ABX_3 motif to form three dimensional perovskite structures. Therefore, bismuth-containing perovskite structures can only be obtained by heterovalent substitution of Pb^{2+} with a combination of Bi^{3+} (bismuth, trivalent cation) and M^{1+} (monovalent cation). Based on this, corner-sharing octahedra of $Bi^{III}X_6$ and $M^{I}X_6$ alternate to construct the three dimensional double perovskite structure, with a formula unit of $A_2M^{I}Bi^{III}X_6$ (**Figure 1.15**). This type of quaternary halide double perovskite structure was first found in mixed-valent metals, such as $Cs_2TI^{+}TI^{3+}X_6$ (X=F or Cl) and $Cs_2Ag^{+}Ag^{3+}I_6$. Metal-Halide double perovskites can also be formed based on monovalent alkali metal and trivalent metal ions such as In^{3+}, La^{3+}, $Sb^{3+}$and Bi^{3+}.[81] For bismuth-based double perovskite materials, various compounds have been studied structurally, theoretically and practically, especially in their electronic and optical properties. Experimentally, Cs_2AgBiX_6 (X=Cl, Br) and $CH_3NH_3KBiCl_6$ have been well-studied for their potential as light harvesting materials as analogues to lead-halide perovskites. Both $Cs_2AgBiCl_6$ and $Cs_2AgBiBr_6$ are semiconductors, with indirect bandgap of 2.7 eV for $Cs_2AgBiCl_6$ and 1.95 eV for $Cs_2AgBiBr_6$.[82] Besides, $Cs_2AgBiBr_6$ is demonstrated to have long room-temperature fundamental photoluminesce life time of 660 nm, with good stability in air and under moisture.[83] Devices based on $Cs_2AgBiBr_6$ show a promising 2.46% PCE after annealing over 200 degrees, with superior stability compared to lead-halide perovskite.[58]

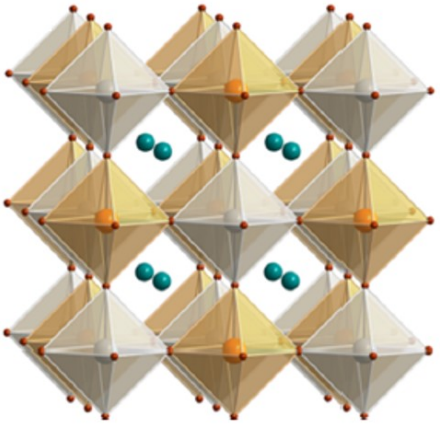

Figure 1.15 Crystal structure of the double perovskite $Cs_2AgBiBr_6$. Orange, grey, turquoise, and brown spheres represent Bi, Ag, Cs, and Br atoms, respectively. Figure is reproduced from Ref. 82

1.6.7 Silver Bismuth Iodide

Studies on silver bismuth iodide as PV materials started to become a popular topic from 2016, where a close-packed iodide sub-lattice was demonstrated in the crystal structure of $AgBi_2I_7$. This structure is highly favourable for photovoltaic applications, since the edge-sharing octahedra occupied by Ag^+ or Bi^{3+} give rise to the 3D inorganic network, and thus facilitate the charge carrier mobility within the absorber.[84] Application of this material in a solar cell device leads to the efficiency of 1.22%, with excellent stability under ambient environment. The crystal structure however has been questioned and corrected as an Ag-deficient $AgBiI_4$ structure. Based on this study, Zhu *et al* have studied the influence on crystal structures by using different ratios of AgI/BiI_3 as the starting materials, with efficiency of 2.1% achieved by silver bismuth iodide in $Fd\bar{3}m$ space group, while much lower PCE by the material adopting $R\bar{3}m$ space group.[85] This study has been continued by Ivan Turkevych *et al* to investigate the ratio of Bi and Ag in the silver bismuth iodide. They have demonstrated a new family of edge-sharing octahedra built by alternating Ag and Bi, with general formula of $Ag_aBi_bI_c$, x=a+3b (**Figure 1.16**). They have named this family as Rudorffites, and efficiency of 4.3% has been achieved by using Ag_3BiI_6 as the photovoltaic absorber.[56]

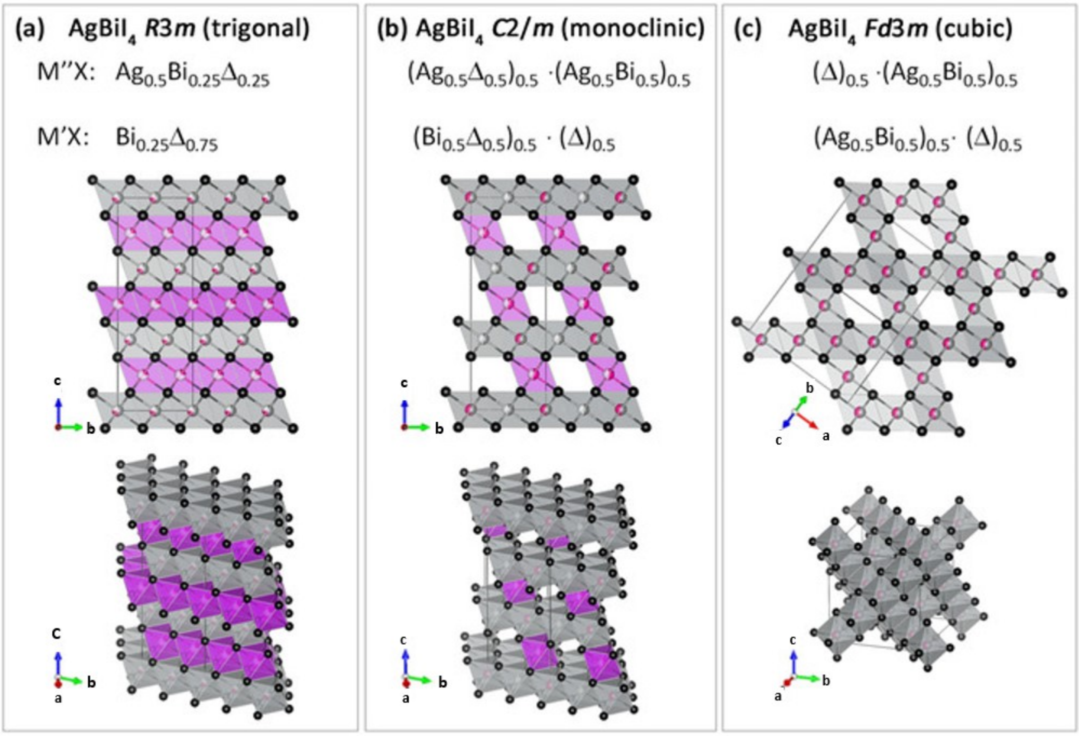

Figure 1.16 $AgBiI_4$ phase adopting (a) R3m triclinic, (b) C2/m monoclinic and (c) $Fd\bar{3}m$ cubic symmetries with their corresponding occupancies of Ag and Bi. Figure is reproduced from Ref. 56.

1.7 Supercapacitors

1.7.1 Introduction

Demand for efficient, economic and eco-friendly energy storage systems is growing dramatically in today's world, especially in the application of electronic appliances and electrical vehicles. Supercapacitors are energy storage devices with much higher capacitance than normal capacitors.[86] Unlike batteries which suffer from severe performance decrease after multiple charge and discharge cycles or under cold environmental temperature, supercapacitors embrace merits including high specific power, rapid charge-discharge properties and superior cycle stability.[87,88] The specific energy versus specific power plot for different energy storage devices can be found in **Figure 1.17**.

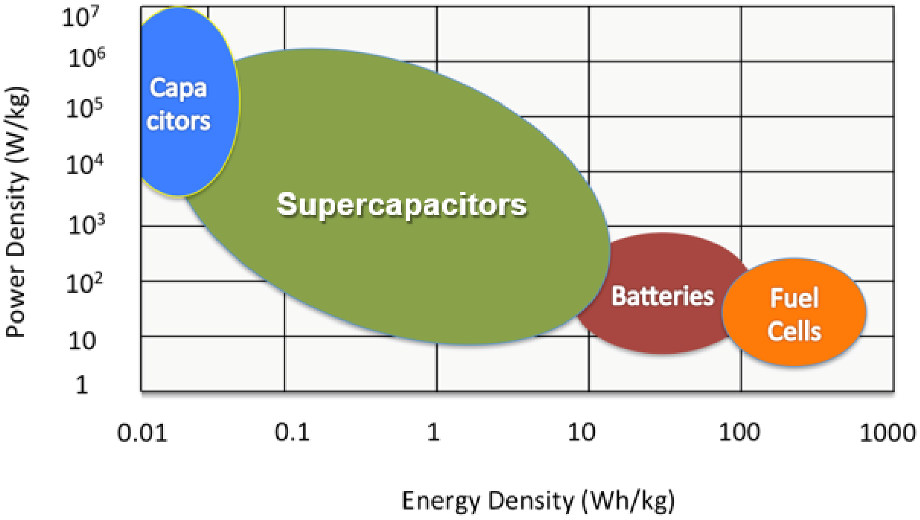

Figure 1.17 Specific energy vs specific power plot for common energy storage devices. Figure is reproduced from Ref. 88.

1.7.2 Charge storage mechanisms of supercapacitors

Supercapacitors can be categorized into electric double layer capacitors (EDLC), pseudocapacitors and hybrid capacitors, based on the mechanism of energy storage.[84] EDLC stores the charges in a physical manner where charges are absorbed and accumulated at the interface of electrode and electrolyte. When the external voltage is applied, the ions in the electrolyte diffuse over the ion-permeable separator and thus the accumulation of charges will occur at the electrode surface.[89,90] In pseudocapacitors, redox reactions take place at the vicinity of the electrode surface, where the energy can be stored and released via oxidative/reductive reactions. In this case, the passage of charge will occur in addition to the double layer, leading to the generation of Faradaic current. Greater capacitance and energy density can be observed in pseudocapacitors, however, they exhibit lower stability and thus shorter lifetime when compared to EDLCs.[91, 92] A hybrid capacitor combines the merits of superior stability from EDLC behaviour together with greater specific capacitance from a pseudocapacitor mechanism. This is achieved by combining two electrodes with different functionalities.[93] The common electrode materials of each type of supercapacitor is listed in the taxonomy graph in **Figure 1.18**.[94] The details of electrode materials of capacitors will be discussed in the next section.

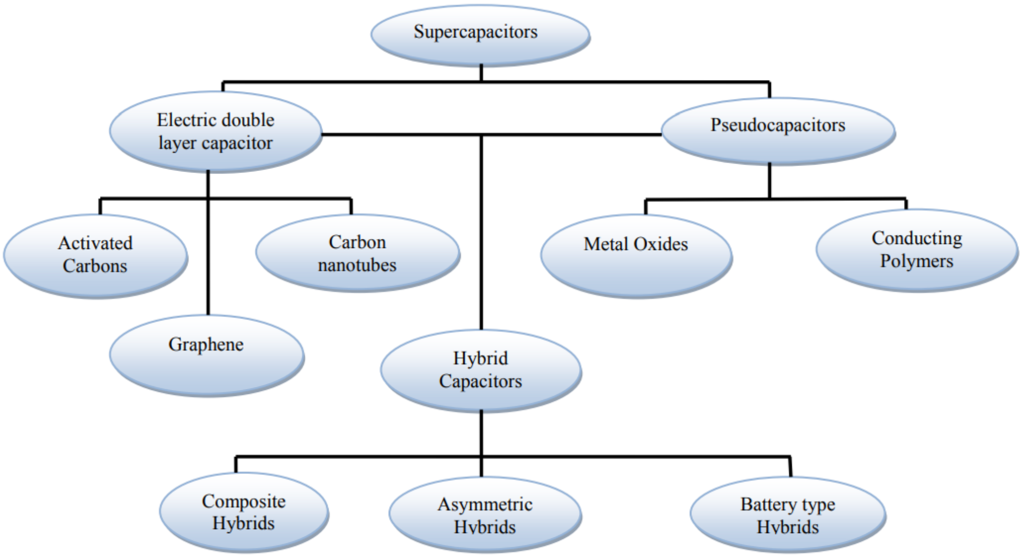

Figure 1.18 Taxonomy graph of electrode materials for supercapacitors. Figure is reproduced from Ref. 94.

The mechanistic differences between electric double-layer capacitors (EDCLs), pseudocapacitors, and batteries can be demonstrated by performing voltammogram (typically CV) and galvanostatic charge-discharge measurements. In particular, the CV results will distinguish EDLCs from pseudocapacitors (**Figure 1.19a**) and the shape of the galvanostatic charge-discharge curve will distinguish capacitors from batteries.[95] (**Figure 1.19b** Specifically, pronounced redox peaks can be observed in batteries and pseudocapacitors compared to the square-shaped curve for EDLCs. This is caused by the Faradaic process in batteries and pseudocapacitors, leading to oxidation and reduction of the electrode materials. In terms of the galvanostatic charge-discharge curves, a linear process can be observed for EDLCs and pseudocapacitors, with the slope difference caused by the varied operational time scales.[88] However, a prominent plateau is shown in the battery curve, attributed to the phase transition in the charge/discharge process.

a)

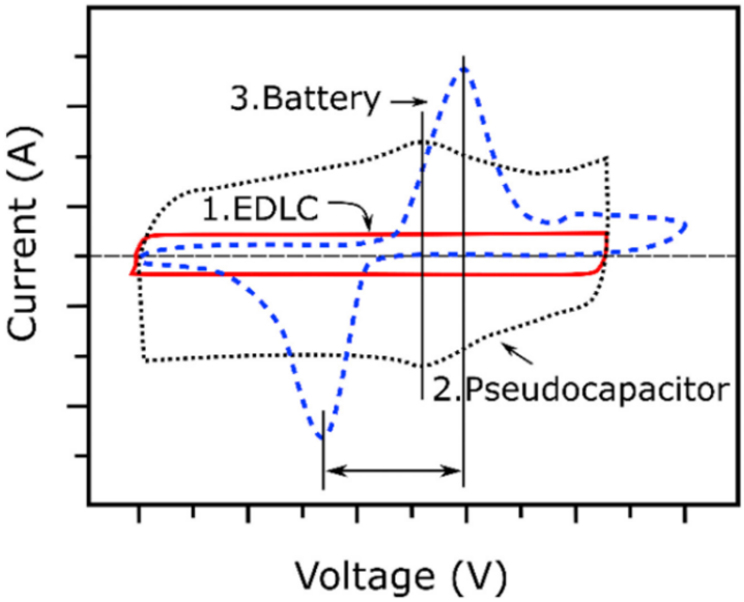

b)

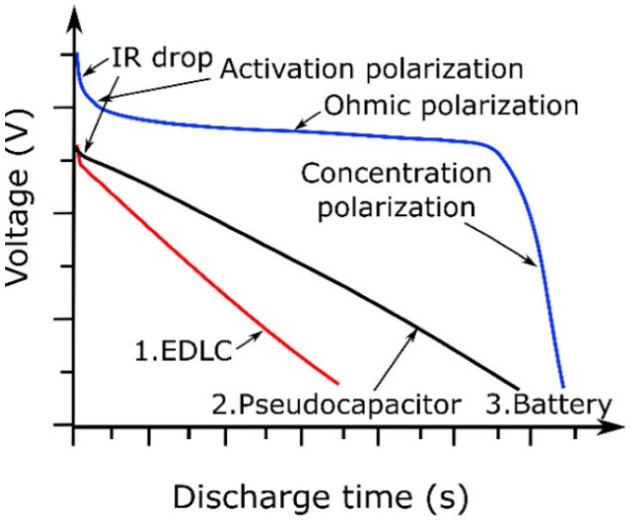

Figure 1.19 (a) Typical CV curves of EDLC (red, 1), pseudocapacitor (black, 2), and battery (blue, 3); (b) Typical Galvanostatic charge-discharge curves of EDLC (red, 1), pseudocapacitor (black, 2), and battery (blue, 3). Figures are reproduced from ref. 95.

1.7.3 Supercapacitor electrode materials

Electrode materials play a crucial role in determining the performance of supercapacitors. Typically, carbon-based materials are widely used as the electrode materials for EDLCs, and Faradaic materials are used for pseudocapacitors. Desirable properties for electrode materials include:[91]

(1) High surface area for charge storage. Nano-structured electrode materials are highly favourable for increasing the surface area, and thus lead to an improved specific capacitance.

(2) Good electronic conductivity. This helps to reduce the capacitance loss with higher scan rate during testing, and at the same time maintain the rectangular shape of CV scans as well as the symmetric curve from the galvanostatic charge-discharge measurements.

(3) High chemical and mechanical stability. This property significantly influence the lifetime of the supercapacitor. Good chemical and mechanical stability can to a large extent avoid side reactions or phase changes of the electrode materials.

(4) Low-cost and ease of fabrication for the commercialization purposes.

1.7.3.1 Carbon-based materials

Carbon materials cover a huge market in the supercapacitor industry, due to their merits including low-cost, easy processing, high surface area and good electrical conductivity. Typically, surface area of carbon materials is the main factor that determines their device performance. To enhance the surface area, different morphologies of carbon materials have been studied, including activated carbon, carbon nanotubes, carbon nanofibers, etc. On top of that, the capacitance can be boosted by adding heteroatoms, functional groups and conducting polymers into the carbon material, which leads to improved absorbance of ions. However, the resistance between carbon particles in the carbon material leads to high series resistance, which can limit performance and add hurdles to achieve higher capacitance. The specific capacitance is typically under 200 F/g for activated carbon, and less than 40 F/g for carbon nanotubes.[96, 97]

1.7.3.2 Faradaic materials

Due to the combined effect from charge storage in the double layer and redox reactions on the electrode surface, much enhanced capacitance can be achieved by using Faradaic materials as electrodes. Generally, Faradaic electrode materials can be categorized into electrical conducting polymers and metal oxides. The common conducting polymers that are used in supercapacitors are polyaniline, polypyrrol, polythiophene and their derivatives. The specific capacitance of pseudocapacitors can be over 1000 F/g, however, mechanical degradation is hard to avoid after charge-discharge cycles.[91]

Metal oxides can potentially provide higher capacitive performance than carbon-based electrode materials because charges can be stored chemically. At the same time, improved mechanical stability is found in metal oxides when compared to conductive polymers. In order to allow redox reactions to happen at the electrode surface, two or more oxidation states are required at the metal site. Common metal oxide electrode materials includes RuO_2, MnO, CoO and NiO. Over 700 F/g capacitance has been proven by using RuO_2 electrodes with KOH or H_2SO_4 as the electrolyte solution.[98]

1.7.3.3 Common Bismuth-based electrode materials

Bismuth oxide materials

Bi_2O_3 is a low-cost and non-toxic material that has been studied in a wide range of applications including gas sensors, fuel cells, supercapacitors and catalysis. In the field of supercapacitors, Bi_2O_3 nanomaterials show good morphology tuning. Over 800 F/g capacitance has been achieved by Sun *et al*, using solvo-themally prepared 3D Bi_2O_3 microspheres.[99] Liu *et al* discovered the processing route to Bi_2O_3 nano-flowers on a mesoscopic carbon substrate, showing a specific capacitance of 386 F/g.[100] Over 1350 F/g capacitance has been achieved by Su *et al* using rod-like Bi_2O_3 as the electrode material, with only 2.4% capacitance decline after 1000 cycles.[101] In Shinde's work, Bi_2O_3 nanostructures with morphologies including coconut shell, marigold, honey nest and rose have been synthesised and studied in capacitor devices, showing a 3D nano-network. Different substrates have been studied for using Bi_2O_3 as the electrode material, including stainless-steel, carbon, Ni-foam graphene and titanium nanotube arrays, reaching capacitance values from 98 F/g to 557 F/g.[102]

Bismuth sulphide materials

Bismuth sulfide is a semiconductor material with a band gap value around 1.4 eV.[103] Recently, Bi_2S_3 has drawn lots of attention because of its versatile optoelectronic properties, and Bi_2S_3 has been studied in a wide range of applications including photocatalysis,[101104] sensors,[105] lithium-ion batteries[106] and supercapacitors.[107-108] In the context of supercapacitor studies, micro-structured Bi_2S_3 has been studied as the supercapacitor electrode material, with over 185 F cm^{-2} capacitance reported by using the micro-flower morphology of Bi_2S_3 to increase the surface area.[109] Vadivel *et al* synthesized a Bi_2S_3 nanorods graphene composite by a precipitation method, exhibiting the specific capacitance of 290 F g^{-1}.[110] Hetero-structured Bi_2S_3 nanorods imbedded in MoS_2 nano-sheet as the electrode has shown impressive performance in supercapacitor, achieving over 1258 F g^{-1} capacitance.[111]

However, alkaline electrolytes are commonly applied in the above-mentioned studies using Bi-based electrodes, which give rise to the strong Faradaic reactions, and causes the devices to behave in a battery-like manner. In this case, the lifetime of such electrodes is much shorter compared to the electrodes used for EDLCs, which may limit their future applications.

1 .8 Aims of this project

The ideal properties of a photovoltaic material include non-toxicity, suitable band gap values, high stability in an ambient environment, high dimensionality of crystal framework, good charge carrier mobility and also low cost for both raw materials and fabrication. In spite of the rapid progress in lead-halide perovskite materials which are toxic and unstable in air, bismuth-based perovskite-like materials are intrinsically non-toxic and highly stable in air. However, more work needs to be carried out on increasing their power conversion efficiency, which constitute the main aims of this thesis as detailed below:

- Study of Bismuth-based materials for solar cell applications
  - Study of iodobismuthates with electrochemically active cations

Currently, simple cations in the widely studied organic-inorganic iodobismuthates are electrochemically inactive, as they rarely contribute to the frontier orbitals at the edge valence band or conduction band. In order to achieve enhanced charge mobility and higher dimensional charge transport ability, the cation introduced in the iodobismuthate framework should be carefully considered. Cations based on aromatic systems with π-conjugation are of great interest, since they may promote electronic interactions with anionic frameworks. The delocalization of π electrons is expected to enable good interaction with the iodobismuthate framework, aiming to build up enhanced intermolecular interactions and higher dimensionality of charge transport. At the same time, cations should be readily available or simply synthesized, and the iodobismuthate complexes should be soluble in organic solvents under mild conditions to provide the possibility of low-cost printable fabrication. In this case, the scope for such hybrid iodobismuthate light absorbers can be expanded, together with further investigations on their device performance.

  - Band gap engineering and optimization for solar cell applications

Optimizing the band gap of hybrid bismuth-based materials can potentially extend the absorption spectrum and thus generate more charge carriers, leading to enhancement of photo-generated current. Sulfur doping has been studied and successfully proven to red-shift the bandgap, however, we should expand the range of dianionic dopants as well as applying band gap engineering to both 0D and 1D iodobsimuthate materials. Moreover, solution-processability is highly desirable for the ease of fabrication and potential for commercialization.

- Study of Bismuth-based materials for supercapacitor applications

  Research on Bi-based electrode materials for supercapacitor applications is of great interest, because they are low-cost, stable, with proven charge storage ability. Despite the fact that Bi_2O_3 and Bi_2S_3 are well-studied in different types of supercapacitors, bismuth chalcohalide and hybrid bismuth-halide materials are relatively unexplored.

  - Bismuth chalcohalide material

    Bismuth chalcohalides have often been overlooked as potential energy storage materials. At the same time, the fabrication of bismuth chalcohalides typically requires high annealing temperatures and laborious, multistep procedures, complicating research efforts and economic viability. To the best of our knowledge, no simple, one-step, solution-processing synthetic route has been reported. In this thesis, a relatively unexplored bismuth chalcohalide material, $Bi_{13}S_{18}I_2$, will be explored by simplify the synthetic procedure, and also use and test as the supercapacitor electrode material.

  - Hybrid bismuth-halide materials

    Bismuth iodide perovskite-like materials have additional advantages compared to $MAPbI_3$ and other lead-halide perovskites such as non-toxicity, air-stability and moisture stability. Despite these advantages however, methylammonium bismuth iodide remains to date the only example studied for supercapacitor studies. In this thesis, we will report here on the synthesis and crystal structure of a novel hybrid iodobismuthate, thiourea bismuth iodide (TBI). Additionally, the electrode materials are commonly dispersed in a non-dissolving solvent during the deposition process, leading to the limitation of large scale production. Solution-processed method with flexible substrate in this case is desirable for the large-scale roll-to-roll industrial production.

The aspects above have led to the aims of this project, including materials synthesis and characterizations for solar cell applications, band-gap engineering for 0D and 1D iodobismuthates, and also supercapacitor studies based on a solution-processable bismuth chalcohalide and a hybrid iodobismuthate. Details of each aspect will be discussed in the following chapters.

1.9 Reference

1 BP, *Statistical Review of World Energy*, 2018.

2 K. Jager, O. Isabella, A. H. M. Smets, R. A. C. M. M. van Swaaij and M. Zeman, *Delft Univ. Technol.*, 2016, 29746.

3 O. Ellabban, H. Abu-Rub and F. Blaabjerg, *Renew. Sustain. Energy Rev.*, 2014, **39**, 748-764.

4 Varun, R. Prakash and I. K. Bhat, *Renew. Sustain. Energy Rev.*, 2009, **13**, 2716-2721.

5 M. Iqbal, *An introduction to solar radiation*, Academic Press, Canada,1983.

6 P. Würfel, *Physics of Solar Cells: From Basic Principles to Advanced Concepts, 2nd Edition*, John Wiley & Sons, 2009.

7 L. M. Fraas, *Low-cost solar electric power*, Springer, 2014.

8 Charles Kittel, *Introduction to Solid State Physics*, 8th edition, John Wiley & Sons 2004.

9 P. S. Priambodo, N. R. Poespawati and D. Hartanto, Solar Cells - Silicon Wafer-Based Technologies, IntechOpen, 2011.

10 F. A. Lindholm, J. G. Fossum and E. L. Burgess, *IEEE Trans. Electron Devices*, 1979, **26** (3), 165.

11 R. W. Erickson, D. Maksimovic, *Fundamentals of Power Electronics,* Springer, 2001

12 T. Markvart and L. Castañer, *Practical Handbook of Photovoltaics (thrid edition)*, Academic Press, 2018.

13 L. C. Chen, J. C. Chen, C. C. Chen and C. G. Wu, *Nanoscale Res. Lett.*, 2015, **10**, 312.

14 W. Shockley and H. J. Queisser, *J. App. Phys,* 1961, **32** (3), 510-519.

15 A. Polman, M. Knight, E. C. Garnett, B. Ehrier and W. C. Sinke, *Science*, **352**, 307-317.

16 C. Fritts, *Am. J. Sci.*, 1883, **26**, 465.

17 E. P. Wigner, *Phys. Today*, 1949, **2** (7), 24.

18 J. Perlin, From space to earth: the story of solar electricity, Harvard University Press, 2002.

19 R. W. Miles, K. M. Hynes and I. Forbes, *Prog. Cryst. Growth Charact. Mater.*, 2005, **51**, 1-42.

20 S. Kharbish, E. Libowitzky and A. Beran, *Eur. J. Mineral.*, 2009, **21**, 325–333.

21 S. K. Deb, *Renew. energy*, 1996, **8**, 375-379.

22 J. Britt and C. Ferekides, *Appl. Phys. Lett.*, 1993, **62**, 2851.

23 M. A. Green, *Prog. Photovoltaics Res. Appl.*, 2011, **9** (2), 123-135.

24 M. A. Green, *Physica E: Low-Dimensional Systems and Nanostructures*, 2002, **14**, 65-70.

25 M. K. Nazeeruddin, E. Baranoff and M. Grätzel, *Sol. Energy*, 2011, **85** (6), 1172-1178.

26 P. V. Kamat, *J. Phys. Chem. C*, 2008, **112** (48), 18737-18753.

27 M. Grätzel, *Nat. Mater.*, 2014, **13**, 838–842.

28 A. Kojima, K. Teshima, Y. Shirai and T. Miyasaka, *J. Am. Chem. Soc.*, 2009, **131** (17), 6050-6051.

29 M. A. Green, Y. Hishikawa, E. D. Dunlop, D. H. Levi, J. Hohl-Ebinger and A. W. Y. Ho-Baillie, *Prog. Photovoltaics Res. Appl.*, 2018, **26** (7), 427-436.

30 N. G. Park, *Mater. Today*, 2015, **18**, 65-72.

31 H. J. Snaith, *J. Phys. Chem. Lett.*, 2013, **4**, 3623-3630.

32 C. Eames, J. M. Frost, P. R. F. Barnes, B. C. O'Regan, A. Walsh and M. S. Islam, *Nat. Commun.*, 2015, **6**,

7497.

33 H. S. Kim, C. R. Lee, J. H. Im, K. B. Lee, T. Moehl, A. Marchioro, S. J. Moon, R. Humphry-Baker, J. H. Yum, J. E. Moser, M. Grätzel and N. G. Park, *Sci. Rep.*, 2012, **2**, 591-597.

34 M. M. Lee, J. Teuscher, T. Miyasaka, T. N. Murakami and H. J. Snaith, *Science,* 2012, **338**, 643-647.

35 L. Etgar, P. Gao, Z. Xue, Q. Peng, A. K. Chandiran, B. Liu, M. K. Nazeeruddin and M. Graetzel, *J. Am. Chem. Soc.*, 2015, **40**, 674-680.

36 W. S. Yang, J. H. Noh, N. J. Jeon, Y. C. Kim, S. Ryu, J. Seo and S. Il Seok, *Science*, 2015, **348**, 1234-1237.

37 N. J. Jeon, J. H. Noh, W. S. Yang, Y. C. Kim, S. Ryu, J. Seo and S. Il Seok, *Nature*, 2015, **517**, 476–480.

38 M. A. Green, A. Ho-Baillie and H. J. Snaith, *Nat. Photonics*, 2014, **8**, 506–514.

39 H. S. Jung and N. G. Park, *Small*, 2015, **11**, 10-25.

40 A. Marchioro, J. Teuscher, D. Friedrich, M. Kunst, R. Van De Krol, T. Moehl, M. Grätzel and J. E. Moser, *Nat. Photonics*, 2014, **8**, 250-255.

41 N. K. Noel, S. D. Stranks, A. Abate, C. Wehrenfennig, S. Guarnera, A.-A. Haghighirad, A. Sadhanala, G. E. Eperon, S. K. Pathak, M. B. Johnston, A. Petrozza, L. M. Herz and H. J. Snaith, *Energy Environ. Sci.*, 2014, **7**, 3061–3068.

42 M. H. Kumar, S. Dharani, W. L. Leong, P. P. Boix, R. R. Prabhakar, T. Baikie, C. Shi, H. Ding, R. Ramesh, M. Asta, M. Graetzel, S. G. Mhaisalkar and N. Mathews, *Adv. Mater.*, 2014, **26**, 7122–7127.

43 F. Hao, C. C. Stoumpos, D. H. Cao, R. P. H. Chang and M. G. Kanatzidis, *Nat. Photonics*, 2014, **8**, 489–494.

44 Y. Itzhaik, O. Niitsoo, M. Page and G. Hodes, *J. Phys. Chem. C*, 2009, **113** (111), 4254-4256.

45 K. T. Butler, S. McKechnie, P. Azarhoosh, M. Van Schilfgaarde, D. O. Scanlon and A. Walsh, *Appl. Phys. Lett.*, 2016, **108**, 112103.

46 S. J. Moon, Y. Itzhaik, J. H. Yum, S. M. Zakeeruddin, G. Hodes and M. Grätzel, *J. Phys. Chem. Lett.*, 2010, **1**(10), 1524-1527.

47 S. Yuan, H. Deng, X. Yang, C. Hu, J. Khan, W. Ye, J. Tang and H. Song, *ACS Photonics*, 2017, **4** (11), 2862-2870.

48 R. Nie, A. Mehta, B. W. Park, H. W. Kwon, J. Im and S. Il Seok, *J. Am. Chem. Soc.*, 2018, **140**, 872–875.

49 L. Martinez, A. Stavrinadis, S. Higuchi, S. L. Diedenhofen, M. Bernechea, K. Tajima and G. Konstantatos, *Phys. Chem. Chem. Phys.*, 2013, **15**, 5482-5487.

50 R. E. Brandt, R. C. Kurchin, R. L. Z. Hoye, J. R. Poindexter, M. W. B. Wilson, S. Sulekar, F. Lenahan, P. X. T. Yen, V. Stevanović, J. C. Nino, M. G. Bawendi and T. Buonassisi, *J. Phys. Chem. Lett.*, 2015, 6 (21), 4297-4302.

51 N. F. Coutinho, R. B. Merlo, N. F. V. Borrero and F. C. Marques, *MRS Adv.*, 2018, **3** (55), 3233-3236.

52 N. T. Hahn, A. J. E. Rettie, S. K. Beal, R. R. Fullon and C. B. Mullins, *J. Phys. Chem. C*, 2012, **116** (47), 24878-24886.

53 A. M. Ganose, K. T. Butler, A. Walsh and D. O. Scanlon, *J. Mater. Chem. A*, 2016, **4**, 2060-2068.

54 B. W. Park, B. Philippe, X. Zhang, H. Rensmo, G. Boschloo and E. M. J. Johansson, *Adv. Mater.*, 2015, **27**, 6806–6813.

55 Y. Kim, Z. Yang, A. Jain, O. Voznyy, G. H. Kim, M. Liu, L. N. Quan, F. P. Garcia de Arquer, R. Comin, J. Z. Fan and E. H. Sargent, *Angew. Chemie - Int. Ed.*, 2016, **55**, 9586–9590.

56 I. Turkevych, S. Kazaoui, E. Ito, T. Urano, K. Yamada, H. Tomiyasu, H. Yamagishi, M. Kondo and S. Aramaki, *ChemSusChem*, 2017, **10**, 3754–3759.

57 W. Gao, C. Ran, J. Xi, B. Jiao, W. Zhang, M. Wu, X. Hou and Z. Wu, *ChemPhysChem*, 2018, **19** (14), 1696-1700.

58 E. Greul, M. L. Petrus, A. Binek, P. Docampo and T. Bein, *J. Mater. Chem. A*, 2017, **5**, 19972–19981.

59 Z. Zhang, X. Li, X. Xia, Z. Wang, Z. Huang, B. Lei and Y. Gao, *J. Phys. Chem. Lett.*, 2017, **8** (17), 4300-4307.

60 U. Muller and J. Wiley, *Zeitschrift fur Krist. - New Cryst. Struct.*, 1999, **625**, 192-194.

61 M. H. Du and D. J. Singh, *Phys. Rev. B - Condens. Matter Mater. Phys.*, 2010, **82**, 1–5.

62 G. A. Fisher and N. C. Norman, *Adv. Inorg. Chem.*, 1994, **41**, 233–271.

63 M. Lindsjö, A. Fischer and L. Kloo, *Eur. J. Inorg. Chem.*, 2005, **631**, 1497-1501.

64 R. A. Wheeler and P. N. V. P. Kumar, *J. Am. Chem. Soc.*, 1992, **114**, 4776–4784.

65 L. M. Wu, X. T. Wu and L. Chen, *Coord. Chem. Rev.*, 2009, **253**, 2787-2804.

66 V. Sharutin and I. Egorova, *Russ. J. Coord. Chem.*, 2008, **78**, 1326-1329.

67 R. L. Z. Hoye, R. E. Brandt, A. Osherov, V. Stevanovic, S. D. Stranks, M. W. B. Wilson, H. Kim, A. J. Akey, J. D. Perkins, R. C. Kurchin, J. R. Poindexter, E. N. Wang, M. G. Bawendi, V. Bulovic and T. Buonassisi, *Chem. - A Eur. J.*, 2016, **22**, 2605–2610.

68 J. K. Pious, M. L. Lekshmi, C. Muthu, R. B. Rakhi and V. C. Nair, *ACS Omega*, 2017, **2** (9), 5798-5802.

69 B. W. Park, B. Philippe, X. Zhang, H. Rensmo, G. Boschloo and E. M. J. Johansson, *Adv. Mater.*, 2015, **27**, 6806–6813.

70 A. J. Lehner, D. H. Fabini, H. A. Evans, C.-A. Hébert, S. R. Smock, J. Hu, H. Wang, J. W. Zwanziger, M. L. Chabinyc and R. Seshadri, *Chem. Mater.*, 2015, **27**, 7137–7148.

71 M. Lyu, J. H. Yun, M. Cai, Y. Jiao, P. V. Bernhardt, M. Zhang, Q. Wang, A. Du, H. Wang, G. Liu and L. Wang, *Nano Res.*, 2016, **9**, 692–702.

72 V. F. Machulin, F. V. Motsnyi, E. Y. Peresh, O. M. Smolanka and G. S. Svechnikov, *Fiz. Nizk. Temp.*, 2004, **30**, 964,

73 G. A. Bowmaker, J. M. Harrowfield, A. M. Lee, B. W. Skelton and A. H. White, *Aust. J. Chem.*, 1998, **51**, 293-309.

74 D. B. Mitzi and P. Brock, *Inorg. Chem.*, 2001, **40**, 2096-2104.

75 A. M. Goforth, M. D. Smith, L. Peterson and H. C. Zur Loye, *Inorg. Chem.*, 2004, **43**, 7042–7049.

76 S. V. Krivovichev and S. K. Filatov, *Am. Mineral.*, 1999, **84**, 1099–1106.

77 Y. Chen, Z. Yang, C. X. Guo, C. Y. Ni, Z. G. Ren, H. X. Li and J. P. Lang, *Eur. J. Inorg. Chem.*, 2010, **33**, 5326–5333.

78 N. A. Yelovik, A. V Mironov, M. A. Bykov, A. N. Kuznetsov, A. V Grigorieva, Z. Wei, E. V Dikarev and A. V Shevelkov, *Inorg. Chem.*, 2016, **55**, 4132–4140.

79 A. J. Dennington and M. T. Weller, *Dalt. Trans.*, 2016, **45**, 17974–17979.

80 G. Huang, Y.-Q. Sun, Z. Xu, M. Zeller and A. D. Hunter, *Dalton Trans.*, 2009, **26**, 5083–93.

81 G. Volonakis, M. R. Filip, A. A. Haghighirad, N. Sakai, B. Wenger, H. J. Snaith and F. Giustino, *J. Phys. Chem. Lett.*, 2016, **7**, 1254–1259.

82 E. T. McClure, M. R. Ball, W. Windl and P. M. Woodward, *Chem. Mater.*, 2016, **28**, 1348–1354.

83 A. H. Slavney, T. Hu, A. M. Lindenberg and H. I. Karunadasa, *J. Am. Chem. Soc.*2016, 138, **7**, 2138-2141

84 Y. Kim, Z. Yang, A. Jain, O. Voznyy, G. H. Kim, M. Liu, L. N. Quan, F. P. García de Arquer, R. Comin, J. Z. Fan and E. H. Sargent, *Angew. Chemie - Int. Ed.*, 2016, **55**, 9586–9590.

85 H. Zhu, M. Pan, M. B. Johansson and E. M. J. Johansson, *ChemSusChem*, 2017, **10** (12), 2592-2596.

86 A. González, E. Goikolea, J. A. Barrena and R. Mysyk, *Renew. Sustain. Energy Rev.*, 2016, **58**, 1189-1206.

87 M. Jayalakshmi, K. Balasubramanian, *Int. J. Electrochem. Sci.*, 2008, **3**, 1196 - 1217.

88 M. Winter and R. J. Brodd, *Chem. Rev.*, 2004, **104** (10), 4245-4269.

89 P. Sharma and T. S. Bhatti, *Energy Convers. Manag.*, 2010, **51** (12), 2901-2912.

90 R. Signorelli, D. C. Ku, J. G. Kassakian and J. E. Schindall, *Proc. IEEE*, 2009, 97 (11), 1837-1847.

91 Z. Yu, L. Tetard, L. Zhai and J. Thomas, *Energy Environ. Sci.*, 2015, **8**, 702-730.

92 B. E. Conway, *J. Electrochem. Soc.*, 1991, **138**, 1539-1548.

93 Y. M. Vol'fkovich and T. M. Serdyuk, *Russ. J. Electrochem.*, 2002, **38** (9), 935-958.

94 Z. S. Iro, C. Subramani and S. S. Dash, *Int. J. Electrochem. Sci.*, 2016, **11** (12), 10628-10643.

95 J. Xie, P. Yang, Y. Wang, T. Qi, Y. Lei and C.M Li, *Journal of Power Sources*, 2018 **401**, 213-223.

96 L. L. Zhang and X. S. Zhao, *Chem. Soc. Rev.*, 2009, **38**, 2520-2531.

97 K. Wang, P. Zhao, X. Zhou, H. Wu and Z. Wei, *J. Mater. Chem*., 2011,**21**, 16373-16378 .

98 J. P. Zheng, *J. Electrochem. Soc.*, 1995, **142** (8), 2699-2703.

99 J. Sun, J. Wang, Z. Li, Z. Yang and S. Yang, *RSC Adv.*, 2015, **5**, 51773-51778,

100 N. Xia, D. Yuan, T. Zhou, J. Chen, S. Mo and Y. Liu, *Mater. Res. Bull.*, 2011, **46** (5), 687-691,.

101 H. Su, S. Cao, N. Xia, X. Huang, J. Yan, Q. Liang and D. Yuan, *J. Appl. Electrochem.*, 2014, **44** (6), 735-740.

102 N. M. Shinde, Q. X. Xia, J. M. Yun, R. S. Mane and K. H. Kim, *ACS Appl. Mater. Interfaces*, 2018, **10**, 11037–11047.

103 M. Bernechea, Y. Cao and G. Konstantatos, *J. Mater. Chem. A*, 2015, **3**, 20642-20648.

104 K. Liang, C. Wang, X. Xu, J. Leng and H. Ma, *Phys. Lett. Sect. A Gen. At. Solid State Phys.*, 2017, **381** (6), 652-657.

105 T. X. Fu, *Mater. Res. Bull.*, 2018, **99**, 460-465.

106 S. Liu, Z. Cai, J. Zhou, A. Pan and S. Liang, *J. Alloys Compd.*, 2017, **715**, 432-437.

107 H. Lu, Q. Guo, F. Zan and H. Xia, *Mater. Res. Bull.*, 2017, **96**, 471-477.

108 S. S. Raut, J. A. Dhobale and B. R. Sankapal, *Phys. E Low-Dimensional Syst. Nanostructures*, 2017, **87**, 209-212.

109 L. Ma, Q. Zhao, Q. Zhang, M. Ding, J. Huang, X. Liu, Y. Liu, X. Wu and X. Xu, *RSC Adv.*, 2014, **4**, 41636-41641.

110 S. Vadivel, A. N. Naveen, V. P. Kamalakannan, P. Cao and N. Balasubramanian, *Appl. Surf. Sci.*, 2015, **351**, 635-645.

111 L. Fang, Y. Qiu, T. Zhai, F. Wang, M. Lan, K. Huang and Q. Jing, *Colloids Surfaces A Physicochem. Eng. Asp.*, 2017, **535**, 41-48.

Chapter 2: Experimental Details

2.1 Single crystal growth methods

A crystalline material is a regular arrangement of the basic unit cell building blocks of a material and the symmetry operations of the unit cell can be found throughout the crystal structure.[1] Crystallisation is the process where the atoms or molecules arrange themselves in a repeating pattern to form crystals. Two models, classical and two-step, have been primarily studied to explain the nucleation process, with more merit given to the latter. [2–4] The first step of crystallisation is nucleation, which is highly dependent on the impurities that exist in the solution, or simply the unevenness of the vessel surface. A high energy barrier must be overcome during the nucleation process. The second step is crystal growth based on this nucleus. The rate of crystal growth is controlled by heat transfer at the solid-liquid interface, which drives the diffusion and thus phase transformation.[4] The overall transformation rate is closely related to temperature (T) as seen in **Figure 2.1**. At high T, close to T_m, large and coarse grains of crystals are expected to form due to the high growth rate and low nucleation rate, while much smaller and finer grains are formed at low temperature.

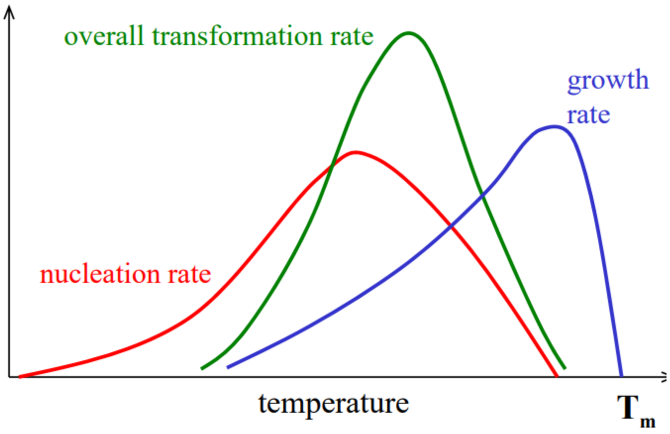

Figure 2.1 nucleation rate, growth rate and overall transformation rate during the crystallization process. Figure reproduced from Ref. 1

Common methods for obtaining single crystals from solution are discussed in the following.[5,6]

Slow solvent evaporation

Single crystals of the target material can be obtained by slow solvent evaporation of its concentrated solution. This uses the nearly-saturated solution without any disturbance during the slow evaporation process. The rate of evaporation may be hard to control, therefore the evaporation temperature and the coverage of the solution should be carefully considered.[7,8] A common crystallization set up using slow evaporation is shown in **Figure 2.2a**.

Vapour diffusion

The crystallization process happens in a binary solvent system, where two solvents with different volatility and dissolvability of the target material are used. A common set up is illustrated in **Figure 2.2b**, where the target compound is soluble in S1 while poorly soluble in S2. The whole set up should be completely air-tight and without disturbance. During the diffusion process, highly volatile S2 enters the S1 solution and lead to an equilibrium environment.[9] The 'hanging-drop model' suggests the nucleation process happens at the equilibrium at the vapour droplet surface, where a transient concentration gradient is generated. Compared to slow evaporation methods, much less target material is needed for the crystallization process.[10]

Liquid-liquid diffusion

This method is based on solvent diffusion where two liquids are layered and contacting with each other with a small interface, as seen in **Figure 2.2c.** The target material should not be soluble in S2, while possessing good solubility in S1. Discrete layers of the two solvents can be formed and reducing the contact layer area can help the binary solvent system to have a good separation and slow diffusion process, thus better quality crystals are expected.[11,12]

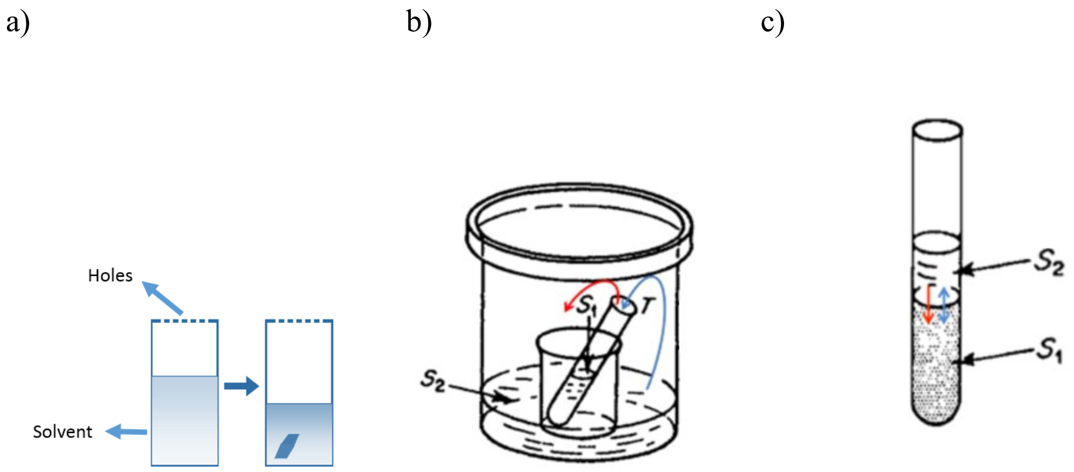

Figure 2.2 Illustration of crystallization methods: a) slow solvent evaporation; b) vapour diffusion; c) liquid-liquid diffusion. The sample material has good solubility in S1 whilst limited solubility in S2 in both b) and c). Red arrows represent the diffusion process of S1 and blue arrows represent the diffusion of S2. Figures are reproduced from Ref 6.

2.2 X-ray diffraction

2.2.1 Single crystal X-ray diffraction

Single crystal X-ray diffraction (XRD) is a powerful technique for determining the positions of atoms, and therefore reveals the crystal structure. In a diffractometer, X-rays are generated by applying a high voltage to a tungsten filament to produce electrons which are then accelerated towards a target material at positive potential. The impact of the electrons on the target materials cause inner shell electrons to be knocked out and produce an unstable atom. To release the stored energy, outershell electrons move to occupy these holes and the energy is released as X-ray radiation with a characteristic wavelength, related to the target material. The single crystal is mounted between the X-ray source and detector and acts as a diffraction grating, which the X-ray beams interact with. Due to the periodicity of the crystal lattice, atoms are arranged in regular arrays in the crystal lattice as shown in **Figure 2.3**. The wavelength of X-rays is in the same order of magnitude as that of the inter-planar spacing in the crystal lattice (in the order of Å), so that interference can occur, either constructive or destructive interference. The diffracted X-ray beams will be shifted in phase due to the penetration of the beam into the deeper planes of the crystal. Constructive interference occurs when the inter-atomic plane distance and incident angle satisfy Bragg's Law, see Equation 2.1,

$$2d\sin\theta = n\lambda \quad \text{(Equation 2.1)}$$

where d is the spacing distance between two diffraction planes and θ is the incident X-ray wavelength. By rotating the single crystal in an X-ray beam while measuring, limitations from the orientation of the crystal can be minimized, and therefore increase the amount of data to be collected. [1]

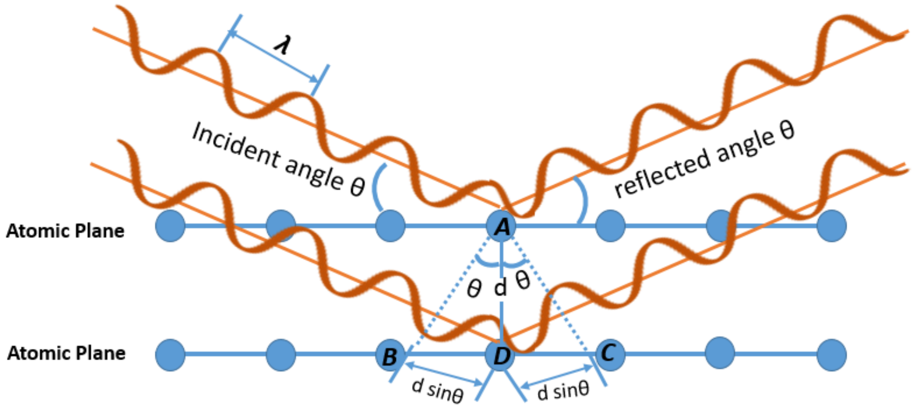

Figure 2.3 Schematic diagram of Bragg's law, where the relationships can be determined from the triangle ABD or ADC. Figure reproduced from Ref 1.

Experimental

In this thesis, the single-crystal structures of the studied compounds were determined by Dr. Gary S. Nichol from the University of Edinburgh single-crystal X-ray structure determination service. For each compound, a suitable-sized crystal was selected and mounted on a MITIGEN holder in Paratone oil on a Rigaku Oxford Diffraction SuperNova diffractometer. The data collection was carried out at $T = 120.0$ K using MoKα radiation with wavelength λ=0.71069 Å (T=125 K for **[py][BiI$_4$]**). Olex 2[13] was used when solving the structure with the ShelXS[14] structure solution program. Direct methods were used for all crystals. For each compound, the model was refined with version 2014/6 of ShelXL using Least Squares minimisation. All non-hydrogen atoms were refined anisotropically, and positions of hydrogen atoms were calculated geometrically and refined using the riding model.

2.2.2 Powder X-ray diffraction

To characterise polycrystalline materials structurally, PXRD techniques are commonly used. During the measurement, the crystalline material is mounted in the diffractometer in the form of powder or thin-film. Crystal monochromaters, such as Ge or Si, are used to produce monochromatic X-rays. The intensity of the diffracted X-rays is received and analysed by the detector. If the atomic inter-planar distance satisfies Bragg's law, constructive interference is occurs and a reflection of given intensity can be observed. A diffraction pattern is a plot of (constructive interference) intensity against the angle of diffracion 2θ. [15]

Experimental

X-ray diffraction data were collected on powder samples for the compounds of interest over a 2θ scattering angle range of 5-50 degrees using CuK$_\alpha$ radiation with wavelength of 1.5418 Å . The samples were spin-coated onto glass slides (see details in the film formation section) or finely ground as powders form for measurements. The measurement was performed at room temperature on a Bruker D2 Advance diffractometer, with a rotation speed of 8°/min, and an stepsize of 0.05° on 2θ.

2.3 Optical and electrical measurements

2.3.1 Diffuse reflectance

Optical absorption measurements are one of the most important methods to determine the energy band gaps of semiconductors. The optical energy band gap is the minimum energy needed to excite an electron from the top of valence band to the bottom of conduction band.[1] However, different from the UV-Vis absorption spectroscopy carried out using transparent solution, diffuse reflectance spectroscopy is suitable for analysing samples in the form of nanoparticles or powder.[16] It is a non-destructive technique and easy to carry out. When light with a certain wavelength illuminates the sample, part of the radiation penetrates into the sample, part of it is reflected to the surface, and part of it is absorbed by the sample if the incident light has suitable energy. By integrating the non-absorbed part of the incident light that is reflected, we can in principle calculate the portion of light being absorbed by the sample material at certain wavelength. However, inhomogeneity of the sample material composed of light-scattering and light-absorbing particles in a matrix complicates the determination of absorption; therefore we need to use approximations. Kubelka-Munk theory is one of the most popular theories for approximating the absorption from the diffuse reflectance measurement.[17] The reflectance data can be converted into absorption according to the Kubelka-Munk function ($F(R_\infty)$) as:

$$F(R_\infty) = \frac{k}{s} = \frac{(1-R_\infty)^2}{2R_\infty} \quad \text{(Equation 2.2)}$$

Where

k is the absorption of the sample;

s is the scattering of the sample;

R_∞ is the reflectivity assuming the sample has infinite thickness.

The optical band gap of the sample in powder form can be then calculated by using the Tauc Plot,[18] which correlates the absorption coefficient to the incident photon energy by Equation 2.3:

$$(\alpha h\upsilon)^{1/n} = A(h\upsilon - E_g) \qquad \text{(Equation 2.3)}$$

Where α is the absorption coefficient, $h\upsilon$ is the incident light energy, A is the tailing of the absorption onset, n is determined by the electronic transition (n=1/2 for direct band gap transition and n=2 for indirect band gap transition), and E_g is the bandgap value to be calculated. [19,20] In practice, the vertical axis plotted is $F(R_\infty)$, which is proportional to the absorption coefficient α. Therefore, α in the Tauc Plot is substituted by $F(R_\infty)$,[21] expressed as

$$(F(R_\infty)h\upsilon)^{1/n} = A(h\upsilon - E_g) \qquad \text{(Equation 2.4)}$$

Experimental

Diffuse reflectance measurements were carried out on a Jasco V-670 spectrophotometer with SpectaManager software. Each powder sample was diluted at 2 % weight in $BaSO_4$ and ground thoroughly to a fine powder. $BaSO_4$ was also used as a reference compound to plot the baseline. The Kubelka-Munk function was used to analyse the data collected from diffuse reflectance measurements, and values of direct and indirect band gaps of each compound were constructed by Tauc plots. The validity of assumptions on allowed direct or indirect lowest energy transitions was further considered together with the result from DFT calculations.

Diffuse reflectance measurements were also performed on the spin-coated thin film of each compound. Details for the spin coating methods can be found in the section on film formation.

2.3.2 SEM

Scanning electron microscope (SEM) has been widely used for surface microscopic topography, composition and imaging studies. It produces an image of the sample surface by scanning the specimen with a narrow electron beam. The atoms in the sample interact with the incident electron beam, known as the primary electrons, resulting in energy transfer and causing electrons to escape from the specimen. The escaped electrons are known as secondary electrons, which are subsequently collected by the detector and then translated to produce an image of the topography.[26] For elemental analysis, an Energy-dispersive X-ray spectroscopy (EDX) system is equipped together with the SEM for detecting the elemental composition of the sample. When the incident beam of electrons strikes the specimen, an electron in the inner shell is excited and ejected, and the relaxation of higher electrons leads to the generation of X-ray photons. This vacant site is then filled by an electron from outer shell with higher energy, and the extra energy is released and emitted in the form of X-ray, detected by the EDS. Since the energy difference between outer shell and inner shell is characteristic to each element, the composition can be determined.[27] For lead-halide perovskite materials, SEM has been widely used in studying the film morphologies, grain boundaries and defects in the solid crystalline state.[28]

Experimental

SEM images were collected using a Carl Zeiss SIGMA HD VP Field Emission SEM, operated in InLens mode with a 10 kV accelerating voltage. SEM-EDS measurements were made on the same instrument, using an Oxford AZtec ED X-ray analysis set up.

2.3.3 TEM

Similar to SEM, transmission electron microscopy (TEM) is a microscopic technique that allows in-depth study of morphology and elemental composition. However, the electron beam used in TEM has enough energy to transmit through the specimen, and is therefore capable of imagining at much higher resolution. The sample for TEM measurement has to be very thin (less than 100 nm) or as powder form dispersed on a mesh grid, commonly made of copper. Due to the penetration ability of the electron beam during a TEM measurement, degradation mechanisms of perovskite materials in a solar cell have been studied *in situ*, with special attention paid to processes at the interfaces.[29,30]

Experimental

TEM images and elemental EDX were studied in the University of St. Andrews with Dr. Julia Payne and Dr. David Miller. The samples were scraped off from the as-formed thin film and dispersed on carbon fibre or copper mesh for high resolution TEM measurements. The measurement was conducted on a FEI Titan Themis electron microscope with a Super-X high sensitivity windowless EDX detector.

2.4 Electrochemical measurements

2.4.1 Three-electrode system

A three-electrode system is a common set up for electrochemistry. It is composed of a working electrode (WE), a counter electrode (CE) and a reference electrode (RE). The redox reaction take places on the working electrode, which is normally made of platinum wire (**Figure 2.4a**). In the case of solid-state electrochemical study, samples can be deposited on conductive glass as working electrode (**Figure 2.4b**). Current is then passed via the counter electrode to complete the circuit. A standard reference electrode provides a reference for the potential applied to the known potential of the electrode.[31] In this work, Ag/AgCl reference electrode was used, where a thinly AgCl-coated Ag wire is surrounded by LiCl solution. The reference electrode functions as a redox electrode with equilibrium between Ag and AgCl as shown in the equation below:

$$AgCl\ (s) + e^- \leftrightarrow Ag\ (s) + Cl^-$$

a)

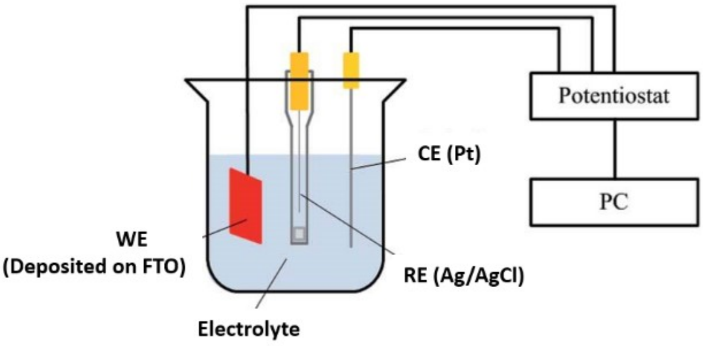

b)

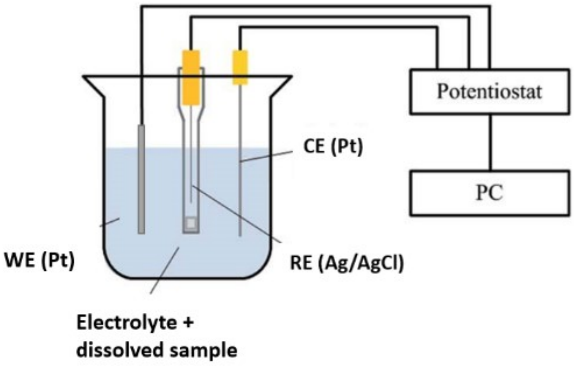

Figure 2.4 Schematic diagram of (a) three-electrode system with solid-state material deposited on FTO glass as working electrode and (b) with material dissolved and with Pt as working electrode. Figure reproduced from Red 31.

2.4.2 Cyclic Voltammetry

Cyclic voltammetry is an electrochemical technique to study the current response when applying a cycling potential to the working electrode, from where the energy profile of the studying material can be determined. A three-electrode system is commonly set up for this measurement, where the potential range and scan rate is set to allow forward and backward linear scans. The applied potential to the working electrode is measured against the reference electrode, and a typical applied potential signal is shown in **Figure 2.5a**, with the current response plotted against the applied potential shown in **Figure 2.5b**.

Oxidation process:

From t_0 to t_1: positive scan is applied to the working electrode. This process can be referred to from point a to d on **Figure 2.5b**, showing the oxidation process. Almost no current response can be seen from process a, since the applied potential is too low to initiate any oxidation. However, as the potential increases, an exponential rise of current is shown during process b. This process is caused by the accumulation of oxidised species at the working electrode. The current peaks at point c, where all of the materials have been oxidised at the working electrode, leading to the anodic peak current (I_{pa}). The corresponding potential is called anodic peak potential (E_{pa}). A decline of current can be observed from c to d, where the mass transfer is substantially limited.

Reduction process

The potential has changed its scan direction from t_1 to t_2, where a reverse scan is applied to the working electrode. In this case, the reduction process starts to take place once the potential is negative enough at point e, and peaks at f where the cathodic peak current (I_{pc}) is reached. The potential at this point is accordingly the cathodic peak potential.

In a reversible process shown in **Figure 2.5b**, the cathodic peak current equals the anodic peak current ($I_{pc} = I_{pa)}$, while $E_{pa} - E_{pc} = 0.59/n$ V, where n is the number of electrons transferred during the reaction. As the scan rate increases, peak currents will increase as the square root of scan rate, while the peak potential will remain the same. However, if an irreversible process is measured, E_{pa} and E_{pc} will not remain the same when the scan rate is changed.

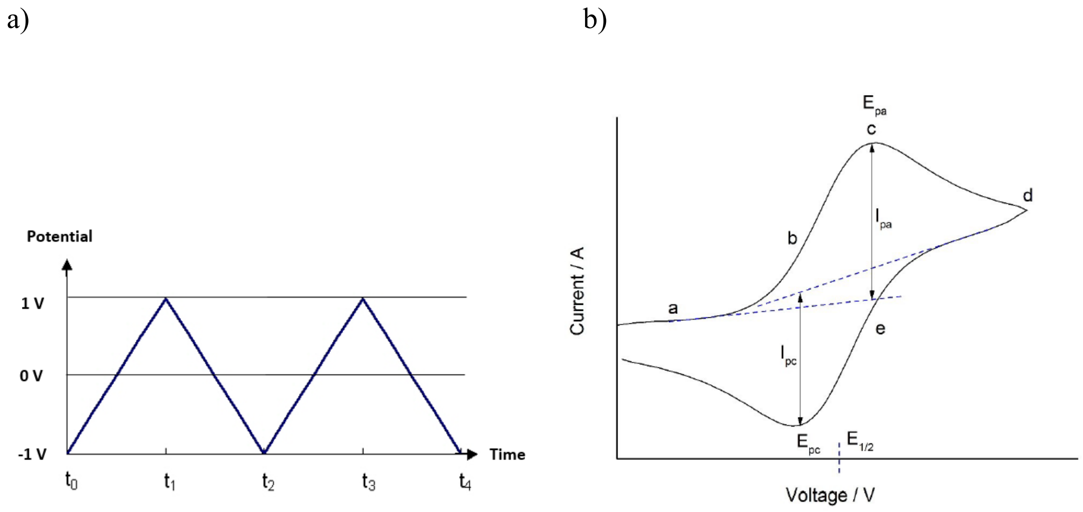

Figure 2.5 A typical cyclic voltammetry potential waveform (a), and a reversible cyclic voltammgram (b). Figure reproduced from Ref 32.

2.4.3 Probing the energy profile from electrochemistry measurement.

Electrochemistry reveals the energy required for adding/removing electrons from the material under an applied potential. By performing electrochemical measurement, the energy profile of the material can be probed, including the ionization potential (IP), electron affinity (EA) and electric energy band gap. For solid state materials, IP is determined by the difference from valence band maximum (VBM) to the vacuum level, and the EA is the energy level difference from conduction band minimum (CBM) to the vacuum level. The electric energy band gap is defined as the energy difference between the ionization potential and electron affinity (Equation 2.5), known as the fundamental gap (E_{fund}). [32]

$$E_{fund} = IP - EA \qquad \text{(Equation 2.5)}$$

Therefore, IP, EA and E_{fund} can be estimated by observing the oxidation and reduction processes. The applied potential for oxidation process corresponds to IP (i.e., electron removal from the VBM), while the applied potential for reduction is related to EA (i.e., the electron addition to the CBM).

During the oxidation process, charges will not be removed until the applied voltage reaches the energy potential of the VBM, and the onset value of the oxidation potential is used to determine IP, noted as E'_{ox}. The onset potential can be estimated on the voltammogram by drawing a tangent line across the steepest point, and E'_{ox} can be obtained from the extrapolation of the tangent line that intercepts with x-axis. When correlating the E'_{ox} to IP, it is necessary to consider the reference to vacuum level. According to the literature,[33,34] the standard hydrogen electrode (SHE) can be referred to the vacuum level with the relationship shown in Equation 2.6

$$E_{SHE} = E_{vac} + 4.6 \qquad \text{(Equation 2.6)}$$

Where E_{SHE} is the potential of standard hydtrogen electrode and E_{vac} is the vacuum potential. We can refer the E_{SHE} to the reference electrode (Ag/AgCl used in this study) according to the literature, and by combining Equation 2.6 we can get:

$$E_{Ag/AgCl} = E_{SHE} - 0.2 = E_{vac} + 4.4 \qquad \text{(Equation 2.7)}$$

Therefore, the relationship of E'_{ox} and E_{vac} can be calculated as:

$$E_{ox} = E'_{ox} + E_{Ag/AgCl} = E'_{ox} + E_{vac} + 4.4 \qquad \text{(Equation 2.8)}$$

Experimental

Cyclic voltammetry for material studies was carried out in N_2-degassed dichloromethane, dissolving 3 M $[N(C_4H_9)_4][BF_4]$ as the electrolyte. A three-electrode cell with an Autolab Type III potentiostat was used, and the results were further analysed on GPES electrochemical software. Spin-coated compounds on FTO conducting glasses were used as working electrodes; Pt was used as counter electrode; Ag/AgCl was used as reference electrode. A scan rate of 50 mV/s was applied in every redox process, unless otherwise stated, with the correction from ferrocenium/ferrocene (Fc^+/Fc) internal standard, taken to be at 0.630 V against Normal hydrogen electrode (NHE) or 0.624 V against standard hydrogen electrode (SHE).[35]

2.4.4 Photo-current measurement

As an alternative to fabricating a solar cell, which requires lots of time and effort, photo current measurements can provide an initial assessment of how the material respond to light. In this case, a three electrode cell can be made, with the active material coated on FTO as working electrode and Pt as counter electrode. The electrodes are in contact with the electrolyte containing a redox species to donate or accept electrons to the active material.

In this study, NaI was used as the electrode to generate I^-/I_2 redox couple and the photo-current measurement was carried out with/without the illumination from the solar simulator (Sciencetech SLB300A).

2.5 Vibrational studies

2.5.1 Raman spectroscopy

When photons from a monochromic laser beam strike onto the material, elastic scattering will occur, where the scattered photons have the same frequency as incident photons. This is called Rayleigh scattering. However, around $1/10^7$ of the scattered photons show a different frequency. This inelastic scattering was named the Raman Effect, discovered by V. C. Raman in 1928 and was awarded the Nobel Prize. Raman spectroscopy is a very important practical method to identify molecules from the perspective of bonding vibrational properties, since each molecule has its unique set of characteristic bonds. Therefore, Raman spectroscopy can provides a molecule's 'fingerprint', as well as more-specific bonding information for both molecular and non-molecular systems.[36]

The Raman Effect is caused by the incident photons interaction with the electric dipole moment of the molecule, leading to gaining or losing an amount of energy equal to the vibrational state. Different from photoluminescence effect where electronic transition occurs when electrons have absorbed energy, excitations to a virtual state that has lower energy than the electronic transition is happening in a Raman measurement. The photon is then emitted with lower or higher energy than the incident photon, depending on the final state of the molecule. If the final state energy is higher than initial state, it is called a Stokes shift, where the scattered photons have lower frequency than incident photons. On the contrary, anti-Stokes shift occurs when the final state energy is lower than the initial state, giving higher frequency to the scattered photons. The schematic diagram of Rayleigh scattering, Stokes Raman scattering, and Anti-Stokes Raman scattering are shown in **Figure 2.6**.

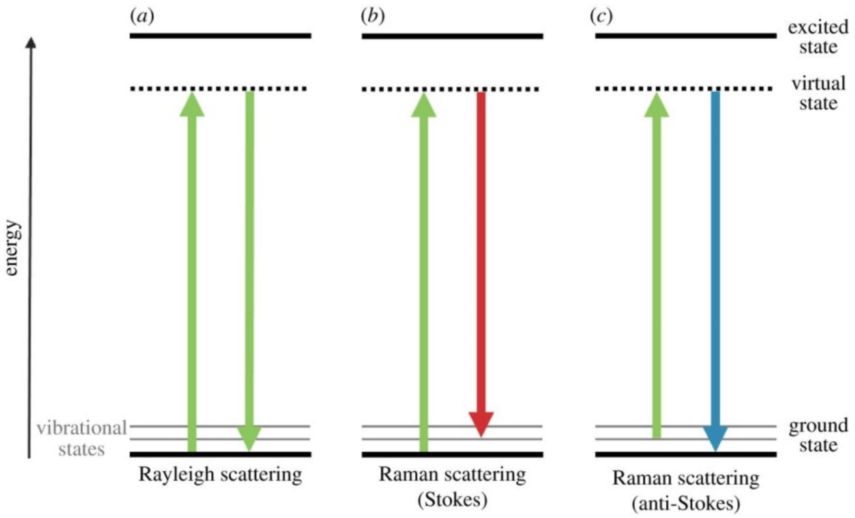

Figure 2.6 Schematic diagram of the energy transitions in a) Rayleigh scattering, b) Stokes Raman scattering and c) Anti-Stokes Raman scattering. Figure is reproduced from the literature.[37]

Experimental

Raman spectra were acquired from a Renishaw InVia Raman Microscope with the excitation laser wavelength of 785nm. The laser beam was perpendicular to the substrate, with a spectral resolution of roughly 1 cm^{-1}.

2.6 X-ray Photoelectron Spectroscopy

X-ray photoelectron spectroscopy (XPS) is widely used in material surface studies for analysing the elemental composition, quantitative ratio and chemical state of the elements. The idea originates from the photoelectric effect, where the incident X-ray photons can lead to emission of a core electron from the atom. The material of interest is deposited on a conductive glass or carbon paste to facilitate the electron flow, and the measurement is conducted under high vacuum. During the XPS measurement, monochromatic X-ray radiation incidents and interacts on the sample material, leading to the ejection of electron from an atomic energy level. The emitted electrons are collected and analysed by the detector for their kinetic energy. The process of photoelectron emission from the 1s shell of an atom is illustrated schematically in **Figure 2.7**, and can be expressed in the equations below:[38]

$$A + h\nu \rightarrow A^{+} + e^{-} \text{ (Equation 2.9)}$$

Where A is the atom in the material of interest, hν is the energy of incident radiation.

From the law of energy conservation we know that:

$$E(A) + h\nu \rightarrow E(A^{+}) + E(e^{-}) \quad \text{(Equation 2.10)}$$

Since the excess energy from X-ray radiation is turned into kinetic energy of the emitted electrons (E_k), again from the energy conservation we can get:

$$E_k = h\nu - (E(A^{+}) - E(A)) \quad \text{(Equation 2.11)}$$

$E(A^{+}) - E(A)$ describes the energy difference of the ionized atom and neutral atom, which is the binding energy (BE) of the electron. Therefore the equation above can be written as:

$$E_k = h\nu - BE \quad \text{(Equation 2.12)}$$

Since the hν of the incident monochromatic radiation is known, and the E_k of emitted electron can be analysed by the detector, by indexing the characteristic BE value to the database we can identify the atom species.

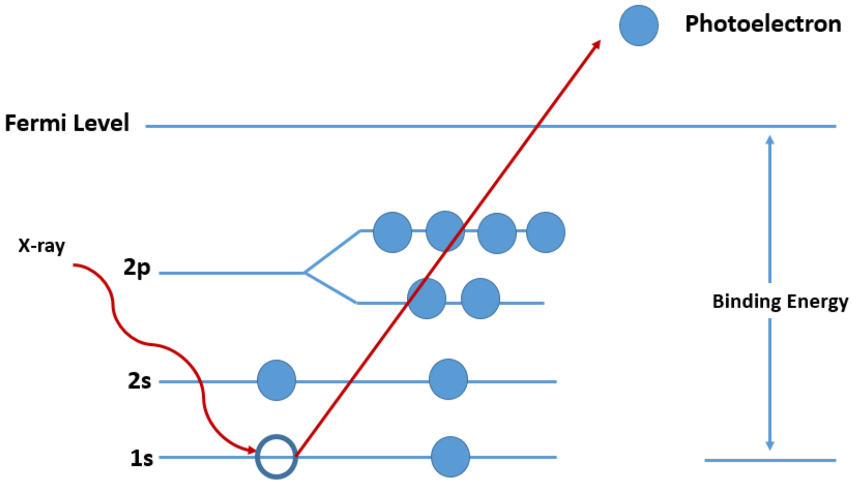

Figure 2.7 Schematic representation of the XPS mechanisms.

Even though both XPS and EDS measurement give insights into the elemental composition of the specimen, the fundamental mechanism of the above two techniques are different. In XPS, X-rays are incident on the sample, while the ejected electrons from the sample are detected. However, in an EDX measurement, electrons are incident onto the sample and generated X-ray photons from sample are detected. Due to the escape depth of electrons, XPS is only surface sensitive, and the main signal comes from atomic layer depth. However, EDX is able to give the composition info about the bulk material, with the penetration depth at the scale around μm. [39]

Experimental

X-ray photoelectron spectra for [Py][BiI_4], [MePy][BiI_4] and [PZ][Bi_2I_9] were obtained at the National EPSRC XPS Users' Service (NEXUS) at Newcastle University. All the spectra were acquired using a Kratos Axis Nova XPS spectrometer. The samples were manipulated using clean plastic tweezers and immobilised on top of a clean aluminium platen using carbon tape. Al-Kα radiation was used as the excitation source. X-ray photoelectron spectroscopy measurement for the rest of the materials studied in this thesis was carried out in the School of Chemistry, using a Sigma Probe X-ray Photoelectron spectrometer, manufactured by Thermo Fisher scientific. Al-Kα radiation was used as the excitation source, with sample scanned from -10.00 eV to 1400 eV in 0.50 eV steps. All of the materials were measured as deposited on FTO conductive glass.

2.7 Computational studies

Computational chemists use mathematical methods to describe theoretical chemistry, and then run simulations and computations on powerful computers to solve chemical problems. There are two aspects where computational studies have the distinct advantages. Firstly, computational results can be compared with the experimental results to provide theoretical support. Moreover, predictions and insights into the chemical process can be studied theoretically via computational modelling. In the field of photovoltaic materials study, computational methods are a powerful tool to gain more insight into the material properties and potential use, especially by analysing the band structure and density of states results. Details will be discussed in the following section.

2.7.1 Density functional theory

Density functional theory (DFT) is a quantum mechanical modelling method to study the electronic structures of many-body systems, and the total energy of the system is described by a unique functional of the electron density, depending on spatial variables x, y, and z.[40] In this method, electron density is translated into functionals to perform the calculations, without any higher dimensional material information as input. Therefore, DFT has developed as one of the most cost-effective and powerful computational methods.[41] Development of approximate density functionals is the key to yield accurate electronic energies for the system, and thus achieve higher accuracy for the approximation. There are hundreds of density-functional approximations to choose from, however, some of them perform better than others for certain types of systems. The three popular functionals, including local density approximation (LDA), Generalised Gradient Approximation (GGA) and hybrid DFT functionals (e.g., B3LYP). LDA is good for dealing with nearly-free electronic materials, where the electron density is a function of distance throughout the model with little variation.[42] However, a shortfall of this scheme is that it tends to overestimate the binding energy in molecular materials where the electron density variation is much greater.[43] The two-parameter dependant GGA functionals are commonly applied in condensed matter simulations, including PW91, PBE and BLYP. Among them, PBE, developed by Perdew, Burke and Ernzerhof in 1996, is the functional of choice for the majority of modellers.[44] Hybrid functions are constructed by combining the Hartree-Fock theory and DFT to tackle the exchange-correlation problems, and B3LYP is by far the most popular choice for cost-effective simulations for gas phase molecules.[45]

2.7.2 Approximations for solid-state materials with a periodic crystal structure

There are urgent research needs for DFT to achieve higher accuracy especially for solid-state materials with periodic crystal structures. Therefore, some correction schemes are applied to tackle these problems. Firstly, weak interactions such as Van der Waal interactions lead to a lack of computational accuracy especially when using GGA functionals to model solid-state materials. DFT+D scheme is applied to account for the dispersion relationships in DFT, so that van der Waals interactions can be taken into account to gain more precision. Secondly, fundamental band gaps in most solids are underestimated in DFT calculations. In the DFT+U correction scheme, an orbital-dependent interaction has been added within LDA or GGA. Moreover, DFT+U has also shown the capability to deal with electron-correlated systems in the presence of external perturbation. Without it however the electron correlations tend to be inaccurately calculated. [46]

2.7.3 Band structure

Different from single molecules, where the energy levels for atomic orbitals are finite, electronic bands of solid-state materials are derived from the overlap of a large number of atomic orbitals with very closely packed energy. In this case, the energy of adjacent levels are too close to be distinguishable and thus electronic band forms. Electronic band structure describes the allowed quantum state wavefunctions of electrons in a periodic lattice. **Figure 2.8** indicates the simplified band structure for metals, semiconductors and insulators. [1]

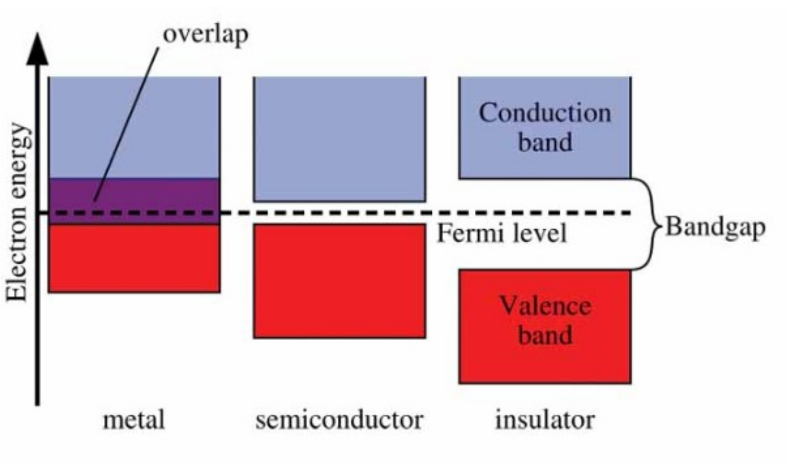

Figure 2.8 Simplified band structure and band gap comparison for a metal, semiconductor and insulator. Figure regenerated from ref 1.

By taking advantage of the crystal lattice periodicity, the energy for an electron in a periodic crystal can be calculated by solving the single-electron Schrödinger equation. This gives the Bloch wave, which is a wavefunction particularly for the periodically-repeating crystal lattice environment.

$$\Psi_{nk}(\mathbf{r}) = d^{i\mathbf{kr}}\, u_{nk}(\mathbf{r}) \quad \text{(Equation 2.13)}$$

Where ***k*** is the wavevector, the specific points on the first Brillouin zone. For each value of ***k***, multiple solutions can be calculated in the equation by varying the n in the Schrödinger equation, which is the number of the energy band. By plotting each of the energy levels against ***k***, we can derive smooth bands of different states, namely the band structure. When calculating the band structure, we can define the **k** vector pathway along the direction of interest, to study the electronic band structure along specific directions in the crystal lattice.[47]

2.7.4 Density of states and partial density of states

Density of states (DOS) describes the number of electronic energy states per unit energy, which can be generated from the band structure calculation. For semiconductors, electronic states are only permitted to exist at certain energy levels, including the valence band and conduction band. The DOS is discontinuous over an interval energy, which forms the region of the band gap.

The DOS can be further projected onto the orbitals of different atomic species to study the electronic level contribution and composition. The projected DOS allows the observation of electronic band structure composition from orbitals of specific atoms and their contribution to the total DOS. Calculating the projected DOS helps us to understand the electronic properties of the material at the atomic orbital level.

Experimental

Density functional theory (DFT) based computational studies were carried out to determine the electronic band structure of the materials, using the CASTEP 16.11[48] computational package utilized with the PBE functional[49] and the TS dispersion correction scheme.[50] The coordinates for each atom obtained from optimized single crystal geometry and generated from VESTA software.[51] 'On-the-fly' pseudopotentials were used for the calculations, which were generated directly from the CASTEP package. A series of single-point energy calculations has been carried out to identify suitable cut-off energies (E_{cut}) for plane wave basis sets ($dE_{tot}/dE_{cut} \leq 0.003$ eV per atom). Unit cell parameters were fixed at experimental values and optimized structures were considered to have been achieved once the convergence criteria (maximum change in system energy $2.0x10^{-5}$ eV/atom, maximum force 0.05eV/ Å, and maximum root-mean square (RMS) atomic displacement 0.002 Å) were reached. A Monkhorst-Pack grid was used for Brillouin zone sampling, with separation between ***k***-points less than 0.08 $Å^{-1}$. Electronic band structure plots were then calculated based on ***k***-vectors linking high symmetry points, and also via selected ***k***-points corresponding to strong intermolecular interactions. Density of States plot (DOS) and partial DOS plots for each crystal structure were generated by OptaDOS, which permits the contributions from different elements to be ascertained.

2.8 Solar cells device studies

2.8.1 Fabrication method for perovskite solar cells with metallic counter electrode

2.8.1.1 Mesoscopic structure TiO_2 sensitized solar cell

Solid-state solar cells have been fabricated and studied for organolead halide perovskite light absorbers. The first solid-state perovskite solar cell was studied by Park *et al* with PCE of 9.7% achieved, using 2, 2', 7, 7'-tetrakis(N, N-p-dimethoxy-phenylamino)–9, 9'–spirobifluorene (spiro-MeOTAD) as solid-state HTM.[52] The cross-sectional SEM of the perovskite solar cell is shown in **Figure 2.9**. Mescoscopic TiO_2 was used as the electron transport layer and sensitized by $MAPbI_3$, as well as scaffolding the perovskite crystals. Commonly, a 2-step procedure for depositing the perovskite is used. A schematic diagram of the experimental procedure is shown in **Figure 2.10**.

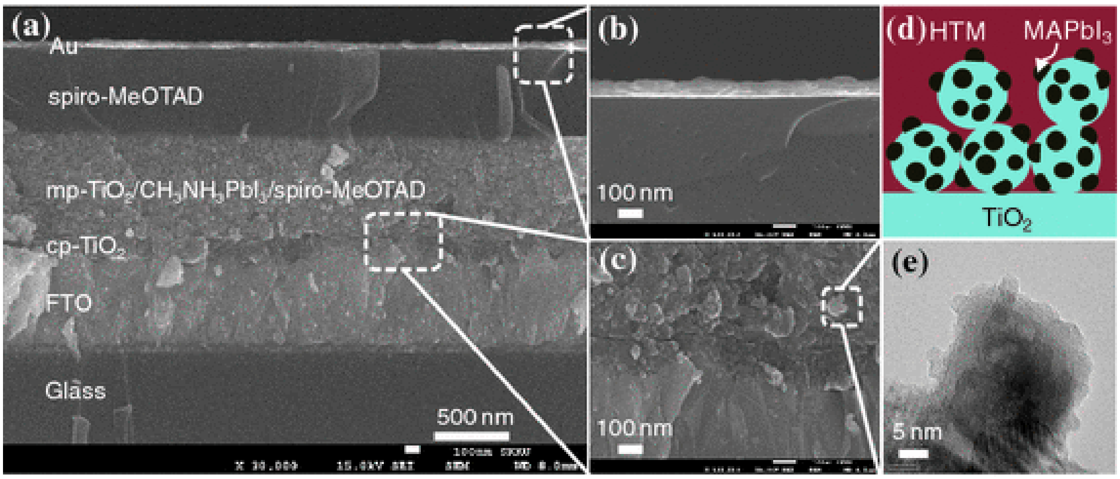

Figure 2.9 Cross-sectional SEM of a mesoscopic perovskite solar cell (a) with higher magnification at the gold-HTM interface (b), TiO_2 blocking layer interface (c), and perovskite nanocrystal (e). The TiO_2 sensitization with perovskite nanocrystal is shown in (d). Figures are reproduced from ref. 49.

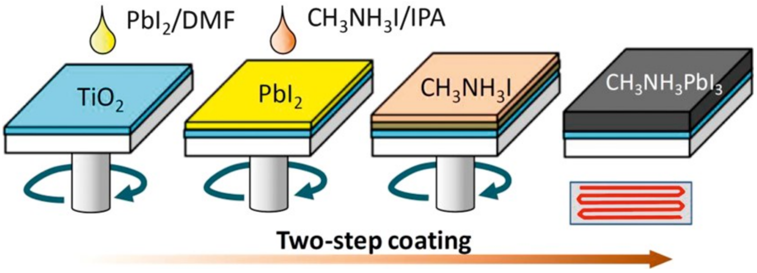

Figure 2.10 Schematic diagram of 2-step perovskite formation process. Figure reproduced from the literature.[54]

2.8.1.2 Planar heterojunction perovskite solar cells

Planar heterojunction perovskite solar cells were developed after the mesoscopic structure, showing high efficiency with much thinner and more flexible architecture. Liu *et al* demonstrated that the vapour-deposited perovskite layer shows much better crystallinity and interfacial contact compared to the solution processing method.[53] The cross-sectional SEM image of a perovskite solar cell with planar structure is shown in **Figure 2.11**, where the perovskite layer is deposited on top of the compact TiO_2 without the presence of mesoscopic TiO_2.[50] This study also demonstrated the electron-transporting ability of lead-halide perovskite material.

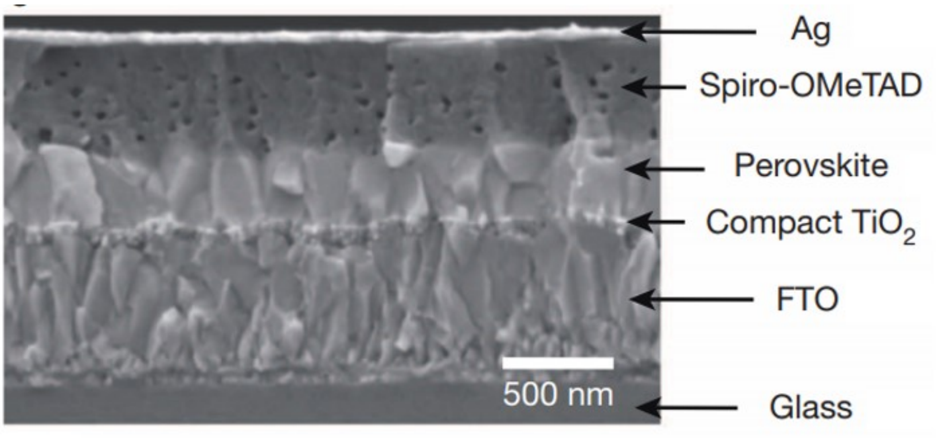

Figure 2.11 Cross-sectional SEM of a heterojunction planar solar cell. Figure reproduced from ref. 50.

2.8.2 Fabrication method for triple mesoscopic perovskite solar cells

Instead of using noble metals as the counter electrode, carbon has also been widely studied as the counter electrode material for solar cells fabrication due to its suitable energy level. On top of this, carbon has many other advantages including cost-effectiveness, screen-printability and enhancement of the stability of the perovskite materials. [55–58]

Han's group has led the study of triple mesoscopic solar cell structure, with the best efficiency achieved of over 15% in the stable lead-halide perovskite solar cell studies.[55,59] The cross-sectional SEM image of a triple mesoscopic solar cell is shown in **Figure 2.12a**. Specifically, mesoscopic TiO_2 (around 500 nm – 1 μm), ZrO_2 (around 500 nm – 1 μm) and carbon (10 μm) are deposited on top of the compact TiO_2 layer on FTO, and the perovskite precursor solution is penetrated throughout the triple layers. No HTM is employed in this case because the perovskite material itself is a good hole-conductor. The insulating ZrO_2 layer is effective in reducing the recombination of photo-generated electrons. The energy level diagram of the solar cell is shown in **Figure 2.12b**.

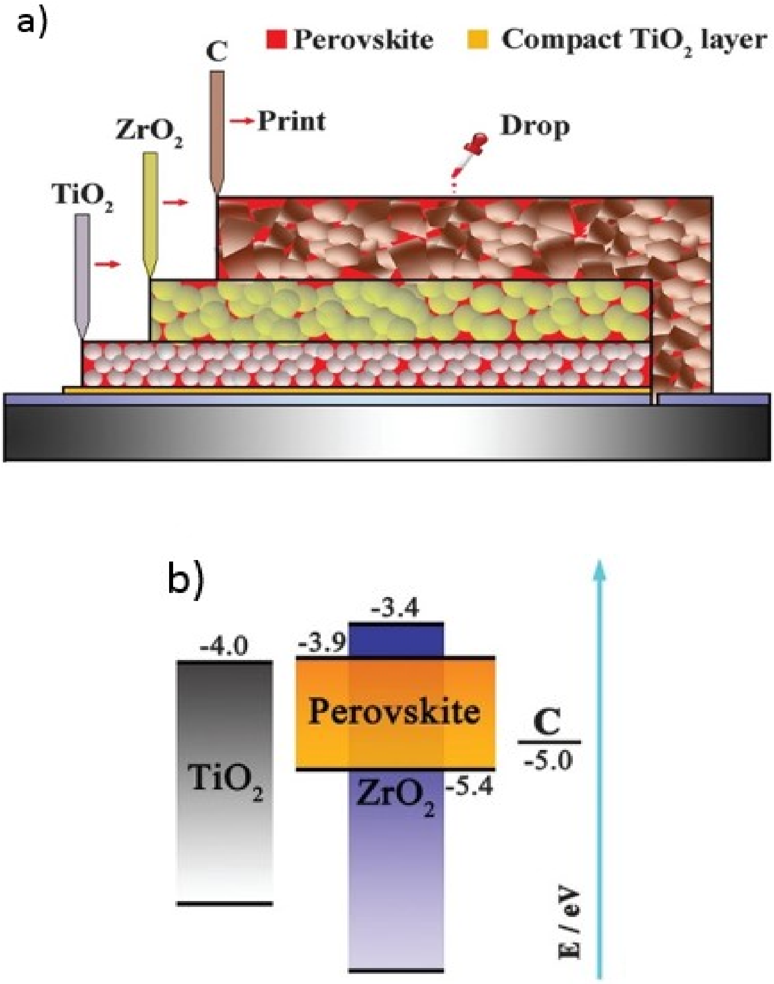

Figure 2.12 Cross-section SEM of a triple-layer mesoscopic structure solar cell (a), the energy level alignment diagram (b) and the structure of lead-halide perovskite. Figures are reproduced from ref 52.

Experimental:

Fluorine doped tin oxide (FTO) glass was first laser etched to form two detached electrodes before being cleaned subsequently with detergents, deionized water and ethanol in an ultrasonic cleaner. Titanium diisopropoxide bis(acetyl acetonate) solution, dissolved in isopropanol, was sprayed on the surface of the FTO at 450°C to form a compact layer of titanium dioxide (TiO_2). Mesoporous layers of TiO_2, ZrO_2 and carbon were then deposited layer by layer by screen printing method. The TiO_2 layer was sintered at 500°C for 40 minutes, followed by depositing and sintering the ZrO_2 and carbon layers at 400°C for 40 minutes. Finally, 2.5μl of the perovskite precursor solution was infiltrated into the triple layer cell, followed by a covered annealing at 60°C for 40 minutes.

2.8.3 Solar testing

Photocurrent density versus voltage characteristics of solar cell devices were characterised by Keithley Model 2400 digital sourcemeter with Newport solar simulator (model 91192) in Huazhong University of Science and Technology. An irradiance of 100 mW/cm^2 was calibrated by the standard reference cell (Newport Oriel PV reference cell, model 91150 V) prior to the measurements. A black mask with a circular aperture (0.07 cm^2) was used to cover the active area of the device. The J–V testing was performed at 25 °C with both reverse and forward scan directions at 250 mV·s^{-1} (sweep delay time of 100 ms). The set-up can be illustrated schematically in **Figure 2.13**. The IPCE spectra were measured using a 150 W xenon lamp (Oriel) fitted with a monochromator (Cornerstone 74004) as a monochromatic light source. Calibration with the Oriel Si detector was carried out before IPCE measurements.

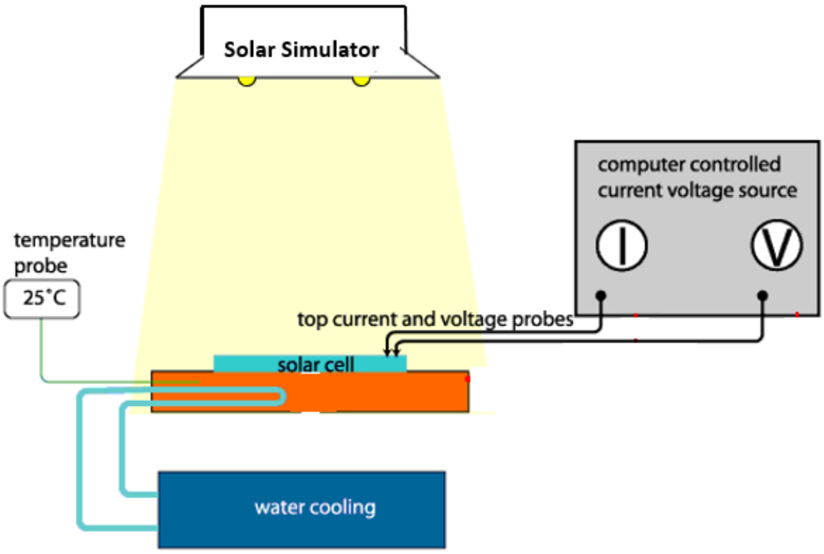

Figure 2.13 Schematic diagram of a solar testing device, where solar cell is tested under the illumination from a solar simulator and connected to an autolab for current/voltage data analysis.

2.8.4 Hysteresis and capacitive behaviour measurement

Current-voltage (J-V) hysteresis behaviour is often found in lead-halide perovskite solar cells, where a loss of photocurrent and voltage occurs when the device undergoes a reverse to forward scan compared to forward to reverse scan. Such J-V hysteresis behaviour present a challenge for the determination of the actual power conversion efficiency of perovskite solar cells.[60] The possible underlying origin of hysteresis behaviour is elucidated by many mechanism studies, with proposed mechanisms including (i) trapping of charge carriers at the interface; (ii) ion migration; (iii) ferroelectric polarization and (iv) capacitive effects.[61] Hysteresis effects for printable triple-mesoscopic perovskite solar cells have also been evaluated, with hysteresis-normal, hysteresis-free or hysteresis-inverted behaviours depending on the deposition method of the compact-TiO_2 layer in the device.[62] In our study, we evaluated the hysteresis effect of printable triple-mesoscopic solar cells employing **[AT][BiI_4]** as the light absorber, by measuring the actual photocurrent I_p, stabilized current and device capacitance.

Experimental

Cyclic voltammetry (CV) tests for solar cell devices were measured with a ZAHNER Zennium Electrochemical Workstation in the dark with sweep rate of 100 mV s^{-1}. The stabilized current was tested under a bias voltage of 0.27 V with the same sourcemeter and solar simulator. No preconditioning protocol was used before the characterization. The cell capacitance was calculated from the CV measurement of the device, according to the equation:

$$C = \frac{i}{s} \quad \text{(Equation 2.14)}$$

where ‘i’ is the average of cathodic current and ‘s’ is the scan rate for the measurement.

The areal capacitance was calculated according to the equation:

$$C_{areal} = \frac{2C}{A} \quad \text{(Equation 2.15)}$$

where ‘A’ is the electrode area.

2.9 Supercapacitor device studies

2.9.1 Fabrication method for symmetric supercapacitors

A supercapacitor consists of two electrodes, electrolyte and an ion-permeable separator that prevents electrodes from contacting each other. The electrode is made by coating active materials onto the current collectors, and in the case of symmetric supercapacitors, both of the electrodes are identical. We used a solution-processed method for active material deposition. Specifically, the precursor solution was made by dissolving the active material in 1 mL DMF and mixing with activated charcoal powder and PTFE powder, to make a final active material : charcoal: PTFE mixture with a weight ratio of 85:10:5 (total mass: about 500 mg). The resulting suspension was sonicated until homogenized, and around 200 μL was drop-coated onto 1 cm^2 of conductive carbon cloth (ELAT, NuVant Systems Inc.) substrate. Absorbing tissue was placed underneath the carbon cloth to absorb excess solution in order to maximize surface coverage and film homogeneity of the carbon cloth while reducing excess mass loading of the active material layer. The coated electrodes were then annealed at 150 ℃ for 1 h on a hotplate. The dimensions of the carbon cloth was measured under an optical microscope, and the mass of active material was determined by subtracting the mass of carbon cloth (density: 13.0 mg/cm^2, shown on the product manual) from the total mass of the dried electrode (estimated error: ±0.4 mg based on multiple repeat measurements). A thin (25μm) microporous membrane (Celgard 3501) previously soaked in a saturated $NaClO_4$ (aq.) electrolytic solution was sandwiched between two of these as-coated electrodes, and the entire set-up was assembled in a standard capacitor test cell (ECC-std, EL-CELL GmbH) for tight packing and ease of measurement (**Figure 2.14**).

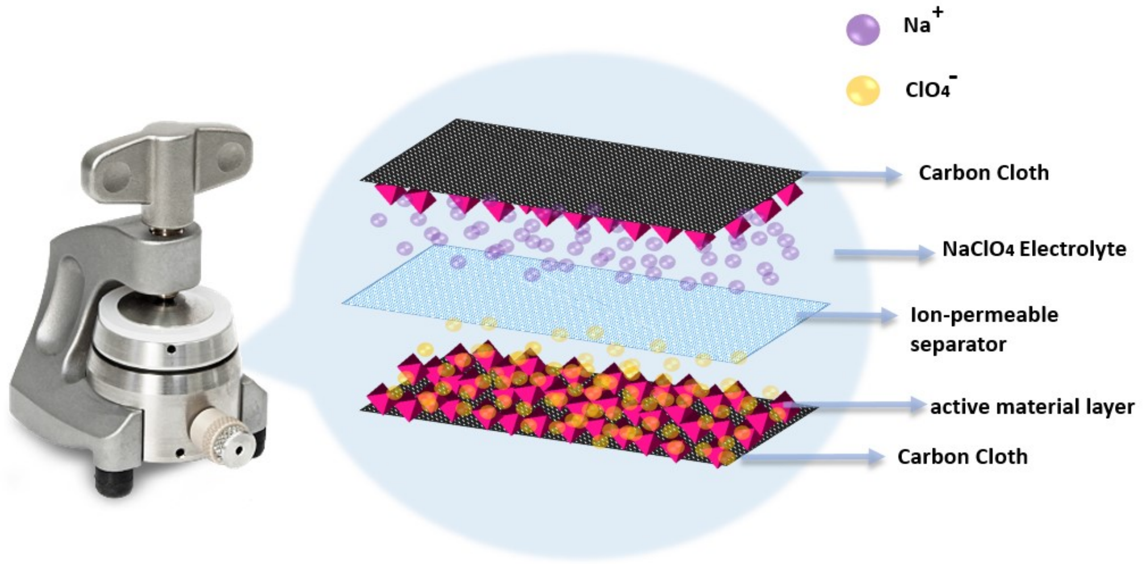

Figure 2.14 Schematic diagram of a symmetric EDLC used in our study.

The controlled experiment with electrodes deposited from the active material suspension solution was also prepared. A mixture of active material: charcoal: PTFE = 85:10:5 was dispersed and sonicated for 15 min in 1 mL ethanol, with same weight ratio and a total mass of 500 mg.

2.9.2 Capacitive and long-term cycle stability tests

The common methods for determining the capacitance of am EDLC device are cyclic voltammetry (CV), galvanostatic charge-discharge measurement and electrochemical impedance spectroscopy (EIS). CV is performed to plot the applied bias versus the current under different scan rates, and for an ideal capacitor, the CV curve should be a rectangular shape (**Figure 2.15a**). Under a given voltage, the following relationship is obeyed by a capacitor:

$$Q = CV \quad \text{(Equation 2.16)}$$

Where Q is the total charge stored in a capacitor, V is the applied voltage and C is the capacitance. Differentiation of the above equation with time gives the following equation,

$$\frac{dQ}{dt} = C\,\frac{dV}{dt} \quad \text{(Equation 2.17)}$$

Where $\frac{dV}{dt}$ is the scan rate (s) and $\frac{dQ}{dt}$ is the current (I). Due to the non-idealities of a real-life capacitor, the average cathodic current over the applied voltage window was used, which corresponds to the discharging process. The areal and specific capacitances of an assembled supercapacitor device were calculated from the CV curves according to the Equations 2.18 and 2.19:[43]

$$C_{areal}\ [=]\ {}^{F}/_{cm^2} = \frac{\int_{\Delta V} i\, dV}{\Delta V \times s \times A} \quad \text{(Equation 2.18)}$$

$$C_{specific}\ [=]\ {}^{F}/_{g} = \frac{\int_{\Delta V} i\, dV}{\Delta V \times s \times m} \quad \text{(Equation 2.19)}$$

where ΔV is the voltage window of the negative (cathodic) current (V), s is the constant scan rate (V s^{-1}), A is the average geometric area of the two electrodes (cm^2), and m is the combined mass of the active material on both electrodes (g).

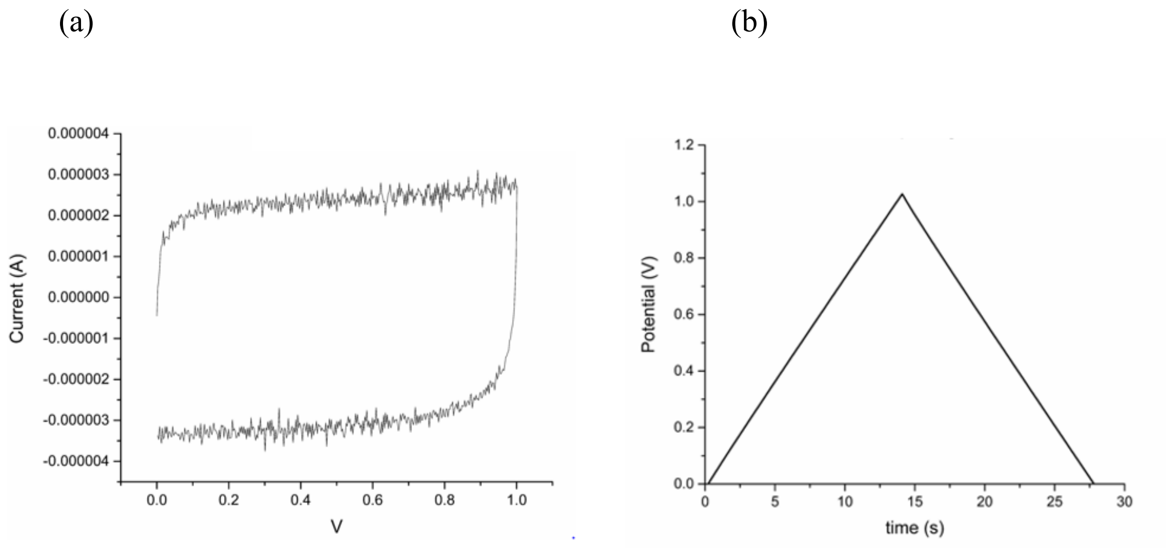

Figure 2.15 Cyclic voltammetry (a) curve and Galvanostatic charge-discharge curve (b) measured from a standard commercial EDLC (10V, 100µF).

In Galvanostatic charge-discharge method, a constant current is applied to the device during the measurement process, and the change of voltage versus time is recorded. Ideally, a symmetric triangle-shaped curve can be obtained from an EDLC, with a constant rate of potential increment during both charging and discharging process (**Figure 2.15b**). However, the non-idealities of the supercapacitor device give rise to the non-symmetrical curves, and the discharging process is considered when calculating the capacitance. Rearranging Equation 2.17 we can get:

$$C = \frac{\frac{dQ}{dt}}{\frac{dV}{dt}} = \frac{i}{s} \quad \text{(Equation 2.17)}$$

where i is the current and s is the slope of discharge curve. The areal and specific capacitances were also calculated from the slope of the discharge curves in their linear regimes according to:

$$C_{areal} = {}^{F}/_{cm^2} = \frac{i}{\frac{dV}{dt} \times A} \quad \text{(Equation 2.18)}$$

$$C_{specific} = {}^{F}/_{g} = \frac{i}{\frac{dV}{dt} \times m} \quad \text{(Equation 2.19)}$$

Experimental:

Electrochemical measurements were carried out by connecting the test cell in a two-electrode configuration to an Autolab potentiostat using General Purpose Electrochemical System (GPES) software. For the long-term cycle stability test, cyclic voltammetry was performed 5000 times under a scan rate of 0.1 V/s. The capacitance retention diagram was plotted with the capacitance calculated every 200 cycles.

2.9.3 Electrochemical impedance spectroscopy

Electrochemical impedance spectroscopy (EIS) is a powerful diagnostic tool to characterize the physical and electrochemical processes of the supercapacitor in response to AC current at varying frequencies.[60,61] Different from the CV or Galvanostatic charge-discharge measurement, EIS is a perturbative characterization of the dynamics of an electrochemical process. During the measurement, a small amplitude AC signal was generated by a frequency response analyser and imposed to the supercapacitor over a broad frequency range. This is followed by the collection of voltage and current responses to study the resistive, capacitive and inductive behaviours of the device. The imaginary (out-of-phase) impedance versus the real (in-phase) impedance of the supercapacitor is plotted in a Nyquist plot; Bode plots refer to the impedance magnitude and phase angle as a function of applied frequency. Based on the data, a modified Randles equivalent circuit can be simulated to analyse the resistive and capacitive elements in the supercapacitor.

Experimental

EIS analysis was performed by connecting the as-assembled supercapacitor test cell in a two-electrode configuration to an Autolab potentiostat with the FRA2 module, using Frequency Response Analyser (FRA, version 4.9.007) software. Equivalent circuit fitting was conducted using FRA's Fit and Simulation software (version 1.7). All of the EIS measurements were conducted with a baseline potential of 0 V and an AC amplitude of 10 mV at frequencies ranging from 150 kHz to 0.1 Hz.

2.10 References

1 C. Kittel, *Introduction to Solid State Physics (8th Edition)*, John Wiley & Sons Inc, United States, 2004.

2 P. G. Vekilov, *Nanoscale*, 2010, **2**, 2346–2357.

3 C. Guo, J. Wang, J. Li, Z. Wang and S. Tang, *J. Phys. Chem. Lett.*, 2016, **7**, 5008–5014.

4 D. Erdemir, A. Y. Lee and A. S. Myerson, *Acc. Chem. Res.*, 2009, **42**, 621–629.

5 P. C. Weber, *Adv. Protein Chem.*, 1991, **41**, 1–36.

6 L. H. J. George H. Stout, *X-ray structure determination : a practical guide (2nd Edition)*, New York, John Wiley & Sons, 1989.

7 M. Gu, P. Gao, X.-L. Liu, S.-M. Huang, B. Liu, C. Ni, R.-K. Xu and J. Ning, *Mater. Res. Bull.*, 2010, **45**, 636–639.

8 S. Ramukutty and E. Ramachandran, *J. Cryst. Growth*, 2012, **351**, 47–50.

9 H. Adachi, K. Takano, M. Morikawa, S. Kanaya, M. Yoshimura, Y. Mori and T. Sasaki, *Acta Crystallogr. - Sect. D Biol. Crystallogr.*, 2003, **59**, 194–196.

10 A. Messerschmidt, *X-Ray Crystallography of Biomacromolecules: A Practical Guide*, John Wiley & Sons, 2007.

11 M. Tanaka, S. Yamanaka, Y. Shirakawa, A. Shimosaka and J. Hidaka, *Adv. Powder Technol.*, 2011, **22**, 125–130.

12 M. Adam, Z. Wang, A. Dubavik, G. M. Stachowski, C. Meerbach, Z. Soran-Erdem, C. Rengers, H. V. Demir, N. Gaponik and A. Eychmüller, *Adv. Funct. Mater.*, 2015, **25**, 2638–2645.

13 O. V. Dolomanov, L. J. Bourhis, R. J. Gildea, J. A. K. Howard and H. Puschmann, *J. Appl. Crystallogr.*, 2009, **42**, 339–341.

14 G. M. Sheldrick, *Acta Crystallogr. Sect. A Found. Crystallogr.*, 2008, **64**, 112–122.

15 A. Clearfield and N. Bhuvanesh, in *Encyclopedia of Inorganic and Bioinorganic Chemistry*, John Wiley & Sons, 2011.

16 A. B. Murphy, *Sol. Energy Mater. Sol. Cells*, 2007, **91**, 1326–1337.

17 Kubelka and Munk, *Zeit. Für Tekn. Phys.*, 1931, **12**, 593.

18 J. Tauc, *Mater. Res. Bull.*, 1968, **3**, 37–46.

19 M. Nowak, B. Kauch and P. Szperlich, *Cit. Rev. Sci. Instruments Appl. Phys. Lett. J. Appl. Phys. J. Appl. Phys. J. Appl. Phys. J. Appl. Phys. J. Appl. Phys. Appl. Phys. Lett.*, 2009, **801**, 46107–2042.

20 A. Tumuluri, K. L. Naidu and K. C. J. Raju, *Int. J. ChemTech Res*, 2014, **6**, 3353–3356.

21 N. Ntholeng, B. Mojela, S. Gqoba, M. Airo, S. Govindraju, M. J. Moloto, J. Van Wyk and N. Moloto, *New J. Chem.*, 2016, **40**, 10259-1026.

22 K. N. Shinde, S. J. Dhoble, H. C. Swart and K. Park, in *Phosphate Phosphors for Solid-State Lighting*, 2013, **174**, 41–60.

23 J. L. McHale, L. Bergman, *Handbook of Luminescent Semiconductor Materials (1st edition)*, CRC Press, 2011.

24 H. Tang, H. Berger, P. E. Schmid, F. Lévy and G. Burri, *Solid State Commun.*, 1993, **87**, 847–850.

25 S. Zhang, L. Lei, S. Yang, X. Li, Y. Liu, Q. Gao, X. Gao, Q. Cao and Y. Yu, *Chem. Lett.*, 2016, **45**, 592–594.

26 R. F. Egerton, in *Physical Principles of Electron Microscopy*, 2005, pp. 125–153.

27 R. A. Carlton, *Microscope*, 1999, **47**, 5–11.

28 W. Ke, C. Xiao, C. Wang, B. Saparov, H. S. Duan, D. Zhao, Z. Xiao, P. Schulz, S. P. Harvey, W. Liao, W. Meng, Y. Yu, A. J. Cimaroli, C. S. Jiang, K. Zhu, M. Al-Jassim, G. Fang, D. B. Mitzi and Y. Yan, *Adv. Mater.*,

2016, **28**, 5214–5221.

29 G. Divitini, S. Cacovich, F. Matteocci, L. Cinà, A. Di Carlo and C. Ducati, *Nat. Energy*, 2016, **1**, 15012.

30 Q. Jeangros, M. Duchamp, J. Werner, M. Kruth, R. E. Dunin-Borkowski, B. Niesen, C. Ballif and A. Hessler-Wyser, *Nano Lett.*, 2016, **16**, 7013–7018.

31 G. A. Mabbott, *J. Chem. Educ.*, 1983, **60**, 697.

32 Jean-Luc Bredas, *Mater. Horizons*, 2014, **1**, 17–19.

33 M. L., N. F. and H. I., *J. Solid State Electrochem.*, 2002, **7** (1), 55-59.

34 S. Trasatti, *J. Electroanal. Chem.*, 1983, **150**, 1-15.

35 V. V. Pavlishchuk and A. W. Addison, *Inorganica Chim. Acta*, 2000, **298** (1), 97-102.

36 D. Wolverson, *Nature*, 2008, 17, 153–320.

37 C. C. Moura, R. S. Tare, R. O. C. Oreffo and S. Mahajan, *J. R. Soc. Interface*, 2016, **13** (118), 20160182.

38 J. F. Watts, J. Wolstenholme, An Introduction to Surface Analysis by XPS and AES, John Wiley & Sons, 2003.

39 S. Hüfner, *Energy*, 2003, **21**, 189–237.

40 E. Engel and R. M. Dreizler, *Density Functional Theory*, Springer, 2011.

41 M. S. Gordon and M. W. Schmidt, *Theory and Applications of Computational Chemistry*, Elsevier, 1167–1189, 2005.

42 A. D. Becke, *J. Chem. Phys.*, 1993, **98**, 1372–1377.

43 J. Kreutzer, P. Blaha and U. Schubert, *Comput. Theor. Chem.*, 2016, **1084**, 162–168.

44 A. D. Becke, *Phys. Rev. A*, 1988, **38**, 3098–3100.

45 A. Seidl, A. Görling, P. Vogl, J. Majewski and M. Levy, *Phys. Rev. B - Condens. Matter Mater. Phys.*, 1996, **53**, 3764–3774.

46 B. Himmetoglu, A. Floris, S. De Gironcoli and M. Cococcioni, *Int. J. Quantum Chem.*, 2014, **114**, 14–49.

47 L. E. Smart and E. A. Moore, *Solid State Chemistry (4th Edition)*, CRC Press, Florida, 2012.

48 S. J. Clark, M. D. Segall, C. J. Pickard, P. J. Hasnip, M. I. J. Probert, K. Refson and M. C. Payne, *Zeitschrift für Krist.*, 2005, **220**, 567–570.

49 J. P. Perdew, K. Burke and M. Ernzerhof, *Phys. Rev. Lett.*, 1996, **77**, 3865–3868.

50 A. Tkatchenko and M. Scheffler, *Phys. Rev. Lett.*, 2009, **102**, 073005.

51 K. Momma and F. Izumi, *J. Appl. Crystallogr.*, 2011, **44**, 1272–1276.

52 H. S. Kim, C. R. Lee, J. H. Im, K. B. Lee, T. Moehl, A. Marchioro, S. J. Moon, R. Humphry-Baker, J. H. Yum, J. E. Moser, M. Grätzel and N. G. Park, *Sci. Rep.*, 2012, **2**, 591.

53 M. Liu, M. B. Johnston and H. J. Snaith, *Nature*, 2013, **501**, 395–398.

54 J. H. Im, H. S. Kim and N. G. Park, *APL Mater.*, 2014, **2**, 081510.

55 A. Mei, X. Li, L. Liu, Z. Ku, T. Liu, Y. Rong, M. Xu, M. Hu, J. Chen, Y. Yang, M. Grätzel and H. Han, *Science*, 2014, **345**, 295–298.

56 Y. Rong, Z. Ku, A. Mei, T. Liu, M. Xu, S. Ko, X. Li and H. Han, *J. Phys. Chem. Lett.*, 2014, **5**, 2160–2164.

57 Z. Ku, Y. Rong, M. Xu, T. Liu and H. Han, *Sci. Rep.*, 2013, **3**, 3132.

58 J. G. Nam, Y. J. Park, B. S. Kim and J. S. Lee, *Scr. Mater.*, 2010, **62**, 148–150.

59 Y. Hu, Z. Zhang, A. Mei, Y. Jiang, X. Hou, Q. Wang, K. Du, Y. Rong, Y. Zhou, G. Xu and H. Han, *Adv. Mater.*, 2018, **30** (11), 1705786.

60 B. Chen, M. Yang, S. Priya and K. Zhu, *J. Phys. Chem. Lett.* 2016, **7**, 905−917

61 N. K. Elumalai abd A. Uddin, *Solar Energy Materilas and Solar Cells*, 2016, **157**, 476-509.

62 Y. Rong, Y. Hu, S. Ravishankar, H. Liu, X. Hou, Y. Sheng, A. Mei, Q. Wang, D. Li, M. Xu, J. Bisquert and H. Han, *Energy Environ. Sci*., 2017, **10**, 2383

63 J. R. Macdonald, W. B Johnson, *Fundamentals of Impedance Spectroscopy,* John Wiley & Sons, 2005.

64 R. L. Sacci and D. A. Harrington, *ECS Transactions*, 2009, **19** (20), 31-42.

Chapter 3

Hybrid iodobismuthates with 6-membered Heterocyclic Cations as Solar Absorbers: pyridinium, methylpyridinium and pyrazinium iodobismuthates

3.1 Introduction

Zero-dimensional $Cs_3Bi_2I_9$ (CBI) and $[CH_3NH_3][Bi_2I_9]$ (MBI) were some of the first examples studied for the purpose of substituting lead (Pb^{2+}) with bismuth (Bi^{3+}) in the well-studied Cs_3PbI_3 and $CH_3NH_3PbI_3$ perovskites.[1] Due to the difference in chemical valence, the three-dimensional perovskite structure cannot be formed, and instead a crystal structure that is built by $[Bi_2I_9]^{3-}$ binuclear edge-sharing octahedral is formed.[2–4] The dimensionality of the inorganic Bi-I motif depends on the size of A cation, leading to 0-dimensional, 1-dimensional or 2-dimensional structures.[5] Compared to cost-effective 3D lead-halide perovskites, enhanced atmospheric stability and reduced toxicity have been demonstrated by hybrid or inorganic bismuth-halide materials, and maintaining the economical and facile fabrication process that accredit to the possibility of forming a new class perovskite-like solar absorbers.[6] However, the power conversion efficiency (PCE) is far from satisfactory. One reason for the inferior PCE is the dimensionality of charge carrier mobility, which can be demonstrated by the relatively flat band structure with little dispersion at the band edge. The other reason is due to the high band-gap value, typically over 2.0 eV. This leads to a large spectral loss in the visible range, since high energy is needed for electron excitation from valence band to conduction band.[7]

3.2 Research proposal

Careful tailoring of the cationic part of hybrid iodobismuthates may lead to higher structural dimensionality, which could increase the possibility of higher charge carrier mobility and thus potentially increase their photovoltaic performance.[8] Cations based on an aromatic system with π-conjugation are of great interest, since they may promote electronic interactions with anionic frameworks.[9] At the same time, cations should be readily available or simply synthesized, and the iodobismuthate complexes should be soluble in organic solvents under mild conditions to provide the possibility of low-cost printable fabrication. Therefore, pyridinium and its derivatives were chosen as the organic counterion for the bismuth complexes. The delocalization of π electrons has the potential to enable good interaction with the iodobismuthate framework, aiming to build up enhanced intermolecular interactions and higher dimensionality of charge transport. We initiated this work with three simple aromatic cations, pyridinium, methylpyridium and pyrazinium. They are all hytereocyclic rings composed of C and N, also with reasonably small size to pack alongside the inorganic Bi-I framework. To study the new materials structurally, we managed to obtain single crystals of each compound, and single-crystal XRD was performed to determine the crystal structures. With atomic coordinates acquired from the XRD measurements, computational studies were carried out to determine the electronic band structure and the orbital contribution from each element. Optical and electronic properties of each materials using diffuse reflectance, cyclic voltammetry, XPS, etc. Finally, device studies were carried out to evaluate their photovoltaic performances.

3.3 Results and discussions

3.3.1 X-ray diffraction

Pyridinium bismuth iodide $C_5H_6NBiI_4$ (**$[PY][BiI_4]$**), methylpyridinium bismuth iodide $C_6H_8NBiI_4$ (**$[MEPY][BiI_4]$**) and pyrazinium bismuth iodide $C_{31}H_{46}N_{12}O_2Bi_4I_{18}$ (**$[PYZ]_6[Bi_2I_9]_2{\cdot}C_3H_6O{\cdot}C_4H_{10}O$**) have been synthesized and studied. The crystal structure of **$[PY][BiI_4]$**, **$[MEPY][BiI_4]$** and **$[PYZ]_6[Bi_2I_9]_2{\cdot}C_3H_6O{\cdot}C_4H_{10}O$** were determined by single crystal X-ray diffraction, carried out by Dr. Gary S. Nichol. The crystallographic information for the three compounds is shown in **Table 3.1**, and detailed crystallographic information can be found in Appendix **Table A1-A11**.

Table 3.1 Summary of crystallographic data for [PY][BiI_4], [MEPY][BiI_4] and $[PYZ]_6[Bi_2I_9]_2 \cdot C_3H_6O \cdot C_4H_{10}O$.

Compounds	**[PY][BiI_4]**	**[MEPY][BiI_4]**	**$[PYZ]_6[Bi_2I_9]_2 \cdot C_3H_6O \cdot C_4H_{10}O$**
Formula	$C_5H_6BiI_4N$	$C_6H_8BiI_4N$	$C_{31}H_{46}Bi_4I_{18}N_{12}O_2$
$D_{calc.}$/ g cm^{-3}	3.83	3.749	3.266
μ/mm^{-1}	21.656	20.836	16.543
Formula Weight	796.69	810.71	3744.96
Colour	red	red	dark red
Shape	plate	block	block
Max Size/mm	0.28	0.09	0.57
Mid Size/mm	0.21	0.06	0.16
Min Size/mm	0.09	0.06	0.09
T/K	150	120	120
Crystal System	monoclinic	monoclinic	monoclinic
Space Group	$P2_1/c$	$P2_1/c$	$P2_1/c$
a/Å	12.6997(3)	7.7618(5)	22.5586(3)
b/Å	28.3198(6)	14.0412(8)	9.44658(14)
c/Å	7.7160(2)	13.1959(8)	35.7654(5)
β/°	95.2880(10)	92.959(6)	91.9371(13)
V/Å^3	2763.27(11)	1436.24(15)	7617.28(19)
Z	8	4	4
Z'	2	1	1
Θ_{min}/°	1.438	2.901	2.813
Θ_{max}/°	28.313	30.967	25.348
Measured Refl.	9303	7443	252957
Independent Refl.	9303	7443	13930
Reflections Used	7345	5413	13148
Parameters	200	112	608
Restraints	72	0	109
Largest Peak /Å	3.098	2.285	3.946
Deepest Hole /Å	-2.356	-1.785	-2.498
GooF	1.102	0.924	1.283
wR_2 (all data)	0.1785	0.0784	0.0932
wR_2	0.165	0.075	0.0921
R_1 (all data)	0.0859	0.0659	0.0539
R_1	0.0634	0.0427	0.05

*3.3.1.1 Crystallographic study of **[PY][BiI$_4$]***

Single red plate-shaped crystals of **[PY][BiI$_4$]** were formed during slow reaction of an ethanol solution of bismuth iodide and water solution of pyridinium iodide. A monoclinic crystal system was adopted with space group $P2_1/c$ and each unit cell contains two $[BiI_4]^-$ anions and two pyridinium cations. The general crystallographic packing for **[PY][BiI$_4$]** is shown in **Figure 3.1**, displaying an inorganic framework built by one-dimensional edge-sharing $[BiI_4]^-$ anionic chains with cis-configuration along c-axis. The Bi–I bond lengths are shorter (2.9047(19) Å– 3.0556(19) Å) for the terminal iodine atoms than for bridging iodine atoms (3.1326(19) Å – 3.2878(18) Å) in each BiI_6 octahedron. The bond angles for I–Bi–I range from 84.75(5) ° to 95.38(6) °, and the angles of I (bridging)–Bi–I (bridging) in each BiI_6 octahedron are generally smaller than those of I (terminal)– Bi–I (terminal). The deviation of the geometric parameters indicates that the $[BiI_6]^{3-}$ octahedron is distorted, and the difference between terminal and bridging iodine probably originates from the repulsion of Bi^{3+} ions in the BiI_4^- anionic building blocks.[5]

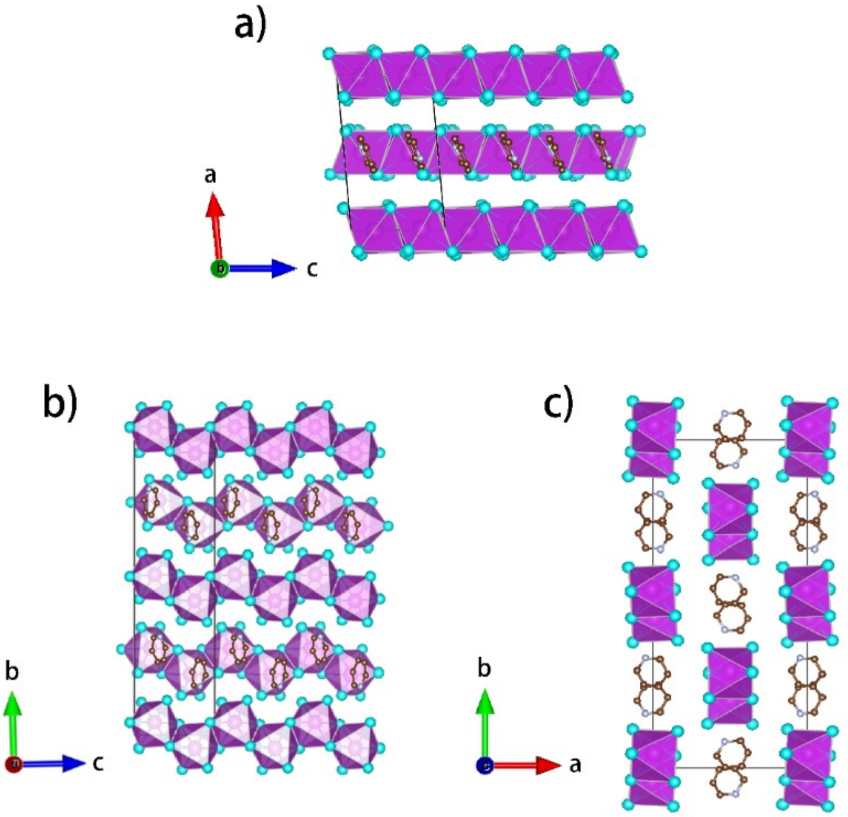

Figure 3.1. Crystallographic packing diagrams of **[PY][BiI$_4$]** when viewed along different axes. Bismuth atoms and $[BiI_6]^{3-}$ octahedra: magenta; iodine atoms: cyan; carbon atoms: brown; nitrogen atoms: violet. Hydrogen atoms are omitted for clarity.

3.3.1.2 Crystallographic study of [MEPY][BiI_4]

Single red block-shaped crystals of **[MEPY][BiI_4]** crystallized in the monoclinic $P2_1/c$ space group at the interface of bismuth iodide ethanol solution and 1-methylpyridinium iodide water solution. Each unit cell contains four BiI_6 octahedra and four methylpyridinium iodide cations. The BiI_6 octahedra are edge-linked into one-dimensional infinite chains of BiI_4^- (**Figure 3.2**) with a trans-configuration, where the adjacent chains are propagated in an anti-zigzagged manner. Shorter bond lengths for the Bi–I bond (2.9098(8) Å – 2.9195(8) Å) are again found for the terminal iodine atoms than that with bridging iodine atoms (3.1027(9) °A – 3.3029(7) °A) in the slightly distorted BiI_6 octahedra. The bond angles for I–Bi–I range from 87.620(19)° to 94.30(2)° with smaller I (bridging)–Bi–I (bridging) than that with terminal I. Bi–I (bridging)–Bi angles range from 92.21(2)° to 93.75(2)°. Again, distortion of $[BiI_6]^{3-}$ octahedra was found, which a common characteristic of iodobismuthates is. It is noteworthy that since both [PY][BiI_4] and [MEPY][BiI_4] are adopting monoclinic system with space group of $P2_1/c$, direct comparison of their crystallographic packing methods can be made when viewing along *a-b-c* of [PY][BiI_4] to *c-b-a* of [MEPY][BiI_4].

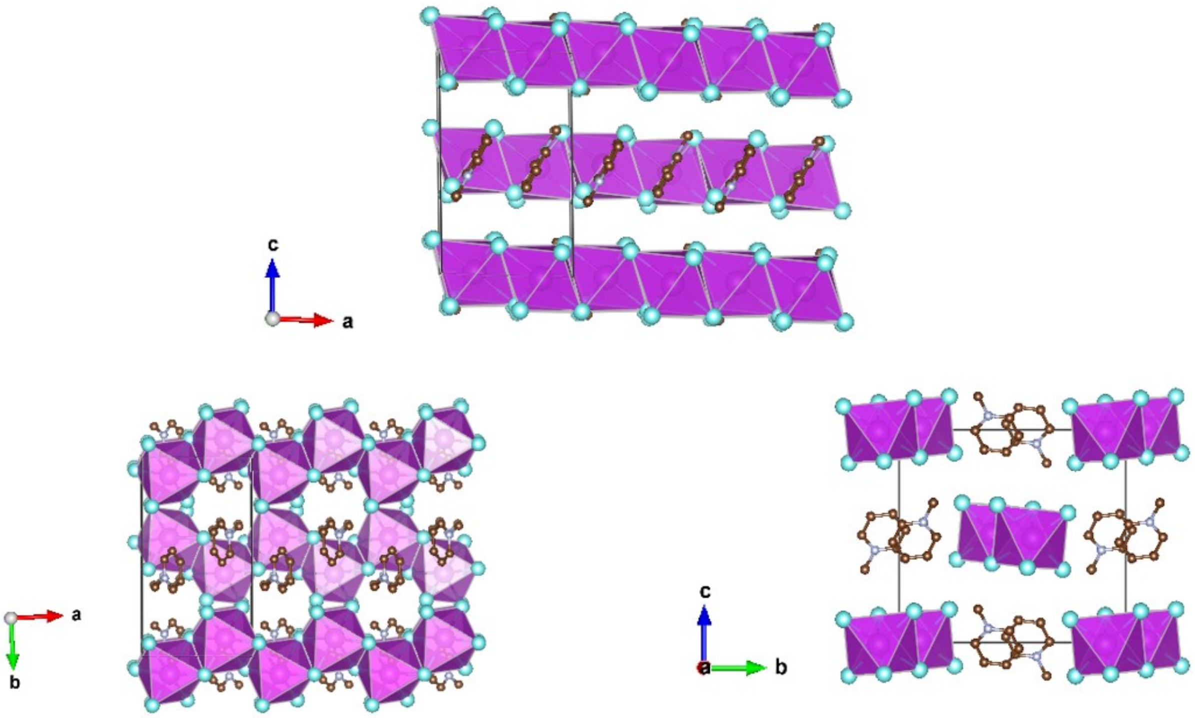

Figure 3.2 Crystallographic packing diagrams of **[MEPY][BiI_4]** when viewed along different axes. Bismuth atoms and $[BiI_6]^{3-}$ octahedra: magenta; iodine atoms: cyan; carbon atoms: brown; nitrogen atoms: violet. Hydrogen atoms are omitted for clarity.

3.3.1.3 Short contacts in [PY][BiI$_4$] and [MEPY][BiI$_4$]

The one-dimensional [BiI$_4$]$^-$ chain propagates along the c axis of the unit cell, and the [BiI$_6$]$^{3-}$ building blocks are connected in an edge-sharing manner. From the electronic perspective, the chain structure is promising for good electron transport when used as a photovoltaic material. An interesting feature of the intermolecular interactions can be found when considering different axes. Short contacts exist between iodine-iodine atoms in two adjacent chains in the **ab** plane (**Figure 3.3a**), where the shortest distance (3.823 Å) between iodine atoms is less than the sum of their Van der Waal's radii (3.98 Å). Additionally, short (H)N…I contacts between the hydrogen on the protonated N atom and iodine, together with I…I, I…C short contacts between chains when looking along the ***a***-axis or ***c***-axis. These features are important for building up the intermolecular interactions and thus potentially enhance the charge carrier mobility in higher dimensionality. Overall, taking the short I…I, I…C and N-H…I interactions into consideration, **[PY][BiI$_4$]** can be regarded as a pseudo-three-dimensional material, which may allow the charge to transfer along the a and b axis besides the anionic chain direction. Similarly, for **[MEPY][BiI$_4$],** the intermolecular interactions and their distances that are smaller than the sum of Van der Waal's radii between atoms are shown in **Figure 3.3b** with details provided in **Table 3.2.**

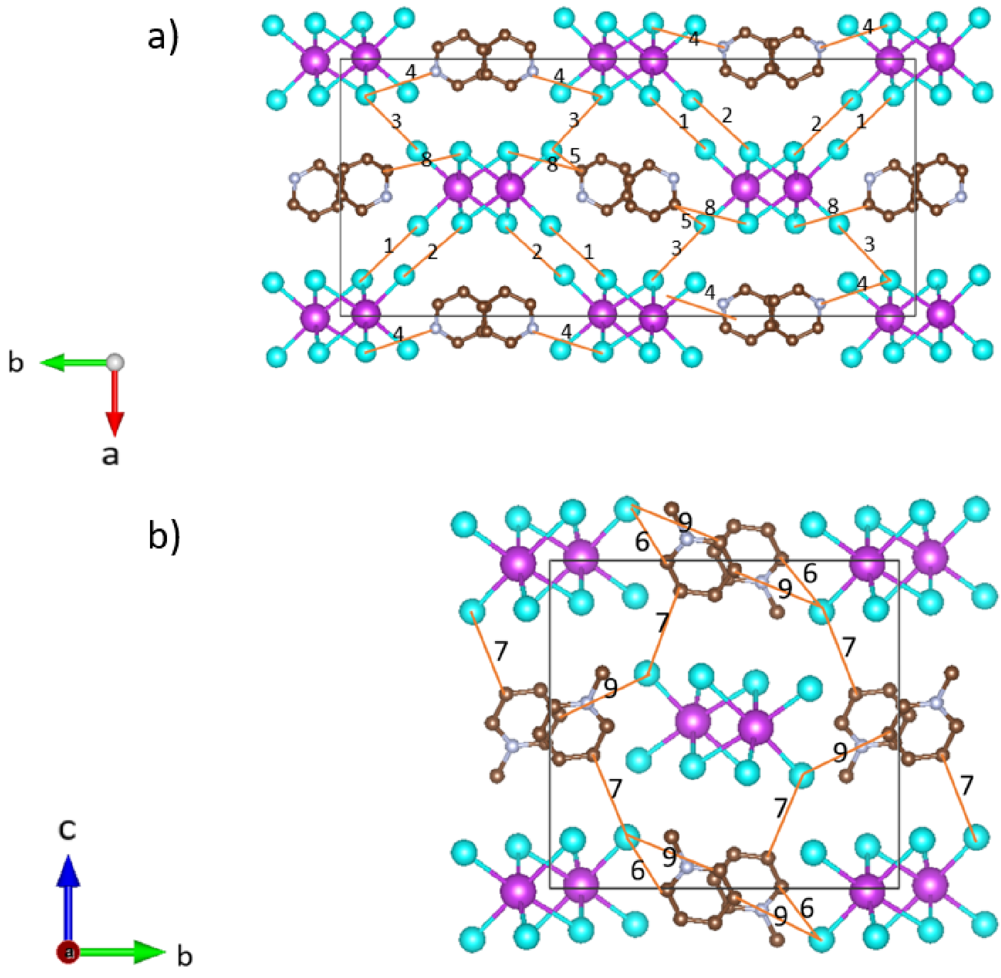

Figure 3.3 Intermolecular interactions (show in orange lines) in **[PY][BiI$_4$]** (a) and **[MEPY][BiI$_4$]** (b) unit cells. Image generated by VESTA (Visualization for Electronic and Structural Analysis) software. Bismuth atoms: magenta; iodine atoms: cyan; carbon atoms: brown; nitrogen atoms: violet. Hydrogen atoms are hidden for clarity. The numbers above orange lines can be referred to Table 3.1.

Table 3.2. Short contacts of I…I, I…C, I…H-N and I…H-C and corresponding atomic distances that less than the sum of Van der Waal's radii in the unit cells of **[PY][BiI$_4$]** and **[MEPY][BiI$_4$].** Numbers in the table can be referred to **Figure 3.3.** The sum of the Van der Waal radii are 3.96 Å for I…I, 3.68 Å for C…I, and 3.18 Å for N(C)-H…I.

Interactions	No.	Distance/ Å
I…I	1	3.845(2)
	2	3.823(5)
	3	3.945(4)
I…H-N	4	2.877(7)
I…C	5	3.667(3)
	6	3.653(5)
I…H-C	7	3.050(8)
	8	2.942(7)
	9	3.172(3)

Less intermolecular interactions can be observed in **[MEPY][BiI$_4$]** when comparing to **[PY][BiI$_4$]**. There are short I…C contacts between the terminal iodine atoms and carbon atoms of the methylpyridinium rings, and hydrogen. No short I…I contacts were found, however, which can be attributed to the methyl group on the organic cation that increases the volume of the organic component. In summary, from the electronic perspective, the chain structure in both **[PY][BiI$_4$]** and **[MEPY][BiI$_4$]** is desirable for charge transport ability along that direction. Additionally, higher dimensional charge transport potentialy can also be achieved by short I…I and I…C contacts, which may promote higher dimensional charge carrier mobility.

3.3.4.2 Crystallographic study of $[PYZ]_6[Bi_2I_9]_2 \cdot C_3H_6O \cdot C_4H_{10}O$

The single crystal XRD study indicates that **$[PYZ]_6[Bi_2I_9]_2 \cdot C_3H_6O \cdot C_4H_{10}O$** crystallizes with a zero-dimensional structure, shown in **Figure 3.4**. The inorganic motif is constituted by $[Bi_2I_9]^{3-}$ binuclear units, and the single protonated N atom on the pyrazinium ring leads to the cationic ion $[PYZ]^+$. In the crystallization process of pyrazinium iodobismuthate, solvent (acetone) and anti-solvent (diethyl ether) were incorporated within the unit cell of the crystal due to interaction with the nitrogen lone pair on the pyrazinium cations. Based on the crystal structure study, we prepared the compound precursor solution with the stoichiometry of BiI_3: pyrizium iodide = 2:3 in DMF/DMSO solvent for further characterization, and **$[PYZ]_6[Bi_2I_9]_2$** will be used to indicate this pyrazinium iodobismuthate compound. As the zero-dimensional $[Bi_2I_9]^{3-}$ complex has been extensively investigated, computational study for the pyrazinium iodobismuthate will not be discussed in this report.

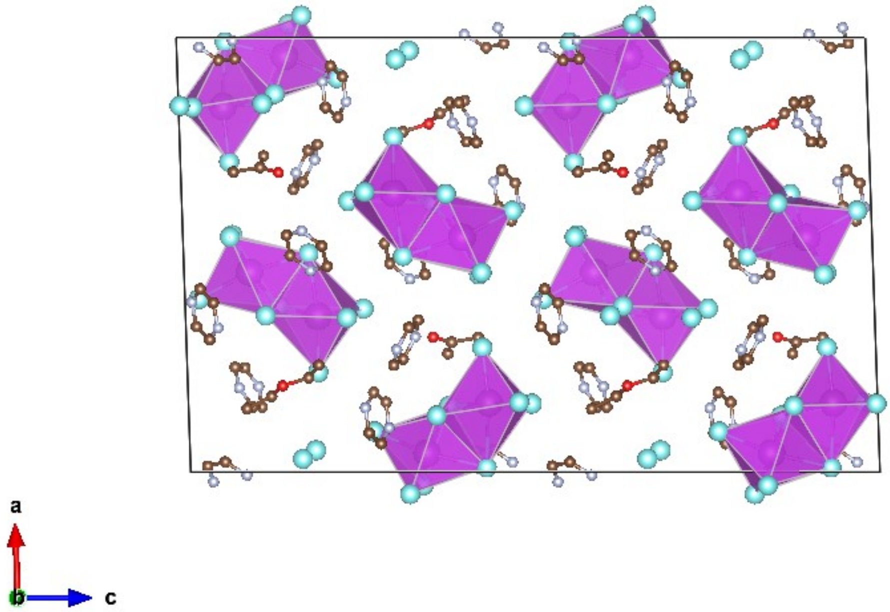

Figure 3.4 Crystal structure of $[PYZ]_6[Bi_2I_9]_2 \cdot C_3H_6O \cdot C_4H_{10}O$ viewing on *a*-*c* plane.

3.3.4.3 Powder X-ray Diffraction

We have prepared thin films of **$[PY][BiI_4]$** and **$[MEPY][BiI_4]$** by a one-step spin-coating method (see the Experimental section). X-ray diffraction was carried out to compare with the theoretical XRD pattern generated from the single-crystal structure to investigate the crystallinity and phase of each material in solid-state thin films (**Figure 3.5**). Both materials as thin films are consistent with the calculated powder XRD pattern, indicating that they are predominately in the same crystallographic phase. There was no indication of the potential BiI_3, I_2 or elemental Bi impurities (**Figure 3.6**) It is noteworthy that strong preferred orientation on the (1 2 0) plane was observed in **$[PY][BiI_4]$**, which corresponds to the plane where the sheet of iodobismuthate chains propagates in a parallel manner to the substrate (**Figure 3.7**). Preferred orientations on planes (0 1 1) and (1 3 2), along with other Bragg peaks in accordance with the simulated XRD pattern were found for **$[MEPY][BiI_4]$**. In addition, the stability of thin films under ambient conditions was also examined by collecting XRD data on thin films after 1 week shown as the purple curve in **Figure**

3.5. The 2θ value of the observed peaks remain unchanged, however, the widths of peaks have increased, indicating no major structural changes but change of crystalline size after one-week.

a)

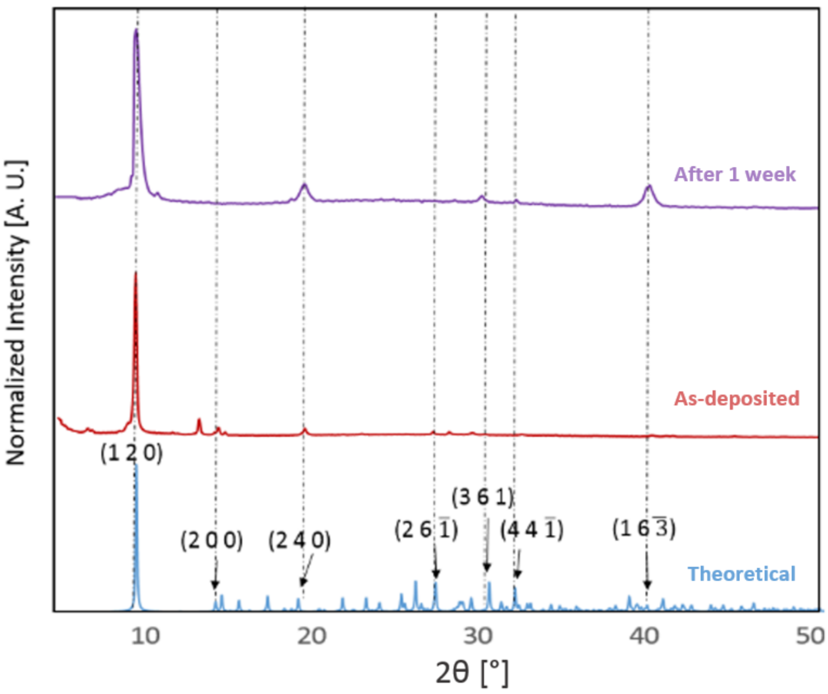

b)

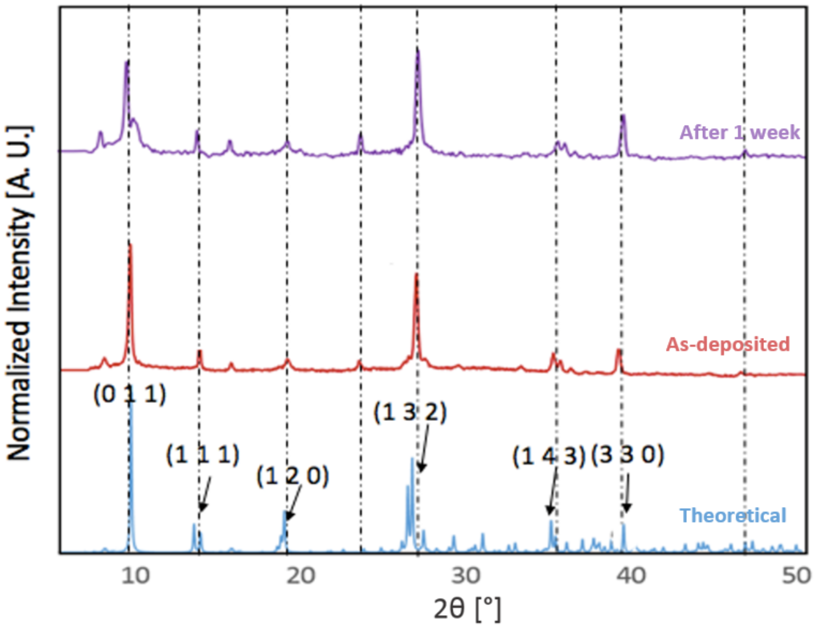

Figure 3.5. X-ray diffraction patterns for thin film of **[PY][BiI$_4$]** (a) and thin film of **[MEPY][BiI$_4$]** film (b) on quartz glass slides, shown as normalized intensity versus 2θ. Simulated diffraction pattern: blue; XRD diffraction pattern for thin-films: red; XRD diffraction pattern for thin-films after one-week exposure to the air: purple.

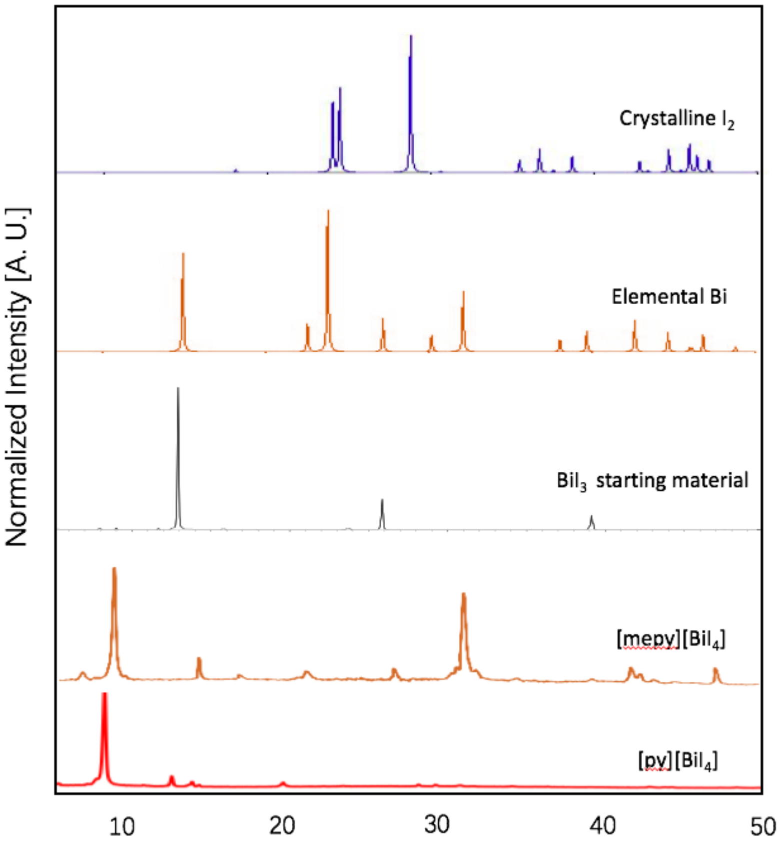

Figure 3.6. XRD patterns of **[PY][BiI_4]**, **[MEPY][BiI_4]**, BiI_3 starting materials, elemental Bi and crystalline I_2.

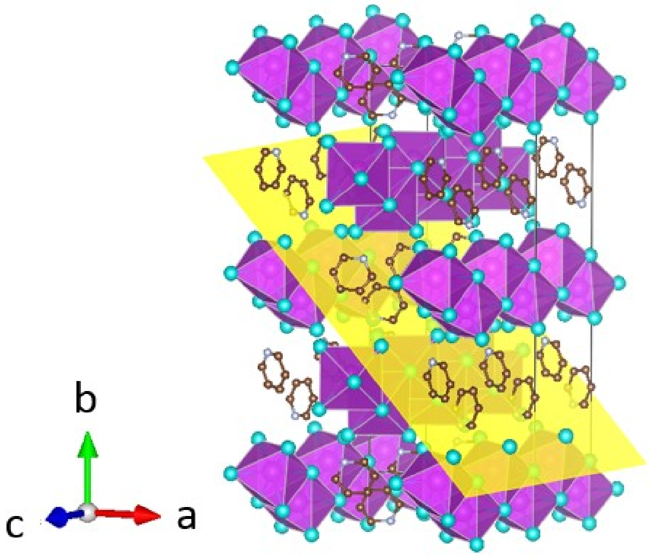

Figure 3.7. (1 2 0) plane of **[PY][BiI_4].**

3.3.2 Computational results

Band structure and projected density of states (DOS) calculations were obtained using CASTEP 16.11[10] to investigate the variation (dispersion) in band energies with respect to high symmetry k-points and directions that correspond to strong intermolecular interactions. For both **[PY][BiI$_4$]** and **[MEPY][BiI$_4$]**, DFT methods were employed with the PBE functional and the Tkatchenko-Scheffler (TS) dispersion correction scheme, using the coordinates for each atom obtained from optimized single crystal geometry. Projected DOS for the p-orbitals of bismuth, iodine, carbon and nitrogen were calculated using the OptaDOS[11] package, with the Fermi level set to 0 eV. Crystal structure packing diagrams and ***k***-point vectors used for both compounds are shown in **Figure 3.8** (left), and the band structures together with projected DOS diagrams can be found in **Figure 3.8** (right).

From the computed band structure diagrams it can be seen that both **[PY][BiI$_4$]** and **[MEPY][BiI$_4$]** are semiconductors,[12] with direct bandgaps of 1.8 eV (at k point (0, 0, -0.25) and 2.1 eV (at k point (-0.25, 0, 0) respectively. As shown in the projected DOS, the main contributor to the valence band maximum (VBM) is the iodine 5p states for both compounds. For **[PY][BiI$_4$]**, relatively large dispersion in the band energies can be seen. Specifically, high dispersions exist along vectors H-Y and G-Z, which correspond to the direction along the infinite $[BiI_4]^-$ chains in real space. More interestingly, there is some small dispersion along the vector path Z-D, which corresponds to the interaction of iodine atoms between the anionic inorganic chains. Minor but noticeable dispersion also occurs along Y-G that arises from the short I…C and I…H contacts. For **[MEPY][BiI$_4$]**, the valence band is generally flat. Small but noticeable dispersions along G-H and E-C in the valence band coincide with the one-dimensional chain direction. Thus, one aspect of valence band dispersion is contributed by the σ-bonding interaction of iodine 5p states with the bismuth 6p states, which leads to the infinite Bi-I covalent bonding that builds the chain structure. The other valence band interaction stemming from the iodine 5p states gives rise to the short I…I, I…C and I…H contacts. However, Louvain *et al*[13] claimed that due to the non-spherical distribution of the bismuth 6s orbital, it is not possible to have ideal antibonding interactions for bismuth with the surrounding six iodine atoms. This is interpreted as the imperfect geometry of the $[BiI_6]^{3-}$

octahedron hindering the Bi-I antibonding interactions, which leads to the relatively small band dispersion compared to lead-halide perovskite.

As presented in **Figure 3.8**, the conduction band minimum (CBM) for both **[PY][BiI$_4$]** and **[MEPY][BiI$_4$]** is almost entirely derived from atomic orbital contributions of nitrogen and carbon from the organic moieties. Although the overall band dispersion is not very significant, it is still worth noting that the cationic organic entities are playing an essential role in the CBM to increase the electronic dispersion of the band structure. Hence, participation of organic entities at band edges were found for both compounds, which may be a strategy that can be further exploited to enable higher charge transport ability in more than one dimension. In conclusion, by taking advantage of extended 1D frameworks together with the high dimensional intermolecular interactions, **[PY][BiI$_4$]** can be regarded as a pseudo-three-dimensional material due to its higher dimensionality in the X-ray structure and calculated band structure.

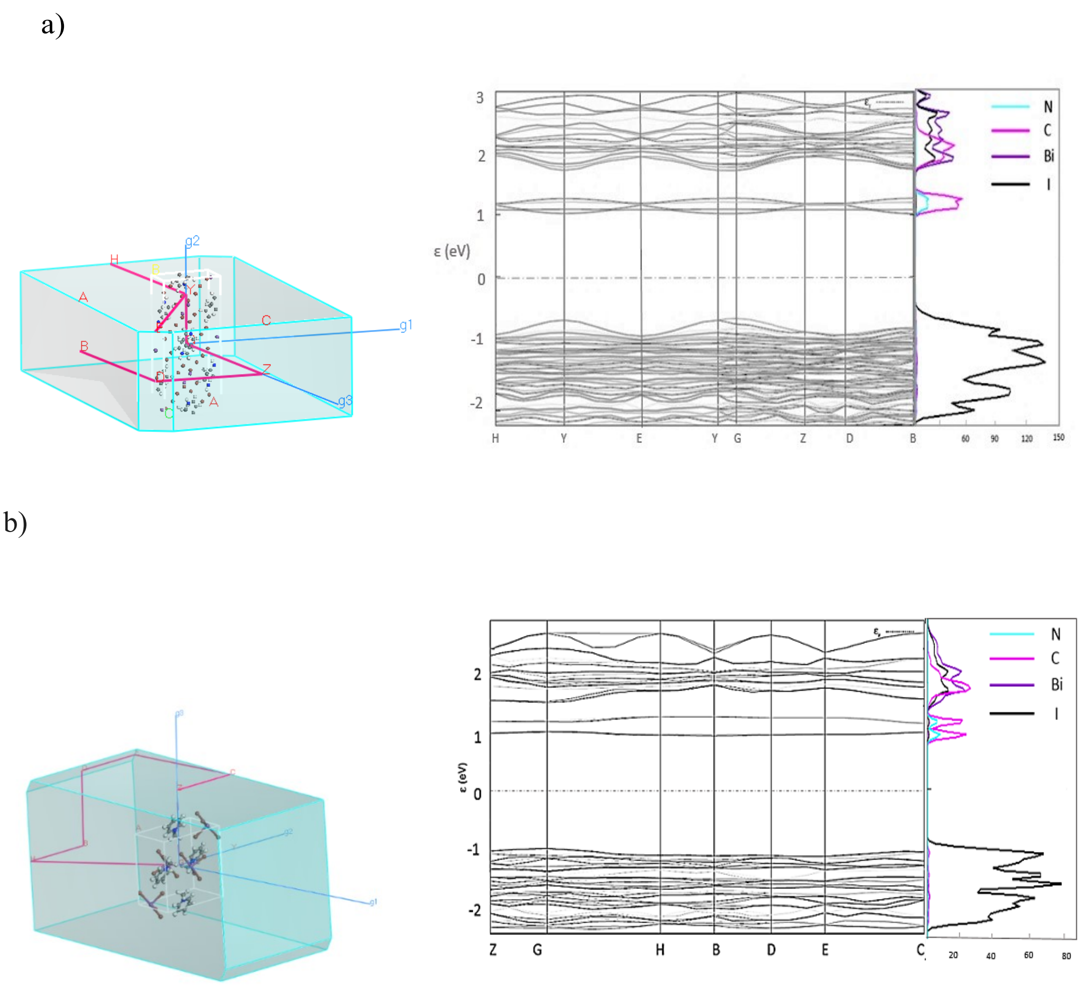

Figure 3.8 *K*-point path in the first Brillion zone and band structures of [PY][BiI$_4$] (a) and [MEPY][BiI$_4$] (b), and corresponding projected DOS (6p orbital for bismuth: purple; 5p orbital for iodine: black; 2p orbital for nitrogen: cyan; 2p orbital for carbon: magenta). The Fermi level was set at 0 eV.

3.3.3 Optical studies

Diffuse reflectance spectra were measured for the three compounds as thin-films spin-coated on glass slides, and their Kubelka-Munk function plots are overlaid and shown in **Figure 3.9a**. Since both **[PY][BiI$_4$]** and **[PYZ]$_6$[Bi$_2$I$_9$]$_2$** are reddish orange coloured, the absorption ranges cover from 300nm to nearly 600nm. However, for **[MEPY][BiI$_4$]** with yellowish orange colour, lower absorption and narrower range was found compared to the other two compounds. When comparing to the solution state measurements in **Figure 3.9b**, it is significant that the absorption range has increased from 450nm to 550 nm and shifts towards the long wavelength region for all three compounds. This can be explained that in the solution state, there are only isolated ions and counter ions without intermolecular interactions; in contrast, extended interactions exist in the solid state, which lead to a broader absorption range.

a)

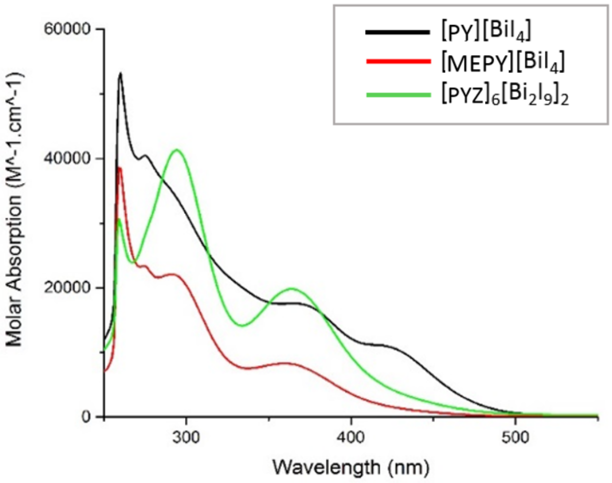

b)

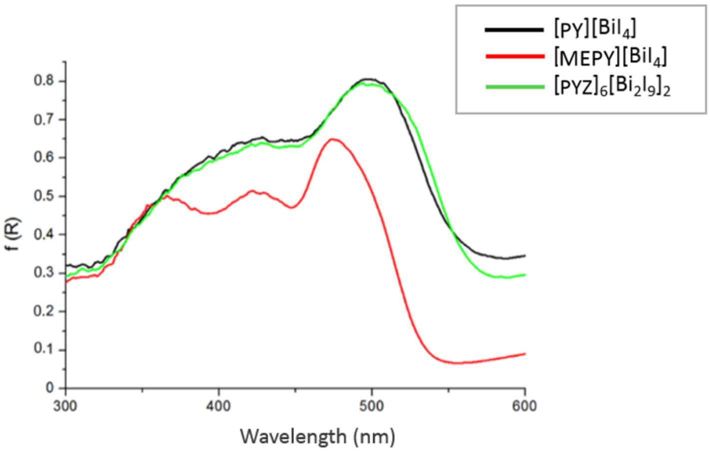

Figure 3.9 Kubelka-Munk function plots from diffuse reflectance measurements for compounds (a) spin-coated on glass slides and (b) solution-state UV-Vis absorption spectra.

The optical bandgap for each compound was determined experimentally by applying the Tauc plot for compounds that deposited as thin films and scratched off as powder form. Band gap values of **[PY][BiI$_4$]**, **[MEPY][BiI$_4$]** and **[PYZ]$_6$[Bi$_2$I$_9$]$_2$** in the powder form are 1.98 eV, 2.17 eV and 1.97 eV, respectively (**Figure 3.10a**), which compare favourably with the values obtained by simulation (DFT is well known to underestimate band gap energies)[14]. The observed variation in band gap for **[PY][BiI$_4$]** and **[MEPY][BiI$_4$]** is mainly caused by the differences in the organic cations present, which lead to a lack of extended inter-chain interactions for the latter compound. Slightly higher band gap values were observed for the compounds when presented as thin films (**Figure 3.10b**), which is likely due to less-reliable measurements caused by the limited thickness of the thin films. Compared to the literature where band gap values of 1.70–1.76 eV was observes for 1D [BiI$_4$]$^-$ compounds with K$^+$ and Li$^+$ as the inorganic cations,[15] it is apparent that both the crystal dimensionality and the organic entities are important in determining the overall optical properties of the material.

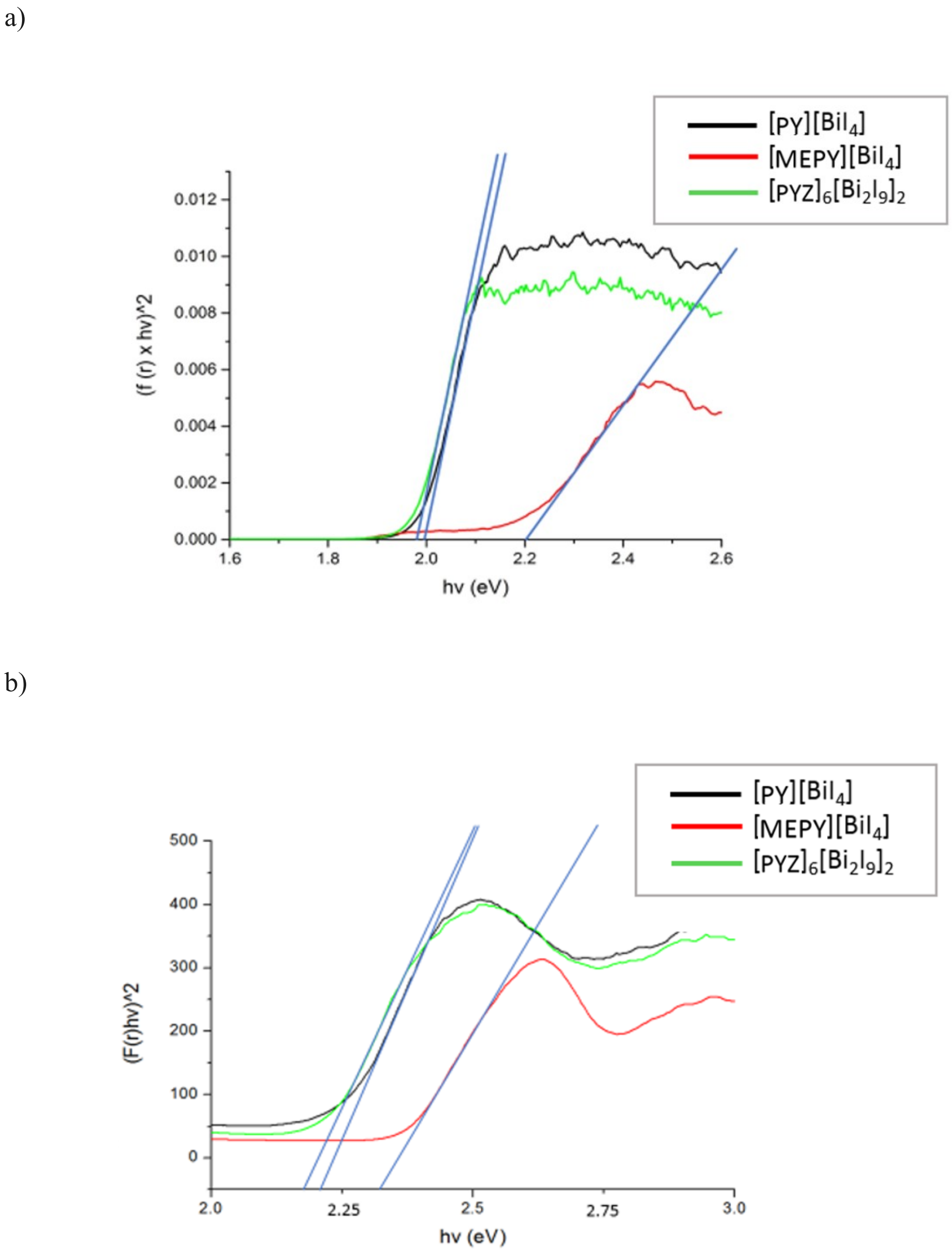

Figure 3.10 Tauc plots and bandgap value estimations of the three compounds, with blue lines illustrating the absorption edges to estimate bandgap values. (a): powder samples diluted in BaSO$_4$. Measured bandgap for **[PY][BiI$_4$]**, **[MEPY][BiI$_4$]** and **[PYZ]$_6$[Bi$_2$I$_9$]$_2$** are 1.98 eV, 2.20 eV and 1.97 eV, respectively. (b): spin-coated on glass slides, measured bandgap for **[PY][BiI$_4$]**, **[MEPY][BiI$_4$]** and **[PYZ]$_6$[Bi$_2$I$_9$]$_2$** are 2.19 eV, 2.20 eV and 2.16 eV, respectively.

3.3.4 Electrochemistry

The cyclic voltammetry measurements for **[PY][BiI$_4$]**, **[MEPY][BiI$_4$]** and **[PYZ]$_6$[Bi$_2$I$_9$]$_2$** were carried out in DCM with TBABF$_4$ as the electrolyte. In this measurement, the compounds were spin-coated on FTO conducting glass slides as working electrodes. By doing so we can investigate the solid state electrochemical properties. Irreversible first oxidation and first reduction processes can be observed for all three materials (**Figure 3.11**), which is likely related to some dissolution of the film after the redox step. When estimating the ionization energy (IE) and the electron affinity (EA) from the redox potential measured experimentally, we need to correlate the vacuum potential to the electrochemical potential. Normally the redox potential is standardized to the normal hydrogen electrode (NHE) and then the potentials are corrected to vacuum level as reference. In this work, the method used for energy level determination is from the literature.[16] It's worth noting that the E_g values are consistent with the computational and optical results, which further proves the validity of the energy level measurements. The electrochemically determined IE, EA and E_g energy levels of each compound are summarized in **Table 3.3**, and energy level diagram is shown in **Figure 3.12**.

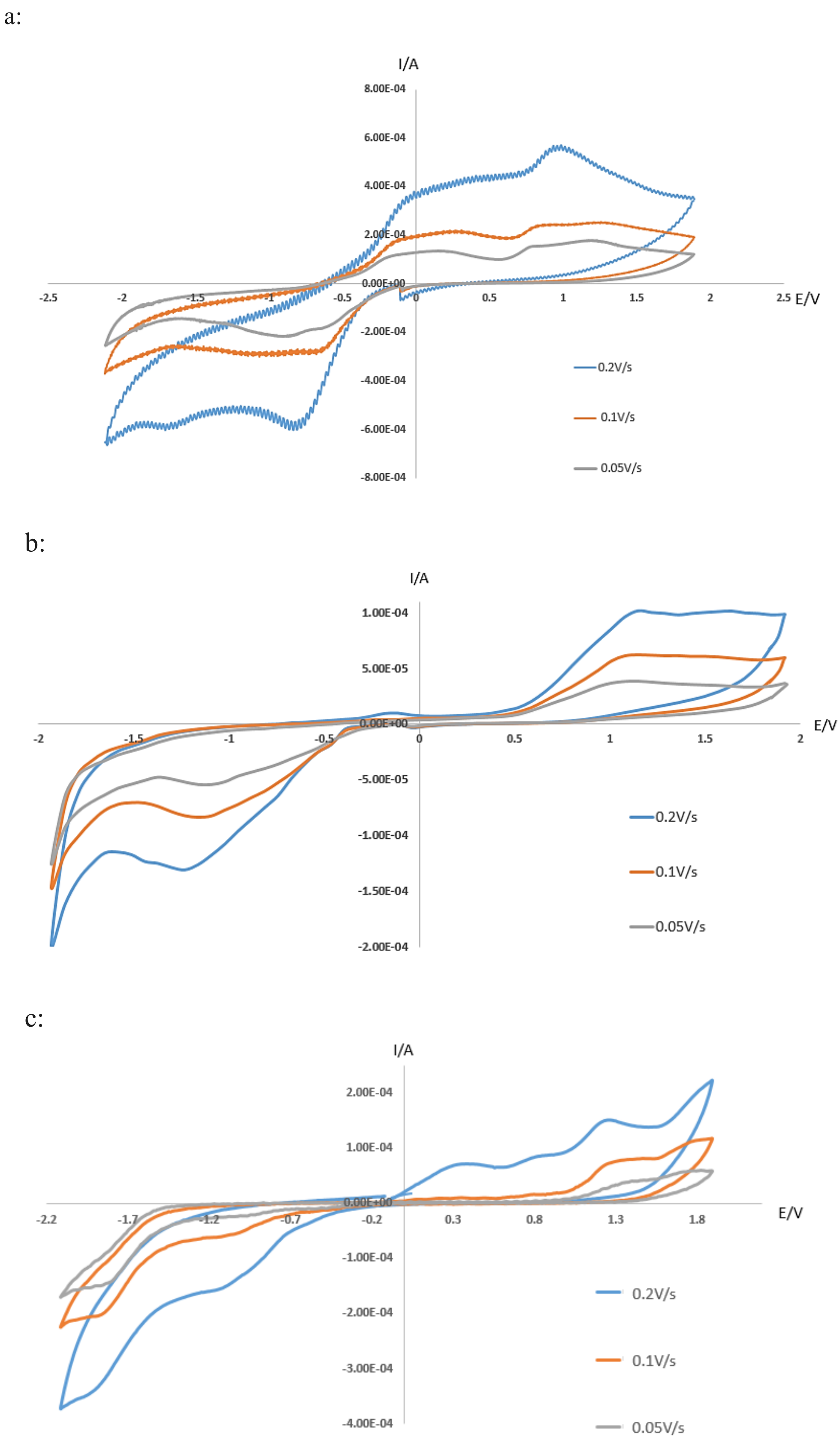

Figure 3.11 Cyclic voltammetry obtained from spin-coated thin films on conducting glasses of **[PY][BiI$_4$]** (a), **[MEPY][BiI$_4$]** (b), and **[PYZ]$_6$[Bi$_2$I$_9$]$_2$** (c) at different scan rates.

Table 3.3 The electrochemical oxidation potential onset (E'ox), electrochemical oxidation potential (E_{ox}), ionization energy (IE), energy band gap (E_g) and estimated electron affinity energy (EA) values for **[PY][BiI_4]**, **[MEPY][BiI_4]**, and **[PYZ]$_6$[Bi_2I_9]$_2$** as thin-films. The potential of the ferrocenium/ferrocene (Fc^+/Fc) couple was used as an internal standard, taken to be at 0.63 V against NHE. (assuming E_{Vac} = 0).

	E'_{ox}(V vs Ag/Ag Cl)	E_{ox} (V vs Ag/Ag Cl)	IE (eV)	Eg (e	EA (eV)
[PY][BiI_4]	0.23	4.63	-4.63	1.7	-2.85
[MEPY][BiI_4]	0.49	4.89	-4.89	2.3	-2.51
[PYZ]$_6$[Bi_2I_9]$_2$	0.77	5.17	-5.17	2.2	-2.97

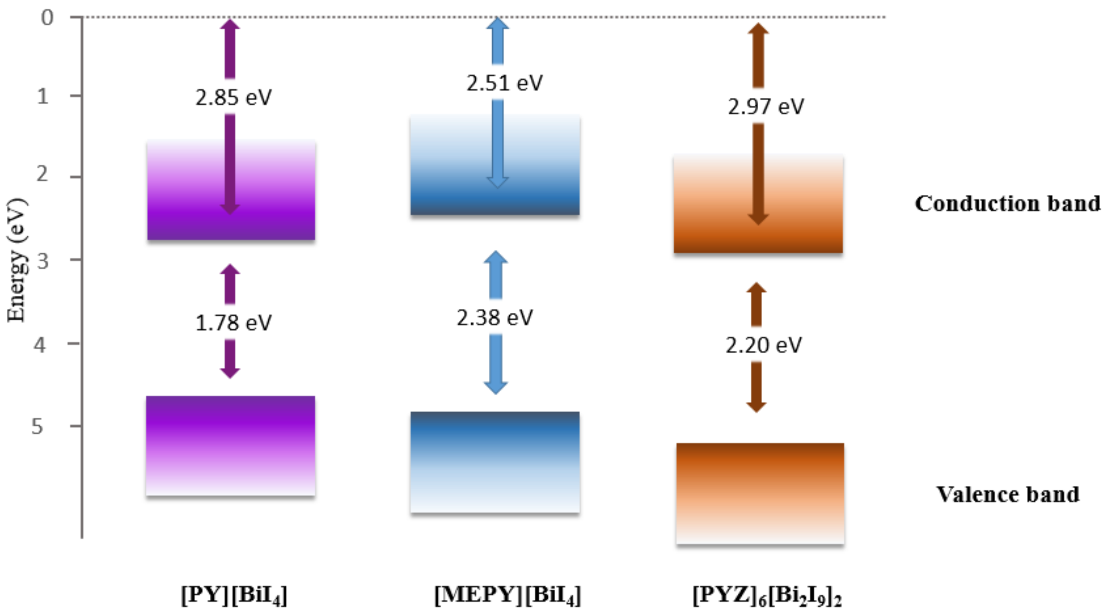

Figure 3.12. Energy level diagram for [PY][BiI_4], [MEPY][BiI_4] and [PYZ]$_6$[Bi_2I_9]$_2$ as thin films. E_{vac} is set to be at 0 eV.

3.3.5 Microscopic images

High-resolution microscopic images for each compound spin-coated on a compact layer of TiO_2 were obtained by optical microscope with 100 times and 400 times magnification, and the surface crystalline morphology was studied and compared. Since the magnification images for compounds on pure glass substrates showed uneven coverage attributed to the poor attachment on the smooth glass surface, and compounds on mesoscopic TiO_2 films were invisible as they were infiltrated into the porous TiO_2 layer, a compact layer of TiO_2 was found to be most suitable for observing the surface morphology and the images are shown in **Figure 3.13**. It can be seen that all of the three compounds show high crystallinity. For **[PY][BiI$_4$]**, needle-like polycrystalline material was formed with an average needle length of 80 μm, and the coverage is quite high and even. However, block-shaped crystals were formed in the thin film for **[MEPY][BiI$_4$]** with poor coverage, and the diameter of the crystal blocks varies significantly (from a few μm to 50 μm). Much thinner needle-like crystals were found for the thin-film of **[PYZ]$_6$[Bi$_2$I$_9$]$_2$** with an average length of 20-30 μm, also with high coverage except for some defects (shown as the black blocks) on the surface, which are assumed to be air bubbles formed during the coating process. Since all of the films were annealed at 100 degrees for 20 minutes after spin-coating, some optimization of film formation is worth carrying out to increase the coverage and uniformity of the crystallinity, especially for **[MEPY][BiI$_4$]**. In the future, scanning electronic microscopy could be applied to the films in devices, which could help us to observe the surface morphology of different compounds.

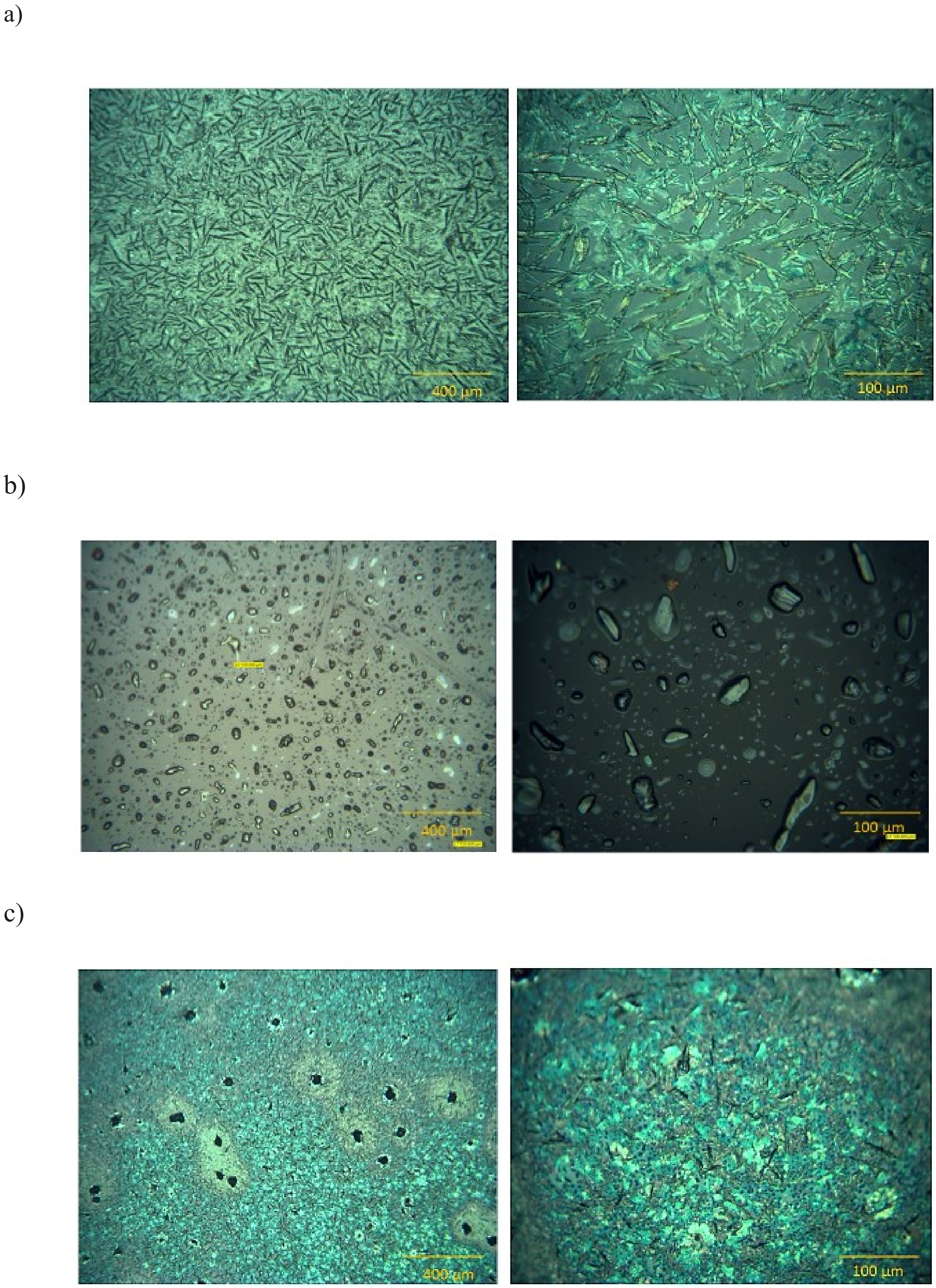

Figure 3.13 Microscopic images of [PY][BiI$_4$] (a), [MEPY][BiI$_4$] (b) and [PYZ]$_6$[Bi$_2$I$_9$]$_2$ (c) on compact layer of TiO$_2$, with 100 times (left) and 400 times (right) magnification

3.3.6 Device studies

The title compounds were tried as light harvesters in solar cells. The device used in this study is based on the FTO/(TiO_2/ZrO_2/Carbon)/absorber structure,[17-19] with the cross-sectional SEM image shown in **Figure 3.14**. **[PY][BiI$_4$]** tends to crystallize on the surface of the carbon film before reaching the TiO_2 layer, thus resulting in poor reproducibility of the devices (**Figure 3.15**). The problem of filling can be minimized by choosing the proper solvent and optimizing the fabrication technique in the future. **Figure 3.15b** shows the performance of a **[PY][BiI$_4$]** solar cell with relatively good filling, giving PCE of 0.90% (with V_{oc}=0.62 V, J_{sc}=2.71 mA cm^{-2}, FF=0.54, reverse to forward scan). Compared to the solar cells with lead-halide perovskite as light absorbers, the major limit for **[PY][BiI$_4$]** performance is due to the J_{sc} values which are around one-order of magnitude lower than the lead-halide perovskite solar cell J_{sc} values.[ref ref] Possible reasons that lead to the limitation of J_{sc} include: 1) the band gap value of **[PY][BiI$_4$]** is about 0.5 eV higher than that of lead-halide perovskite materials, which limits its photo-current harvesting process; 2) the deposition process of **[PY][BiI$_4$]** needs to be further optimized to increase the crystallinity and minimise possible grain boundaries, which may act as the photo-generated charge recombination sites; 3) Using HTM-free solar cell structures can potentially limit the charge-carrier transport process, and thus limits the photocurrent generation. No substantial hysteresis has been found for **[PY][BiI$_4$]** when performing a reverse scan (from V_{OC} to J_{SC}). In contrast, no photovoltaic effect was observed for **[MEPY][BiI$_4$]**, which can be attributed to many reasons, e.g., poor crystallization in the mesoscopic structure, low carrier density and relatively large bandgap. Although up to 4.3% efficiency has been achieved recently by employing silver bismuth-halide materials,[20] our result was comparable with the other best Bi–iodide based cells at the time when the study was carried out. Our result is still the highest reported efficiency of bismuth-based solar cell based on the HTM-free and fully printable solar cell structure.

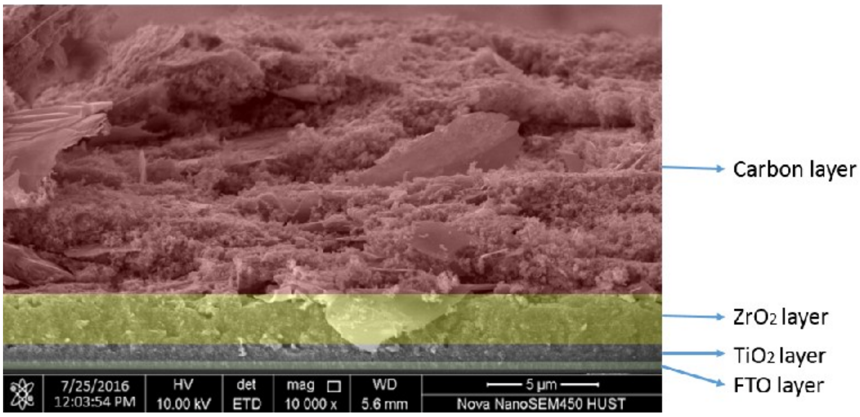

Figure 3.14. Cross-sectional SEM image of the mesoscopic triple-layer solar cell architecture.

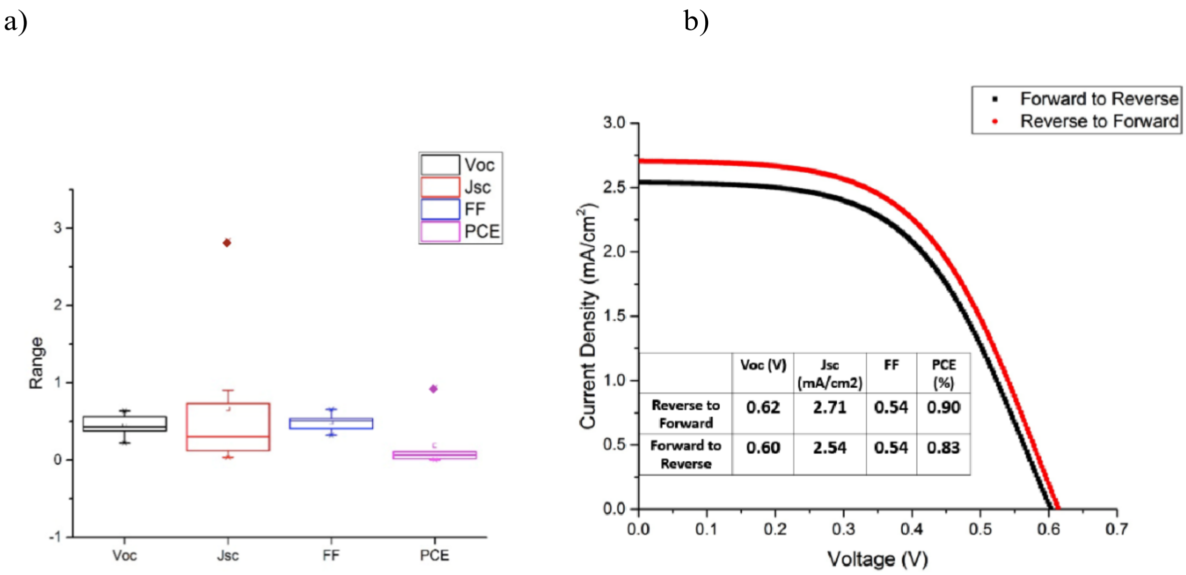

Figure 3.15 a) Box diagram of solar cell performances showing variabilities of solar cell parameters; b) Boltzmann-fitted J-V curve of [py][BiI$_4$] champion cell.

3.4 Conclusions and Future work

Synthesis, characterization, and evaluation have been carried out for three organic-inorganic iodobismuthate compounds to assess their potential as third-generation lead-free photovoltaics absorbers. The crystallographic structures for both **[PY][BiI$_4$]** and **[MEPY][BiI$_4$]** feature one-dimensional $[BiI_4]^-$ infinite anionic chains, while **[PYZ]$_6$[Bi$_2$I$_9$]$_2$** is composed of dimers with $[Bi_2I_9]^{3-}$ anions. Moreover, the organic entities, protonated aromatic heterocycles, significantly contribute to the intermolecular interactions, which may lead to enhanced charge carrier transport ability along the inter-chain directions. This was supported by band structure calculations, and the projected density of states calculations further verified that the organic moieties significantly contribute to the bottom of the conduction band. Moreover, spin-coating has been carried out to prepare thin films for potential device fabrication, and the crystalline properties of the films were examined by powder XRD and microscopic observation. The energy levels of each compound were experimentally determined by combining both electrochemical and optical measurements carried out on powder and solid-state thin films. Although some difficulty was encountered in achieving highly-reproducible PV results, we demonstrated that the efficiency of the perovskite solar cell without HTM can approach 0.9%.[1,18] This was achieved within the approach of a fully-printable cell using a cell structure not explored before for iodobismuthate materials. Considering that no HTM was used in the structure, this performance is very competitive. Overall, this study provides a new perspective in designing lead-free photovoltaics, by seeking to take advantage of both the anionic chain framework and the organic cation for enhanced electronic properties.

3.5 Experimental

3.5. 1 Synthesis of pyridinium iodide

Pyridine (1.0 mL, 12.8 mmol) was added dropwise into 55% hydroiodic acid (4.2 mL, 15 mmol) with continuous stirring under room temperature for 2 hours. The product precipitated out from the solvent during the reaction, and the precipitates were filtered under suction and washed with diethyl ether. The product was dried under vacuum for 2 hours, yielding white solid. (2.65 g, 91%). ^{1}H NMR (500MHz, D_2O) δH: 8.51 (^{2}H, m), 7.93 (^{1}H, $^3J_{H\text{-}H}$= 4.8, triplets), 7.49 (^{2}H, $3J_{H\text{-}H}$=5.2, triplets)

3.5.2 Synthesis of pyridinium bismuth iodide **([PY][BiI_4])**

Water solution (5 mL) of pyridinium iodide (414.0 mg, 2 mmol) was added dropwise into ethanol solution (5 mL) of BiI3 (1.179 g, 2 mmol) in a flask with vigorous stirring for 3 hours. Reddish-orange coloured precipitate formed during the reaction. The precipitate was collected by centrifugation and dried under vacuum for 4 hours, yielding reddish-orange coloured powder (1.356 g, 85.2%). Elemental analysis Calculated for [C_5H_6N][BiI_4]: C 7.53, H 0.75, N 1.76%. Found: C 8.02, H 0.90, N 1.97%.

Single crystals of **[PY][BiI_4]** were recrystallized by solvent layering of an ethanol solution of BiI_3 and water solution of pyridinium iodide. Red plate-shaped crystals were formed at the interface of these two solutions in an NMR tube.

3.5.3 Synthesis of methylpyridinium iodide

To a solution of pyridine (1.0 mL, 12.8 mmol), methyl iodide (1.0 mL, 16 mmol) was added dropwise with continuous stirring under room temperature for 2 hours. The light yellow solid product formed during the reaction, and was filtered under suction and washed with diethyl ether, yielding 2.40 g of final product (85%). ^{1}H NMR (500 MHz, D_2O) δH: 8.81 (2H, $3J_{H-H}$= 5.1, doublets), 8.56 (1H, $3J_{H-H}$= 7.4 triplets), 8.08 (2H, $3J_{H-H}$= 5.4 triplets), 4.43 (3H, singlet)

3.5.4 Synthesis of methylpyridinium bismuth iodide ([MEPY][BiI_4])

Water solution (5 mL) of methylpyridinium iodide (442.8 mg, 2mmol) was added dropwise into a flask containing ethanol solution of BiI_3 (1.184 g, 2 mmol). The mixed solution was stirred vigorously for 3 hours, with bright orange coloured precipitate formed during the reaction. The precipitate was collected by centrifugation and dried under vacuum for 4 hours, yielding bright orange coloured powder (1.189 g, yield 73.3%). Elemental analysis. Found: C 8.51, H 1.08, N 1.62%. Calculated for $[C_5H_6N][BiI_4]$: C 8.89, H 0.99, N 1.73%.

Single crystals of **[MEPY][BiI_4]** were recrystallized by slow diffusion of an ethanol solution of BiI_3 and water solution of methylpyridinium iodide, and red block-shaped crystals were formed at the interface of these two solutions by slow reaction in an NMR tube.

3.5.5 Synthesis of pyrazinium iodide

To a solution of pyrazine (1.0 g, 12.8 mmol) dissolved in diethyl ether (5 mL), hydroiodic acid (2.0 mL, 32 mmol) was added dropwise with continuous stirring at room temperature for 2 hours. The mixture was heated at 50 degrees to remove the unreacted HI for 30 min before filtering under suction and washing with diethyl ether, yielding a yellowish white precipitate (3.35g, 79.7%). ^{1}H NMR (500 MHz, D_2O) δH: 8.68 (4H, singlet)

3.5.6 Synthesis of pyrazinium bismuth iodide

Water solution (5 mL) of pyrazinium iodide (1.005 g, 3 mmol) was added dropwise into the flask containing ethanol solution of BiI_3 (1.180 g, 2 mmol). The mixed solution was stirred vigorously for 3 hours, forming dark red coloured clear solution. The solid products were obtained under rotary evaporation and dried under vacuum for 4 hours, yielding dark reddish coloured powder (1.745 g, 79.9%). Elemental analysis: Calculated for $[C_4H_6N_2]_3$ $[Bi_2I_9]_2$: C 8.00, H 0.67, N 3.11%. Found: C 8.75, H 0.97, N 2.87%.

Single crystals of **$[PYZ]_6[Bi_2I_9]_2 \cdot C_3H_6O \cdot C_4H_{10}O$** were recrystallised from diethyl ether and acetone by vapour diffusion method. Dark red block-shaped single crystals formed after one week in acetone solution.

References

1 B. W. Park, B. Philippe, X. Zhang, H. Rensmo, G. Boschloo and E. M. J. Johansson, *Adv. Mater.*, 2015, **27**, 6806–6813.

2 R. L. Z. Hoye, R. E. Brandt, A. Osherov, V. Stevanovic, S. D. Stranks, M. W. B. Wilson, H. Kim, A. J. Akey, J. D. Perkins, R. C. Kurchin, J. R. Poindexter, E. N. Wang, M. G. Bawendi, V. Bulovic and T. Buonassisi, *Chem. - A Eur. J.*, 2016, **22**, 2605–2610.

3 S. Öz, J.-C. Hebig, E. Jung, T. Singh, A. Lepcha, S. Olthof, F. Jan, Y. Gao, R. German, P. H. M. van Loosdrecht, K. Meerholz, T. Kirchartz and S. Mathur, *Sol. Energy Mater. Sol. Cells*, 2016, **158**, 195–201.

4 T. Singh, A. Kulkarni, M. Ikegami and T. Miyasaka, *ACS Appl. Mater. Interfaces*, 2016, **8** (23), 14542–14547.

5 Anna J. Lehner, Douglas H. Fabini, Hayden A. Evans, Claire-Alice Hébert, Sara R. Smock, Jerry Hu, Hengbin Wang, Josef W. Zwanziger, Michael L. Chabinyc, and Ram Seshadri, Chem. Mater., 2015, **27** (20), 7137–7148

6 M. Lyu, J. H. Yun, M. Cai, Y. Jiao, P. V. Bernhardt, M. Zhang, Q. Wang, A. Du, H. Wang, G. Liu and L. Wang, *Nano Res.*, 2016, **9**, 692–702.

7 T. Li, Q. Wang, G. S. Nichol, C. A. Morrison, H. Han, Y. Hu and N. Robertson, *Dalt. Trans.*, 2018, **47**, 7050–7058.

8 S. A. Adonin, M. N. Sokolov and V. P. Fedin, *Russ. J. Inorg. Chem.,* 2017, **62** (14), 1789-1796

9 A. J. Dennington and M. T. Weller, *Dalt. Trans.*, 2016, **45**, 17974–17979.

10 S. J. Clark, M. D. Segall, C. J. Pickard, P. J. Hasnip, M. I. J. Probert, K. Refson and M. C. Payne, *Zeitschrift für Krist.*, 2005, **220**, 567–570.

11 A. J. Morris, R. J. Nicholls, C. J. Pickard and J. R. Yates, *Comput. Phys. Commun.*, 2014, **185**, 1477–1485.

12 N. W. Ashcroft and N. D. Mermin, *Solid State Physics*, Harcourt College Publishers, USA, 1976.

13 N. Louvain, N. Mercier and F. Boucher, *Inorg. Chem.*, 2009, **48**, 879–888.

14 K. Burke, J. Chem. Phys., 2012, **136**, 150901–150909

15 N. A. Yelovik, A. V. Mironov, M. A. Bykov, A. N. Kuznetsov, A. V. Grigorieva, Z. Wei, E. V. Dikarev and A. V. Shevelkov, *Inorg. Chem.*, 2016, **55**, 9, 4132-4140

16 F. N. Crespilho, V. Zucolotto, J. R. Siqueira, A. J. F. Carvalho, F. C. Nart and O. N. Oliveira, *Int. J. Electrochem. Sci.*, 2006, **1**, 151–159.

17 Z. Ku, Y. Rong, M. Xu, T. Liu and H. Han, *Sci. Rep.*, 2013, **3**, 3132.

18 A. Mei, X. Li, L. Liu, Z. Ku, T. Liu, Y. Rong, M. Xu, M. Hu, J. Chen, Y. Yang, M. Grätzel and H. Han, *Science*, 2014, **345**, 295–298.

19 Y. Sheng, Y. Hu, A. Mei, P. Jiang, X. Hou, M. Duan, L. Hong, Y. Guan, Y. Rong, Y. Xiong and H. Han, *J. Mater. Chem. A*, 2016,**4**, 16731-16736 .

20 I. Turkevych, S. Kazaoui, E. Ito, T. Urano, K.Yamada, H. Tomiyasu, H. Yamagishi, M.Kondo, and S. Aramaki, *Chemsuschem*, 2017, **10** (19), 3754-3759.

Chapter 4

Hybrid iodobismuthates with 5-membered heterocyclic cations as solar absorbers: thiazolium, aminothiazolium and imidazolium iodobismuthates

4.1 Introduction and research proposal

Based on the study of iodobismuthates with 6-membered heterocyclic cations in the last chapter, we noted that more attention should be paid to the geometric and electronic properties of the cationic part.[1] When considering the geometric characteristics of organic entities, the size of cations is important since it impacts the packing strategy and structural dimensionality. At the same time, the geometry of organic cations also influences their interaction with the inorganic iodobismuthate framework. In regards to the electronic properties, counter-ions featuring heterocyclic rings and delocalized π-conjugating effects should be considered and designed in order to tune the energy levels and enhance the intermolecular interactions.[2,3] Specifically, heterocyclic rings like thiazole, which is aromatic and has a relatively small size, planar structure, and oxidative stability is of great interest.[4,5] Based on this, iodobismuthates with 5-membered heterocyclic cations are of great interest, including thiazolium (C_3H_4NS) (TH), imidazolium ($C_3H_5N_2$) (IM) and aminothiazolium ($C_3H_5N_2S$) (AT) rings (**Figure 4.1**). Introducing S and N into the heterocyclic cation can effectively make the cations more electronegative,[5] and thus potentially lower the conduction band minimum level to achieve better energy alignment with common electron transport or hole transport materials in a solar cell device. Incorporating heterocyclic aromatic rings in our study can also potentially contribute to the charge carrier mobility by introducing π-π interactions and enhancing the intermolecular interactions.[1]

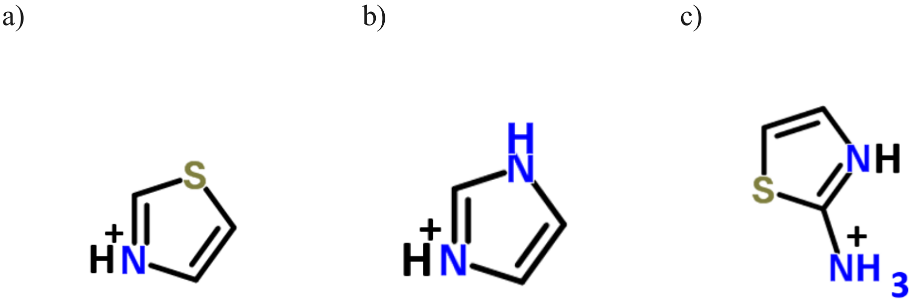

Figure 4.1 Molecular structures of (a) thiazolium (TH), (b) imidazolium (IM), and (c) aminothiazolium (AT).

4.2 Results and Discussions

4.2.1 Crystal structures and intermolecular interactions

A series of crystallisations was set up varying the crystallisation methods, anti-solvents and precursor ratios. **$[TH]_3[Bi_2I_9]$ and $[AT][BiI_4]$** both crystalized in the orthorhombic crystal system with space groups Pbcm and Pbca, respectively. The main crystallographic data of both compounds are shown in **Table 4.1**. The crystal structure of **$[IM]_3[Bi_2I_9]$** has been previously reported by Węcławik *et al*[6]. In **$[TH]_3[Bi_2I_9]$**, one of the thiazolium cations and the $[Bi_2I_9]^{3-}$ unit lie on a crystallographic mirror plane. In the case of the disordered thiazolium ring, the nitrogen and sulfur atoms are interchangeable by substitutional disorder. **Figure 4.2a** shows the schematic packing diagram of the major part (occupancy factors > 0.66) of the disordered crystal. Similarly, highly disordered imidazolium cations were found in both high temperature and low temperature crystal phases of **$[IM]_3[Bi_2I_9]$**, with a high temperature phase of hexagonal P63/mmc and low temperature space group of orthorhombic Cmcm, exhibiting an isomorphous structure to **$[TH]_3[Bi_2I_9]$** (**Figure 4.2b**). The Bi-I (bridging) distances range from 3.2354(12) Å to 3.2758(12) Å, which are longer than that of terminal Bi-I, ranging from 2.9585(12) Å to 2.9624(12) Å. This slight distortion probably originates from the repulsion of bismuth atoms in the binuclear species. When looking at the intermolecular interactions, in the unit cell of **$[TH]_3[Bi_2I_9]$**, two $[BiI_6]^{3-}$ fragments share three iodine atoms in a face-sharing manner to form the binuclear anionic units, with hydrogen bonding interactions to the neighbouring thiazolium rings shown in dashed cyan lines in **Figure 4.3a**. The packing motif of the $[TH]^+$ rings forms layers parallel to (1 2 0) and (-1 2 0) lattice planes (**Figure 4.3b**). In both **$[TH]_3[Bi_2I_9]$** and **$[IM]_3[Bi_2I_9]$**, only hydrogen bonding interactions of (H)-C…I and (H)-N…I can be seen between the organic and inorganic entities, with no short I…I contacts between the anionic units. This implies that almost no intermolecular interaction exists in **$[TH]_3[Bi_2I_9]$** and **$[IM]_3[Bi_2I_9]$,** leading to a lack of extended electronic delocalisation in the crystal lattice.

Table 4.1. Crystallographic data for **[TH]$_3$[Bi$_2$I$_9$]** ($C_9H_{12}Bi_2I_9N_3S_3$), **[AT][BiI$_4$]** ($C_3H_5BiI_4N_2S$) and **[IM]$_3$Bi$_2$I$_9$**

Compounds	**[TH]$_3$[Bi$_2$I$_9$]**	**[AT][BiI$_4$]**	**[IM]$_3$[Bi$_2$I$_9$]**
Formula	$C_9H_{12}Bi_2I_9N_3S_3$	$C_3H_5BiI_4N_2S$	$C_9H_{15}Bi_2I_9N_6$
$D_{calc.}$/ g cm^{-3}	3.598	4.064	-
μ/mm^{-1}	18.937	22.546	18.71
Formula Weight	1818.46	819.77	1767.33
Crystal System	Orthorhombic	Orthorhombic	Orthorhombic
Space Group	Pbcm	Pbca	Cmcm
a/Å	9.8257(2)	18.5429(4)	8.9409(14)
b/Å	14.6666(3)	7.53048(19)	16.749(2)
c/Å	23.2957(4)	19.1421(6)	22.494(3)
V/Å^3	3357.13(11)	2672.94	3368.5(8)
Wavelength/Å	0.71073	0.71073	-
wR_2 *(all data)*	0.1159	0.0803	0.047
wR_2	0.1151	0.0770	0.113
R1 (all data)	0.0609	0.0499	-
R_1	0.0590	0.0412	-

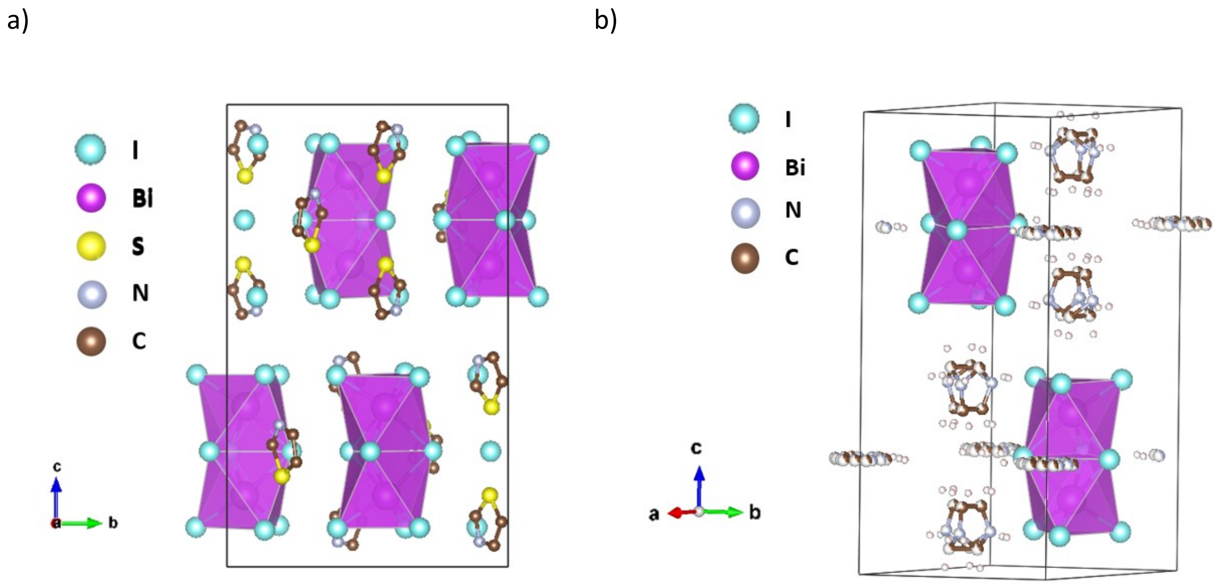

Figure 4.2. Schematic diagram of the major part of the disordered **$[TH]_3[Bi_2I_9]$** (a) and **$[IM]_3[Bi_2I_9]$** (b) unit cell. The unit cell boundary is marked with dark lines, and bismuth iodide octahedra are shown in magenta. Hydrogen atoms in **$[TH]_3[Bi_2I_9]$** are omitted for clarity.

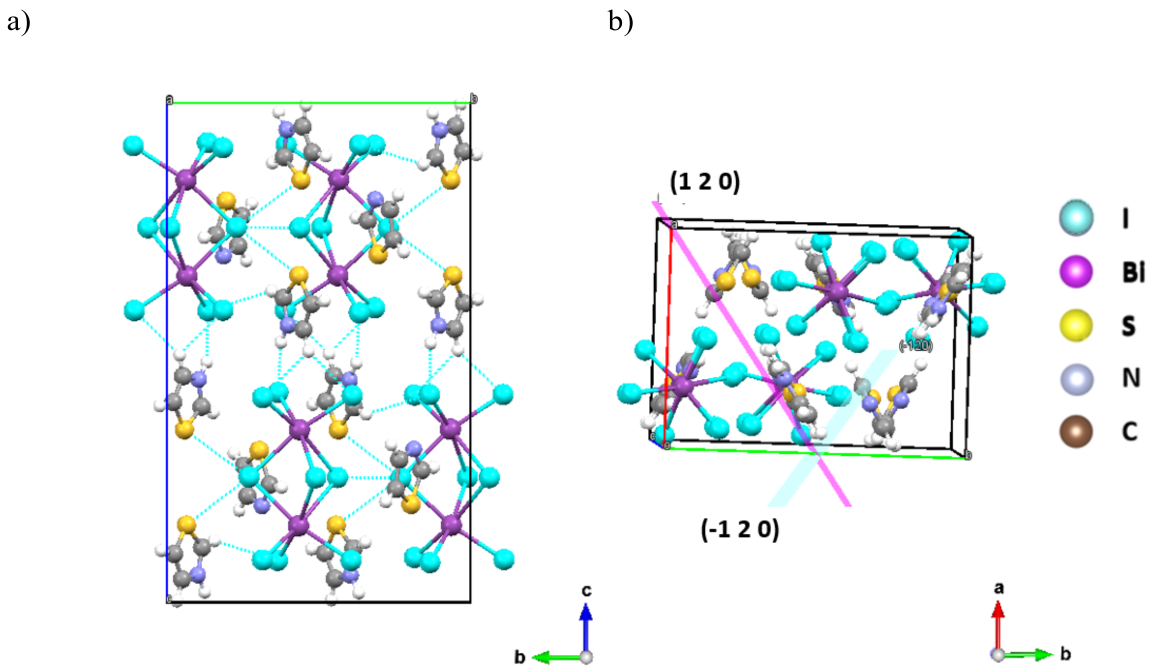

Figure 4.3 Crystallographic packing diagram of **$[TH]_3[Bi_2I_9]$** showing (a) H-bonding between $[Bi_2I_9]^{3-}$ and H...N on$[TH]^+$ cations (b) crystal planes of (1 2 0) (pink) and (-1 2 0) (blue) formed by the $[TH]^+$ cations.

In **$[AT][BiI_4]$**, one-dimensional **$[BiI]_4^-$** anionic chains propagate along the b-axis, with aminothiazolium cationic rings arranged in between the edge-sharing $[BiI_6]^{3-}$ octahedra (**Figure 4.4**). The Bi-I bond lengths range from 2.9219(5) Å to 3.2648(5) Å, with shorter bond lengths for terminal Bi-I than bridging ones. The angles for Bi-I(bridging)-Bi range from 92.314(14)° to

93.046(14)°, while I(terminal)-Bi-I(bridging) range from 85.297(15)° to 97.347(17)°. Such structural distortion of $[BiI_6]^{3-}$ octahedra originates from the repulsion between the heavy bismuth atoms in two adjacent $[BiI_6]^{3-}$ building blocks. Intermolecular interactions can be observed when viewing along different axis in the crystal lattice of **[AT][BiI$_4$]**, where the atomic distance is less than the sum of their Van der Waal's radii (**Figure 4.5, Table 4.3**). Short I…I contacts between two adjacent $[BiI]_4^-$ anionic chains can be seen along the **a**-axis, which enables the possibility of interchain charge delocalisation. In addition, short S…I and (H) N…I contacts between organic entities and inorganic frameworks are also seen in the **b-** and **c-**axis directions. Weak π–π stacking interactions involving the aminothiazolium rings can be found in the crystal structure, with the centroid distance of 3.839 Å and the vector-normal angle less than 20°[8]. Therefore, the $[BiI]_4^-$ anionic chains in the crystal structure of **[AT][BiI$_4$]** facilitate the charge transport ability along that direction, and other short contacts built up by Van der Waals interactions may help to promote higher dimensionality of charge carrier mobility. This is similar to what we observed in our previous work on **[PY][BiI$_4$]**.[1]It is worth-noting that by introducing S and $-NH_3^+$ in the cation, more involvement from the intermolecular interactions from the organic moieties can be seen, increasing the dimensionality of the crystal structure, which together with the increased intermolecular interactions potentially leads to higher dimensionality of the charge carrier transport network.

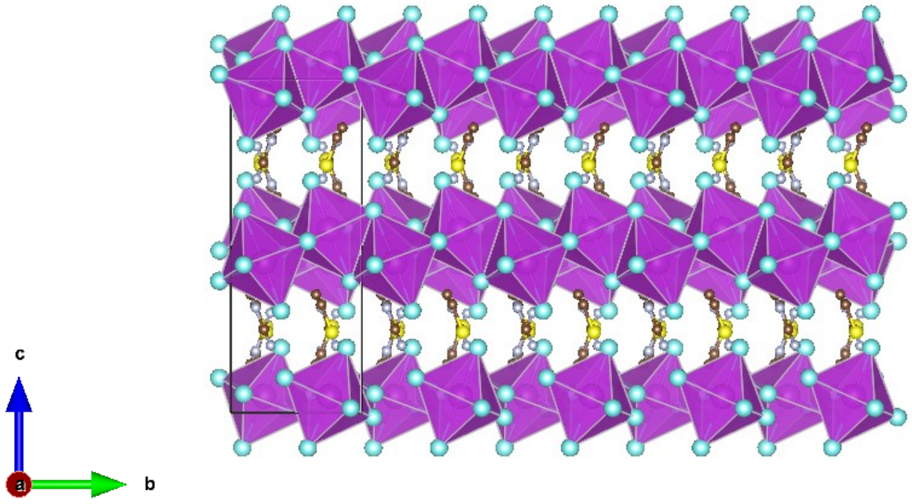

Figure 4.4 Schematic packing diagram of a [AT][BiI$_4$] crystal. The unit cell boundary is marked with dark lines, and bismuth iodide octahedra are shown in magenta. Hydrogen atoms are neglected for clarity.

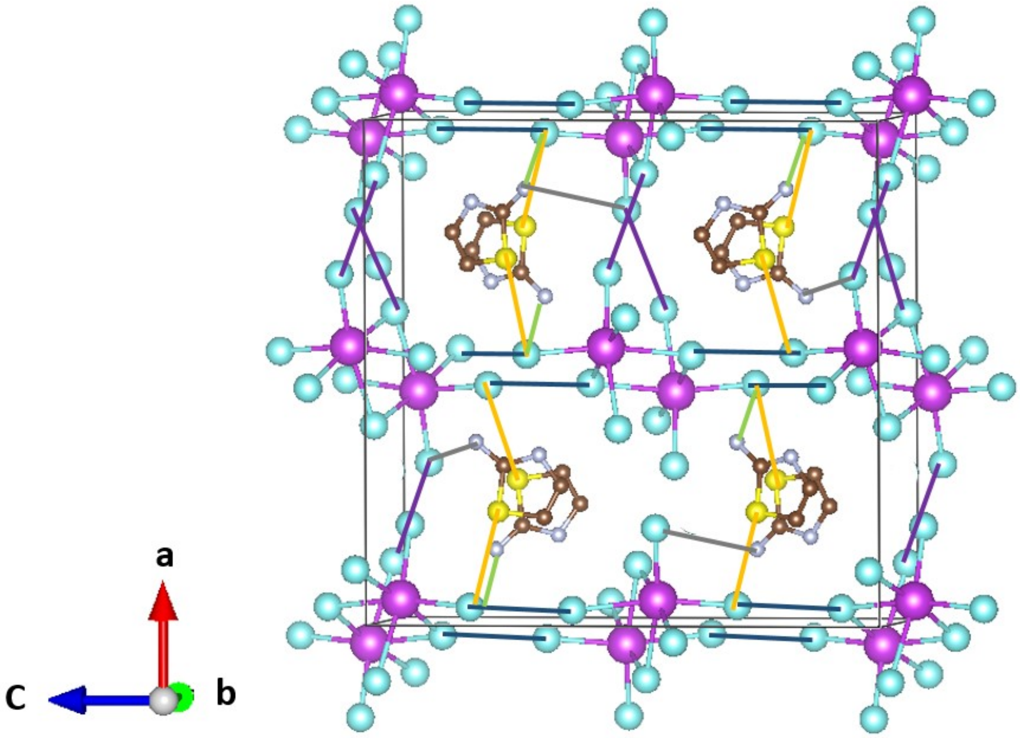

Figure 4.5 Left: **b-axis view of [AT][BiI₄]** unit cell with interchain interactions highlighted in purple or blue (I…I), yellow (I…S) and green or grey (I…N(H)). Right:

Table 4.3 list of short contacts in **[AT][BiI₄]** unit cell below the sum of the Van der Waal's radii (3.96 Å for I…I, 3.78 Å for I…S, and 3.18 Å for I…N(H)).[7]

Interactions	Label	Distance / Å
I…I	🟪	3.862
	🟦	3.884
I…S	🟧	3.691
I…N(H)	⬛	3.054
	🟩	2.885

4.2.2 Computational studies

Density functional theory (DFT) calculations were carried out for both **[TH]$_3$[Bi$_2$I$_9$]** and **[AT][BiI$_4$]** using CASTEP 16.11[9] to investigate the electronic band structure along the high symmetry ***k***-points in the first Brillouin zone, utilising the PBE functional and the Tkatchenko and Scheffler (TS) method to account for Van der Waals (dispersion) interactions. The atomic coordinates for both compounds were taken from the crystal structure, while only the major part (occupancy factors > 0.6) of the disordered **[TH]$_3$[Bi$_2$I$_9$]** crystal structure was considered for the calculation. For each crystal structure, full optimisation of atomic positions and unit cell parameters were undertaken prior to obtaining density of states (DOS) plots which were subsequently broken down to partial DOS plots, to permit observation of contributions from different elements to the electronic bands (**Figure 4.6**).

a)

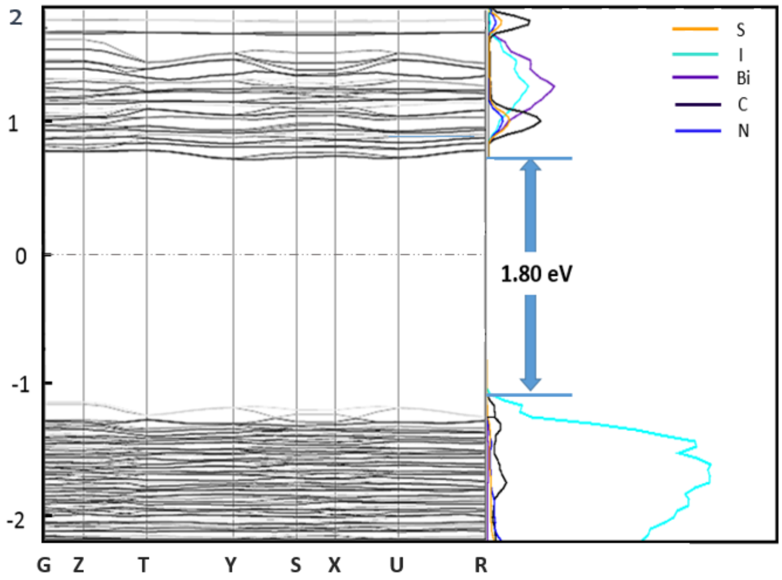

b)

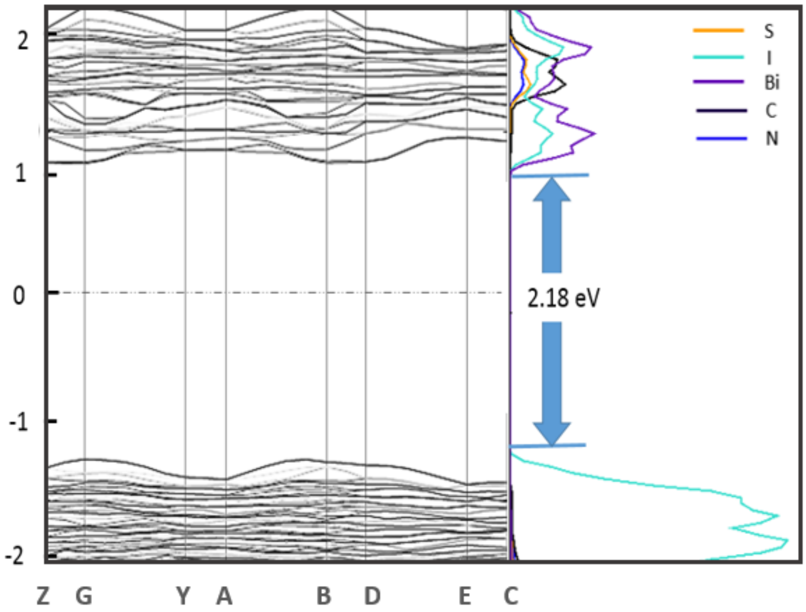

Figure 4.6 Electronic band structures and projected density of states (bismuth 6p orbital: purple; iodine 5p orbital: cyan; sulfur 3p orbital: yellow; carbon 2p orbital: black; nitrogen 2p orbital: navy) for $[TH]_3[Bi_2I_9]$ (a) and $[AT][BiI_4]$ (b). The Fermi level was set at 0 eV.

Direct bandgaps for both materials were calculated, with the value of 1.80 eV at the middle of ***K***-points Y (-0.5, 0.0, 0.0) and S (-0.5, 0.5, 0.0) for **$[TH]_3[Bi_2I_9]$,** and 2.18 eV at B (0.5, 0.0, 0.0) for **$[AT][BiI_4]$**. For both compounds, the main contribution to the valence band maximum (VBM) is from the iodine 5p states, with slightly higher band dispersion noted for **$[AT][BiI_4]$**, especially along the 1D **$[BiI_4]^-$**

chain direction (G-Y and A-B). This band broadening effect is mostly attributed to the polar Bi (6p) – I (5p) σ-bonding interactions. The noticeable dispersion along Z-G corresponds to the inter-chain direction in the crystal structure, which is mainly attributed to the short I…I contacts that exist in between the parallel **$[BiI_4]^-$** chains. Compared with **$[TH]_3[Bi_2I_9]$**, whose conduction band minimum (CBM) has mixed contributions of organic entities together with Bi 6p states, little contribution to the CBM from the organic cations can be seen in **$[AT][BiI_4]$**. The dominant role played by the inorganic entities at the CBM of **$[AT][BiI_4]$** appears to be the σ* antibonding interactions of Bi 6p with iodine 5p states which give rise to band broadening. The generally flat band structure of **$[TH]_3[Bi_2I_9]$**, indicates a limited ability in this material for charge carrier transport. This is ubiquitous among 0D bismuth-halide complexes as the low structural dimensionality inhibits the charge carriers mobilities and hence less electronic dispersion is observed.[10] Note band structure computation was not carried out for **$[IM]_3[Bi_2I_9]$** as similar results to **$[TH]_3[Bi_2I_9]$** were expected.

4.2.3 Powder XRD studies on structure and stability of thin films

We have studied the three title compounds as thin films, prepared by spin-coating on quartz, to explore their structural properties in the solid state. Different temperatures were chosen for annealing after spin-coating, from 70 °C to 130 °C. All three title materials show good consistency with the simulated powder XRD pattern from single-crystal data (**Figure 4.7a-c**), with some preferred orientation evident as thin films. Preferred orientation on the (0 0 2) plane for both **$[TH]_3[Bi_2I_9]$** and **$[IM]_3[Bi_2I_9]$** can be observed as thin films, which corresponds to the plane composed of terminal iodine atoms in the $[Bi_2I_9]^{3-}$ binuclear unit. It is worth noting that **$[TH]_3[Bi_2I_9]$** decomposed back to the starting material BiI_3 after annealing at temperatures higher than 110°C, with the characteristic (0 0 2) plane disappearing as the annealing temperature increased. Higher thermal stability can be observed for both **$[AT][BiI_4]$** and **$[IM]_3[Bi_2I_9]$**, although the intensity of the characteristic (0 0 2) and (2 0 0) planes in **$[AT][BiI_4]$** becomes gradually weaker. These planes are built up by the propagating $[BiI_4]^-$ chains at the unit cell boundaries, parallel to (0 0 1) and (1 0 0) (**Figure 4.7d**) and we assume that higher temperatures lead to less structural coherence of the Bi-I anionic chains. No obvious structural changes occur after two weeks exposure to air in the dark, indicating high stability of all three compounds (**Figure 4.7 e**).

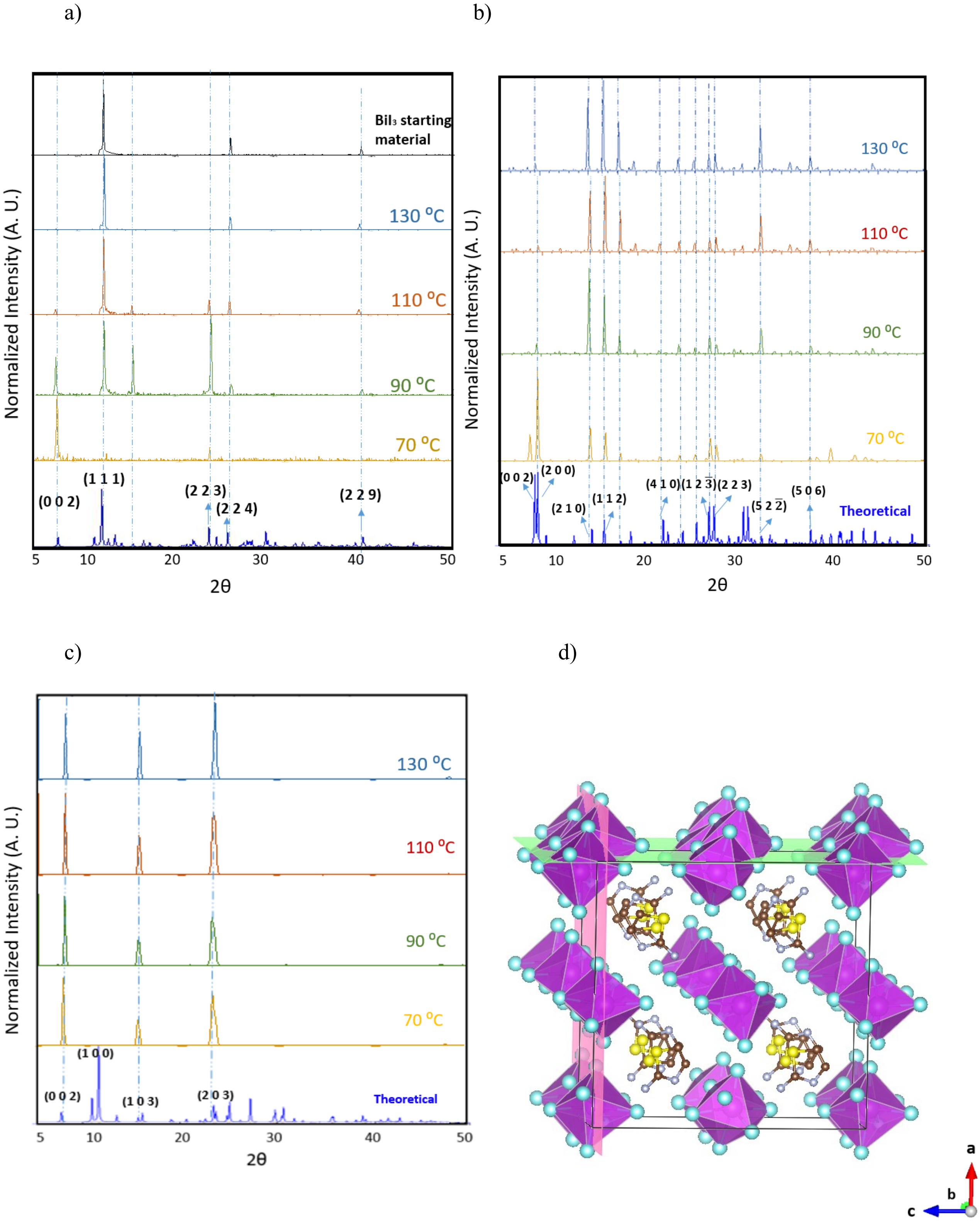
a)
b)
c)
d)
BiI₃ starting material
130 °C
110 °C
90 °C
70 °C
Theoretical
(0 0 2)
(1 1 1)
(2 2 3)
(2 2 4)
(2 2 9)
(2 0 0)
(2 1 0)
(1 1 2)
(4 1 0)
(1 2 3̄)
(2 2 3)
(5 2 2̄)
(5 0 6)
(1 0 0)
(1 0 3)
(2 0 3)
Normalized Intensity (A. U.)
2θ
5
10
20
30
40
50
a
b
c

e)

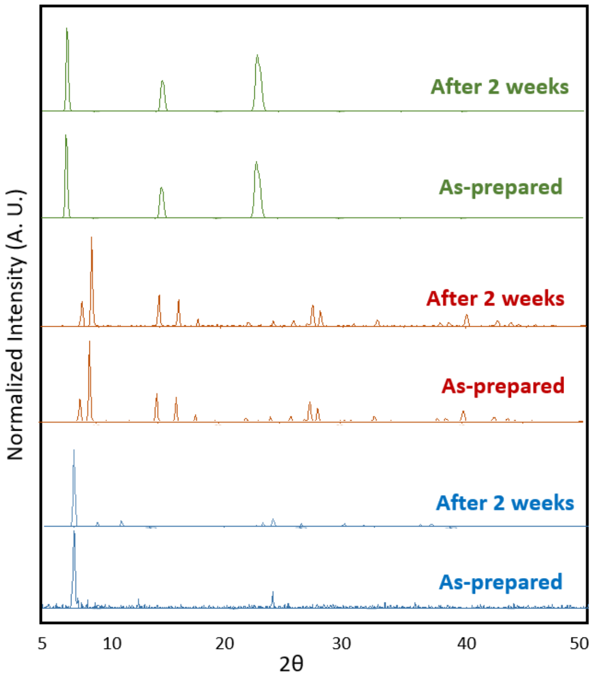

Figure 4.7 Powder XRD patterns on thin films of (a) $[TH]_3[Bi_2I_9]$, (b) [AT][BiI_4], and (c) $[IM]_3[Bi_2I_9]$ annealed at different temperatures comparing to the theoretical patterns predicted from the single-crystal XRD (blue). d) (0 0 1) (coral) and (1 0 0) (green) crystal planes in in the unit cell of [AT][BiI_4]; (e) Powder XRD of three materials as thin films after two weeks exposure to air in dark. Blue: $[TH]_3[Bi_2I_9]$ annealed at 70 ºC ; red: [AT][BiI_4]; green: $[IM]_3[Bi_2I_9]$.

4.2.4 Diffuse reflectance for band-gap determination

Diffuse reflectance measurements were carried out for these materials as powders scratched off from thin films and diluted in $BaSO_4$, to estimate their optical bandgaps by converting their reflectance spectra into Tauc plots (**Figure 4.8**). A band gap value of 2.08 eV was determined for **$[TH]_3[Bi_2I_9]$** annealed at 70°C, while much lower band gap values were observed for thin films annealed at higher temperatures. This corresponds to the thin-film XRD study results, which show the thermal decomposition of **$[TH]_3[Bi_2I_9]$ to BiI_3** when annealing at a temperature higher than 70 °C (**Figure 4.9a**). A band gap value of 1.78 eV was determined for **[AT][BiI_4]** and 2.00 eV for **$[IM]_3[Bi_2I_9]$**, with no substantial change under increased annealing temperatures (**Figure 4.9b,c**). This is consistent with our expectation that higher dimensionality leads to smaller bandgap. Inconsistency can be found when comparing with the calculated bandgap values, which is attributed to the intrinsic limitations of using DFT calculation to determine the bandgap values.[11] The SEM image of **$[TH]_3[Bi_2I_9]$** thin-film shows wire-shaped irregular crystals with a relatively poor coverage, as shown in **Figure 4.10a**. In the case of **[AT][BiI_4]** thin film, good crystallinity when annealed under 150°C can be observed in the SEM, with the rectangular crystal grain dimensions around 8 μm x 10 μm (**Figure 4.10b**)

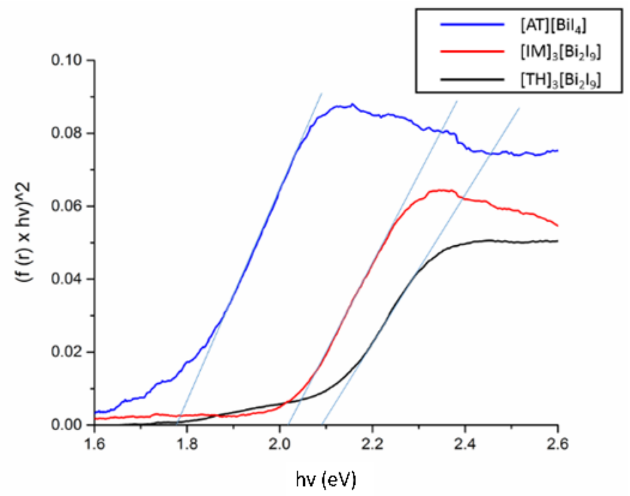

Figure 4.8 Tauc plots from diffuse reflectance measurements on powder samples scratched off from thin films and diluted in $BaSO_4$.

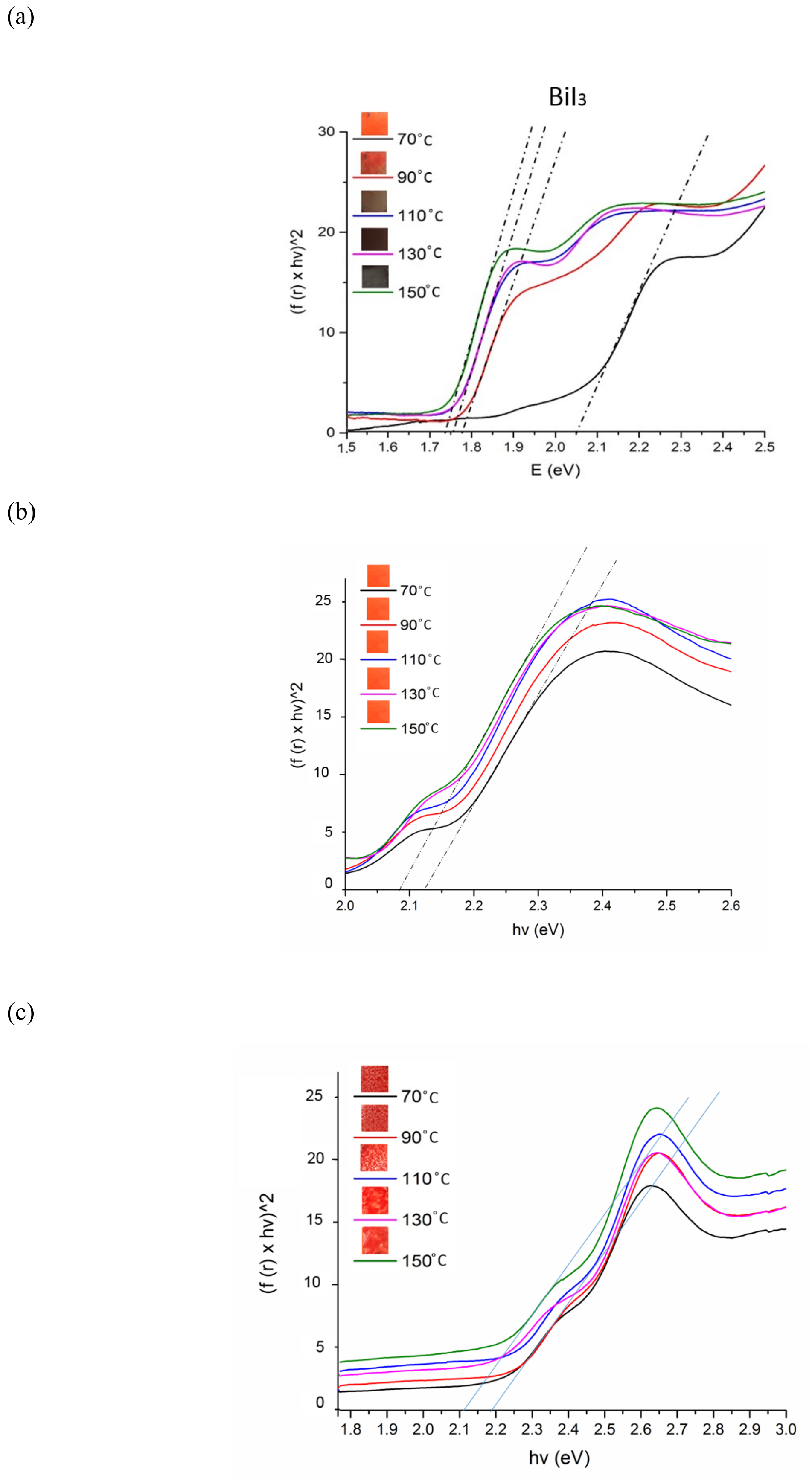

Figure 4.9 Tauc plots and band gap estimations of (a) [TH]$_3$[Bi$_2$I$_9$], (b) [IM]$_3$[Bi$_2$I$_9$] and (c) [AT] [BiI$_4$] thin films annealed at different temperatures. Coloured squares are optical microscope pictures of the actual thin-films surface, for reference to colour changes that occur.

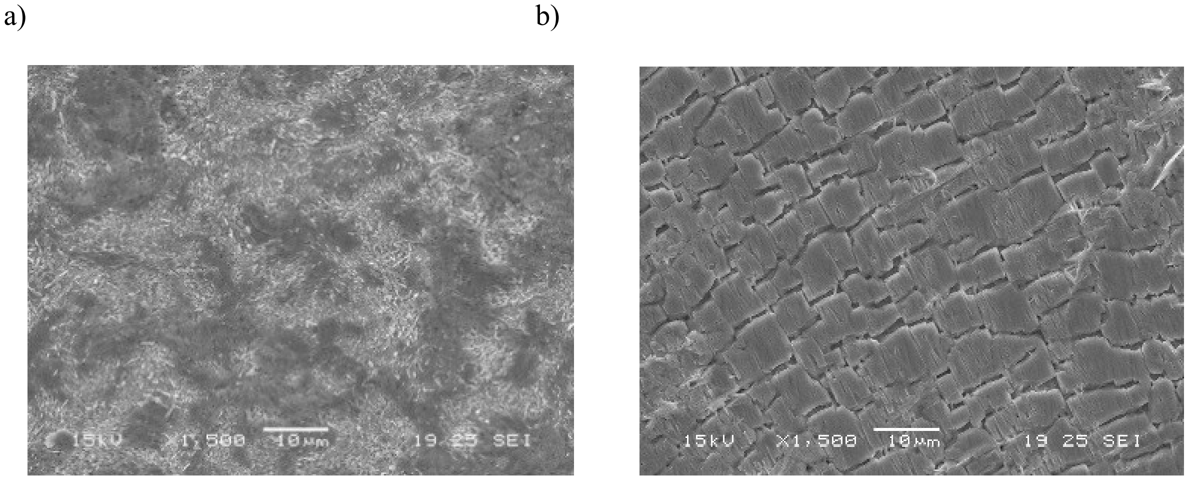

Figure 4.10 SEM image of (a) $[TH]_3[Bi_2I_9]$ and (b) [AT] $[BiI_4]$ thin films deposited on a glass substrate.

4.2.5 Electrochemistry studies

The materials were spin-coated onto conducting glass and used as working electrodes in cyclic voltammetry measurements, in order to study their solid-state electrochemical properties. The ionisation energy (IE) and electron affinity (EA) for both compounds were estimated using the method by Crespilho *et al*,[12] based on the experimentally-measured redox potential. Irreversible oxidation and reduction processes were observed for all materials, and some dissolution of both thin films occurred within minutes. The estimated energy levels are summarized in **Table 4.4**, with the energy level diagram in **Figure 4.11**. Note that the VBM has been pushed to a lower energy level by adding the $–NH_3^+$ group on the thiazolium ring, which potentially facilitates the hole injection into the carbon counter electrode.

Table 4.4 Summary of electrochemical oxidation onset potential (E'_{ox}), electrochemical oxidation potential (E_{ox}), ionisation energy (IE), optically-determined energy band gap (Eg) and estimated electron affinity energy (EA) values for **$[TH]_3[Bi_2I_9]$**, **$[IM]_3[Bi_2I_9]$** and **$[AT][BiI_4]$**. The relationship between oxidation potential onset and Ag/AgCl electrode is shown in the equation $E_{ox} = E'_{ox} + E_{Ag/AgCl} \approx E'_{ox} + E_{vac} + 4.4$[12]

Compounds	E'_{ox} (V vs Ag/AgCl)	E_{ox} (V vs vacuum)	IE (eV)	Eg (eV)	EA (eV)
$[TH]_3[Bi_2I_9]$	0.41	4.81	-4.81	2.08	-2.73
$[AT][BiI_4]$	0.52	4.92	-4.92	1.78	-3.15
$[IM]_3[Bi_2I_9]$	0.28	4.68	-4.68	2.00	-2.68

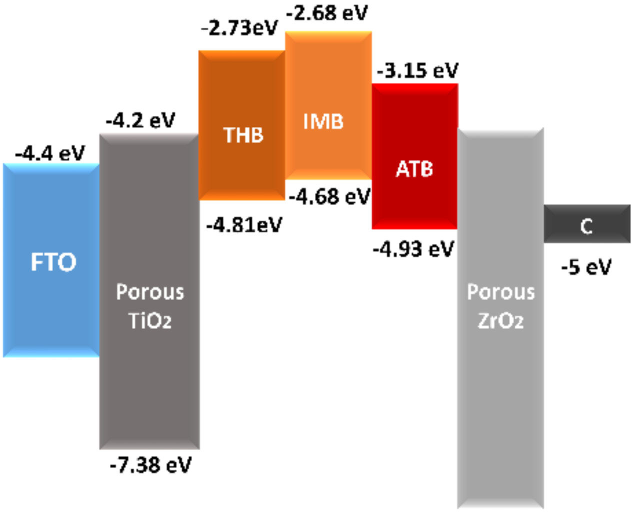

Figure 4.11 Energy level diagram including other components in the solar cell. Energies are expressed in electron volts, reference to the electron energy in vacuum.

4.2.6 Solar cell device studies

The photovoltaic performance of **[AT][BiI$_4$]** was tested in solar cell devices, as it is the most promising material among the three title compounds due to its suitable bandgap value, relatively larger band energy dispersion and better energy level alignment. The solar cell devices in this study are based on FTO / (TiO_2/ZrO_2/Carbon) / perovskite structure, with solution-processable photovoltaic material infiltrated through the triple-layer mesoscopic scaffold (**Figure 4.12a**). The J-V curve thus obtained when **[AT][BiI$_4$]** acts as a light harvester is shown in **Figure 4.12b**. Further studies suggest that the device shows capacitance characteristics, analogous with capacitors formed by common carbon/electrolyte capacitor components in the cell structure. When the bias voltage was applied, the device was charged instantly under the initial potential, followed by charged current release in addition to the photo-generated current (Ip). To further confirm this, we carried out controlled experiments in the dark, and a slightly lower device current was observed. The difference in device performance with/without illumination shows the actual photocurrent Ip from the device (**Figure 4.12b**). Avoiding capacitance effects by scanning forwards from zero volts shows the photovoltaic performance of **[AT][BiI$_4$]** is 0.47%, with open-circuit voltage (V_{oc}) =0.37 V, short-circuit current density (J_{sc}) = 3.29 mA/cm^2 , fill factor (FF) = 0.39.

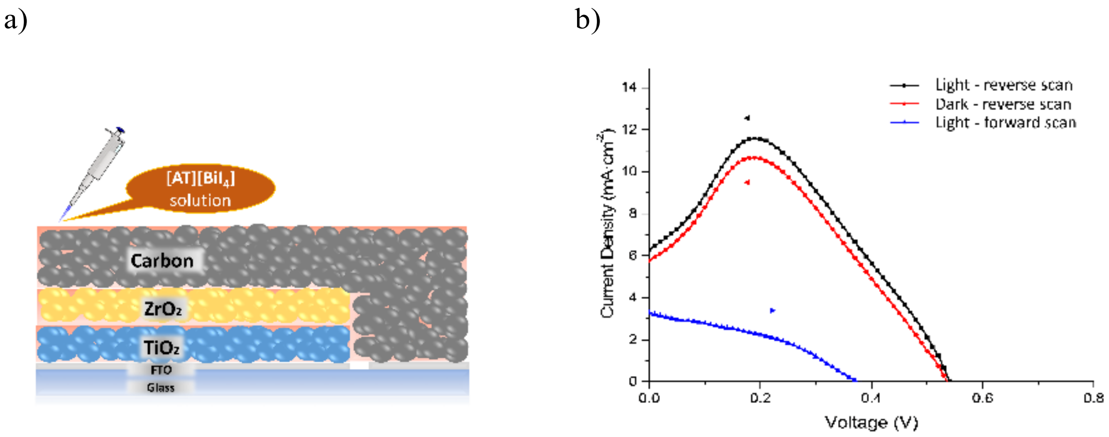

Figure 4.12 (a) Schematic cross section picture of a triple-layer mesoscopic solar cell infiltrated with [AT][BiI$_4$] precursor solution. (b) J-V curve of a [AT][BiI$_4$] solar cell under light condition, reverse scan (black), under dark condition, reverse scan (red) and under light condition, forward scan (blue). The large hysteresis indicates the charging process when voltage was applied in the beginning of a reverse scan.

The incident photon-to-current efficiency (IPCE) measurement is shown in **Figure 4.13**, with most of the yield originating from the ultraviolet to violet spectrum. The integration of the IPCE curve is somewhat lower that the current density of the best solar cell device, but this has been observed before for perovskite solar cells based on this type of structure.[13] Further device studies on photo-generated energy storage were carried out. Firstly, we tested the short-circuit current before and after the JV test to find out 1) If there is any capacity effect caused by light; 2) If there is any capacity effect caused by the applied bias during measurement. Before every test, we illuminated the device under AM1.5 radiation for one minute under open circuit conditions. We then turned off the light and started to record the current. The short circuit current was measured at around 10 s, and we tested the short-circuit current before and after the JV test for comparison. The measured current under a bias voltage of 0 V against time is plotted in **Figure 4.14a**. From the experiment we found that the light soaking contributes to the charge storage to some extent, however, the solar cell devices are charged significantly under the bias potential applied when performing the JV test. We have also compared our results with well-studied 5AVA-MAPbI$_3$ devices to validate that such an effect is brought about by the bismuth-based light absorber (**Figure 4.14b**)

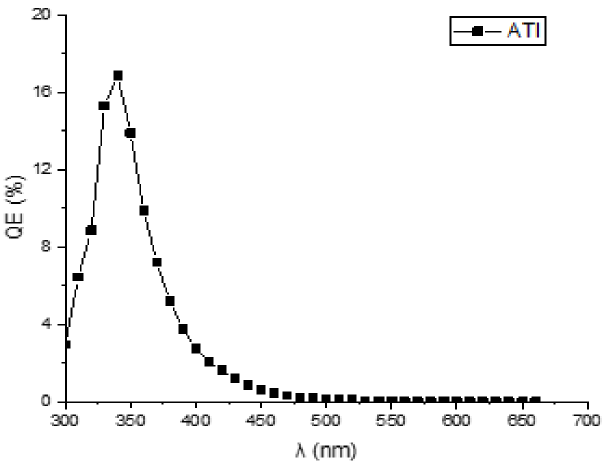

Figure 4.13 IPCE measurement of a [AT][BiI4] solar cell

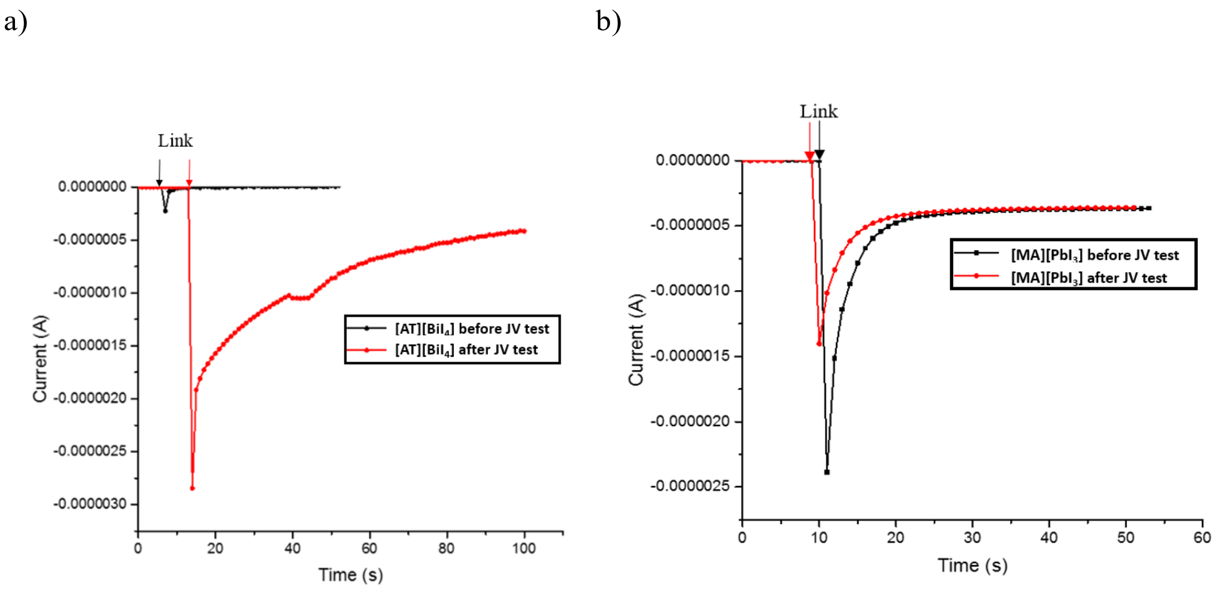

Figure 4.14 Short-circuit current test of (a) [AT][BiI4] and (b) 5AVA-[MA][PbI3] solar cells before and after the JV test after 1 min light soaking.

From the stabilized current measurements, a drop of current can be seen over time (**Figure 4.15a**). No oxidation/reduction reactions of **[AT][BiI$_4$]** were detected during the cyclic voltammetry of the devices (**Figure 4.15b**). We speculate that the origins of the capacitance effect in the device relate to the mesoporous carbon electrode and the presence of potentially mobile protons in the aminothiazolium catioin. The aminothiazolium cation has both a protonated and an unprotonated nitrogen atom, which may provide possibilities for proton migration to and from the TiO_2 layer. Looking into the cyclic voltammetry of the solar cell device, we estimate the capacitance of the device to be 0.12 mF, with areal capacitance of 0.075 mF/cm^2. Thus this report is the first instance of the capacitance effect in a solar cell using a bismuth-based light absorber, which may prove a useful future direction for study of lead-free solar cell/capacitor devices for solar energy generation and storage.

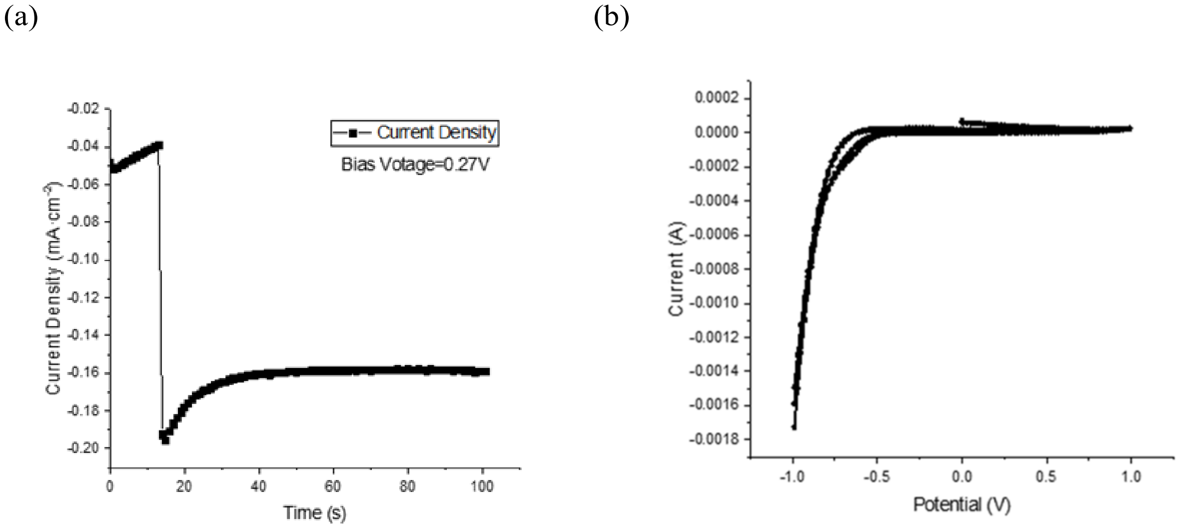

Figure 4.15 a) Stabilised current measurement of [AT][BiI$_4$] solar cell with forward scan bias voltage; b) cyclic voltammetry of a [AT][BiI$_4$] solar cell under dark.

4.3 Conclusions

Three organic-inorganic iodobismuthates were synthesised, characterised and studied as potential lead-free solar absorbers. All the compounds contain organic cations with heterocyclic 5-membered rings, with different inorganic frameworks from 0D for **[TH]$_3$[Bi$_2$I$_9$]** and **[IM]$_3$[Bi$_2$I$_9$]** to 1D **[AT][BiI$_4$]**. Direct band gap values around 2.05 eV were determined for both 0D materials while 1.78 eV was determined for the 1D material. Additionally, the conduction band minimum (CBM) value of **[AT][BiI$_4$]** has been shifted to a lower value, which enables better energy level match with TiO_2 for electron injection purposes. Computational studies suggest that more involvement of organic entities in the conduction band minimum can be found for **[TH]$_3$[Bi$_2$I$_9$]**, while major contributions of Bi 6p and I 5p antibonding interactions were found for **[AT][BiI$_4$]**. Both **[IM]$_3$[Bi$_2$I$_9$]** and **[AT][BiI$_4$]** showed better thermostability than **[TH]$_3$[Bi$_2$I$_9$]**. Device studies with **[AT][BiI$_4$]** as a solar absorber shows 0.47% efficiency (forward scan), with unusual capacitive effects during the reverse scan, likely caused by proton migration between the aminothiazolium cationic entities and the TiO_2 layer. This points towards the possibility that devices with a carbon counter electrode and **[AT][BiI$_4$]** as a light harvester have potential as lead-free solar energy generator and storage device.

4.4 Experimental

4.4.1 Synthesis of thiazolium bismuth iodide **$[TH]_3[Bi_2I_9]$**

Thiazole was firstly diluted in ethanol (by 1:10 volume ratio) before 55% hydroiodic acid was added dropwise with continuous stirring under room temperature for 2 hours (1:1 molar ratio). The product precipitated out from the solvent during the reaction, and the precipitates were filtered under vacuum suction and washed with diethyl ether three times. The product was dried under vacuum for 2 hours, yielding white solid as thiazolium iodide (95% yield).

Single dark red plate-shaped crystals of **$[TH]_3[Bi_2I_9]$** were recrystallised from a mixture of BiI_3 ethanol solution (1 mM) and thiazolium iodide water solution (1 mM) by solvent layering, resulting in dark red blocks and dark red plate-shaped crystals formed after 1 week.

4.4.2 Single crystal X-ray diffraction of $[TH]_3[Bi_2I_9]$

Despite their apparent good quality, diffraction from the block crystals of **$[TH]_3[Bi_2I_9]$** was very poor. The crystals shattered when flash-cooled at 120, 150 and 200 K. At 250 K diffraction was reasonable but diffraction from the plate-shaped crystals was much better and it is the structure from a plate crystal which is presented here in the thesis.

4.4.3 Synthesis of imidazolium bismuth iodide **$[IM]_3[Bi_2I_9]$**

The synthesis and crystallographic data of **$[IM]_3[Bi_2I_9]$** can be found in the literature[6]

4.4.4 Synthesis of aminothiazolium bismuth iodide **$[AT][BiI_4]$**

Aminothiazole was first dissolved in ethanol (1:10 volume ratio) before 55% hydroiodic acid was added dropwise with continuous stirring under room temperature for 2 hours. (Molar ratio of 1:1) The product precipitated out from the solvent during the reaction, and the precipitate was filtered under suction and washed with diethyl ether. The product was dried under vacuum for 2 hours, yielding yellowish-white solid as aminothiazolium iodide (78%).

Single crystals of **$[AT][BiI_4]$** were formed at the interface of aminothiazolium iodide water solution (1 mM) and BiI_3 ethanol solution (1 mM) in an NMR tube over one week. The compound crystallized as dark red block-shaped crystals.

4.4.5 Film formation

Thin-films of **$[TH]_3[Bi_2I_9]$, $[IM]_3[Bi_2I_9]$** and **$[AT][BiI_4]$** were prepared by spin-coating on glass or FTO substrates. The precursor solution for each compound was prepared by mixing the counter-ion salt with BiI_3 according to the stoichiometry of their chemical formulas. DMF:DMSO=7:3 solvent was used for all of the compounds to prepare a 1 M precursor solution for spin coating. For thin-films used in powder XRD, SEM and CV measurements, a spin speed of 2000 rpm was used for 1 min. For thin-films used in the solid-state diffuse reflectance measurement, 1000 rpm spin speed was used for 1 min.

4.5 References

1 T. Li, Y. Hu, C. Morrison, W. Wu, H. Han and N. Robertson, *Sustain. Energy Fuels*, 2017, **1**, 308–316.

2 P. Qin, X. Yang, R. Chen, L. Sun, T. Marinado, T. Edvinsson, G. Boschloo and A. Hagfeldt, *J. Phys. Chem. C*, 2007, **111**, 1853–1860.

3 M. Anil Reddy, B. Vinayak, T. Suresh, S. Niveditha, K. Bhanuprakash, S. Prakash Singh, A. Islam, L. Han and M. Chandrasekharam, *Synth. Met.*, 2014, **195**, 208–216.

4 H. Jung, J. Yu, E. Jeong, J. Kim, S. Kwon, H. Kong, K. Lee, H. Y. Woo and H. K. Shim, *Chem. - A Eur. J.*, 2010, **16**, 3743–3752.

5 E. Zaborova, P. Chávez, R. Bechara, P. Lévêque, T. Heiser, S. Méry and N. Leclerc, *Chem. Commun.*, 2013, **49**, 9938–9940.

6 M. L. Petrus, J. Schlipf, C. Li, T. P. Gujar, N. Giesbrecht, P. Müller-Buschbaum, M. Thelakkat, T. Bein, S. Hüttner and P. Docampo, *Adv. Energy Mater.*, 2017, **7**, 2017.

7 C. E. Housecroft and A. G. Sharpe, *Inorganic Chemistry (4th edition)*, Pearson, 2012.

8 C. Janiak, *J. Chem. Soc., Dalton Trans.,* 2000, **0**, 3885-3896.

9 S. J. Clark, M. D. Segall, C. J. Pickard, P. J. Hasnip, M. I. J. Probert, K. Refson and M. C. Payne, *Zeitschrift für Krist.*, 2005, **220**, 567–570.

10 Z. Xiao, W. Meng, J. Wang, D. B. Mitzi and Y. Yan, *Mater. Horiz.*, 2017, **4**, 206–216.

11 A. Seidl, A. Görling, P. Vogl, J. A. Majewski, and M. Levy, *Phys. Rev. B*, 1996, **53**, 3764.

12 F. N. Crespilho, V. Zucolotto, J. R. Siqueira, A. J. F. Carvalho, F. C. Nart and O. N. Oliveira, *Int. J. Electrochem. Sci.*, 2006, **1**, 151–159.

13 Y. Hu, Z. Zhang, A. Mei, Y. Jiang, X. Hou, Q. Wang, K. Du, Y. Rong, Y. Zhou, G. Xu and H. Han, *Adv. Mater.*, 2018, **30** (11), 1705786.

Chapter 5

Bandgap engineering of iodobismuthates by dianionic substitution

5.1 Introduction and research proposal

Iodobismuthates have drawn appreciable interest recently because of their potential to substitute Pb in lead-halide perovskite photovoltaic materials. However, one reason hindering bismuth-based materials in high photovoltaic performance is their relatively high band-gap value (around 2.1 eV).[1–4] Studies on 0 D iodobismuthates including $[CH_3NH_3][Bi_2I_9]$(MBI) and $Cs_3Bi_2I_9$ (CBI) have shown a wide bandgap of 2.3 eV with the best solar-cell efficiency achieved of 1.64% for MBI[5] and 1.09% for CBI,[4] with extensive studies on device optimisation. In the last two chapters, 1D hybrid iodobismuthates were used in fully printable devices with efficiency of 0.90% and 0.40% for **[PY]BiI$_4$** and **[AT]BiI$_4$**, respectively.[6,7] One way to optimise the structure is to employ another +1 metal ion to form a 3D double perovskite structure. Such bismuth based double perovskite structure materials include $Cs_2AgBiCl_6$, $Cs_2AgBiBr_6$, and $[CH_3NH_3]_2KBiCl_6$,[8–10] with the best efficiency (2.4%) achieved by $Cs_2AgBiBr_6$.[11] However, the band gap values for these are still around 2 eV since the halide component is bromide or chloride, rather than iodide. Introducing a new direction, Turkevych et al studied silver bismuth halide materials based on the 3D Rudorffite structure with a band gap at around 1.8 eV, which increased the efficiency of bismuth-based solar cells to 4.3% by using Ag_3BiI_6 as a solar absorber.[12] This family of materials however, offers limited options for further materials tuning. Another method to lower the band gap value is by doping the low dimensional iodobismuthate materials with sulfur, which seems to be a facile way to lower the bandgap.[13]

In this chapter, we will explore bandgap engineering by introducing 2^- anions, including $[SiF_6]^{2-}$, $[TiF_6]^{2-}$ and S^{2-} into the crystal lattice of high bandgap iodobismuthates. In the first part, band gap engineering of 1D **[PY]BiI$_4$** by a sulfur-doping method will be discussed, where the S dopants were introduced using bismuth xanthate, $Bi(C_3H_5S_2O)$ ($Bi(xt)_3$). $Bi(xt)_3$ is an organobismuth precursor that can introduce bismuth together with the sulfur dopant via a thermal decomposition method.[14] In Chapter 3 and 4, we introduced hybrid organic-inorganic iodobismuthates with one dimensional structures that give promising performance in solar cells, and we will explore the use of bismuth xanthate to introduce sulfur doping to reduce the bandgap of such materials, and thus potentially increase the light harvesting ability. In the second part, we will extend the 2^- anions from S^{2-} to $[SiF_6]^{2-}$and $[TiF_6]^{2-}$ as the dopant for 0D high bandgap $Cs_3Bi_2I_9$ (CBI). In this study, we will employ drop casting and spin coating post-treatment methods to introde dianions, followed by crystal structure characterization using powder XRD. We will then use XPS and Raman measurements to study the bonding environment of bismuth and probe the mechanisms. We will also perform photo-generated current measurement to test the photocurrent generation performance of the dianion treated CBI materials, especially under long wavelength light.

5.2 Results and Discussions

5.2.1 Band Gap Engineering of 1D [PY]BiI$_4$ via Sulfur Doping

5.2.1.1 Synthesis and structural study of S doped thin films

In this study, Sulfur-doped one-dimensional pyridinium bismuth iodide (**[PY]BiI$_4$**) was synthesized via a solution-processing method. PyI and bismuth xanthate (Bi(xt)$_3$) were used as the precursor compounds. Sulfur was introduced and doped into [PY]BiI$_4$ by thermal decomposition of xanthate (**Figure 5.1**). 1:3 and 1:4 ratios of Bi(xt)$_3$ and PyI were studied in the precursor solution to optimize the doping and thin-film crystallinity, under annealing temperature of 80°C, 100 °C, 120 °C and 140 °C after spin-coating onto a glass slide. Powder XRD patterns of the thin films under different annealing temperatures are shown in **Figure 5.2**, which match that expected for **[PY][BiI$_4$]**. When the ratio is 1:3, thermal decomposition of bismuth xanthate with film formation is complete when the annealing temperature is above 100°C. From 100°C to 140°C, no structural change occurred, showing the film has good thermal stability (**Figure 5.2a**). For the 1:4 precursor ratio, an intermediate phase exists from 80°C to 120°C, and the film forming process is complete when the annealing temperature is above 140 °C (**Figure 5.2b**). Strong preferred orientation in the films can be found, showing (1 2 0) and (2 4 0) planes and also weaker peaks at (2 0 0), (2 6 $\bar{1}$) and (4 8 0). No structural change or significant peak shift was observed compared to pristine **[PY]BiI$_4$**, which suggests any uptake of S in the **[PY]BiI$_4$** crystal lattice is small, without altering the original crystal structure.

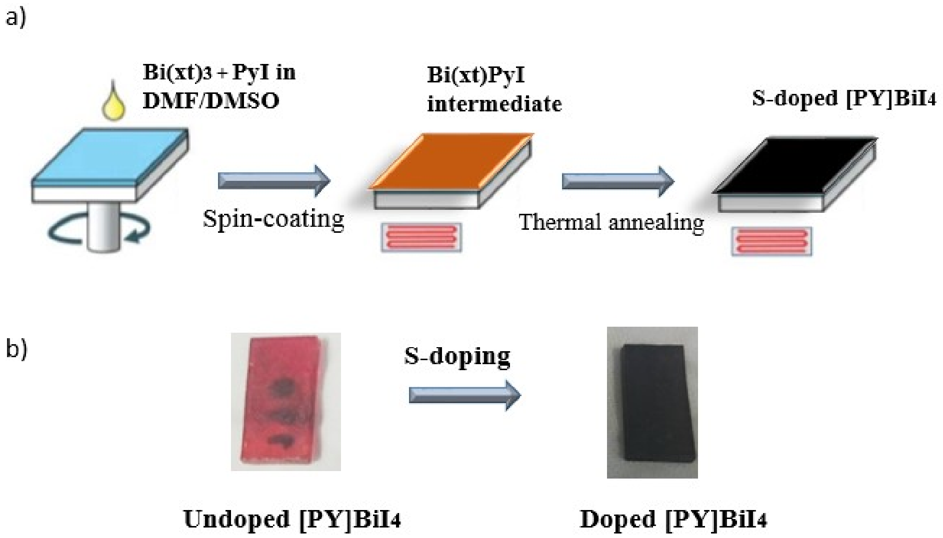

Figure 5.1 (a) Schematic diagram of spin coating and thermal decomposition method by using $Bi(xt)_3$ and PyI as precursors; (b) photograph of the material deposited on FTO glass showing with/without the doping treatment.

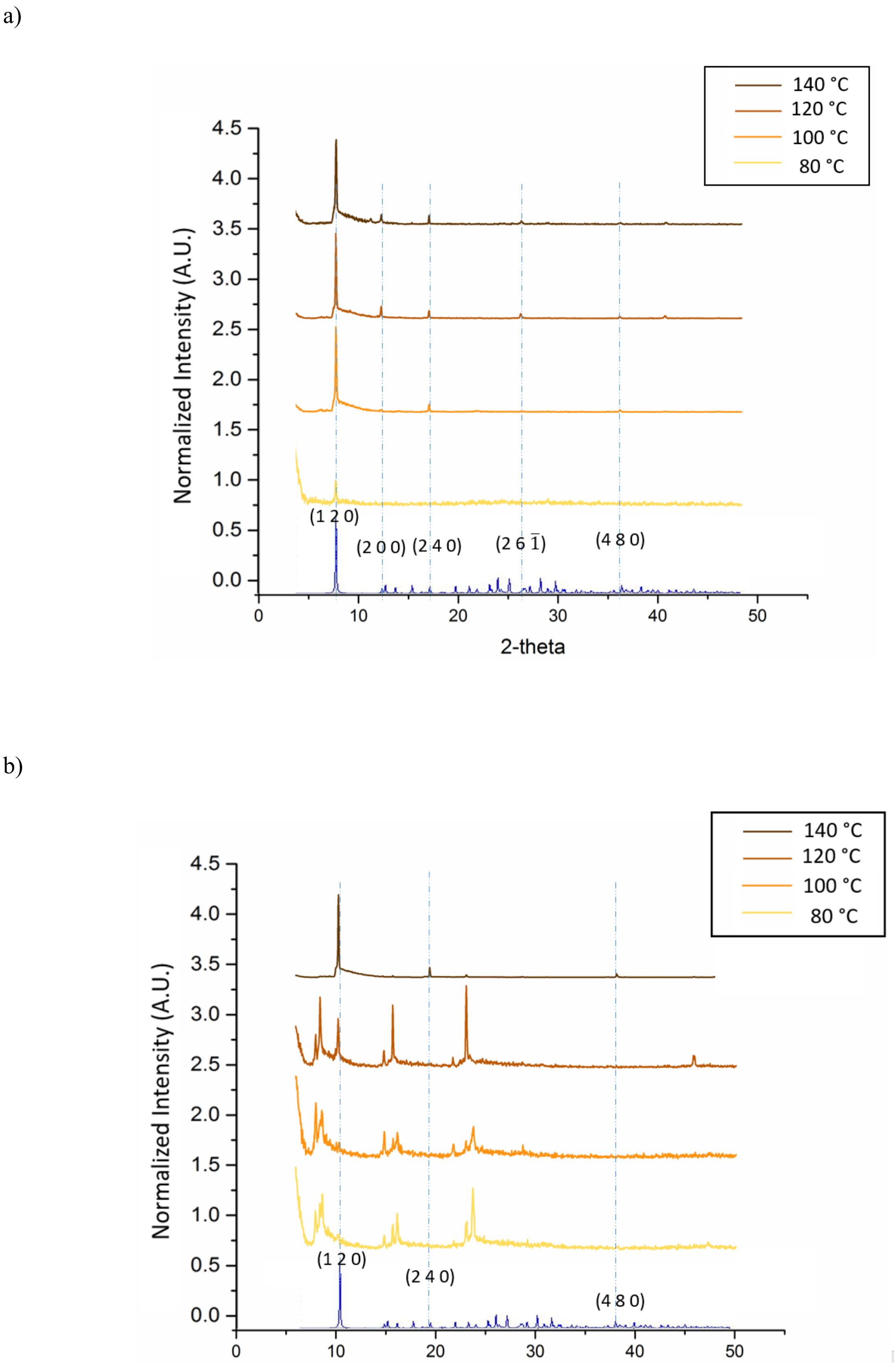

Figure 5.2 Powder XRD patterns for S-doped thin-films annealed under different temperatures with PyI : Bi(xt)$_3$ ratio of 1:3 (a) and 1:4 (b), with simulated powder XRD pattern of [PY]BiI$_4$ shown in blue for comparison.

5.2.1.2 Optical measurements

The band gap values of the thin films annealed at different temperatures were estimated via diffuse reflectance measurement. For both 1:3 and 1:4 precursor ratios, the bandgap energy decreases with the increase of annealing temperature. Similar bandgap values were obtained from the 1:3 ratio of precursors annealed above 100°C, whilst due to the incomplete formation of the final doped product at lower temperature, a steady band gap change under increasing temperature can be found for thin films deposited with 1:4 ratio of precursors (**Figure 5.3**). The resulting bandgap value of 1.55 eV strongly indicates S-doping of the **[PY]BiI$_4$** material. Compared to undoped **[PY]BiI$_4$ of 1.98 eV band gap value**, around 165 nm broader absorption of the solar spectrum can potentially occur and the tuned bandgap value is in the desirable range for a photovoltaic material according to the Shockley–Queisser limit.[15]

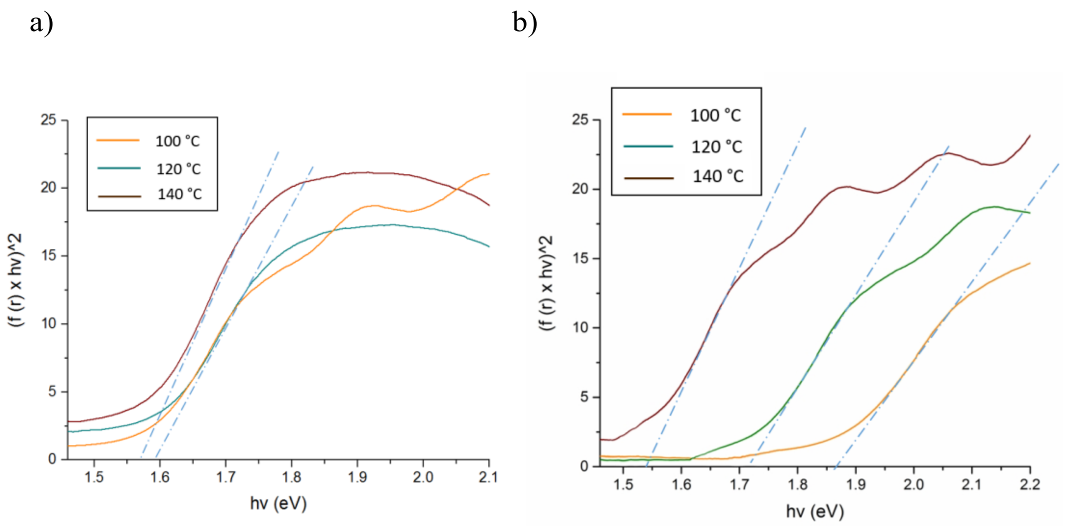

Figure 5.3 Tauc Plots of S-doped **[PY]BiI$_4$** thin films Under different annealing temperatures for films prepared from 1:3 (a) and 1:4 (b) precursor ratio.

5.2.1.3 XPS analysis

To further study the surface properties, XPS measurements were carried out for films produced from the 1:3 precursor ratio. The survey spectrum and valence band spectrum are shown in **Figure 5.4**, with high resolution spectra for bismuth 4f and I 3d shown in **Figure 5.5**. Binding energy of 158.7 eV and 164.0 eV can be found for Bi 4f 7/2 peak and Bi 4f 7/5 peak respectively. Binding energy of 619.6 eV and 631.1 eV are measured for I 3p 5/2 and I 3p 3/2 respectively. This indicates no chemical valence change has occurred after the sulfur doping. Small but noticeable 2s peaks can be found in between the bismuth peaks, proving the existence of S in the doped sample.

a)

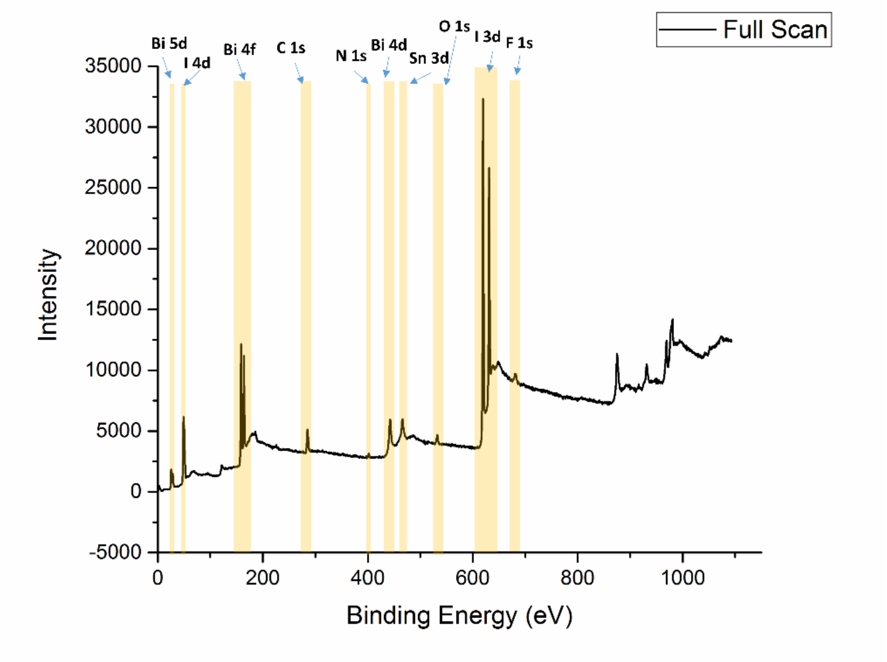

b)

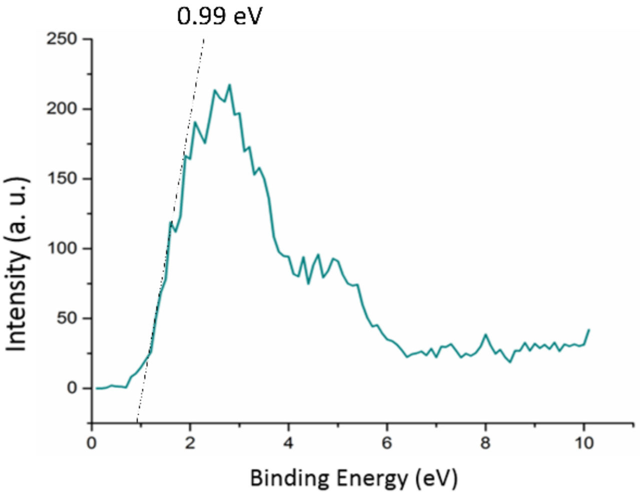

Figure 5.4 (a) Survey spectra and (b) valence band spectrum of S-doped **[PY]BiI$_4$** deposited on FTO (fluorine-doped tin oxide) conductive glass.

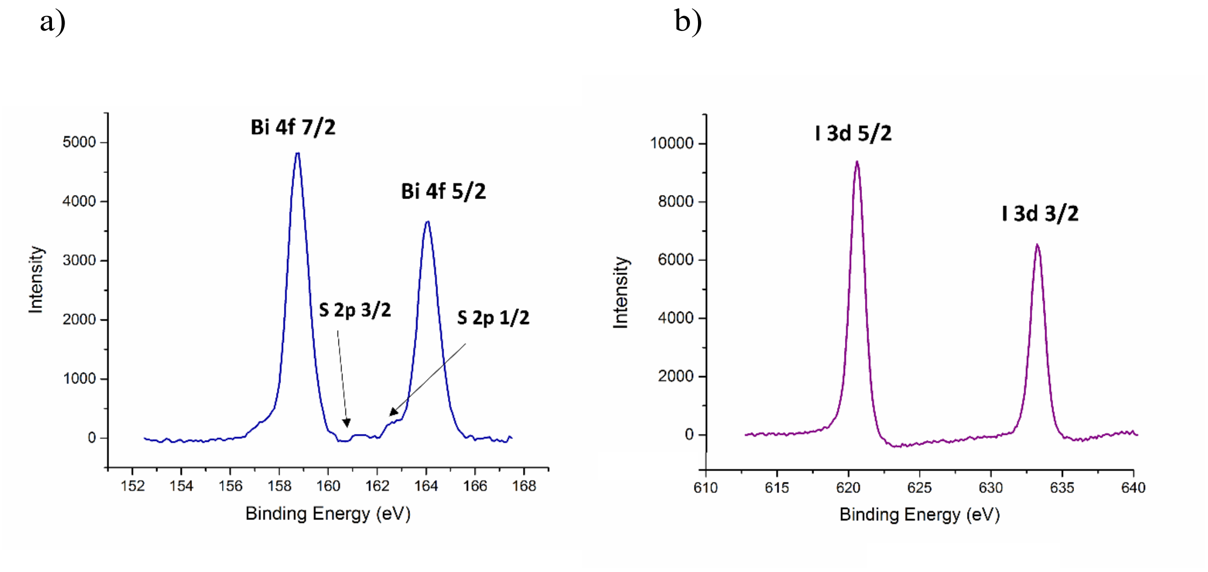

Figure 5.5 High resolution XPS spectra of (a) Bi 4f and S 2p, and (b) I 3d of S-doped **[PY]BiI$_4$** prepared from 1:3 precursor ratio.

5.2.1.3 Raman vibrational studies

Vibrational studies were carried out by Raman spectroscopy to investigate the bonding environment and compare the different vibrational modes between doped and undoped materials (**Figure 5.6, Table 5.1**). Laser light with wavelength of 785 nm was used for this study, which can penetrate through the thin-film sample. According to the experimental and computational vibrational studies in the literature,[16] peaks below 200 cm^{-1} are mostly assigned to I-Bi-I or Bi-I-Bi scissoring or Bi-I stretching. This is consistent with our study, where the strong vibrational intensity caused by Bi-I antisymmetric vibration mode at 133.5 cm^{-1} can be found in both S-doped and pristine [PY][BiI$_4$] samples. However, the weak Bi-I stretching mode at 103.0 cm^{-1} was missing or obscured after doping, with some new peaks found; the vibration at 115.3 cm^{-1} is attributed to stretching of the bridged iodines,[16,17] while the bands at 223.8 cm^{-1} and 285.5 cm^{-1} are attributed to Bi-S bonding mode according to the literature.[18] It is important to note that characteristic Bi-S vibrational modes at 238 cm^{-1} and 260 cm^{-1} in Bi_2S_3 lattice are not observed in our study,[18] which confirms that the low-energy absorption and XPS results are not caused simply by the presence of Bi_2S_3 impurity. The presence and shifting of Bi-S bonding modes demonstrate the successful partial incorporation of sulfur in the crystal lattice of **[PY]BiI$_4$**.

a)

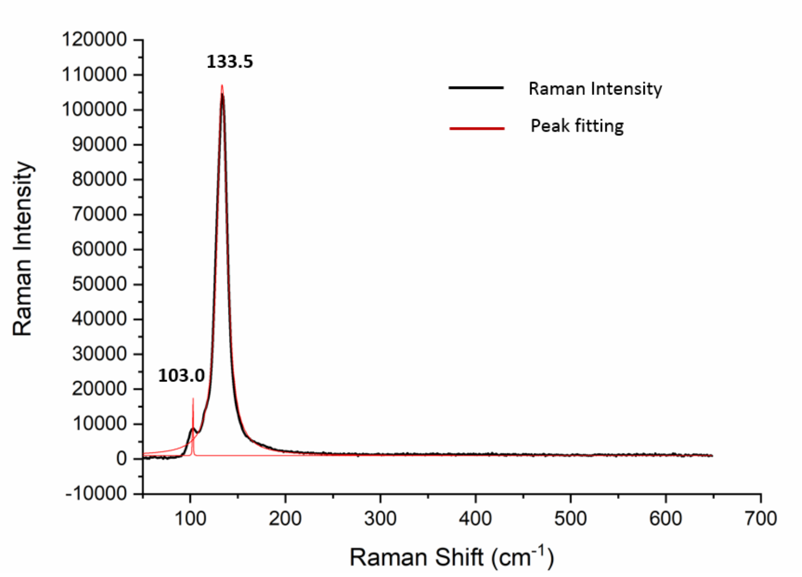

b)

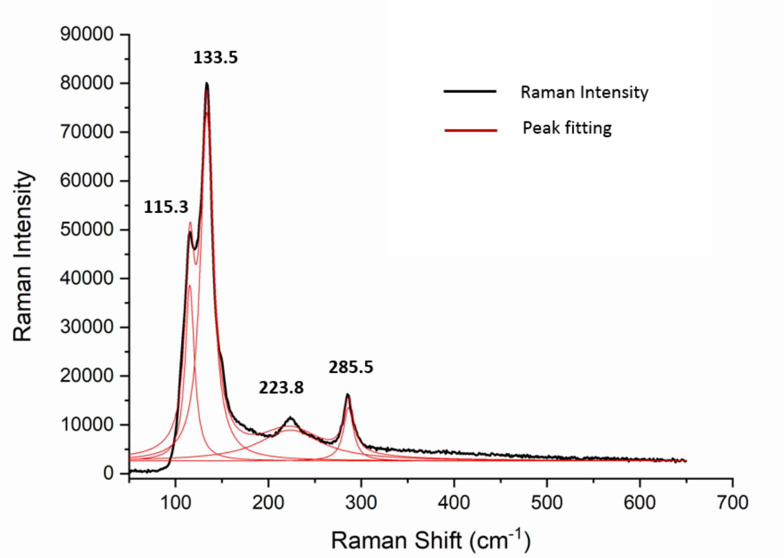

Figure 5.6. Raman spectra of (a) pristine **[PY][BiI₄]** and (b) S-doped **[PY]BiI₄** thin films under laser wavelength of 785 nm (1.58 eV). In both cases, data are in black with Lorentzian fitted peaks shown as red curves.

Table 5.1 Experimental wavenumbers (cm^{-1}) and assignment of vibrational spectra of **[PY][BiI₄]** and (b) S-doped **[PY]BiI₄**

Wavenumber (cm^{-1})	Assignment	Reference
103.0	ν (Bi–I)	19
115.3	ν (Bi–I)	19
133.5	ν (Bi–I)	20
223.8	ν (S-S)	21
285.5	ν (S-S)	21

ν = stretching mode

5.2.1.4 SEM and TEM studies

To investigate the film quality and morphology microscopically, we carried out SEM and TEM characterization for both **[PY]BiI$_4$** and S-doped **[PY]BiI$_4$** on FTO substrates. In the SEM images, hexagonal shaped crystals with dimensions around 1 μm can be seen from the original **[PY]BiI$_4$** film deposited on the FTO substrate, shown in **Figure 5.7** (**a**) and (**b**). The majority of crystals standing in an edge-on manner, which can be attributed to the contact between the **[PY]BiI$_4$** crystals and the FTO substrate. Similar characteristic hexagonal shaped crystals can be observed in S-doped **[PY]BiI$_4$** films. Compared to the SEM image of original **[PY]BiI$_4$** film where the dimension of crystallites are evenly distributed, S-doped **[PY]BiI$_4$** crystals show various dimensions ranging from 500 nm to 3 μm shown in **Figure 5.7** (**c**) and (**d**). The arrangement of the hexagonal S-doped **[PY]BiI$_4$** crystals is less ordered, as overlapping and fusing exist in the as-prepared film. This is potentially caused by the reaction rate competition of $Bi(xt)_3$ thermal decomposition and formation of S-doped **[PY]BiI$_4$** in the preparation process. However, the crystallinity is maintained and proven by the consistence of hexagonal characteristic in keeping with the PXRD data. To further confirm the crystallinity of S-doped **[PY]BiI$_4$** thin film, the as-deposited S-doped **[PY]BiI$_4$** was scratched from the thin film and loaded on copper/carbon fibre host before carrying out the TEM measurements. High crystallinity can be found from HRTEM surface profile image shown in **Figure 5.8** with a magnification of 5 nm. The crystalline pattern shown in the HRTEM corresponds to the 1D bismuth-iodine chain structure, with an inter-chain distance of 8.3 Å measured based on the scale bar of HRTEM image. This is consistent with the inter-chain distance measured from single crystal structure of **[PY]BiI$_4$** (**Figure 5.9**). In the EDS spectrum, peaks can be observed where expected for Sulfur, albeit difficult to clearly observe due to masking by bismuth. Overall, we can conclude that good crystallinity of thin films prepared from spin coating can be found after S-doping, and also the 1D crystal structure is maintained in the crystal lattice. This provides promising film quality for thin-film based third generation solar cells, with solution processability to enable large scale solar cell fabrication.

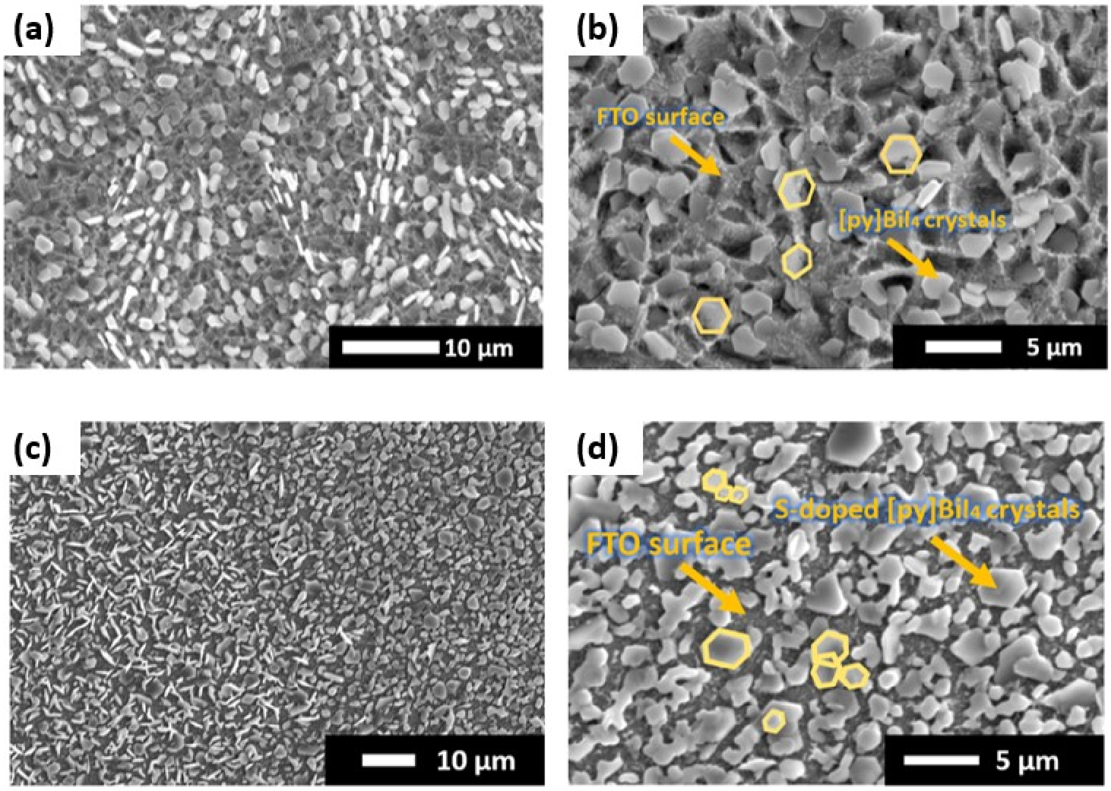

Figure 5.7 SEM images of (a) (b) original **[PY]BiI$_4$** and (c) (d) S-doped [PY]BiI$_4$ on FTO substrate. The surface of FTO substrate and the hexagonal-shaped **[PY]BiI$_4$** crystals are denoted and highlighted in yellow frames.

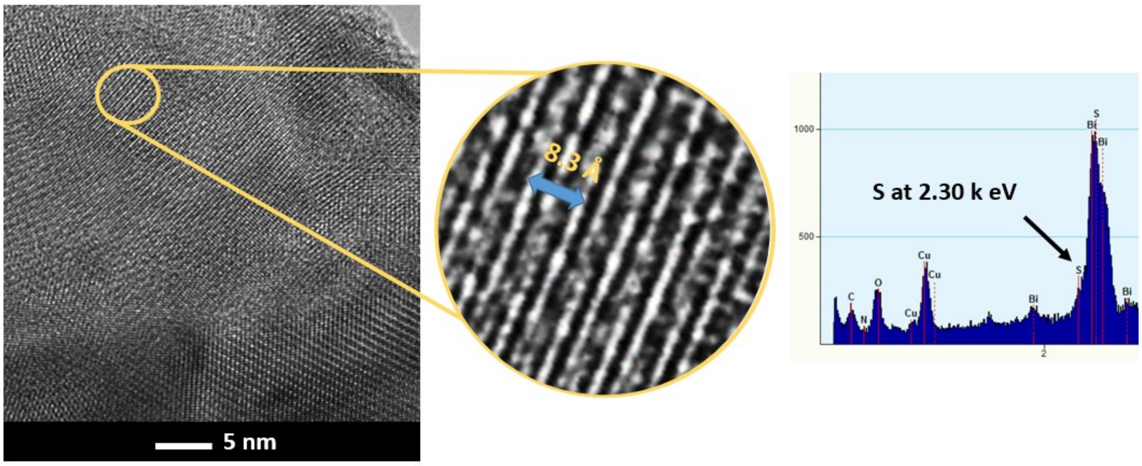

Figure 5.8. HRTEM surface profile images of S-doped **[PY]BiI$_4$** on carbon fibre with resolution of 5 nm, with area enlarged for inter-Bi-I chain distance measurement and corresponding EDS spectrum.

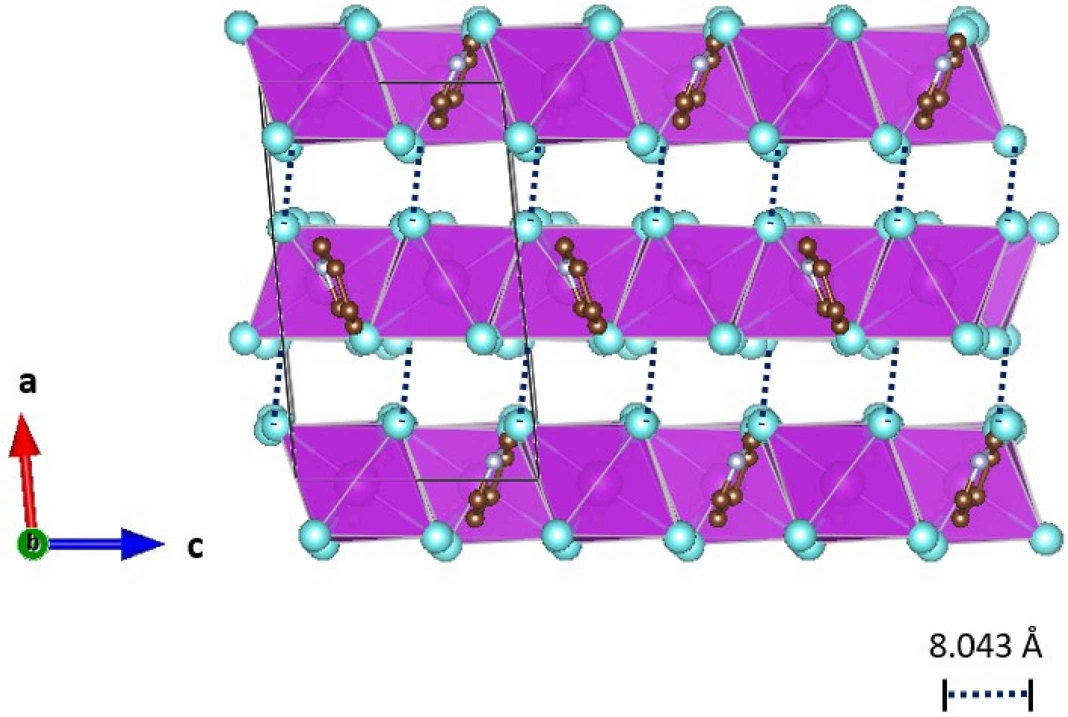

Figure 5.9 Bi-I inter-chain distance (black dashed lines) calculated from single crystal XRD, image generated from VESTA software.

5.2.1.5 Photo-generated current measurement

Photo-generated current measurement was carried out to study and compare the photo-response of **[PY]BiI$_4$** and sulfur-doped **[PY]BiI$_4$**. In order to examine if the bandgap engineering is favourable for photo-energy conversion, i.e., the performance under long wavelength irradiation, the photocurrent measurement was performed under filtered light. An acetone solution of **[PY]BiI$_4$** was used to filter the light and largely remove the wavelengths that can be absorbed by undoped **[PY]BiI$_4$**. The photocurrent measurement was carried out in a three-electrode system in 0.1M NaI aqueous electrolyte, with **[PY]BiI$_4$** or S-doped **[PY]BiI$_4$** on conductive FTO glass slides as working electrode, Pt wire was used as the counter electrode, and Ag/AgCl as the reference electrode. The photo-generated currents under different potential bias are shown in **Figure 5.10**. Anodic current can be observed for both materials, with increased current density as potential bias increases. Higher photocurrent density was observed for S-doped **[PY]BiI$_4$** than the undoped sample, especially under lower applied potentials.

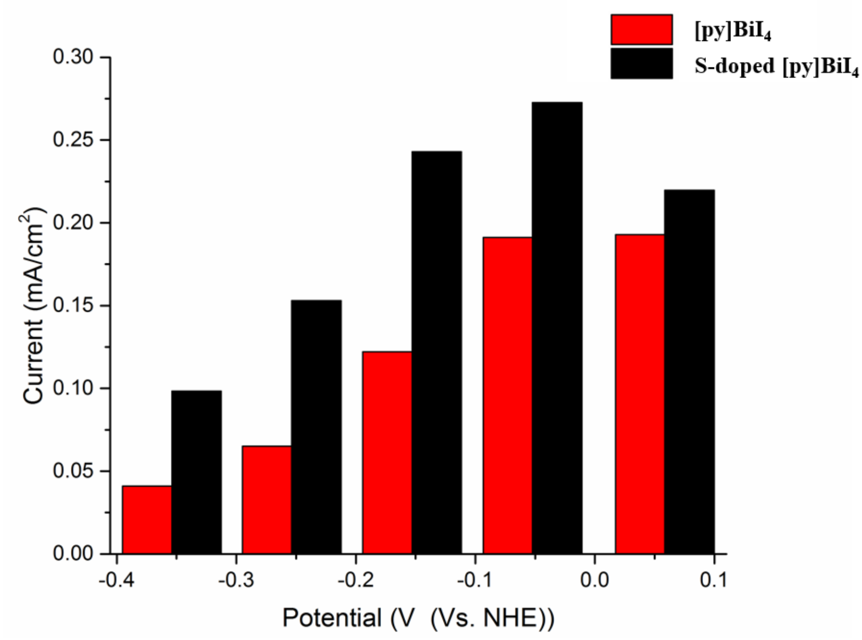

Figure 5.10 Photocurrent measurement of S-doped and un-doped **[PY]BiI4** under irradiation of wavelength over 576 nm. Working electrodes are made with glass/FTO/TiO_2/absorber material.

5.2.2 Band Gap Engineering of 0D $Cs_3Bi_2I_9$ via Dianion Substitution for photovoltaic applications

5.2.2.1 Synthesis and structural study of dianion doped thin films

CBI films were prepared by spin-coating onto mesoporous TiO_2 / FTO glass substrates. After annealing the as-formed CBI films, a drop casting followed by spin coating method was applied to introduce the dianions into the crystal lattice (**Figure 5.11**). Powder XRD patterns of treated CBI thin films alongside both untreated and theoretical CBI are shown in **Figure 5.12**. Since the ionic radii of I^- (220 pm) is different from $[SiF_6]^{2-}$ (259 pm), $[TiF_6]^{2-}$ (289 pm), and S (184 pm), substantial anionic exchange would lead to peak shift in the XRD pattern. However, no peak shifting was observed compared to the untreated CBI, which suggests only small uptake of the dianion without disturbing the original crystal structure. We note however, that the crystallinity of the films appears slightly poorer after treatment, suggested by lower peak intensity in the XRD pattern.

Figure 5.11 Schematic diagram of dianion-treated CBI thin film fabrication process

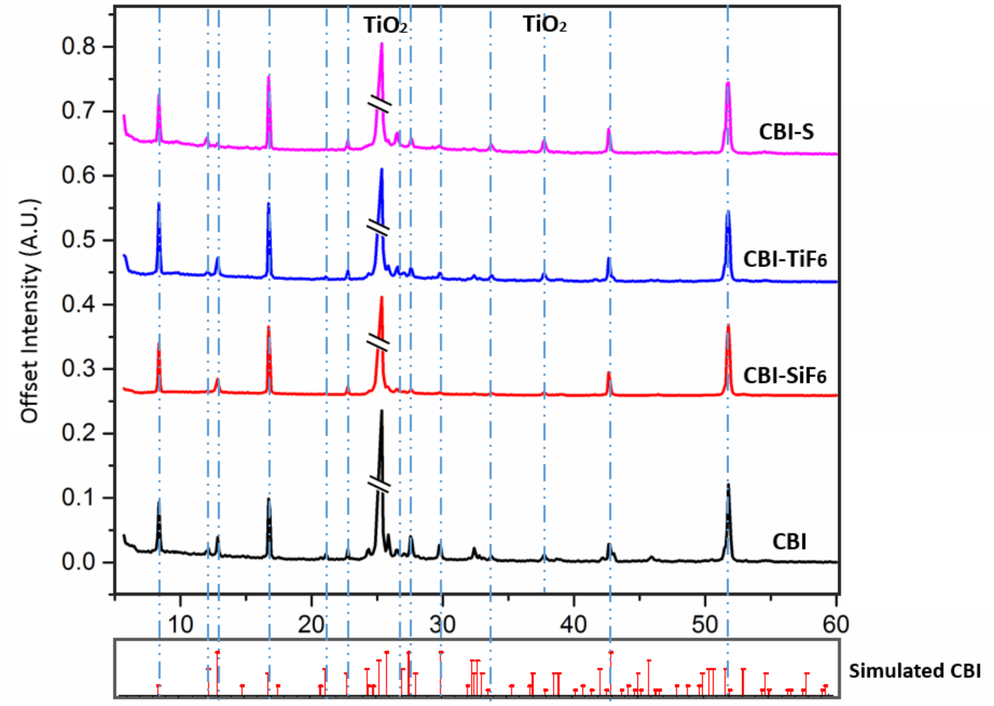

Figure 5.12 Powder XRD patterns of CBI and dianion treated CBI thin film on mesoporous TiO_2 / FTO glass substrates. Red bars: simulated powder XRD pattern of CBI; black curve: untreated CBI; red curve: $[SiF_6]^{2-}$ treated CBI; blue curve: $[TiF_6]^{2-}$ treated CBI; pink curve: S^{2-} treated CBI.

5.2.2.2 Optical measurement

UV-Vis diffuse reflectance for dianion treated films were measured to investigate their band gap change. The reflectance spectra were converted into Tauc plots, by plotting $(\alpha h\nu)^{1/2}$ against photon energy in eV, where α is the absorbance derived by the Kubelka-Munk function (Details can be found in Chapter 2). The Tauc plots for treated and as-prepared CBI are shown in **Figure 5.13**, with the thin-film colour and estimated band gap values shown on the right hand side. From the Tauc plots, it can be clearly seen that the band gap energy of the dianion substituted CBI materials has red shifted to lower values (1.80 – 1.87 eV) compared to untreated CBI (2.03 eV). The band gap shift can also be observed by the colour change of the thin films before (reddish orange) and after (brownish black) treatment. A significant shift of the band gap indicates that dianion treated materials have the potential to absorb a broader wavelength range for photo-to-current energy conversion.

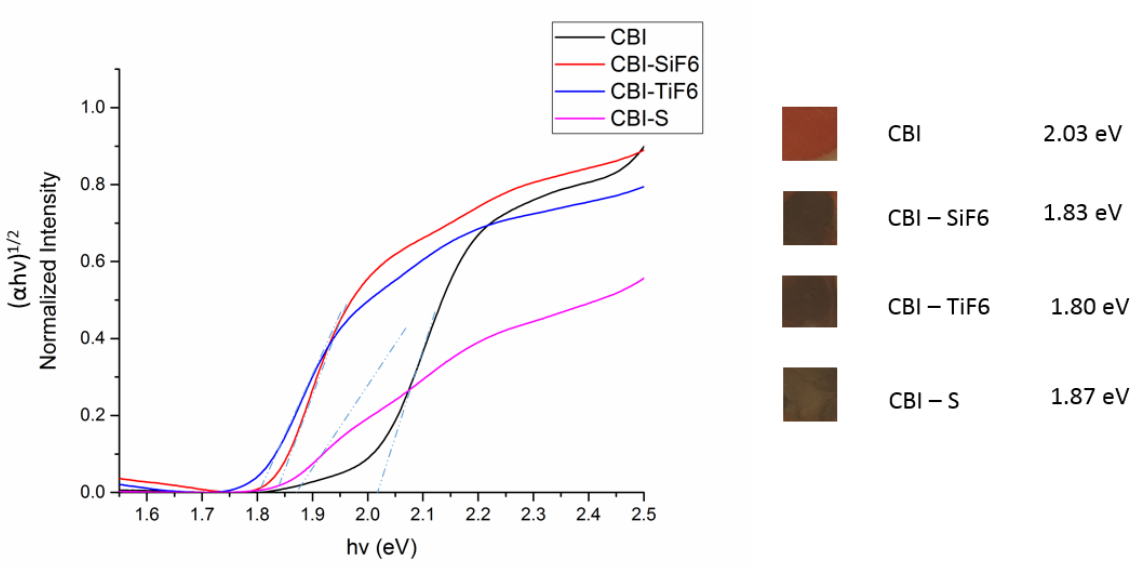

Figure 5.13 Tauc Plots of CBI and dianion treated CBI thin films on mesoporous TiO_2 / FTO glass substrates. Coloured blocks indicate the colour difference before and after dianionic treatment. Black: CBI; red: $[SiF_6]^{2-}$ treated CBI; blue: $[TiF_6]^{2-}$ treated CBI; magenta: S^{2-} treated CBI, with estimated band gap values of 2.03 eV, 1.83 eV, 1.80 eV and 1.87 eV respectively.

5.2.2.3 Raman vibrational studies

In addition to the optical investigations, Raman spectroscopy was carried out to determine the difference in vibrational modes of dianionic treated materials (**Figure 5.14, Table 5.2**). A 785 nm laser source was used for the measurement, which can penetrate around 10 μm into the sample (sample film thickness is about 1 μm). For iodobismuthate materials featuring Bi-I octahedra, wavenumbers below 200 cm^{-1} can be assigned to I-Bi-I, Bi-I-Bi scissoring or Bi-I stretching according the literature.[19] For untreated CBI, previous vibrational studies suggest that the three bridging and six terminal iodine atoms that exist in the $[Bi_2I_9]^{3-}$ octahedra lead to terminal stretches at 120 cm^{-1} (shoulder) and bridging stretches at 105 cm^{-1}.[20] This is consistent with our study. However, some differences can be found for the dianionic treated samples, with new vibrational peaks at 115-116 cm^{-1} and much weaker vibrational peaks 147-148 cm^{-1}. The former can be attributed to the stretching mode of Bi-I (bridging), and the latter to the Bi-I (terminal) according to both experimental and computational studies,[16] although we note that the gas-phase calculations on isolated species may have limitations as comparisons for measurements carried out for materials in the solid state. The changes in the vibrational modes of Bi-I indicate partial changes of Bi-I bonding environment, brought about by dianionic substitution. We note that extra peaks at 260 cm^{-1}, 278 cm^{-1} and 474 cm^{-1} can be found in the case of CBI-S, which arise from the presence of Bi_2S_3[18] and the evolution of sulfur (S_8),[21] while no other peaks can be observed at higher wavenumber for CBI-SiF_6 or CBI-TiF_6. Overall, the Bi-I stretching modes remain in the same spectral region for treated CBI films, while the specific differences found when comparing to the untreated CBI films can be attributed to partial dianionic substitution. The difference of vibrational mode before and after dianionic treatment stems from some disappearance of Bi-I terminal and bridging stretching modes, suggesting the partial substitution of iodide with dianions at specific site in $[Bi_2I_9]^{3-}$ binuclear octahedra.

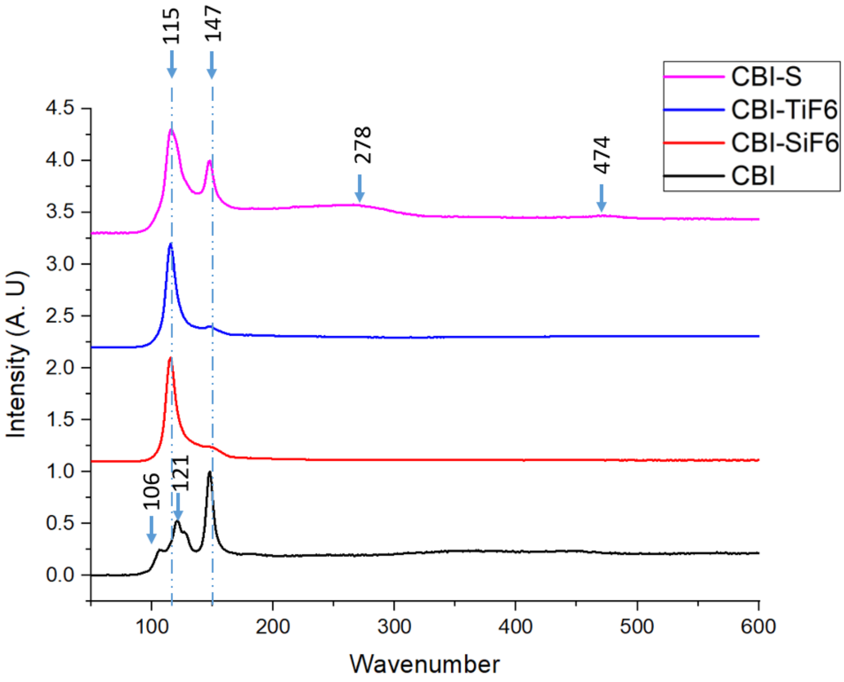

Figure 5.14 Raman spectra of CBI, CBI-SiF_6, CBI-TiF_6 and CBI-S respectively at room temperature, under laser wavelength of 785 nm (1.58 eV)

Table 5.2 Experimental wavenumbers (cm^{-1}) and assignment of vibrational spectra of CBI, CBI-SiF_6, CBI-TiF_6 and CBI-S.

Wavenumber (cm^{-1})	Compounds	Assignment	Reference
106	CBI	ν (Bi–I)	19
115	CBI-SiF_6, CBI-TiF_6 and CBI-S	ν (Bi–I)	19
121	CBI	ν (Bi–I)	22
147	CBI, CBI-SiF_6, CBI-TiF_6 and CBI-S	ν (Bi–I)	22
278	CBI-S	ν (S-S)	21
474	CBI-S	ν (S-S)	21

ν = stretching mode

5.2.2.4 SEM

SEM measurements allow us to analyse the thin-film quality and make direct comparison of crystallinity before/after the dianionic treatment. The original CBI crystallizes in a disc-shaped manner with the crystallite sizes ranging from 3.8 μm to 6.8 μm. Both edge-on and flat discs can be observed, with a medium coverage on the mesoporous TiO_2 substrate (**Figure 5.15a**). Compared to the original CBI film, there are no obvious changes in terms of the crystalline dimension distribution and coverage (**Figure 5.15b, c** and **d**). There is no amorphous material present in the SEM images.

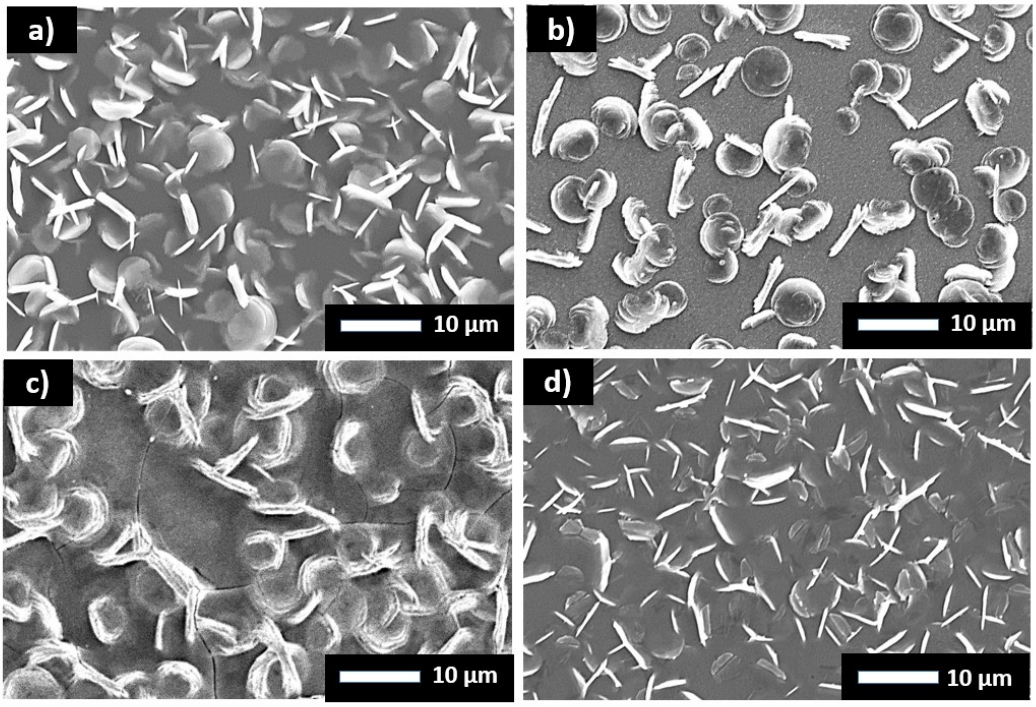

Figure 5.15 SEM images of (a) original CBI, (b) CBI-SiF6, (c) CBI-SiF6 and (d) CBI-S films on FTO/meso-TiO_2 substrate.

5.2.2.5 XPS analysis

Elemental composition and the bonding characteristics around the bismuth atoms have been investigated by X-ray photoelectron spectroscopy (XPS). The survey spectrum of each material indicates the existence of Bi, I, Cs, Ti and O atoms. Ti and O are from the mesoporous TiO_2 layer as substrate, F can be found in both CBI-SiF_6 and CBI-TiF_6, while S exclusively exists in CBI-S (**Figure 5.16**, **Figure 5.17**). However, due to the low concentration of Si, the peak for Si 2p is not observable in CBI-SiF_6. High resolution spectra of bismuth 4f are shown in **Figure 5.18**, where S 2p peaks fall in the same region as bismuth 4f shown in **Figure 5.18c**. Gaussian fitting was used to further the bismuth 4f peak analysis, showing a different bonding environment of the bismuth 4f orbitals for the dianion-treated materials. Specifically, in both CBI-SiF_6 and CBI-TiF_6 films, small shifting of the Bi 4f 5/2 peak can be found, with lower binding energy than the Bi-I peak in CBI. The changes, attributed to differences of electronegativity of the anions, in Bi-[SiF_6] and Bi-[TiF_6] bonding formed after treatment are indicated in Figure 5.19 b and c respectively. For CBI-S, both Bi 4f 7/2 and 4f 5/2 peaks are asymmetric, attributed to the existence of both Bi-S bonding and Bi-I bonding. In addition, evidence of the elemental Sulfur can be seen in between bismuth 4f 7/2 and 4f 5/2peaks. From the high resolution Bi 4f XPS spectra analysis, we can conclude that Bi-S, Bi-SiF_6 and Bi-TiF_6 bonds are formed during the treatment, likely by substituting two iodine atoms with one dianion. Valence band cut-off energy is redshifted after the dianionic treatment in each case, shown in **Figure 5.19**. A small but noticeable presence of metallic bismuth can also be seen in the CBI sample. Such reduction of bismuth was also reported in previous studies,[19] which is potentially due to the vacuum environment during the XPS measurement. High resolution spectra of I, F and Si can be found in **Figure 5.18**.

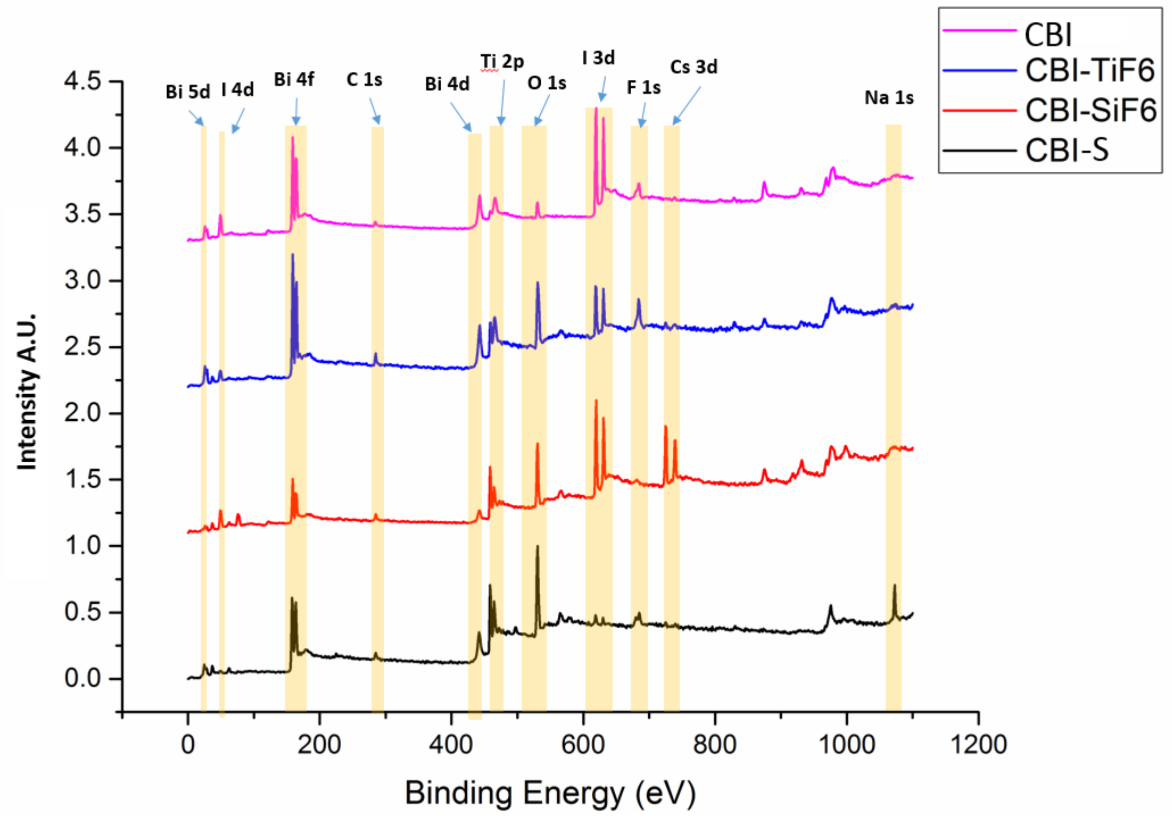

Figure 5.16 XPS survey spectra of CBI (magenta), CBI-TiF_6 (blue), CBI-SiF_6 (red) and CBI-S (black) as thin films deposited on TiO_2

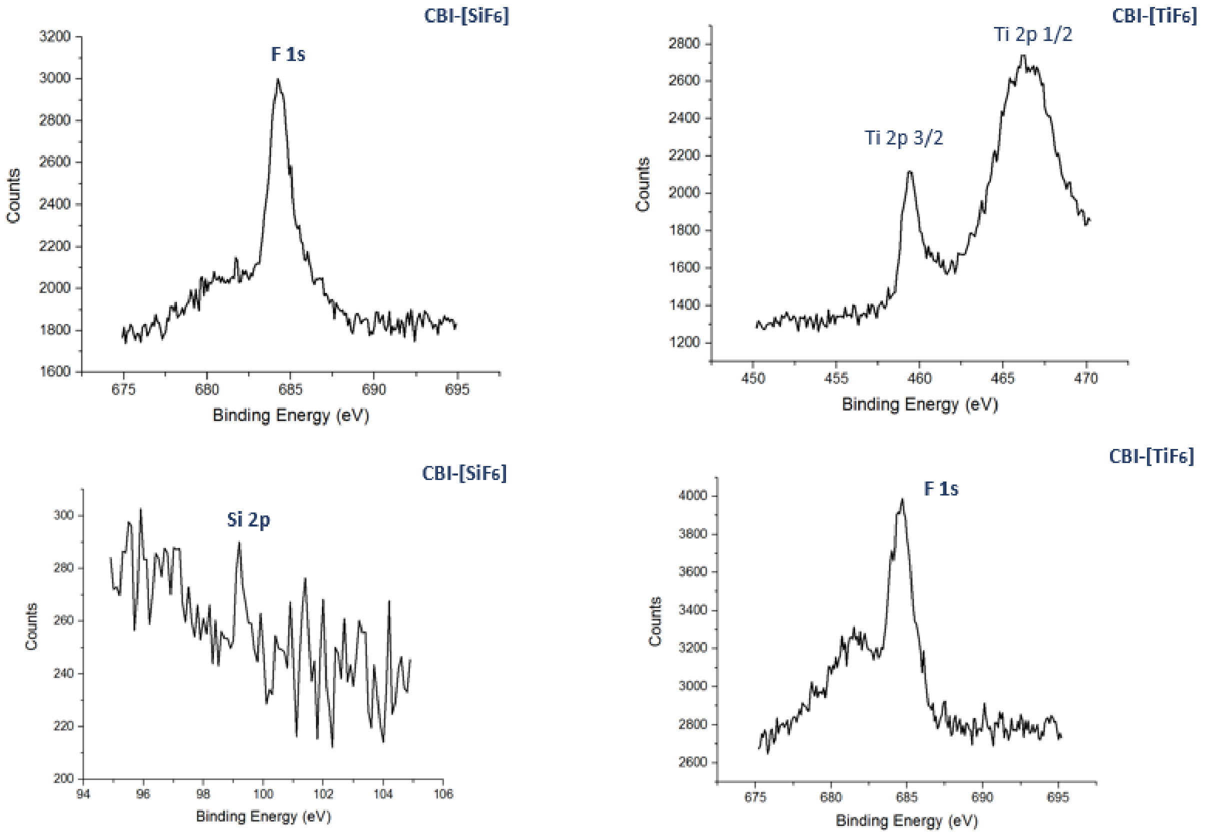

Figure 5.17 High resolution XPS spectra for F 1s in CBI-SiF$_6$ (a), Ti 2p in CBI-TiF$_6$ (b), Si (2p) in CBI-SiF$_6$ (c) and F 1s in CBI-S (d).

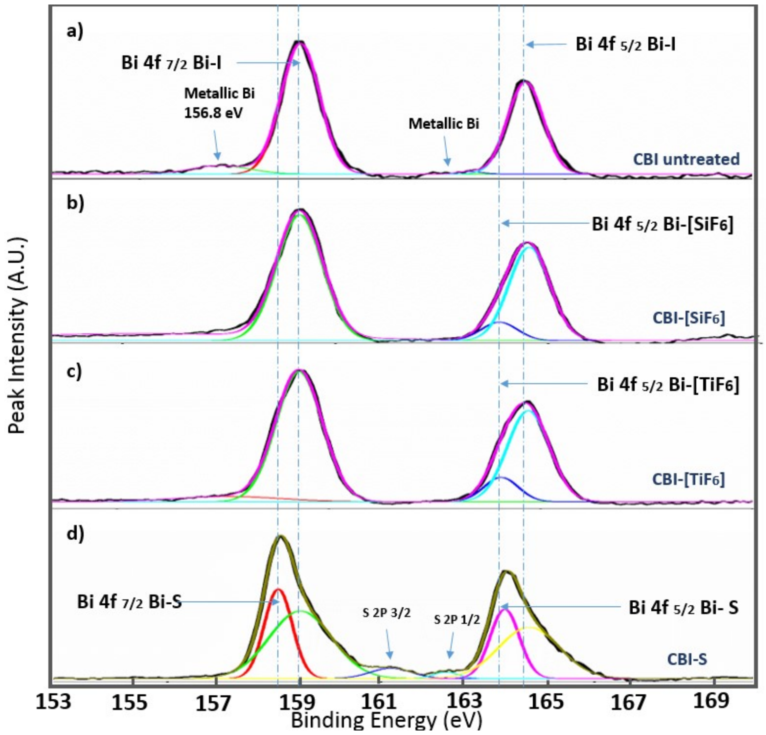

Figure 5.18 High resolution XPS spectra of bismuth 4f orbitals measured on thin films of CBI and treated CBI: a) untreated CBI; b) CBI treated with $[SiF_6]^{2-}$; c) CBI treated with $[TiF_6]^{2-}$; d) CBI treated with S^{2-}.

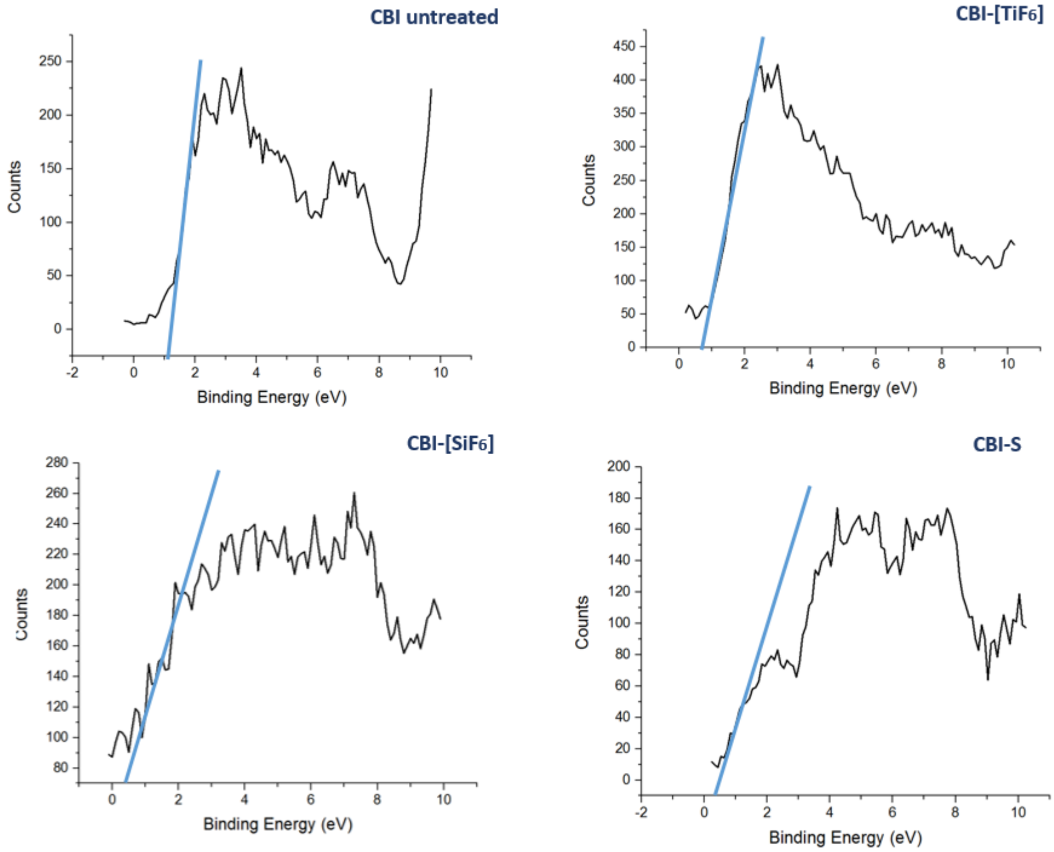

Figure 5.19 Valence band spectra of each material as indicated, redshift can be observed for dianionic treated materials.

5.2.2.6 Photo-generated current measurement

In order to study the photo response of the dianion-treated thin films, photo-generated current measurements were carried out in a three-electrode system. CBI and treated-CBI as thin films on conductive glass were used as working electrodes, and 1 mM CBI acetone solution was used as a light filter to only allow the irradiation in the long wavelength range (over 560 nm) to pass. Overall, the photocurrent density of all materials increased with increasing applied bias potential to -0.1 V (against NHE), with much higher current density observed for CBI-SiF$_6$ and CBI-TiF$_6$ as working electrodes (**Figure 5.20**). This suggest that $[SiF_6]^{2-}$ and $[TiF_6]^{2-}$ anionic doped films with darker colour can facilitate improved photo-to-current conversion under longer wavelength irradiation. No improvement however, was observed for S^{2-} doped films under filtered long wavelength light, even though they display a smaller bandgap value. This may be related to the appearance of elemental sulfur indicated by both Raman and XPS spectroscopy, perhaps suggesting less efficient incorporation of dianionic sulphur into the lattice.

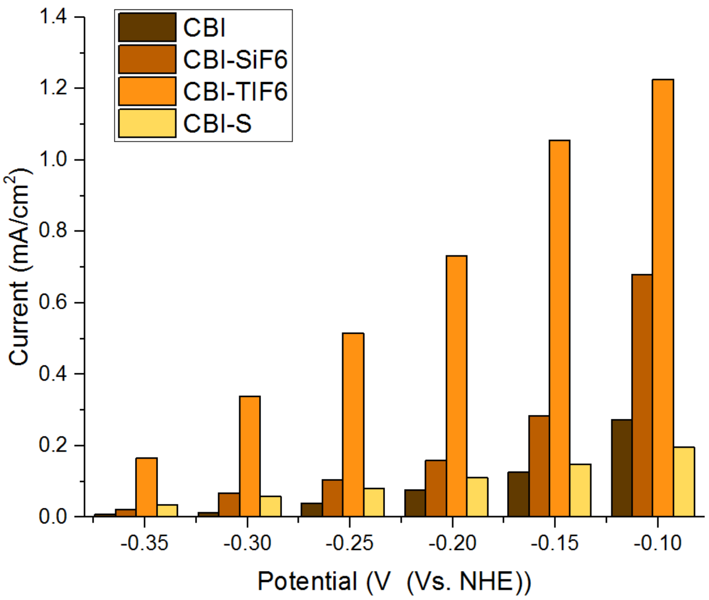

Figure 5.20 Photo-generated current vs. applied potential for three-electrode system in an electrolyte of 0.1 M NaI aqueous solution under irradiation of wavelength over 560 nm. Working electrodes were made with glass/FTO/TiO_2/CBI (and dianionic treated CBI).

5.3 Conclusions

Bandgap engineering has been achieved for 1D [PY]BiI_4 material via a sulfur doping method, where low bandgap material was formed from $Bi(xt)_3$ thermal decomposition and partially substituting the iodine atoms. The band gap energy has been tuned from 1.95 eV to 1.55 eV, which is ideal as a solar photovoltaic material. No crystal structure change has been observed from thin-film XRD measurement, while a different bonding environment for Bi was shown by Raman spectroscopy, suggesting a small uptake of sulfur as dopant. HRTEM images show S-doped [PY]BiI_4 has high crystallinity, presenting an observable 1D chain structure. Improved photo-response was manifested for S-doped [PY]BiI_4 under long wavelength radiation, supported by the photocurrent measurement. The bandgap engineering method is favourable for tuning the optoelectrical properties of higher bandgap iodobismuthate materials, which also sheds light on the material optimization of lead-free perovskite-like photovoltaic materials.

We have also demonstrated facile bandgap engineering by dianionic substitution for 0-dimensional light absorber CBI. The bandgap value of CBI has decreased from over 2.0 eV to around 1.8 eV, with colour change from orange to brownish black. Powder XRD measurements showed no crystal structure change after the treatment, however XPS and Raman spectroscopy indicate that the bonding properties of Bi-I octahedral have changed after the dianionic treatment, where the dianions are partially incorporated. Finally, photocurrent measurements under long wavelength irradiation have been carried out, which demonstrated that CBI films treated with $[SiF_6]^{2-}$ and $[TiF_6]^{2-}$ anions are capable of generating much higher photocurrent density at longer wavelengths. This method provides a facile route to dianion treatment for bandgap engineering, showing that $[SiF_6]^{2-}$ and $[TiF_6]^{2-}$ can lower the high-bandgap of bismuth-halide photovoltaic materials.

5.4 References

1 A. J. Lehner, D. H. Fabini, H. A. Evans, C.-A. Hébert, S. R. Smock, J. Hu, H. Wang, J. W. Zwanziger, M. L. Chabinyc and R. Seshadri, *Chem. Mater.*, 2015, **27**, 7137–7148.

2 J. K. Pious, M. L. Lekshmi, C. Muthu, R. B. Rakhi and V. C. Nair, *ACS Omega*, 2017, **2** (9), 5798-5802.

3 R. L. Z. Hoye, R. E. Brandt, A. Osherov, V. Stevanovic, S. D. Stranks, M. W. B. Wilson, H. Kim, A. J. Akey, J. D. Perkins, R. C. Kurchin, J. R. Poindexter, E. N. Wang, M. G. Bawendi, V. Bulovic and T. Buonassisi, *Chem. A Eur. J.*, 2016, **22**, 2605–2610.

4 B. W. Park, B. Philippe, X. Zhang, H. Rensmo, G. Boschloo and E. M. J. Johansson, *Adv. Mater.*, 2015, **27**, 6806–6813.

5 Z. Zhang, X. Li, X. Xia, Z. Wang, Z. Huang, B. Lei and Y. Gao, *J. Phys. Chem. Lett.*, 2017, **8** (17) 4300-4307.

6 T. Li, Q. Wang, G. S. Nichol, C. A. Morrison, H. Han, Y. Hu and N. Robertson, *Dalt. Trans.*, 2018, **47**, 7050–7058.

7 T. Li, Y. Hu, C. Morrison, W. Wu, H. Han and N. Robertson, *Sustain. Energy Fuels*, 2017, **1**, 308–316.

8 E. T. McClure, M. R. Ball, W. Windl and P. M. Woodward, *Chem. Mater.*, 2016, **28**, 1348–1354.

9 A. H. Slavney, T. Hu, A. M. Lindenberg and H. I. Karunadasa, 2016, **3**, 3–6.

10 F. Wei, Z. Deng, S. Sun, F. Xie, G. Kieslich, D. M. Evans, M. A. Carpenter, P. D. Bristowe and A. K. Cheetham, *Mater. Horiz.*, 2016, **3**, 328-332.

11 E. Greul, M. L. Petrus, A. Binek, P. Docampo and T. Bein, *J. Mater. Chem. A*, 2017, **5**, 19972–19981.

12 I. Turkevych, S. Kazaoui, E. Ito, T. Urano, K. Yamada, H. Tomiyasu, H. Yamagishi, M. Kondo and S. Aramaki, *ChemSusChem*, 2017, **10**, 3754–3759.

13 M. Vigneshwaran, T. Ohta, S. Iikubo, G. Kapil, T. S. Ripolles, Y. Ogomi, T. Ma, S. S. Pandey, Q. Shen, T. Toyoda, K. Yoshino, T. Minemoto and S. Hayase, *Chem. Mater.*, 2016, **28**, 6436–6440.

14 A. J. Maclachlan, F. T. F. O'Mahony, A. L. Sudlow, M. S. Hill, K. C. Molloy, J. Nelson and S. a. Haque, *ChemPhysChem*, 2014, **15**, 1019–1023.

15 W. Shockley and H. J. Queisser, *J. Appl. Phys.*, 1961, **32**, 510–519.

16 J. Laane and P. W. Jagodzinski, *Inorg. Chem.*, 1980, **19**, 44–49.

17 C. Hrizi, A. Samet, Y. Abid, S. Chaabouni, M. Fliyou and A. Koumina, *J. Mol. Struct.*, 2011, **992**, 96–101.

18 S. Kharbish, E. Libowitzky and A. Beran, *Eur. J. Mineral.*, 2009, **21**, 325–333.

19 S. Öz, J.-C. Hebig, E. Jung, T. Singh, A. Lepcha, S. Olthof, F. Jan, Y. Gao, R. German, P. H. M. van Loosdrecht, K. Meerholz, T. Kirchartz and S. Mathur, *Sol. Energy Mater. Sol. Cells*, 2016, **158**, 195–201.

20 F. Cariati, G. Marcotrigiano, L. Menabue, F. Morazzoni, G. C. Pellacani and G. M. Zanderighi, *Spectrochim. Acta Part A Mol. Spectrosc.*, 1978, **34**, 801–805.

21 O. El Jaroudi, E. Picquenard, N. Gobeltz, A. Demortier and J. Corset, *Inorg. Chem.*, 1999, **38**, 2917–2923.

22 Z. Ma, S. Peng, Y. Wu, X. Fang, X. Chen, X. Jia, K. Zhang, N. Yuan and N. Dai, *Physica B*, 2017, **526,** 136–142

Chapter 6

Study of $Bi_{13}S_{18}I_2$ and thiourea bismuth iodide as electrode materials for supercapacitor applications

6.1 Introduction and research proposal

Electric double-layer capacitors (EDLCs) are best known for their fast charge-discharge cycles, high power densities, long life cycles, and greater energy densities compared to conventional capacitors.[1] However, EDLCs typically suffer from poorer energy densities compared to so-called pseudo-capacitors or conventional batteries that employ strong Faradaic reactions to chemically store charge.[2] Consequently, there has been a recent wave of research efforts directed toward advancing the energy densities of environmentally-benign, economical, and durable electrode materials for EDLC applications in order to enhance their commercial viability without sacrificing long-life cycle stability.

Bismuth-based electrode materials featuring low-cost and high-stability have attracted lots of research attention. Bismuth chalcogenides including Bi_2S_3 and Bi_2O_3 have been widely studied and applied as high-performing active electrode materials intended as supercapacitors, albeit typically with substantial Faradaic mechanism.[3] On the other hand, bismuth chalcohalides have often been overlooked as potential energy storage materials. In the first part of this chapter, a relatively unexplored bismuth chalcohalide material, $Bi_{13}S_{18}I_2$, will be discussed both in the synthetic route and its device performance. Traditionally, such materials are fabricated under high pressure and high temperature conditions requiring long reaction times.[4–6] A facile and solution-processed synthetic route to $Bi_{13}S_{18}I_2$ would be desirable for the supercapacitor electrode preparation and potentially large-scale industrial production. Conducting a combination of cyclic voltammetry (CV) and galvanostatic charge-discharge measurement, we can study the device capacitance performance and also probe the charge storage mechanism. Electrochemical impedance spectroscopy (EIS) studies will be carried out subsequently, to further understand the device response to an applied AC current at various frequencies.

At the same time, studies on hybrid metal-halide materials for supercapacitor applications have recently drawn attention . A literature report using $MAPbI_3$ perovskite as the active electrode material in a symmetric planer-structured electrochemical capacitor has shown a capacitance of 4.6 μF/cm^2 with limited device stability.[7] Due to the concern over lead's toxicity, bismuth was used as a substitute for lead, forming bismuth-halide perovskite-like materials. In this regard, zero-dimensional MBI (methylammonium bismuth iodide) has been reported as a promising electrode material for symmetrical electrochemical capacitors, achieving an areal capacitance of 5.5 mF/cm^2 with 84.8% performance retained after 10,000 cycles.[8] Additionally, studies in Chapter 4 on [AT][BiI_4] have also shown capacitance effect in a carbon-based solar cell device.[9] These studies indicate that hybrid Bi-based materials are of great research interest to be further explored for energy storage applications. The second part of this chapter is focused on the crystal structure, supercapacitor device performance and mechanistic probing of a novel Bi-based electrode material, thiourea bismuth iodide (TBI).

6.2 Results and Discussion

6.2.1 Facile Synthesis and Characterization of $Bi_{13}S_{18}I_2$ Films as a Stable Supercapacitor Electrode Material

6.2.1.1 Solution-based $Bi_{13}S_{18}I_2$ synthetic route

The initial solution-processed synthetic route and material characterization for $Bi_{13}S_{18}I_2$ on glass substrates were carried out by Alba Franco Gonzalez, who was a project student in our group working with the author. $Bi_{13}S_{18}I_2$ was synthesised via thermal decomposition of a precursor solution containing bismuth xanthate ($Bi(xt)_3$), a sulfur-containing organobismuth material, and BiI_3. $Bi(xt)_3$ was synthesized from potassium xanthate and bismuth nitrate in a one-step reaction previously reported by Vigneshwaran and colleagues (Scheme 6.1).[10] A $Bi(xt)_3$:BiI_3 molar ratio of 18:1 was utilized for precursor solution preparation, using DMF as the solvent. The as-prepared solution was spin-coated onto the glass substrate, forming a thin film which was subsequently annealed at 150°C on a hot plate for 30 minutes. We note that $Bi_{13}S_{18}I_2$ has been previously reported as $[Bi(Bi_2S_3)_9I_3]_{2/3}$[5] and $Bi_{19}S_{27}I_3$,[4,11] prompting Groom and colleagues to reconsider the crystal structure and propose the formula $Bi_{13}S_{18}I_2$,[12] which we adopt in our study. $Bi_{13}S_{18}I_2$ contains $[Bi_2]^{4+}$ dimers, which justifies the close proximity of the bismuth cations positioned at the origin of the unit cell. The crystal structure of $Bi_{13}S_{18}I_2$ is shown in **Figure 6.1**, where one of the Bi site is disordered with an occupancy factor of 0.25.

Scheme 6.1. Synthesis of $Bi_{13}S_{18}I_2$ from different ratios (a:b) of a $Bi(xt)_3$:BiI_3 precursor solution.

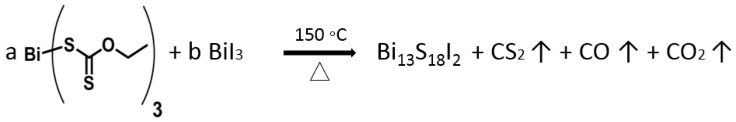

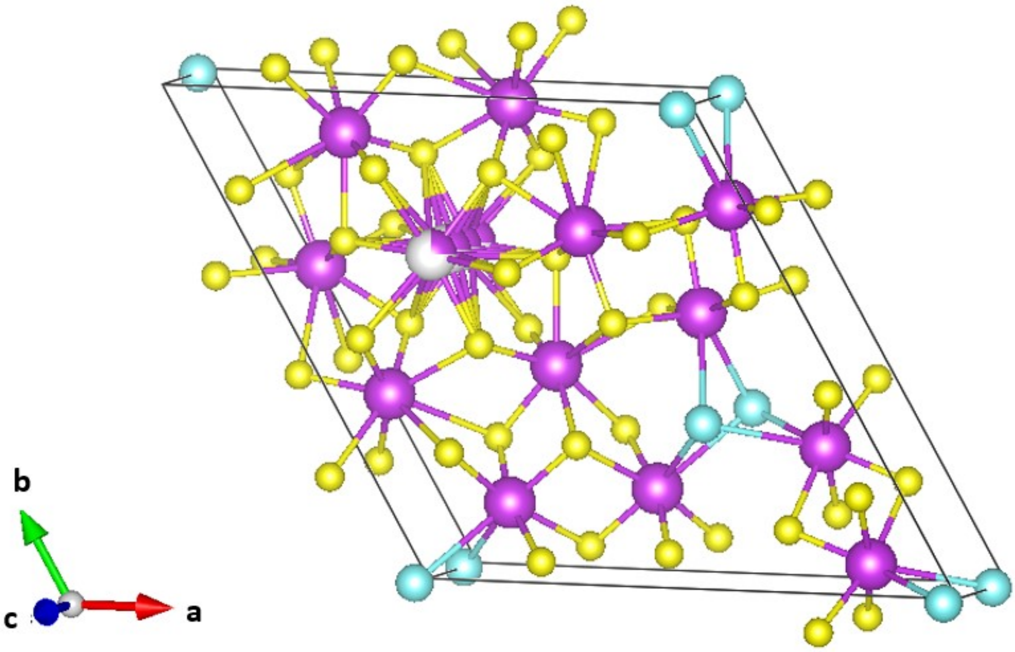

Figure 6.1 The crystal structure of $Bi_{13}S_{18}I_2$ unit cell presented Bismuth magenta; Iodine: cyan; Sulfur: yellow. The disordered bismuth is shown in grey/magenta with an occupancy factor of 0.25.[12]

6.2.1.2 Electrode preparation

The performance of $Bi_{13}S_{18}I_2$ as the active electrode material in an EDLC-type symmetric supercapacitor was evaluated using cyclic voltammetry (CV), galvanostatic charge-discharge, and electrochemical impedance spectroscopy (EIS). The $Bi_{13}S_{18}I_2$-based electrodes were fabricated with a facile, single-step, and solution-processable procedure, based on that developed in our group to deposit films of this material on glass. An 18:1 mixture of $Bi(xt)_3$ and BiI_3 was combined with activated charcoal and polytetrafluoroethylene (PTFE) powder and dispersed in DMF in sufficient relative amounts to form a 85:10:5 weight ratio of $Bi_{13}S_{18}I_2$: charcoal: PTFE upon subsequent thermal decomposition of the $Bi(xt)_3$. This heterogeneous solution was then drop-cast on 1 cm^2 section of carbon cloth and heated at 150 °C to achieve a high mass loading of approximately 8-10 mg cm^{-2} on each electrode. Although the $Bi_{13}S_{18}I_2$ constitutes the primary active material for the supercapacitor electrodes, the activated charcoal and PTFE are added for enhanced electrical conductivity and mechanical stability respectively of the overall layer. The powder XRD pattern of as-prepared $Bi_{13}S_{18}I_2$ electrode is shown in **Figure 6.2**, which matches the theoretical XRD pattern[12]. A thin (25µm) microporous membrane (Celgard 3501) previously soaked in a saturated $NaClO_4$ (aq.) electrolytic solution was sandwiched between two of these as-coated electrodes, and the entire set-up was assembled in a standard capacitor test cell (ECC-std, EL-CELL GmbH) for tight packing and ease of measurement (Figure 6.3a). The SEM images of the as-prepared electrodes show good coverage of the underlying carbon cloth with the activated $Bi_{13}S_{18}I_2$ material, with rod-shaped $Bi_{13}S_{18}I_2$ layering on top of the carbon cloth as well as binding directly to the carbon fibres (**Figure 6.3b**).

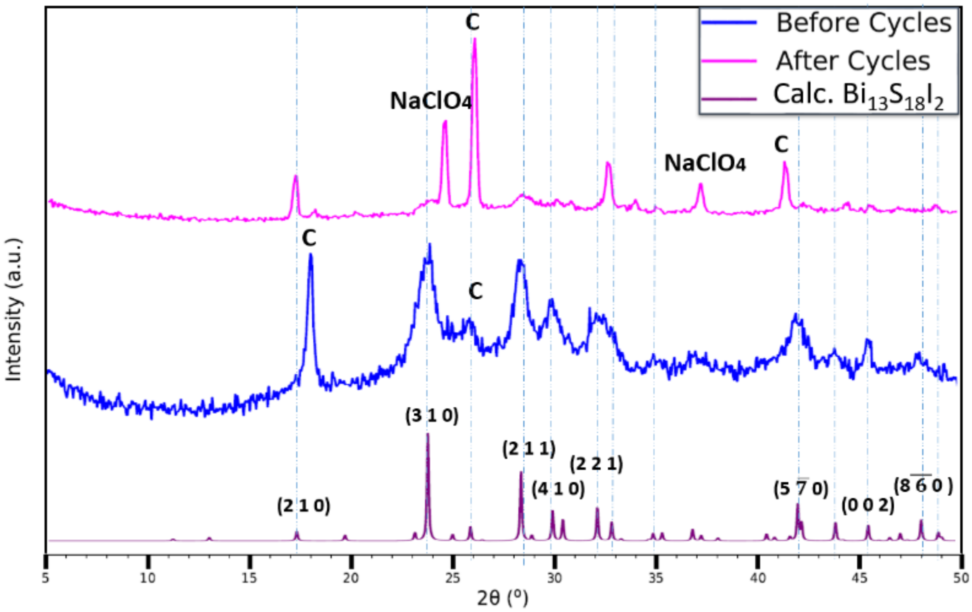

Figure 6.2 Powder XRD patterns of (blue) as-prepared $Bi_{13}S_{18}I_2$ electrode on carbon cloth with PTFE and activated charcoal as additives, (magenta) $Bi_{13}S_{18}I_2$ electrode after 5000 cycles stability test and (purple) calculated powder XRD pattern of $Bi_{13}S_{18}I_2$, Carbon peaks assigned after ICDD PDF 00-056-0159.

a)

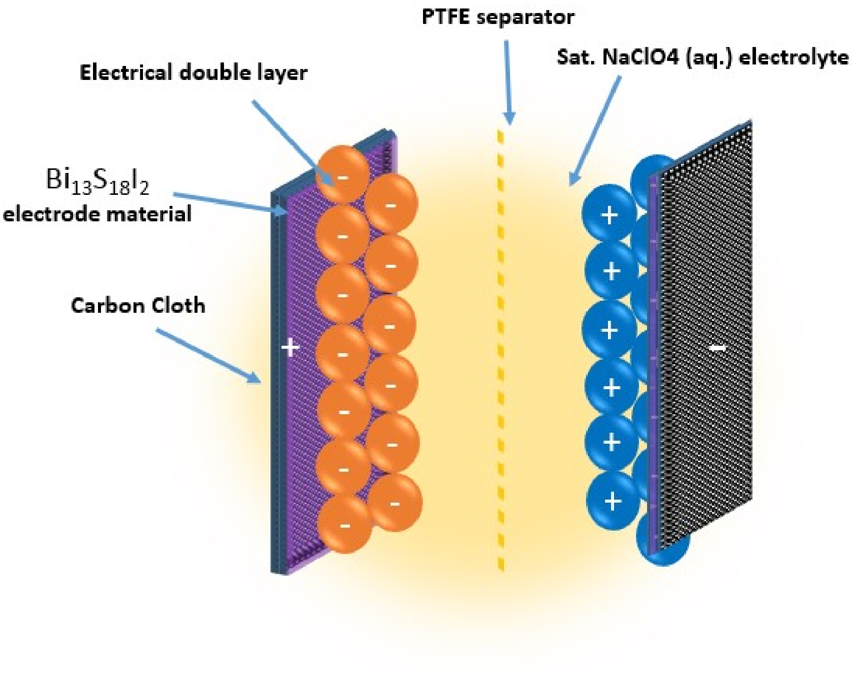

b)

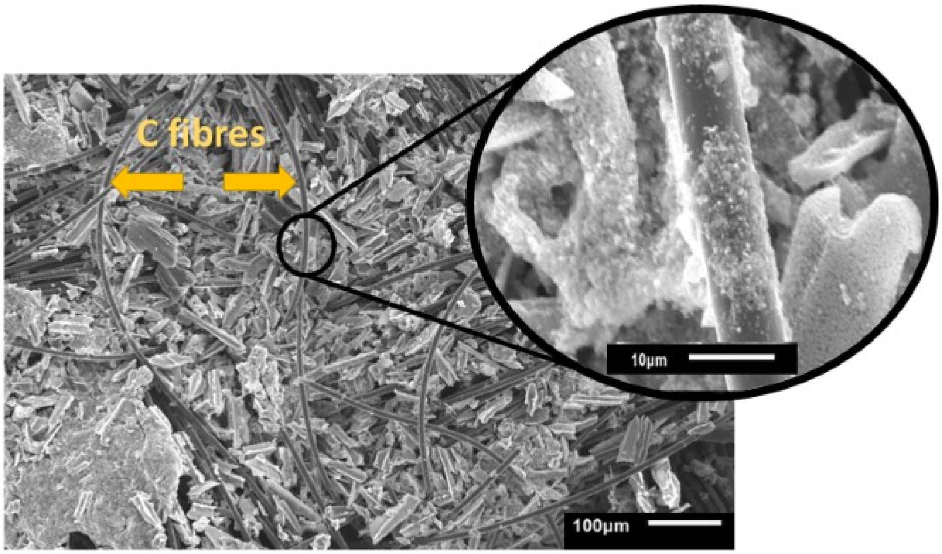

Figure 6.3 a) Schematic diagram of the EDLC in our study. b) SEM image of an as-prepared $Bi_{13}S_{18}I_2$ electrode on carbon cloth.

6.2.1.3 Cyclic Voltammetry and Galvanostatic Charge-Discharge Tests

The predominant charge storage mechanism of the $Bi_{13}S_{18}I_2$-based supercapacitor was investigated through cyclic voltammetry (CV) scans and galvanostatic charge-discharge cycles. The CV tests were performed in a voltage window ranging from 0.0 V to 0.6 V, with scan rates varying from 500 mV s^{-1} to 10 mV s^{-1} (**Figure 6.4**). No oxidation or reduction peaks were observed in this window, with the lowest 10 mV s^{-1} scan rate displaying a rounded-rectangular shape indicative of a predominantly non-Faradaic charge storage mechanism. We note that the potential values recorded for this two-electrode device are different from the three-electrode CV measurement above, where a separate reference electrode was used. For the two-electrode measurements we carried out on the supercapacitor device, we restricted the scans to a range where we saw no Faradaic peaks to ensure we are only probing EDLC-type capacitance behaviour. The non-symmetry of the CV curves at the higher scan rates are attributed to the resistivity during the ultra-fast charging process. Such non-Faradaic behaviour is characteristic of electric double layer capacitors, in contrast with so-called pseudocapacitors or supercapatteries, which rely on strong Faradaic reactions to store charge.[2] The areal and specific capacitances of the assembled supercapacitor device were calculated from the CV curves according to the following equations:[13]

$$C_{areal} = {}^{F}\!/_{cm^2} = \frac{\int_{\Delta V} i\,dV}{\Delta V \times s \times A} \text{ (Equation 6.1)}$$

$$C_{specific} = {}^{F}\!/_{g} = \frac{\int_{\Delta V} i\,dV}{\Delta V \times s \times m} \text{ (Equation 6.2)}$$

where ΔV is the voltage window of the negative (cathodic) current (V), s is the constant scan rate (V s^{-1}), A is the average geometric area of the two electrodes (cm^2), and m is the combined mass of the active material on both electrodes (g). The device's areal and specific capacitances as calculated from the CV curves spread from 53.65 mF cm^{-2} to 6.70 mF cm^{-2} and from 3.35 F g^{-1} to 0.42 F g^{-1} for scan rates increasing from 0.01 V s^{-1} to 0.5 V s^{-1}. The decrease in capacitance with increasing scan rate is a common feature of EDLCs and is caused by the different time regimes of charge transport and ion diffusion for the varying scan rates. At lower scan rates, electrolytic ions have sufficient time to diffuse into the pores of the $Bi_{13}S_{18}I_2$ active layer, increasing the charge accumulation and thus the capacitance. At higher scan rates, charge accumulation is confined to the surface of the electrodes, decreasing the electrodes' capacitances.

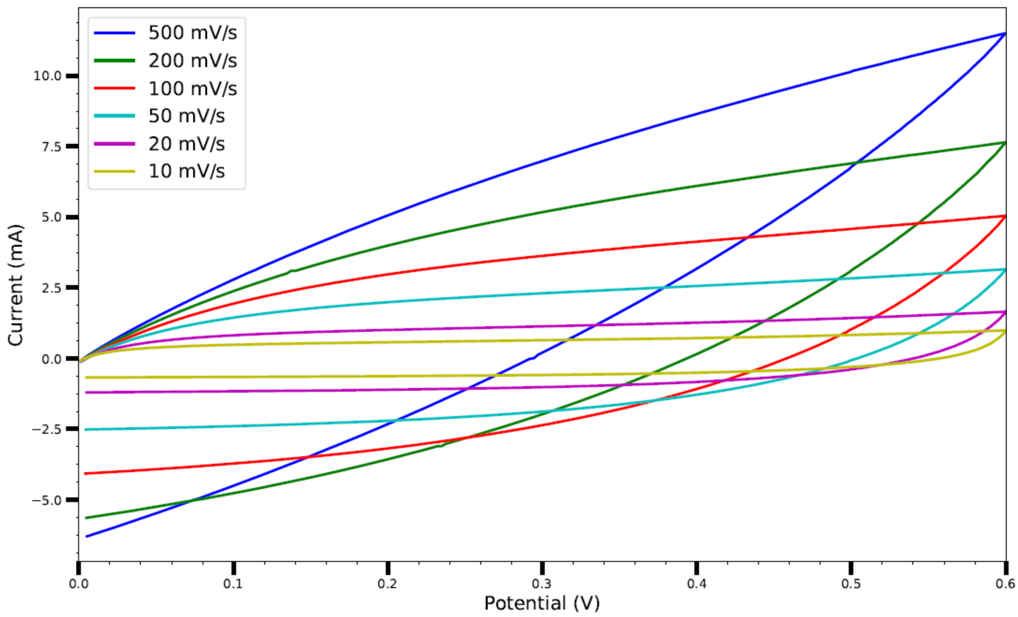

Figure 6.4 Cyclic voltammograms of the $Bi_{13}S_{18}I_2$ –based EDLC at varying scan rates.

The galvanostatic charge-discharge measurements were similarly carried out over a 0.0 – 0.6 V window, with current densities varying from 2.0 mA cm^{-2} to 0.1 mA cm^{-2} (**Figure 6.5**). The charge-discharge curves are largely symmetric and the discharge curve displays remarkable linearity following an initial iR drop even at the lowest current densities, corroborating the non-Faradaic, EDLC behaviour of the $Bi_{13}S_{18}I_2$ supercapacitor. The areal and specific capacitances were also calculated from the slope of the discharge curves in their linear regimes according to:

$$C_{areal} = {}^{F}\!/_{cm^2} = \frac{i}{\frac{dV}{dt}\times A} \text{ (Equation 6.3)}$$

$$C_{specific} = {}^{F}\!/_{g} = \frac{i}{\frac{dV}{dt}\times m} \text{(Equation 6.4)}$$

where i is the constant current (A), $\frac{dV}{dt}$ is the slope of the discharge curve taken in the voltage range 0.0-0.1 V for consistency, and m and A retain their previously defined meanings. The device's areal and specific capacitances derived from the galvanostatic charge-discharge curves ranged from 105.34 mF cm^{-2} to 57.83 mF cm^{-2} and from 6.58 F g^{-1} to 3.61 F g^{-1} for current densities increasing from 0.1 mA cm^{-2} to 2 mA cm^{-2}. Pious and colleagues previously integrated $(CH_3NH_2)_3Bi_2I_9$ in a similar symmetric EDLC device and reported an electrode areal capacitance of 5.5 mF cm^{-2}.[8] Since our supercapacitor device employs two symmetrical electrodes in series, the electrode capacitance is equal to twice the device capacitance, or 210.68 mF cm^{-2} for our best trial at the lowest tested current density. The energy density and power density calculated from CV and Galvanostatic charge-discharge measurements are summarized in **Table A15**, and the energy density can be potentially increased by operating in a larger potential window. Control experiments were carried out showing that the capacitance arises from $Bi_{13}S_{18}I_2$ rather than the carbon cloth substrate or additives (**Figure A1**, **Table A16**). In addition, an electrode prepared from $Bi_{13}S_{18}I_2$ powder suspension was also tested, showing only about 1/10 capacitance compared to solution-processed $Bi_{13}S_{18}I_2$ electrode (**Figure A2, Table A17**). This is caused by inferior surface area of the active material $Bi_{13}S_{18}I_2$ in powder form as shown in the SEM images (**Figure A3**).

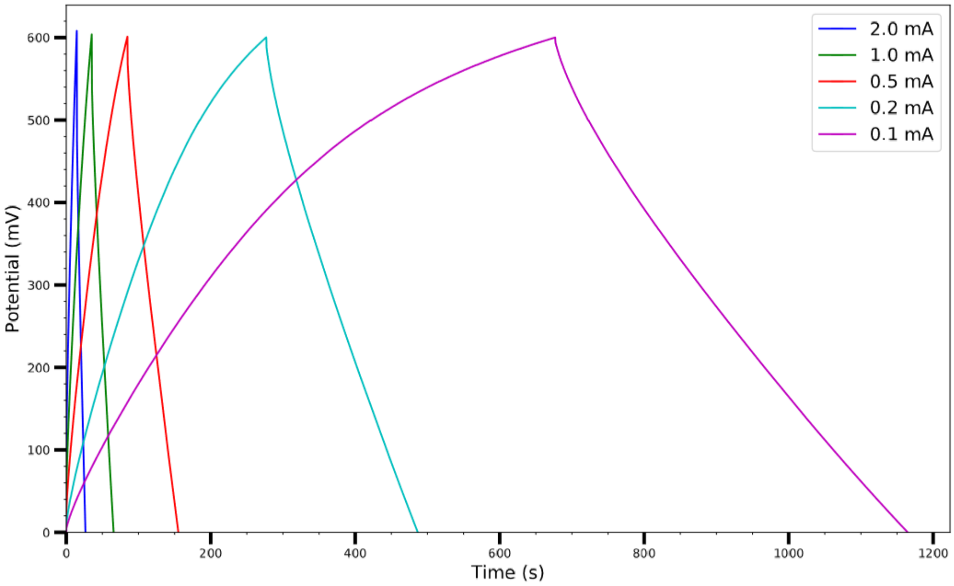

Figure 6.5 Galvanostatic charge–discharge curves of the $Bi_{13}S_{18}I_2$ –based EDLC under varying current density.

6.2.1.4 Cyclic stability test

The long-term cycle stability of the $Bi_{13}S_{18}I_2$ electrodes was evaluated by performing 5000 sequential galvanostatic charge-discharge cycles at the high current density of 2 mA cm^{-2}. Even after 5000 cycles, the device retains 99.7% of its initial capacitance, demonstrating the electrodes' remarkable stability under intense electrical conditions (**Figure 6.6a**).

a)

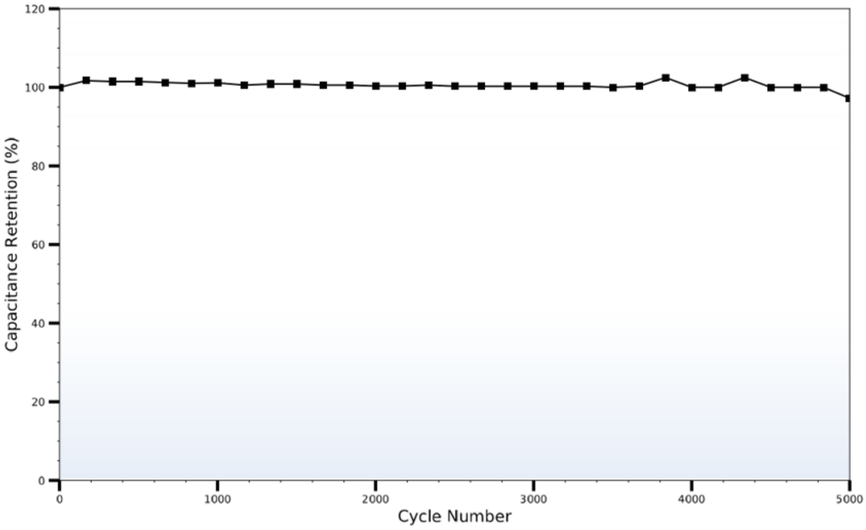

b)

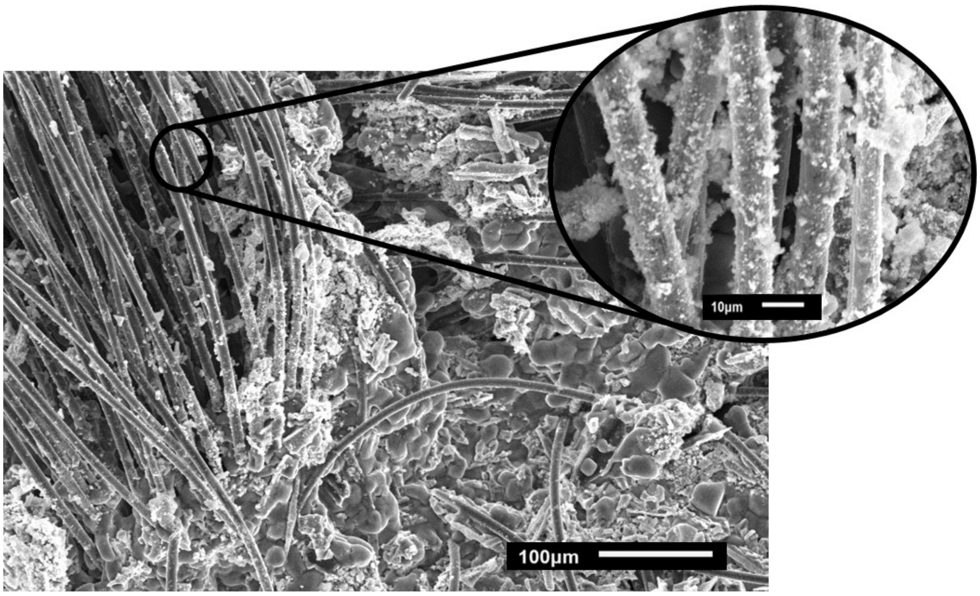

Figure 6.6 (a) Capacitance retention of the $Bi_{13}S_{18}I_2$ –based EDLC over 5000 cycles; (b) SEM images of $Bi_{13}S_{18}I_2$ electrode after 5000 cycles, with spread-out coverage of active material on carbon fibres. The area with smooth surface coverage indicated the coating from $NaClO_4$ electrolyte.

Moreover, SEM images of electrodes after undergoing the 5000 cycles indicate that the surface coverage of the carbon fibres with the activated $Bi_{13}S_{18}I_2$ remained largely the same after cycling (**Figure 6.6b**). We note however that limited information can be obtained from the SEM images, as the electrodes become heavily coated and obscured with crystallized $NaClO_4$ after use in the supercapacitor device. Raman spectra of the electrodes after cycling display the same vibrational peaks as those of the non-tested electrodes with no significant shifts in the Raman shifts (**Figure 6.7**), indicating that the $Bi_{13}S_{18}I_2$ material underwent no systematic chemical degradation during the 5000 cycles. The Raman shift has also been compared to the measured Raman shift in ref 12 in **Table 6.1**, showing consistent vibrational modes of $Bi_{13}S_{18}I_2$ in this study and in the literature. The obviously reduced intensity of the Raman spectrum for the cycled-electrodes is likely due to the thick $NaClO_4$ coating concealing the active layer. Finally, XRD was used to evaluate the crystal structural stability of $Bi_{13}S_{18}I_2$ over the 5000 cycles. **Figure 6.2** compares the electrodes' XRD pattern both before and after the 5000 cycles with the XRD peaks calculated for the pure $Bi_{13}S_{18}I_2$ powder. Although the intensity of diffraction peaks observed from the XRD pattern of $Bi_{13}S_{18}I_2$ drop after cycling, the peaks near 24°, 28.5°, 30°, and 32° demonstrate that the $Bi_{13}S_{18}I_2$ largely retains its crystal morphology throughout the electrochemical cycling, with reduced signal due to the presence of $NaClO_4$. The extra, sharp peaks are attributed to crystalline $NaClO_4$ and exposed carbon cloth fibres.

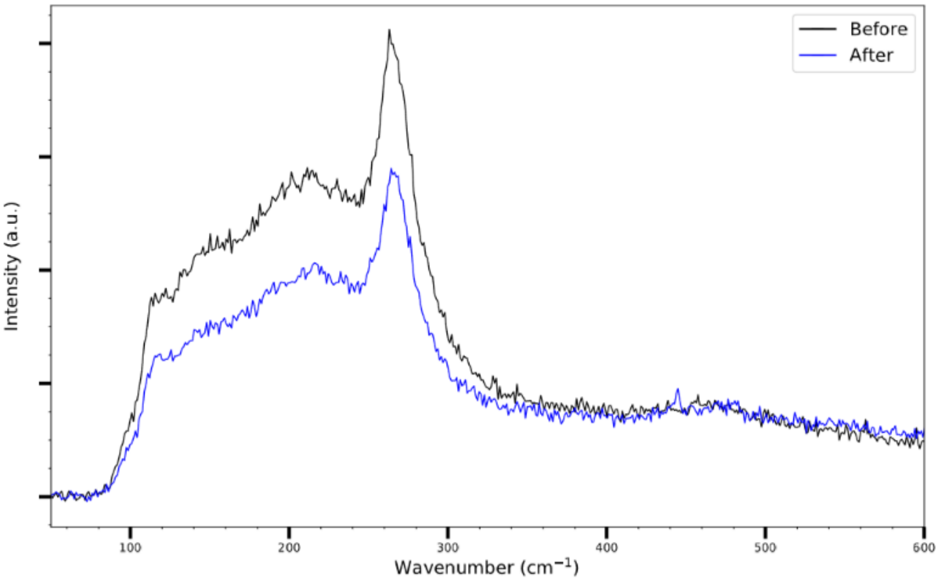

Figure 6.7 Raman spectra (shifted vertically for clarity) of $Bi_{13}S_{18}I_2$ as electrode material deposited on carbon cloth, compared before and after conducting 5000 cycles of stability test.

Table 6.1 comparison of measured wavenumber / cm-1 in this study and wavenumbers reported in ref 12.

measured wavenumber / cm^{-1} in this study	Wavenumber / cm^{-1} reported in ref 12
115	-
149	148
213	215
263	266
468	433

The high capacitance performance is attributed to a combination of reasons. Firstly, the crystal structure of $Bi_{13}S_{18}I_2$ indicates the presence of both Bi (III) and Bi (II) ions.[12] This illustrates an ability of the Bi centre to accommodate varying charge which may explain the capacitance mechanism and would be of great interest to investigate further. The significance of Bi^{2+} is supported by the calculated band structure that was previously reported[11] and showed the lowest unoccupied states to be predominantly derived from the Bi^{2+} centres along with contributions from the immediately-adjacent Bi^{3+} and sulfur ions. As would be expected, the highest occupied states were predominantly iodide in character. Both the valence band and conduction band showed notable dispersion, at least along some directions, pointing towards an ability to delocalise and hence accommodate the added charge. Secondly, enhanced active material coverage and homogeneity have been achieved via a new solution-deposition method, which should facilitate the electrolyte diffusion into the pores. This process is also favourable for large scale solution-based manufacturing, and using flexible carbon fibre as substrate provides the possibility for roll-to-roll production methods. Finally, pH neutral $NaClO_4$ aqueous solution was used as the electrolyte, which has been shown to be economic, eco-friendly and electrochemically superior with a wide potential window.

6.2.1.5 Electrochemical Impedance Spectroscopy

Electrochemical impedance spectroscopy (EIS) was performed to characterize the physical and electrochemical processes of the $Bi_{13}S_{18}I_2$ supercapacitor in response to AC current at varying frequencies. All of the EIS measurements were conducted with a baseline potential of 0 V and an AC amplitude of 10 mV at frequencies ranging from 150 kHz to 0.1 Hz. **Figure 6.8** displays the imaginary (out-of-phase) impedance versus the real (in-phase) impedance of the $Bi_{13}S_{18}I_2$ supercapacitor in a Nyquist plot prior to the 5000 galvanostatic charge-discharge cycles. From the

Nyquist plot, Bode plot and frequency vs. phase component plot (**Figure 6.9a** and **b**), a modified Randles equivalent circuit was fitted and shown as an inset in the Nyquist plot to analyse the resistive and capacitive elements in the supercapacitor.

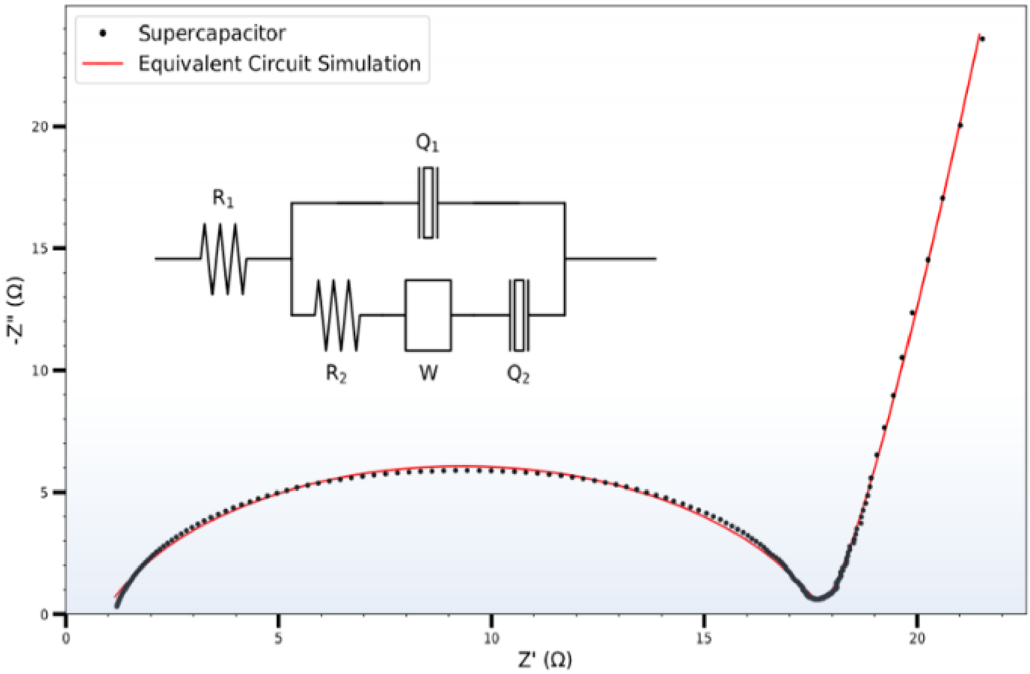

Figure 6.8 Experimental (black) and simulated (red) Nyquist plots, with an equivalent circuit inserted.

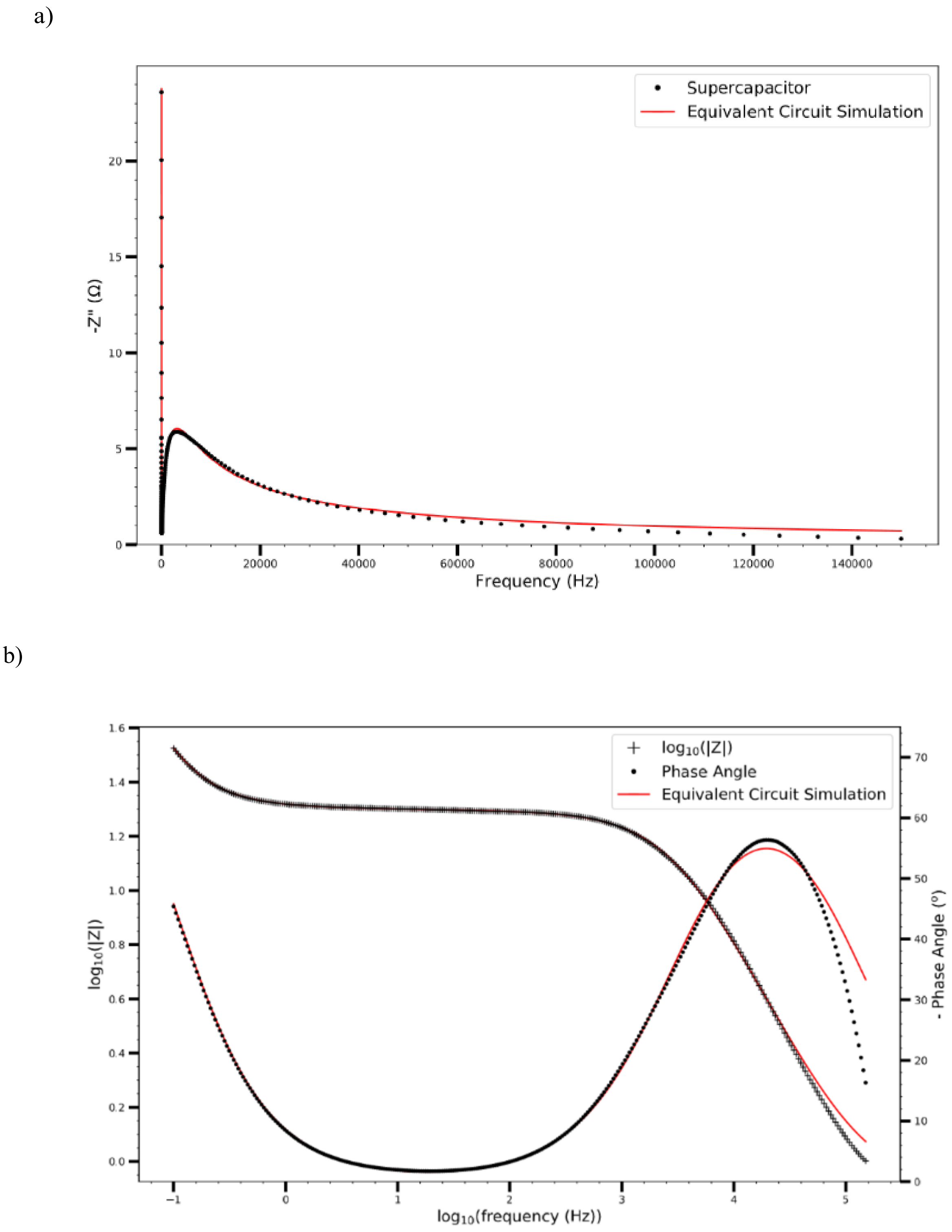

Figure 6.9 Bode plot (a) and frequency versus out of phase component plot (b) showing both experimental (black) and simulated from equivalent circuit (red).

The Nyquist plot shows typical EDLC-type behaviour with a semi-circle in the high-frequency regime and a linear branch in the low-frequency region. The intercept of the high-frequency end of the semi-circle with the real (Z') axis gives the value of R_1 in the equivalent circuit, representing the combined resistance due to the aqueous $NaClO_4$ electrolyte and the resistance in the current collectors, often referred to as equivalent series resistance (ESR). Since all charge migration during the charge-discharge process occurs through the electrolyte, R_1 is fitted in series with the other circuit elements and found to have a value of 0.89 Ω (**Table 6.2**). The curvature and diameter of the semi-circle are simulated with constant phase element Q_1 and resistor R_2, which are fitted in parallel to represent the two possible behaviours of the electrolyte during the charging and discharging of the supercapacitor. At higher frequencies or shorter charging times, the electrolytic ions have insufficient time to penetrate the surface of the $Bi_{13}S_{18}I_2$ electrodes, instead forming an electrostatic capacitive layer at the surface of the electrodes. This electrostatic capacitor is modelled with a constant phase element Q_1 with an ideality factor of 0.80, signifying an imperfect capacitor, and a relatively limited Y_0 of 22.8 $\mu(F\ s^{-0.20})^{1.25}$. Y_0 is the numerical value of admittance at ω=1 rad/s, [13] and Q – Y_0 is given by the Frequency Response Analyser EIS software as:

$$Z = \frac{1}{(Y_0 j\omega)^n} \text{ (Equation 6.5)}$$

where Z is the complex impedance, $j = \sqrt{-1}$, ω is the angular frequency, and n is the ideality factor. Q – Y_0 can be approximated as the capacitance of the CPE with units of Farads, but such false-equivalence has been strongly criticized. Instead, we report Y_0 with its proper units of $(F\ s^{n-1})^{1/n}$ to avoid confusion, but note that at high n (n ≈ 1), the approximation Y_0 = C becomes increasingly valid[14] The non-ideality of Q_1 is attributed to surface roughness and uneven coverage of the carbon cloth with the activated $Bi_{13}S_{18}I_2$ layer, which is apparent in the SEM images of the coated electrodes (**Figure 6.3b**). At moderate frequencies, however, the ions penetrate the electrodes' active layer, introducing R_2 with a calculated value of 16.8 Ω, representing the charge transfer resistance and the bulk resistance of the active material and electrode pores. In series with R_2 is a Warburg impedance element W, a characteristic feature of a Randles circuit that simulates the charge transport and mass diffusion of the electrolyte into the activated electrodes at mid to low frequencies. The fitted Warburg impedance gives a so-called Warburg coefficient with $W - Y_0$ giving the admittance of the impedance at an angular frequency of 1 rad/s:

$$\sigma = {}^{1}\!/_{\sqrt{2}\,Y_0} \text{ (Equation 6.6)}$$

Our simulated W gives $W - Y_0$ = 0.45 $\Omega^{-1}\ s^{1/2}$. A simple Randles circuit without the addition of Q_2 will produce linear behaviour with a 45° angle with respect to the Z' axis, characteristic of the Warburg diffusion element. The Nyquist plot for our experimental data, however, displays linear behaviour with a much steeper angle approaching 81.8°. To model this increased slope, we add a second constant phase element Q_2 in series with R_2 and W with an ideality factor n = 0.95 and Y_0 = 71 mF. The high n value suggests that Q_2 acts very nearly as an ideal capacitor, and the $Q_2 - Y_0$ closely matches the measured device capacitances derived from the CV and galvanostatic charge-discharge curves at lower scan rates or currents. We attribute this second, low-frequency regime capacitance to strong electrostatic charge storage once the electrolytic ions fully diffuse into the pores of the active $Bi_{13}S_{18}I_2$ layer.

Table 6.2. Electrochemical Impedance Spectroscopy equivalent circuit elements, for $Bi_{13}S_{18}I_2$ supercapacitor both before and after 5000 cycles

Circuit Element	Value Before Cycles	Value After Cycles
R_1	0.89 Ω	0.81 Ω
$Q_1 - n$	0.80	0.85
$Q_1 - Y_0$	22.8 $\mu(F\ s^{-0.20})^{1.25}$	13.0 $\mu(F\ s^{-0.15})^{1.18}$
R_2	16.8 Ω	19.0 Ω
$W - Y_0$	0.45 $\Omega^{-1}\ s^{1/2}$	0.45 $\Omega^{-1}\ s^{1/2}$
$Q_2 - n$	0.95	0.95
$Q_2 - Y_0$	71.0 $m(F\ s^{-0.05})^{1.05}$	70.0 $m(F\ s^{-0.05})^{1.05}$

EIS was also used to characterize the stability of the $Bi_{13}S_{18}I_2$ supercapacitor after the 5000 charge-discharge cycles. **Figure 6.10** compares the experimental Nyquist plot for the same $Bi_{13}S_{18}I_2$ supercapacitor before and after the cycle stability test was performed. While the low-frequency behaviour remained largely the same after cycling, R_1 decreased slightly from 0.89 **Ω** to 0.81 **Ω**, $Q_1 - Y_0$ decreased from 22.8 µF to 13 µF, and R_2 increased from 16.8 **Ω** to 19.0 **Ω**. The slight decrease in the electrolyte resistance R_1 is likely due to surface film and electrolyte conditioning after multiple cycles, while the simultaneous decrease in Q_1-Y_0 and increase in R_2 may be due to mechanical wear, decreased surface area of the active layer, and trapped ions inside the surface pores of the electrodes. The largely unchanged low-frequency behaviour, however, proves the long-term electrochemical stability of the $Bi_{13}S_{18}I_2$ active layer, as long-term pore penetration and ion diffusion does not significantly affect the low-frequency diffusion and capacitive elements.

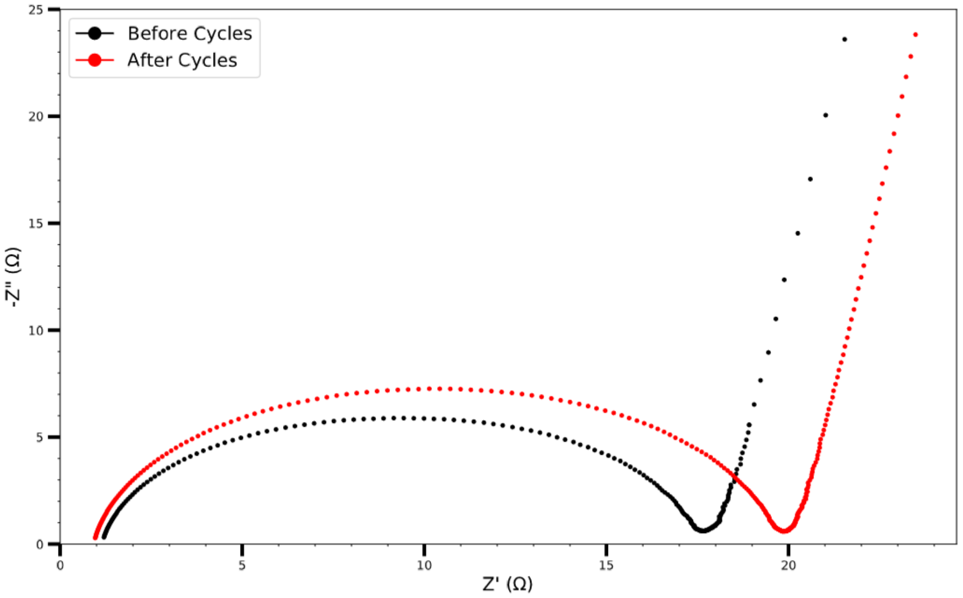

Figure 6.10 Nyquist plot of $Bi_{13}S_{18}I_2$ EDLC before (black) and after (red) 5000 cycles.

6.2.2 Thiourea Bismuth Iodide: Crystal structure, Characterization and High Performance as an Electrode Material for Supercapacitors

The excellent stability and capacity achieved by $Bi_{13}S_{18}I_2$ supercapacitor have motivated us to explore more into such Bi-based materials, and access their performance as the active electrode material for supercapacitor applications. In the second part of this chapter, a new iodobismuthate, thiourea bismuth iodide, will be studied structurally and applied as the supercapacitor electrode material.

6.2.2.1 Crystal structure

The single crystal of thiourea bismuth iodide, $[(NH_2)_2CSH]_3BiI_6$ (TBI) was synthesised by dissolving thiourea iodide with bismuth (III) iodide at 3:1 ratio in HI solution (57 wt% in water), and recrystallization by vapour diffusion from pentane. Single dark orange block-shaped crystals of TBI, with dimensions of (0.42×0.23×0.13) mm^3, were used for X-ray diffraction. TBI crystallised in the monoclinic crystal system with space group of $P2_1/c$. Isolated $[BiI_6]^{3-}$ octahedra comprise the inorganic entity of the crystal structure, showing a zero-dimensional structural motif (**Figure 6.11a, Table 6.3, Table A12-A14**). The $[BiI_6]^{3-}$ octahedron is distorted, with Bi-I bond lengths ranging from 3.3453 (8) Å to 2.9211 (9) Å, and the I-Bi-I angles ranging from 84.55 (2) ° to 94.93 (3) °. The sulfur atom is protonated in the thiourea cation, and the S-C-N bond angles fall into the range of 115.7(8)° to 122.6(9) °, showing distortion from the ideal carbon sp^2 hybridization. This distortion has been reported in previous studies of $(NH_2)_2CSH^+$ cations,[15-17] and in this case, it is potentially caused by the short contact distances between the protonated thiourea and the surrounding $[BiI_6]^{3-}$ octahedra (**Figure 6.11b**).

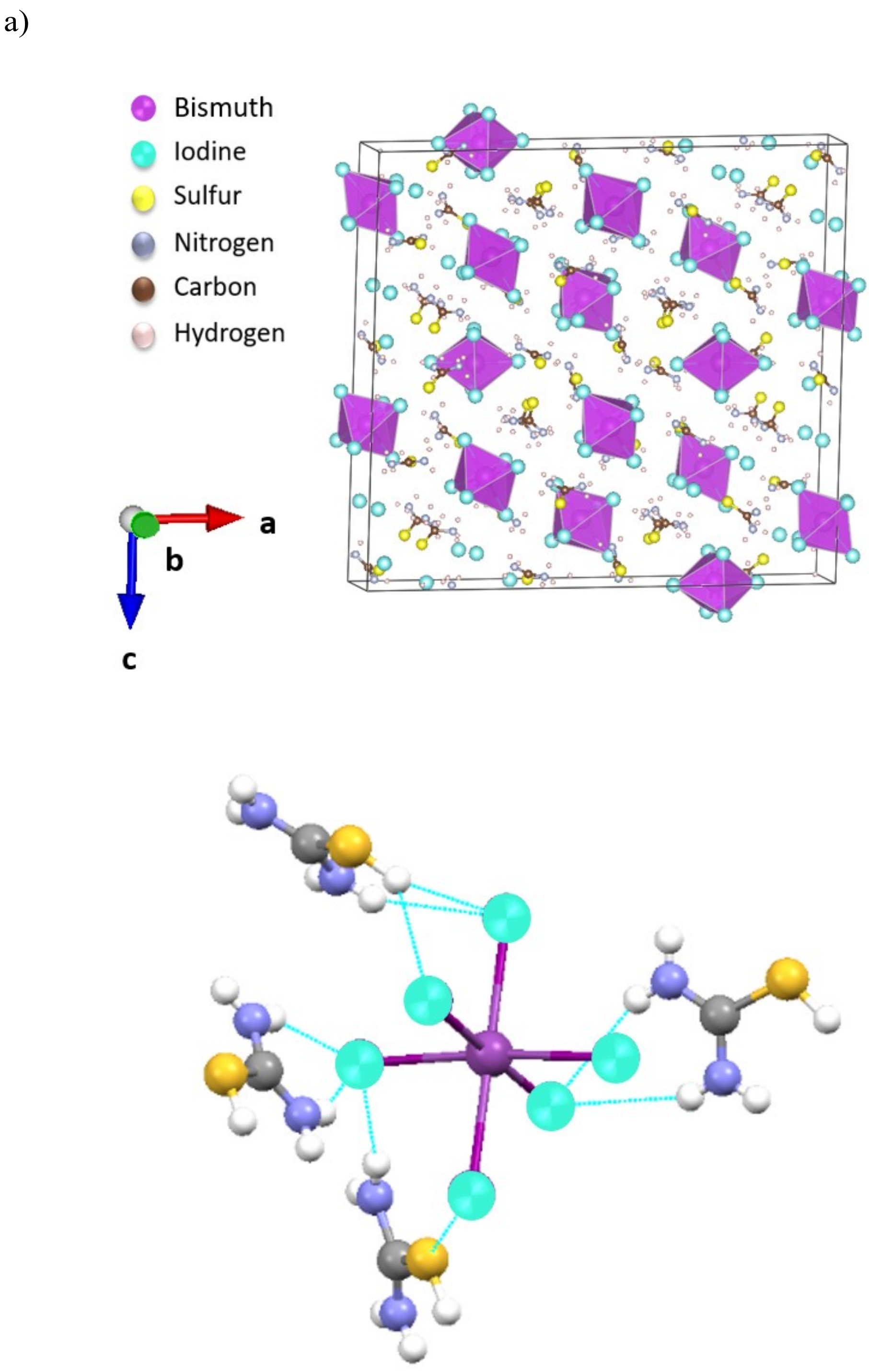

Figure 6.11 (a) Schematic diagram of a TBI unit cell viewed along the b axis. The unit cell boundary is marked with dark lines. Bismuth iodide octahedra are shown in magenta. The figure was generated from Vesta software.[18] (b) Short contacts (blue dashed lines) of the $[BiI_6]^{3-}$ octahedron with its surrounding protonated thiourea molecules. The figure was generated from Mercury software.[19]

Table 6.3 Summary of TBI crystallographic data

Compound	TBI
Formula	$C_3H_{18}BiI_6N_6S_3$
$D_{calc.}$/ g cm^{-3}	3.302
μ/mm^{-1}	15.172
Formula Weight	1204.79
Size/mm^3	0.42×0.23×0.13
T/K	120.0
Crystal System	monoclinic
Space Group	$P2_1/c$
a/Å	33.2403(4)
b/Å	9.44695(12)
c/Å	30.8920(4)
α/°	90
β/°	91.8969(10)
γ/°	90
V/Å^3	9695.4(2)
Z	16
Z'	4
Wavelength/Å	0.71073
GooF	1.083
wR_2 (all data)	0.1164
wR_2	0.1062
R_1 (all data)	0.0724
R_1	0.0544

6.2.2.2 Electrode preparation and characterization

Electrodes based on TBI were fabricated via a solution-processing method, in which TBI was dissolved in DMF and mixed together with activated charcoal to enhance conductivity and PTFE to enhance mechanical integrity of the electrode surface (85:10:5 weight ratio). The suspension was deposited evenly onto carbon cloth, which is used as the charge collecting substrate. Excess solution was removed by an absorbing tissue placed underneath the electrode. TBI crystallizes upon heating the substrate at 150°C for 1 hour on a hotplate to remove the solvent. The as-deposited TBI electrode was characterized by powder XRD, and compared with the calculated powder XRD pattern from the single crystal structure as shown in **Figure 6.12**. The as-deposited solution-processed TBI electrode shows a good peak position match with the theoretical pattern, with corresponding peaks for the 1 1 2, 2 0 4 and 6 0 6 reflections. A broad peak across 23 - 29° on the 2θ scale is attributed to the carbon fibre substrate. Due to an insufficient amount of TBI material in this thin-film form, BET isotherm surface area analysis is not feasible. We explored the surface morphology by SEM measurements. **Figure 6.13** presents the SEM images of solution-processed and, for comparison, suspension-processed TBI electrodes, giving insight into the crystallite size and coverage. It is clearly apparent that more carbon cloth fibres are exposed in the suspension-deposited TBI electrodes, despite the fact that a similar amount of material was deposited onto the carbon cloth. This is caused by the aggregation of pre-formed TBI crystallites when using the suspension-deposited method. However, the solution-processing results in higher surface coverage while minimizing the aggregation. The advantage of using a solution-processed electrode preparation method has also been investigated and proven in our previous work.[20] This enhanced coverage of TBI crystallites is anticipated to increase the charge storage ability, and therefore improve the capacitance of the device.

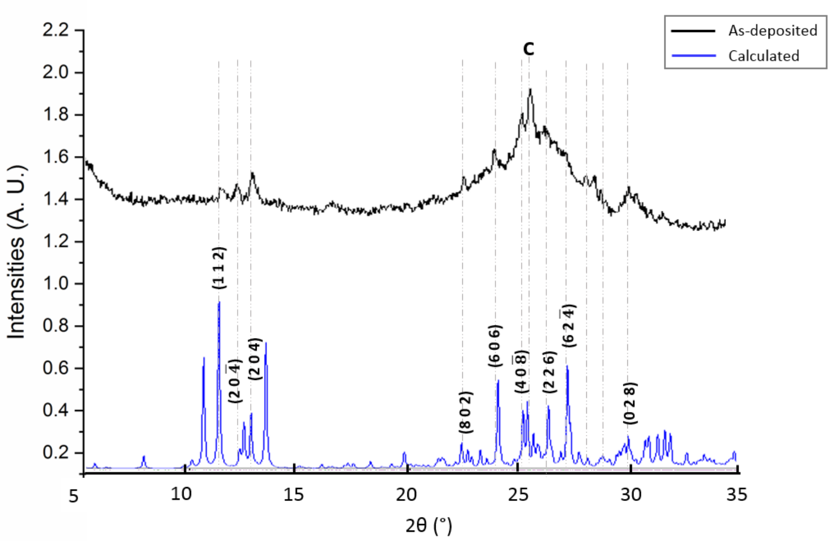

Figure 6.12 Powder XRD pattern of TBI as-deposited on carbon cloth (black), compared to the calculated XRD pattern (blue).

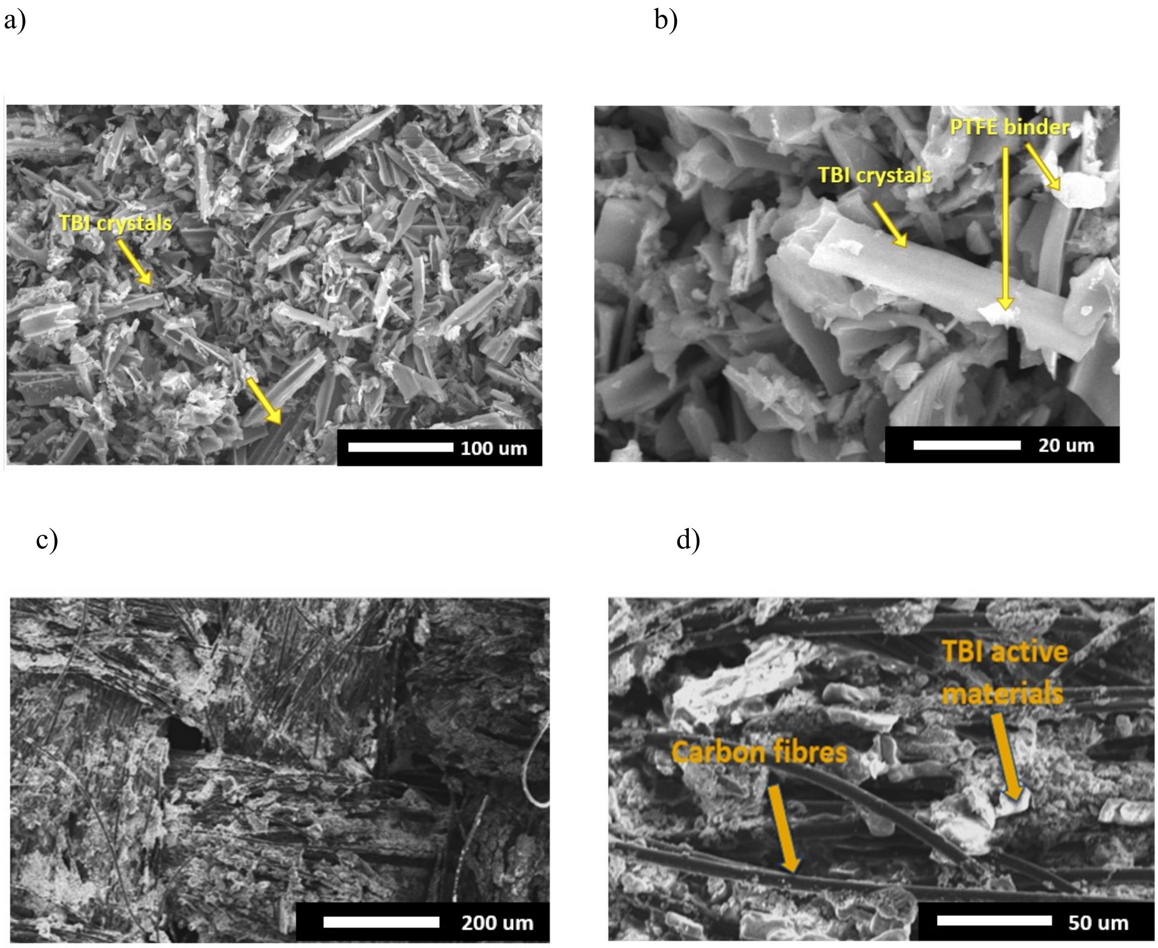

Figure 6.13. SEM images of as-deposited electrodes with solution-processed (a) (b) and suspension-processed (c) (d) TBI on carbon cloth substrate.

6.2.2.3 Device and charge storage mechanism studies with cycle stability test

To construct the supercapacitor device, a membrane separator was soaked in saturated $NaClO_4$ electrolyte solution before being sandwiched between two TBI coated carbon cloth electrodes. For better reproducibility and ease of measurement, the entire device was compressed in a standard test cell to give a firmly packed architecture (**Figure 6.14**). The TBI-based supercapacitor performance was examined using both cyclic voltammetry (CV) and galvanostatic charge-discharge measurements. Varying the time and applied voltage/current density regimes during the measurements allowed the evaluation of the capacitive performance and analysis of the charge storage mechanism.

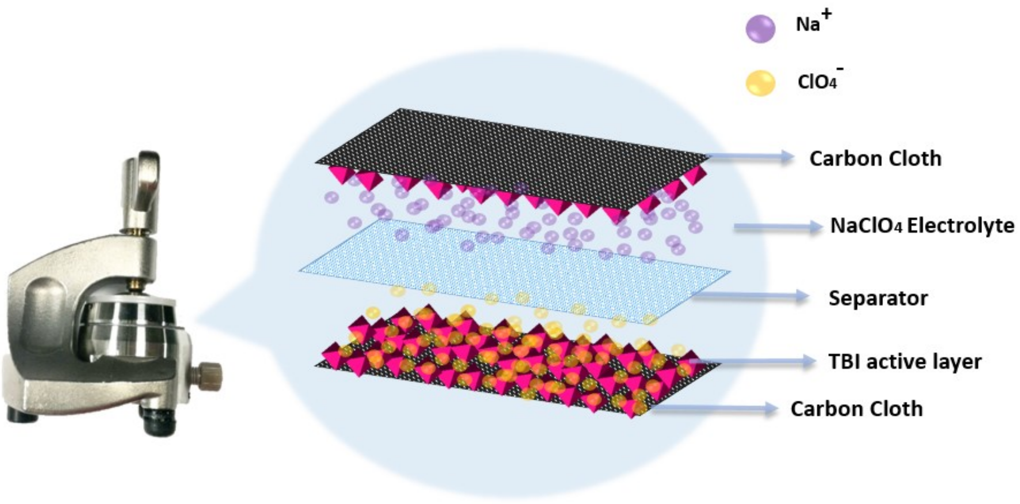

Figure 6.14 Schematic diagram of a TBI-based supercapacitor device that is compressed in a standard test cell.

The CV study was conducted in a voltage window of 0.0 – 0.6 V with a linear scan rate that varies from 0.01 V s^{-1} to 0.5 V s^{-1}, and **Figure 6.15** depicts the CV curves measured at different scan rates, with the measured capacitance summerized in **Table 6.4**. When a fast scan rate (0.5 V s^{-1}) is applied to the device, a rapid increase in the curent density versus potential gives an oval-shaped curve. The large slope of the charging onset indicates a strong resistive response from the device. This is mainly caused by insufficient time for Na^+ and ClO_4^- ions to diffuse to the electrode surface. Consequently, the fast scan rates cause the current to flow through the device in a resistive manner. As the sweep rate is reduced, more rectangular-shaped cuves can be obtained from the CV scans as the resistive effect caused by insufficient operating time is gradually minimized. The rectangular shaped CV curves, with a peakless plateau, indicate an effectively pure EDLC charge storage mechanism, where Na^+ and ClO_4^- ions diffuse and are stored in the micro-sized pores on the electrode surface through electrostatic interactions.

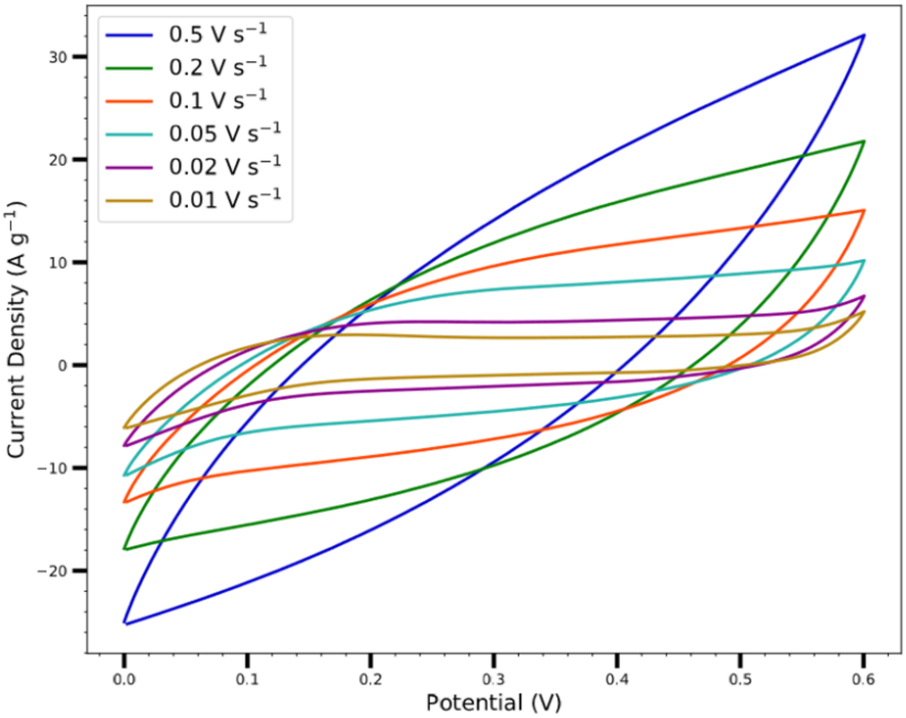

Figure 6.15 Cyclic voltammograms of the supercapacitor measured at different scan rates.

Table 6.4 Areal and specific capacitance measured from CV under different scan rate

Scan rate / V s^{-1}	areal capacitance / mf cm^{-2}	specific capacitance / F g^{-1}	Electrode areal capacitance / mf cm^{-2}	Electrode specific capacitance / F g^{-1}
0.5	23.7	14.7	47.4	29.4
0.2	44.5	27.7	89	55.4
0.1	61.2	38.0	122.4	76
0.05	79.0	49.1	158	98.2
0.02	108	67.0	216	134
0.01	140	87.2	280	174.4

The measured systemic capacitance increased from 23.7 mF cm^{-2} to 87.2 mF cm^{-2} (14.7 F g^{-1} to 87.2 F g^{-1}) as the scan rate decreased from 0.50 V s^{-1} to 0.01 V s^{-1}, showing that the scan rate interplays with the charge storage ability of the supercapacitor device. Note that the areal capacitance from Equation (1) is the systemic capacitance of the whole device; for comparison we have also listed the electrode areal capacitance for each electrode in **Table 6.4** (i.e., double the systemic capacitance).

Galvanostatic charge-discharge measurement was carried out in addition to CV, where the voltage of the capacitor is plotted against time during charge-discharge cycles under a constant current (**Figure 6.16**). The device was tested under different current densities (from 0.40 A g^{-1} to 3.50 A g^{-1}), with the capacitance summerized in **Table 6.5**. Largely triangular charge-discharge curves can be observed, particularly at higher current density, showing typical capacitative behaviour. However, a non-constant slope of the charge-discharge curve can be observed when lower current density is applied during the measurement. Initially upon charging, a steep onset can be found under the 10s time scale, showing fast charge storage at the easily-accesible electrode surface. This is followed by a less steep charging curve, as the longer time regime (over 10s) allows the ions to diffuse into the kinetically-limited deeper holes. As charges cover the full surface of both electrodes, the charge storage is saturated, represented by the flatening curve. During the discharge process, rapid potential drop is again attributed to the device internal resistance, followed by release of both electrostatically stored easily-accessible surface charge and kinetically-limited charge release.

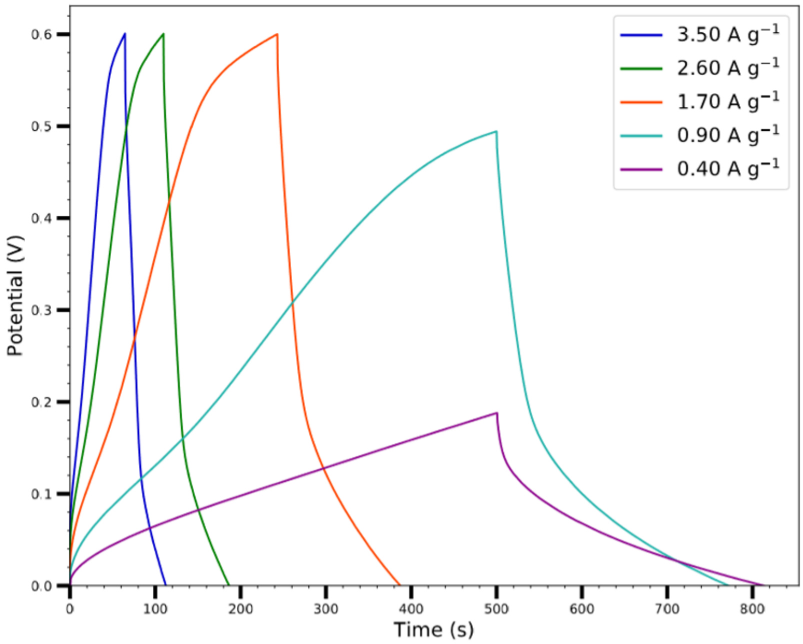

Figure 6.16 Galvanostatic charge-discharge curves measured at varies current densities

Table 6.5 Galvanostatic charge-discharge measurement under different specific current density

specific current density / A g^{-1}	areal capacitance / mf cm^{-2}	specific capacitance / F g^{-1}	Electrode areal capacitance / mf cm^{-2}	Electrode specific capacitance / F g^{-1}
3.50	943	586	1886	1172
2.60	1060	656	2120	1312
1.70	1290	803	2580	1606
0.90	1660	1030	3320	2060
0.40	1450	899	2900	1798

As the applied constant current density decreases from 3.50 A g^{-1} to 0.40 A g^{-1}, the measured capacitance increased from 941 mF cm^{-2} to 1450 mF cm^{-2} (586 F g^{-1} to 899 F g^{-1}), reaching a systemic peak capacitance of 1660 mF cm^{-2} (or 1030 F g^{-1}) under a constant current of 0.90 A g^{-1}. At the same time, the charge-discharge cycle time is approximately inversely-proportional to the applied current density, which to a large extent influences the charge storage mechanism as discussed above. This can be readily illustrated by plotting the instantaneous capacitance based on different points on the discharge curve, whereby the differential is taken and calculated according to Equation 3 and 4, with results in **Figure 6.17**.

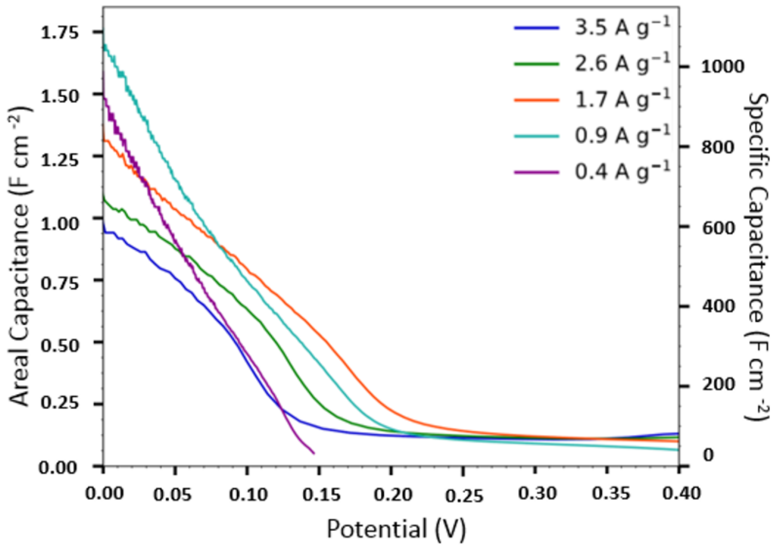

Figure 6.17 Instantaneous areal capacitance of the supercapacitor versus the potential based on galvanostatic charge-discharge measurement.

The long-term stability of the TBI supercapacitor device is proven experimentally, showing no capacitance loss after 5000 charge-discharge cycles (**Figure 6.18**). The initial increase of capacitance is attributed to the some modification of the electrode material surface and/or morphology during cycles under the charging-discharging environment, which can also explain the discrepancy between the CV curve shape of the 1st cycle and 5000th cycle (**Figure A4**). The powder XRD pattern of the TBI electrode after 5000 cycles however, shows mainly the heavily $NaClO_4$ coated carbon cloth, making it difficult to compare with the theoretical pattern (**Figure 6.19a**). Therefore, to further demonstrate the material stability under cycle testing, we carried out Raman spectroscopy measurements. The Raman spectra of the TBI electrodes before/after 5000 cycles show no substantial changes regarding the Bi-I vibrational modes, however, higher background noise was observed for the electrode after cycing, which again may be attributed by $NaClO_4$ coating (**Figure 6.19b**).

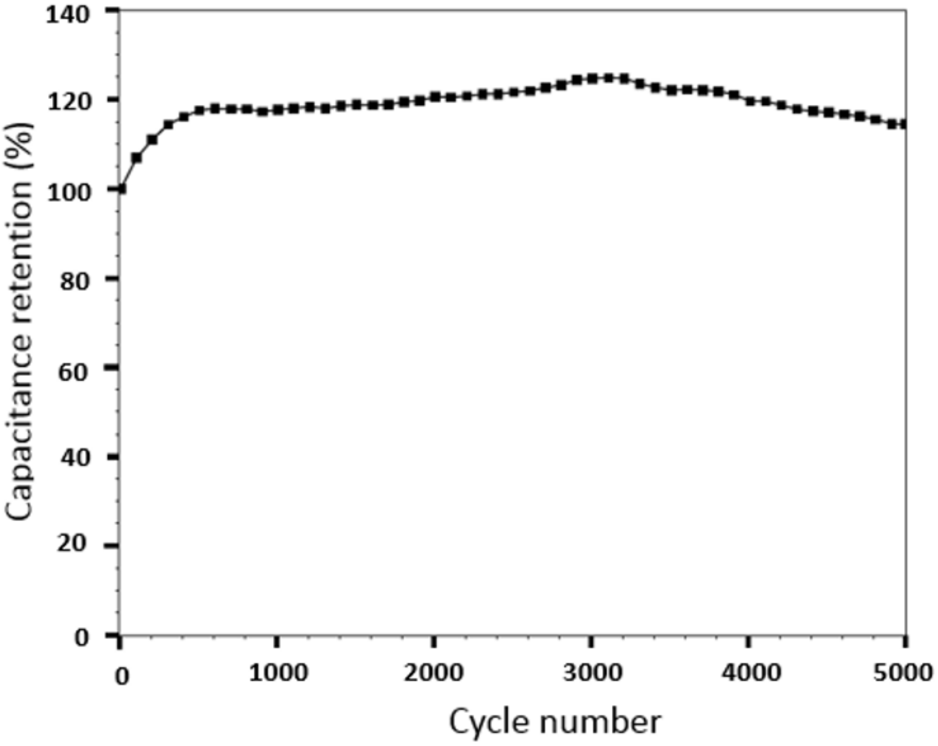

Figure 6.18 Capacitance retention of the TBI – based supercapacitor tested for 5000 CV cycles at a scan rate of 0.1V s^{-1}.

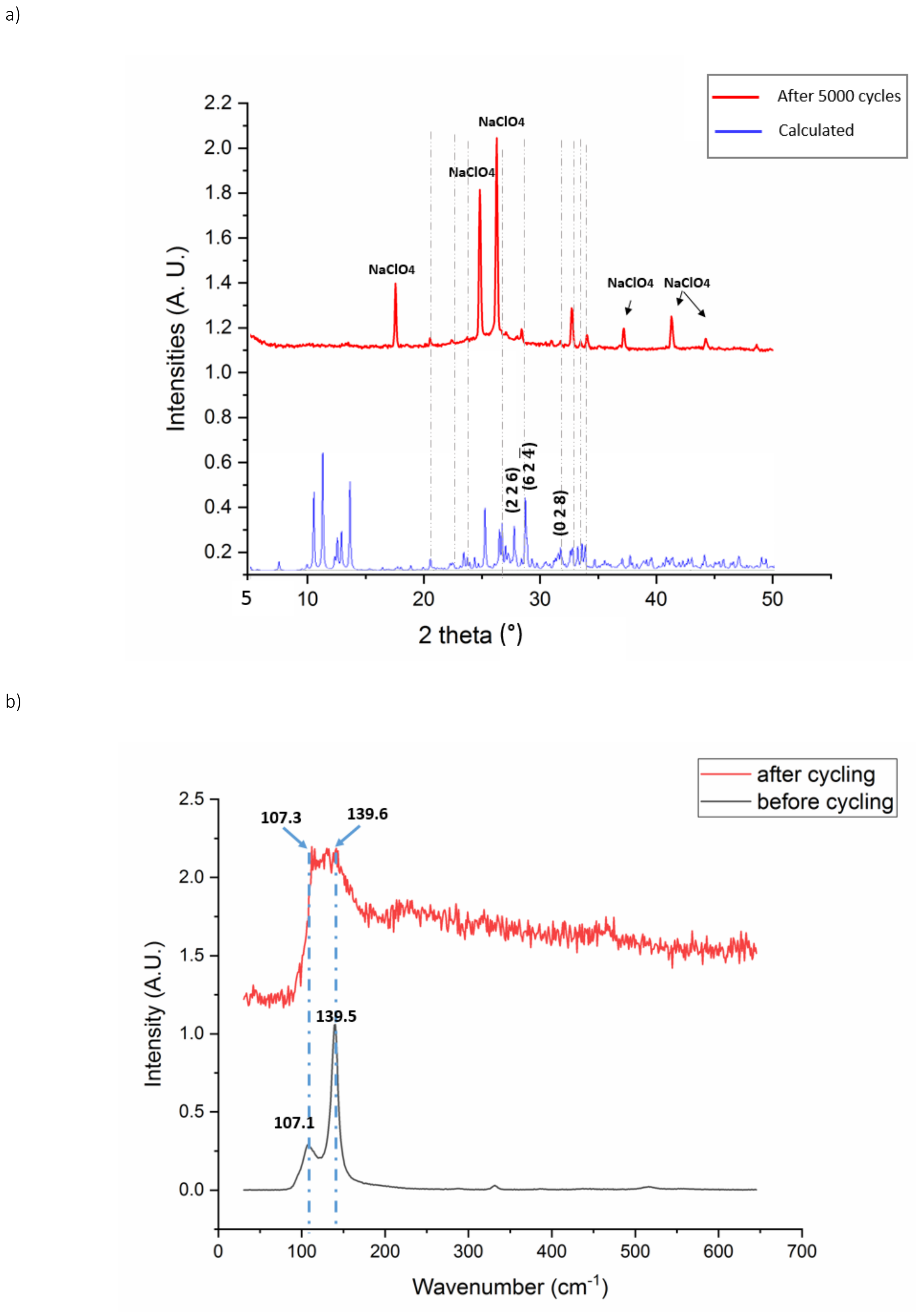

Figure 6.19. (a) Powder XRD pattern of TBI electrode after 5000 cycles compared (red) with the theoretical pattern (blue). (b) Raman spectra of as-prepared TBI electrode (black) and after 5000 cycling test (red).

In summary, using $NaClO_4$ as the electrolyte and TBI as the active electrode material with an optimized solution-processed deposition method, we have achieved over 600 times higher (electrode) areal capacitance compared to the previous work on a similar 0D hybride iodobismuth material,[8] and over 5 orders of magnitude higher than the study on a 3D lead-halide perovskite.[7]

6.2.2.4 Electrochemical impedance spectroscopy and equivalent circuit

To further investigate the device operation and charge storage mechanism, electrochemical impedance spectroscopy (EIS) measurements were carried out under AC potential to probe the equivalent circuit of the device.[13] In this study, the circuit response under applied frequency ranging from 0.01 Hz to 150 kHz was collected with an amplitude of ±10 mV at open circuit potential (OCP). **Figure 6.20** depicts the in-phase versus out-of-phase impedance (Nyquist plot) of a TBI-based supercapacitor at OCP of 0 V, and **Figure 6.21** shows the frequency response of the circuit, known as Bode plot. Based on the above two plots, we probed the equivalent circuit (inserted in **Figure 6.20**) to simulate the physical processes in the supercapacitor device.

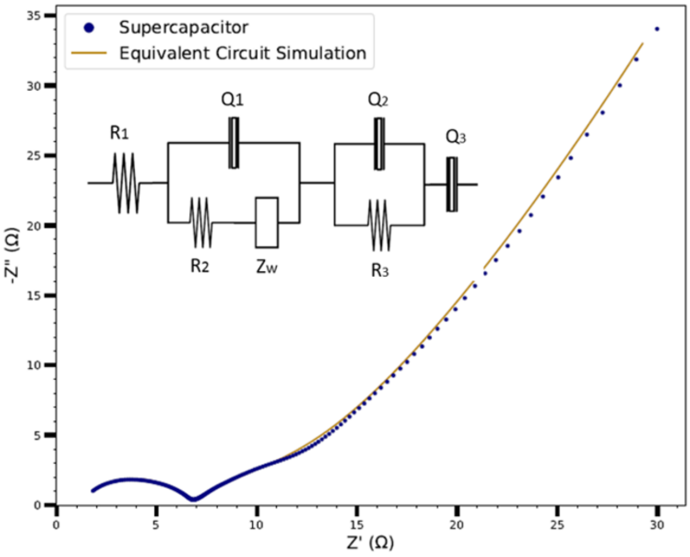

Figure 6.20 Nyquist plot of a TBI-based supercapacitor (blue) with fitted curve based on simulated circuit (yellow); simulated equivalent circuit diagram is inserted.

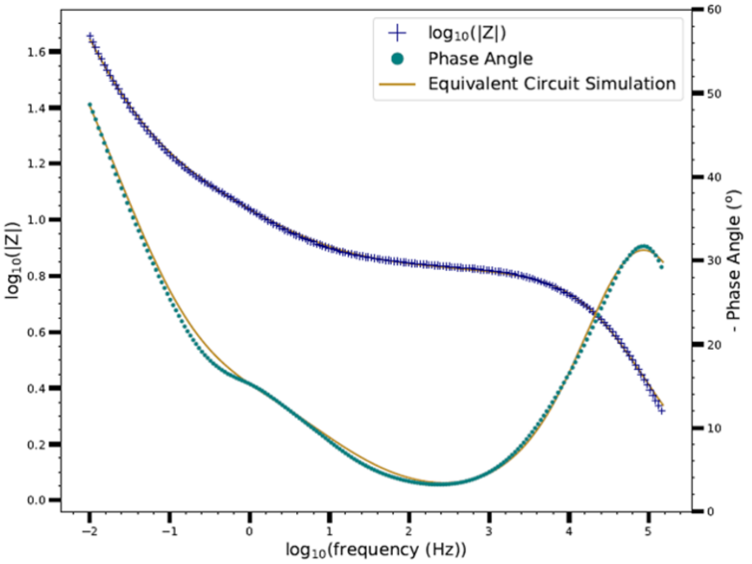

Figure 6.21 Bode plot of a TBI-based supercapacitor showing absolute impedance (blue), phase angle (green) with fitted curve based on equivalent circuit (yellow).

In the high frequency region, the high oscillation leads to insufficient time to form the double layer, leading to a more resistive response in the circuit. This is simulated as the bulk resistance (R_1) corresponding to the resistance from the $NaClO_4$ electrolyte and carbon cloth current collector, with a value of 1.137 Ω matching the interception of the Nyquist curve on the Z' axis. The first semicircle on the Nyquist plot is attributed to the charge transfer process between the electrode active material and current collector. Due to the intrinsically low density of states of carbon cloth, the contact capacitance is non-zero and can be simulated by a constant Q_1 phase element (CPE) of 2.057 µF with an ideality factor of 0.7554, demonstrating a small capacitance contribution to the circuit.[22,23] In parallel with Q_1, the charge transfer resistance R_2 is simulated to be 5.47 Ω from the equivalent circuit, showing negligible discrepancy from the diameter of the 1st semicircle on the Nyquist plot. The sum of R_1 and R_2 is known as the internal resistance, which corresponds to the resistance calculated from the iR drop in galvanostatic charge-discharge measurement.[24] The capacitance attributed to electrostatically stored charges in easily-accessible surface sites is simulated as Q_2, which is in parallel with device leakage resistance R_3.[23] The dominant capacitive behavior is simulated as another CPE (Q_3), with a capacitance of 0.7063 F and an ideality factor of 0.9007. This is attributed to the capacitative charge-storage behavior of the full material surface, broadly consistent with the specific capacitance (0.7373 F) from the Galvanostatic charge-discharge measurement, with a small discrepancy due to the AC measurement environment. The values and errors of each simulated circuit element are summarized in **Table 6.6**. The EIS measurement and equivalent circuit analysis for the device after 5000 cycles stability test was also carried out as shown in **Figure 6.22**, with the values of equivalent circuit elements tabulated in **Table A18**. The same equivalent circuit can be simulated, however, a smaller series resistance value but larger charge transfer resistance values were observed for the post-cycled device, attributed to some minor modification of the material surface through ionic diffusion and interaction during cycles.

Table 6.6 Summary of the values and errors (%) of equivalent circuit elements.

Circuit Element	Value	% Error
R_1	1.137 Ω	8.433
$Q_1 - \boldsymbol{n}$	0.7554	1.857
$Q_1 - Y_0$	2.057 μF	13.787
R_2	5.47 Ω	2.005
$Q_2 - \boldsymbol{n}$	0.5642	1.502
$Q_2 - Y_0$	0.0737 F	3.200
R_3	4.28 Ω	5.330
$Q_3 - \boldsymbol{n}$	0.9007	0.311
$Q_3 - Y_0$	0.7063 F	0.810
Z_w	0.1775 Ω^{-1} $s^{1/2}$	4.357

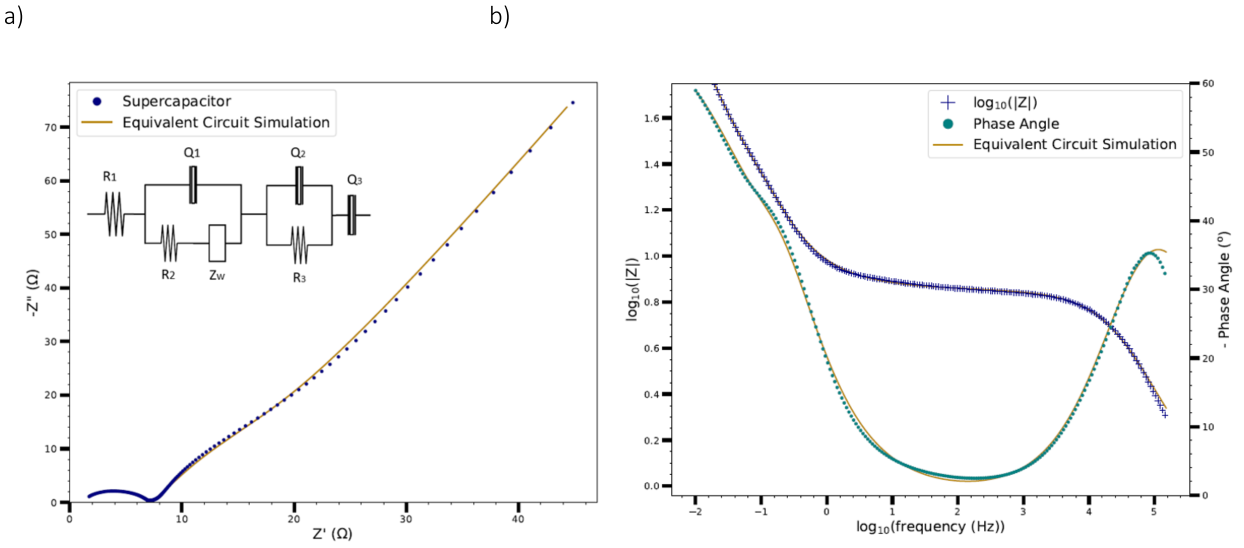

Figure 6.22. (a) Nyquist plot and (b) Bode plot of TBI-based supercapacitor after 5000 long-term cycle test, with simulated circuit and results inserted.

6.3 Conclusions

Two Bi-based materials were studied and explored as the electrode materials for supercapacitor applications. In the first part of this chapter, a facile, low-temperature and solution-processing synthesis method of a relatively-unexplored bismuth chalcohalide, $Bi_{13}S_{18}I_2$, was developed and employed as the active material in an EDLC device. Optimization of the active material deposition via solution-processing methodology and choice of electrolyte solution have together enhanced the EDLC performance. Utilizing saturated aqueous sodium perchlorate as the electrolyte, we have achieved a non-Faradaic EDLC with a superior areal capacitance of 210.68 mF cm^{-2} and an excellent 99.7% capacitance retention over 5000 charge–discharge cycles. In the second part of this chapter, a novel organic-inorganic iodobismuthate material, TBI, was synthesized, structurally characterized and studied as a stable electrode material for supercapacitor applications. Using carbon cloth as the current collector and aqueous $NaClO_4$ solution as the electrolyte, we fabricated low-cost and stable TBI-based supercapacitor devices and investigated the charge storage mechanism by cyclic voltammetry, galvanostatic charge-discharge measurement and EIS. A maximum electrode areal capacitance over 3.32 F/cm^2 and a systemic specific capacitance over 1030 F/g have been achieved, which is 600 times higher capacitance than the only literature precedents of similar materials. In sum, this chapter highlights the promising future of iodobimsuthate materials for supercapacitors applications in addition to optimize the device performance and extending the previously studied material range.

6.4 References

1 P. Sharma and T. S. Bhatti, *Energy Convers. Manag.*, 2010, **51** (12), 2901-2912.

2 B. E. Conway, *J. Electrochem. Soc.*, 1991, **138**, 1539-1548.

3 J. Ni, X. Bi, Y. Jiang, L. Li and J. Lu, *Nano Energy*, 2017, **34**, 356–366.

4 Y. Yan, Y. Xu, S. Lei, X. Ou, L. Chen, J. Xiong, Y. Xiao and B. Cheng, *Dalt. Trans.*, 2018, **47**, 3408–3416.

5 C.-H. Ho, Y.-H. Chen, Y.-K. Kuo and C. W. Liu, *Chem. Commun.*, 2017, **53**, 3741–3744.

6 B. Xu, T. Feng, M. T. Agne, Q. Tan, Z. Li, K. Imasato, L. Zhou, J. H. Bahk, X. Ruan, G. J. Snyder and Y. Wu, *Angew. Chemie - Int. Ed.*, 2018, **57**, 2413–2418.

7 S. Zhou, L. Li, H. Yu, J. Chen, C. P. Wong and N. Zhao, *Adv. Electron. Mater.*, 2016, **2**, 1600114.

8 J. K. Pious, M. L. Lekshmi, C. Muthu, R. B. Rakhi and V. C. Nair, *ACS Omega*, 2017, **2** (9), 5798-5802.

9 T. Li, Q. Wang, G. S. Nichol, C. A. Morrison, H. Han, Y. Hu and N. Robertson, *Dalt. Trans.*, 2018, **47**, 7050–7058.

10 M. Vigneshwaran, T. Ohta, S. Iikubo, G. Kapil, T. S. Ripolles, Y. Ogomi, T. Ma, S. S. Pandey, Q. Shen, T. Toyoda, K. Yoshino, T. Minemoto and S. Hayase, *Chem. Mater.*, 2016, **28**, 6436–6440.

11 Y. Wu, H. Pan, X. Zhou, M. Li, B. Zhou, C. Yang, W. H. Zhang, J. Jie and C. Li, *Chem. Sci.*, 2015,**6**, 4615-4622.

12 R. Groom, A. Jacobs, M. Cepeda, R. Drummey and S. E. Latturner, *Chem. Mater.*, 2017, **29**, 3314–3323.

13 E. Barsoukov and J. R. Macdonald, *Impedance Spectroscopy: Theory, Experiment, and Applications*, 2005.

14 P. Zoltowski, *J. Electroanal. Chem.*, 1998, **443**, 149-154.

15 M. J. Janssen, *Spectrochimica Acta*, 1961, **17**, 475-485.

16 M. Li and R. K. Li, *Dalton Trans.,* 2014, **43**, 2577.

17 O. V. Rudnitskaya, E. K. Kultyshikina, E. V. Dobrokhotova, V. S. Podvoyskaya, P. V. Dorovatovskii, V. A. Lazarenko, Y. V. Zubavichus, V. Khrustalev, *Polyhedron,* 2017, **134**, 114-119.

18 K. Momma and F. Izumi, *J. Appl. Crystallogr.*, 2011, **44**, 1272-1276.

19 C. F. Macrae, I. J. Bruno, J. A. Chisholm, P. R. Edgington, P. McCabe, E. Pidcock, L. Rodriguez-Monge, R. Taylor, J. van de Streek and P. A. Wood, *J. Appl. Cryst.,* 2008, **41**, 466-470,.

20 K. Adams, A. Franco Gonzalez, J. Mallows, T. Li, J. H. J. Thijssen and N. Robertson, *J. Mater. Chem. A,* 2018*, J. Mater. Chem. A,* 2019, **7**, 1638-1646

21 J. Xie, P. Yang, Y. Wang, T. Qi, Y. Lei and C. M. Li, *J. Power Sources*, 2018, **201**, 213-223.

22 H. Ji, X. Zhao, Z. Qiao, J. Jung, Y. Zhu, Y. Lu, L. Zhang, A. H. MacDonald and R. S. Ruoff, *Nat Comm,* 2014, **5**, 3317.

23 C. Lei, S Markoulidisa, Z. Ashitakab, C. Lekakoua, *Electrochimica Acta* 2013, **92**, 183– 187

24 B. Mei, O. Munteshari, J. Lau, B. Dunn and L. Pilon, *J. Phys. Chem. C* 2018, **122**, 194-206

Chapter 7 Conclusion and Outlook

The rapid growth in electrical energy demand is driven by increasing population, modernization and urbanization of society. Providing the world with energy in a sustainable, environmentally-benign and climate-friendly manner poses one of the most significant challenges to humanity. At the same time, how to store energy cost-efficiently and in an eco-friendly manner also brings about constant challenges to the world. As one of the most readily-available and inexhaustible energy sources, solar energy is playing and will increasingly play a crucial role in sustainable energy utilization. Because of this, researchers have been working over decades on solar cells to achieve higher power conversion efficiency with lower cost.

Silicon-based photovoltaic technology is known as first generation solar cells, which is now dominating the market with decreasing production cost. However, the indirect bandgap of silicon leads to the bulky and thick Si-based solar cell architecture. Flexible, light-weight and cost-effective solar PV technologies are urgently required for a broader range of applications. Second generation thin-film solar cells, featuring a much thinner absorbing layer, have stepped into the market in recent years. However, due to the use of rare elements, the cost of such thin-film solar technologies is still too high for larger-scale, wider and more cost-effective applications. This has motivated research efforts into the third generation solar cells. Lead-halide perovskite solar cells have fascinated researchers over the past 7 years, with merits including low-cost, ease of fabrication, ultrathin and flexible light-absorbing layer, as well as comparably-high power conversion efficiency as the Si-based solar cells. However, concerns over the toxicity of lead have been raised. This leads to the main topic of this thesis – designing and studying lead-free perovskite-like materials for photovoltaic applications, which constitutes Chapter 3-5 of this thesis. At the same time, such novel Bi-based materials have been almost unexplored in supercapacitor applications. As expected, electrode materials should show good energy density, good power density, low cost, good safety and long lifetime. All of these can potentially be met by the Bi-halide materials in this thesis.

The work contained in this thesis demonstrates a series of such bismuth-based materials for photovoltaic and supercapacitor applications, ranging from hybrid iodobismuthates to bismuth chalcohalides. The crystal structures of the new hybrid iodobismuthate materials were determined by single crystal XRD, showing 0D to quasi-3D structures with different crystal packing motifs. Further solid-state material characterisation was carried out to investigate their optical and electrochemical properties. For instance, the optical bandgap can be estimated by performing diffuse reflectance measurements to assess their suitability as solar absorbers; the chemical composition of the deposited thin-films can be studied by conducting XPS measurement; the energy level can be estimated by running cyclic voltammetry and analysing the electrochemical behaviours; the thin-film morphology and grain size can be observed by using electron microscopy, including SEM and TEM. At the same time, we have also conducted theoretical studies based on DFT calculations, to calculate the band gap values, study the electronic band structures of the new materials, and reveal the elemental energy level contributions to band edges. A combination of experimental and theoretical study of the materials has allowed us to better understand their properties and evaluate their potential as photovoltaic absorbers. Promising Bi-based materials, including [PY][BiI_4] and [AT][BiI_4] were chosen from the characterization results to conduct solar cell device studies. For the device fabrications, collaboration with Prof. Han's group in Huazhong University of Science and Technology has been carried out. A cost-effective and fully-printable solar cell structure has been applied in our study, where the absorber material was infiltrated through the triple TiO_2/ZrO_2/C mesoscopic scaffold. This type of cell has not previously been used with Bi-based absorbers. We have achieved solar cell efficiencies of 0.90% using [PY][BiI_4] as the light absorber and 0.47% using [AT][BiI_4] as the light absorber, which are comparable with the other reported Bi-iodide based cells, demonstrating new perspectives in lead-free material designing for photovoltaic applications.

In addition to the solar cell applications, we have also applied novel Bi-based materials to supercapacitor studies, including $Bi_{13}S_{18}I_2$ and thiourea bismuth iodide (TBI). From the material preparation perspective, we have revealed the crystal structure of TBI as a novel 0D material, and demonstrated the first facile, low-temperature, and solution-processing synthesis of the relatively-unexplored $Bi_{13}S_{18}I_2$. In extensive supercapacitor device studies, both TBI and $Bi_{13}S_{18}I_2$ were employed as the active material in EDLC devices, demonstrating a simple and economical electrode fabrication process. Optimization of the active material deposition via solution-processing methodology and choice of electrolyte solution have together enhanced the EDLC performance. Utilizing saturated aqueous sodium perchlorate as the electrolyte, we have achieved non-Faradaic EDLCs for both $Bi_{13}S_{18}I_2$ and TBI. Superior device areal capacitance of 105 mF cm^{-2} (3.32 F cm^{-2}) and specific capacitance of 6.58 F g^{-1} (1030 F g^{-1})has been demonstrated for $Bi_{13}S_{18}I_2$ (TBI), which is hundreds of times higher than the only reported work based on similar structured material, together with excellent long-term cycling stability, demonstrating over

98% capacitance retention after 5000 charge-discharge cycles. The EDLC mechanism is supported by the lack of any redox peaks in the cyclic voltammogram and a largely linear galvanostatic discharge curve, together with in-depth mechanism probing by performing electrochemical impedance spectroscopy measurement.

In conclusion, this research has focussed on property characterizations, theoretical calculations and device studies to assess the potential of Bi-based materials for photovoltaic and energy storage applications. The study of hybrid bismuth-halide functional materials is still in the early research stage, however, promising features have been demonstrated in this thesis. Thus, for the Bi-based photovoltaic material studies, the ongoing and future work using iodobismuthates as functional energy materials will focus on deeper physical and chemical mechanism studies, including using transient spectroscopy to measure the lifetime of charge carriers, probing possible recombination routes in the solar cell devices, and conducting solar cell device optimizations. For the supercapacitor applications, in-depth interactions between charge storage and material properties can be further probed, by employing *in-situ* spectroscopies and *in operado* techniques. Additionally, supercapacitor device optimization can be further carried out in the future, with particular interest on exploring the charge storage ability using asymmetric capacitor designs under different electrolyte/current collector systems.

Appendix

Table A1: Fractional Atomic Coordinates (×10^4) and Equivalent Isotropic Displacement Parameters (Å^2×10^3) for **[PY][BiI$_4$]**. U_{eq} is defined as 1/3 of the trace of the orthogonalised U_{ij}.

Atom	x	y	z	U_{eq}
Bi1	19924.7(7)	5444.3(3)	17491.0(12)	19.4(2)
I1	18404.3(15)	6110.8(7)	15854(3)	40.2(5)
I2	21390.6(13)	5438.7(5)	14441(2)	24.5(4)
I3	21427.3(13)	4623.7(6)	19442(2)	26.5(4)
I4	21307.8(16)	6171.8(7)	19080(3)	39.8(5)
Bi2	14999.9(7)	7046.8(3)	11932.2(13)	20.5(2)
I5	16384.3(14)	7114.5(6)	15414(2)	29.0(4)
I6	13598.1(13)	7089.4(5)	8402(2)	25.2(4)
I7	16479.1(15)	6348.0(6)	10825(3)	35.1(4)
I8	13579.2(14)	6330.0(6)	13170(3)	31.3(4)
N1	20480(30)	6654(11)	13190(40)	61(7)
C1	21030(40)	7038(13)	13880(70)	72(11)
C2	20600(30)	7455(14)	13670(60)	67(10)
C3	19630(30)	7528(14)	12910(60)	61(9)
C4	19060(30)	7141(11)	12190(60)	61(9)
C5	19540(30)	6697(12)	12390(50)	53(7)
C10	24340(50)	5813(19)	17460(50)	95(11)
C9	23890(50)	5464(18)	17990(70)	103(12)
C8	24270(50)	5053(19)	17850(60)	98(12)
C7	25320(50)	5020(20)	17430(60)	97(12)
C6	25880(50)	5367(19)	16940(60)	103(12)
N2	25360(40)	5794(15)	16940(40)	96(10)

Table A2: Anisotropic Displacement Parameters (×10^4) **[PY][BiI$_4$].** The anisotropic displacement factor exponent takes the form: $-2\pi^2[h^2a^{*2} \times U_{11} + \ldots + 2hka^* \times b^* \times U_{12}]$

Atom	U_{11}	U_{22}	U_{33}	U_{23}	U_{13}	U_{12}
Bi1	22.4(5)	16.7(4)	19.1(5)	1.3(3)	2.2(4)	-0.1(3)
I1	34.6(10)	40.1(10)	46.9(13)	22.7(9)	8.5(9)	15.3(8)
I2	26.8(8)	24.5(8)	22.9(9)	-2.3(6)	6.5(7)	-8.3(6)
I3	28.0(9)	27.8(8)	24.9(9)	6.5(7)	8.3(7)	9.9(7)
I4	40.6(11)	34.1(10)	45.4(12)	-17.5(9)	7.6(9)	-15.6(8)
Bi2	21.8(5)	16.0(4)	23.7(5)	0.2(3)	2.0(4)	0.6(3)
I5	26.8(9)	28.3(8)	30.7(10)	-5.1(7)	-3.3(7)	9.4(7)
I6	25.7(8)	22.7(8)	26.8(9)	3.2(6)	0.2(7)	-7.1(6)
I7	32(1)	31.8(9)	40.6(11)	-13.7(8)	-1.1(8)	11.8(8)
I8	31.8(9)	25.0(8)	36.6(10)	8.8(7)	1.4(8)	-6.7(7)
N1	76(15)	49(12)	62(18)	-3(10)	31(12)	6(10)
C1	78(15)	49(12)	90(30)	-10(13)	16(16)	9(11)
C2	68(14)	43(12)	90(30)	-8(12)	21(15)	1(10)
C3	69(14)	39(11)	80(20)	1(11)	25(14)	0(10)
C4	70(14)	43(11)	70(20)	1(12)	26(14)	-2(10)
C5	73(15)	43(11)	48(18)	1(11)	33(12)	-2(10)
C10	150(30)	90(18)	30(20)	7(14)	-47(18)	-25(19)
C9	160(30)	89(18)	60(20)	3(18)	-28(19)	-20(20)
C8	150(30)	84(18)	50(30)	6(16)	-20(20)	-26(19)
C7	150(30)	94(18)	40(20)	5(15)	-24(19)	-21(19)
C6	150(30)	106(19)	40(20)	12(18)	-32(18)	-28(19)
N2	160(30)	97(18)	26(16)	5(14)	-47(17)	-35(18)

Table A3: Bond Lengths in Å for [PY][BiI$_4$].

Atom	Atom	Length/Å
Bi1	I1	2.9047(19)
Bi1	I2	3.1326(19)
Bi1	I2^1	3.2872(17)
Bi1	I3	3.2830(18)
Bi1	I3^2	3.0556(19)
Bi1	I4	2.904(2)
I2	Bi1^1	3.2873(17)
I3	Bi1^2	3.0556(19)
Bi2	I5^3	3.2379(19)
Bi2	I5	3.078(2)
Bi2	I6	3.116(2)
Bi2	I6^4	3.2877(18)
Bi2	I7	2.9105(19)
Bi2	I8	2.9338(19)
I5	Bi2^4	3.2379(18)
I6	Bi2^3	3.2878(18)
N1	C1	1.37(5)
N1	C5	1.31(5)
C1	C2	1.30(5)
C2	C3	1.33(6)
C3	C4	1.40(5)
C4	C5	1.40(5)
C10	C9	1.23(7)
C10	N2	1.39(7)
C9	C8	1.27(7)
C8	C7	1.40(8)
C7	C6	1.30(7)
C6	N2	1.38(7)

----

^{1}4-X,1-Y,3-Z; ^{2}4-X,1-Y,4-Z; ^{3}+X,3/2-Y,-1/2+Z; ^{4}+X,3/2-Y,1/2+Z

Table A4: Bond Angles in ° for [PY][BiI$_4$].

Atom	Atom	Atom	Angle/°
I1	Bi1	I2^1	90.43(6)
I1	Bi1	I2	95.38(6)
I1	Bi1	I3	173.92(6)
I1	Bi1	I3^2	88.82(6)
I2	Bi1	I2^1	88.16(5)
I2	Bi1	I3	88.87(5)
I3^2	Bi1	I2	175.53(5)
I3	Bi1	I2^1	85.35(5)
I3^2	Bi1	I2^1	90.28(5)
I3^2	Bi1	I3	86.83(5)
I4	Bi1	I1	94.27(7)
I4	Bi1	I2^1	173.34(6)
I4	Bi1	I2	86.70(6)
I4	Bi1	I3^2	94.53(6)
I4	Bi1	I3	90.30(6)
Bi1	I2	Bi1^1	91.84(5)
Bi1^2	I3	Bi1	93.17(5)
I5	Bi2	I5^3	89.12(5)
I5	Bi2	I6	174.21(5)
I5	Bi2	I6^4	86.36(5)
I5^3	Bi2	I6^4	84.75(5)
I6	Bi2	I5^3	86.60(5)
I6	Bi2	I6^4	89.36(5)
I7	Bi2	I5	88.07(6)
I7	Bi2	I5^3	90.34(6)
I7	Bi2	I6^4	172.62(6)
I7	Bi2	I6	95.85(6)
I7	Bi2	I8	93.32(6)
I8	Bi2	I5^3	174.96(6)
I8	Bi2	I5	94.47(6)
I8	Bi2	I6	89.57(5)
I8	Bi2	I6^4	91.93(5)
Bi2	I5	Bi2^4	94.36(5)
Bi2	I6	Bi2^3	92.66(5)
C5	N1	C1	121(3)
C2	C1	N1	119(5)
C1	C2	C3	124(4)
C2	C3	C4	119(4)
C5	C4	C3	117(4)
N1	C5	C4	120(4)
C9	C10	N2	122(6)
C10	C9	C8	121(8)
C9	C8	C7	117(6)
C6	C7	C8	125(6)
C7	C6	N2	112(7)
C6	N2	C10	120(5)

----

^{1}4-X,1-Y,3-Z; ^{2}4-X,1-Y,4-Z; ^{3}+X,3/2-Y,-1/2+Z; ^{4}+X,3/2-Y,1/2+Z

Table A5: Torsion Angles in ° for **[PY][BiI$_4$]**.

Atom	Atom	Atom	Atom	Angle/°
N1	C1	C2	C3	5(8)
C1	N1	C5	C4	1(6)
C1	C2	C3	C4	-5(7)
C2	C3	C4	C5	3(6)
C3	C4	C5	N1	-2(6)
C5	N1	C1	C2	-3(7)
C10	C9	C8	C7	13(8)
C9	C10	N2	C6	3(6)
C9	C8	C7	C6	-10(8)
C8	C7	C6	N2	2(7)
C7	C6	N2	C10	1(6)
N2	C10	C9	C8	-11(8)

Table A6: Fractional Atomic Coordinates (×10^4) and Equivalent Isotropic Displacement Parameters (Å^2×10^3) for **[MEPY][BiI$_4$]**. U_{eq} is defined as 1/3 of the trace of the orthogonalised U_{ij}.

Atom	x	y	z	U_{eq}
Bi1	2494.0(6)	4100.8(3)	5094.0(3)	10.74(10)
I1	4115.6(9)	2786.6(5)	6557.2(5)	15.60(17)
I2	-597.8(9)	4340.5(4)	6471.4(5)	14.22(16)
I3	896.4(9)	2551.0(5)	3907.8(5)	16.30(16)
I4	5633.0(8)	4099.2(5)	3726.0(5)	13.81(16)
N1	7953(11)	1068(6)	5658(7)	17(2)
C1	7999(14)	126(7)	5554(8)	20(3)
C2	7264(15)	-287(8)	4714(9)	25(3)
C3	6529(16)	272(8)	3954(9)	29(3)
C4	6493(15)	1242(9)	4071(9)	27(3)
C5	7206(12)	1637(7)	4956(8)	14(2)
C6	8855(14)	1510(7)	6568(8)	19(2)

Table A7: Anisotropic Displacement Parameters (×10^4) **[MEPY][BiI$_4$]**. The anisotropic displacement factor exponent takes the form: $-2\pi^2[h^2a^{*2} \times U_{11} + \ldots + 2hka^* \times b^* \times U_{12}]$

Atom	U_{11}	U_{22}	U_{33}	U_{23}	U_{13}	U_{12}
Bi1	10.59(18)	9.91(16)	11.7(2)	0.57(15)	0.82(15)	-0.35(18)
I1	16.1(4)	16.4(3)	14.1(4)	2.6(3)	-1.1(3)	1.9(3)
I2	15.2(4)	13.2(3)	14.6(3)	2.4(3)	3.9(3)	2.4(3)
I3	19.9(4)	14.3(3)	14.6(3)	-1.9(3)	-0.1(3)	-3.6(3)
I4	14.1(4)	13.5(3)	14.2(4)	-2.6(3)	3.5(3)	-1.9(3)
N1	8(5)	19(5)	24(5)	-4(4)	0(4)	1(4)
C1	26(7)	17(6)	17(6)	5(5)	3(5)	7(5)
C2	13(7)	19(6)	42(8)	1(5)	-1(5)	-6(5)
C3	32(8)	39(7)	19(6)	-5(6)	12(5)	-10(6)
C4	18(7)	40(7)	24(7)	12(6)	2(5)	-6(5)
C5	4(6)	17(5)	22(6)	4(4)	-3(4)	-3(4)
C6	17(6)	22(6)	18(6)	1(5)	-3(5)	1(5)

Table A8: Bond Lengths in Å for [MEPY][BiI$_4$].

Atom	Atom	Length/Å
Bi1	I1	2.9098(8)
Bi1	I2	3.1027(9)
Bi1	I2^1	3.3029(7)
Bi1	I3	2.9195(8)
Bi1	I4	3.1063(8)
Bi1	I4^2	3.2699(7)
I2	Bi1^1	3.3029(7)
I4	Bi1^2	3.2699(7)
N1	C1	1.330(12)
N1	C5	1.332(13)
N1	C6	1.494(13)
C1	C2	1.352(15)
C2	C3	1.374(17)
C3	C4	1.372(17)
C4	C5	1.382(15)

-------•

^{1}-X,1-Y,1-Z; ^{2}1-X,1-Y,1-Z

Table A9: Bond Angles in ° for [MEPY][BiI$_4$].

Atom	Atom	Atom	Angle/°
I1	Bi1	I2	90.07(2)
I1	Bi1	I2^1	177.14(2)
I1	Bi1	I3	92.31(2)
I1	Bi1	I4	93.43(2)
I1	Bi1	I4^2	90.44(2)
I2	Bi1	I2^1	87.79(2)
I2	Bi1	I4^2	88.60(2)
I2	Bi1	I4	173.79(2)
I3	Bi1	I2	94.30(2)
I3	Bi1	I2^1	89.74(2)
I3	Bi1	I4^2	176.00(2)
I3	Bi1	I4	90.69(2)
I4^2	Bi1	I2^1	87.620(19)
I4	Bi1	I2^1	88.54(2)
I4	Bi1	I4^2	86.25(2)
Bi1	I2	Bi1^1	92.21(2)
Bi1	I4	Bi1^2	93.75(2)
C1	N1	C5	122.5(9)
C1	N1	C6	118.8(9)
C5	N1	C6	118.6(8)
N1	C1	C2	120.0(10)
C1	C2	C3	119.6(10)
C4	C3	C2	119.7(11)
C3	C4	C5	118.9(11)
N1	C5	C4	119.2(10)

-------•

^{1}-X,1-Y,1-Z; ^{2}1-X,1-Y,1-Z

Table A11: Hydrogen Fractional Atomic Coordinates (×10^4) and Equivalent Isotropic Displacement Parameters (Å^2×10^3) for [MEPY][BiI$_4$]. U_{eq} is defined as 1/3 of the trace of the orthogonalised U_{ij}.

Atom	x	y	z	U_{eq}
H1	8548	-255	6070	24
H2	7255	-961	4649	29
H3	6049	-12	3350	35
H4	5986	1637	3553	32
H5	7163	2305	5064	17
H6A	8025	1878	6944	29
H6B	9769	1934	6350	29
H6C	9361	1010	7006	29

Table A11: Hydrogen Fractional Atomic Coordinates (×10^4) and Equivalent Isotropic Displacement Parameters (Å^2×10^3) for **[MEPY][BiI$_4$]**. U_{eq} is defined as 1/3 of the trace of the orthogonalised U_{ij}.

Atom	x	y	z	U_{eq}
H1	20777	6373	13285	73
H1A	21706	7001	14506	86
H2	21008	7721	14072	80
H3	19331	7836	12866	73
H4	18377	7179	11584	73
H5	19168	6425	11945	63
H10	23975	6106	17395	114
H9	23250	5503	18513	124
H8	23863	4779	18034	117
H7	25639	4716	17504	117
H6	26584	5332	16616	124
H2A	25664	6054	16617	115

Table A12: Bond Lengths in Å for **TBI**.

Atom	Atom	Length/Å
Bi1	I1	3.0389(8)
Bi1	I2	3.0460(8)
Bi1	I3	3.1147(8)
Bi1	I4	3.1207(8)
Bi1	I5	3.0983(8)
Bi1	I6	3.0391(8)
Bi2	I7	3.0613(7)
Bi2	I8	3.0300(7)
Bi2	I9	3.1315(7)
Bi2	I10	3.1015(7)
Bi2	I11	3.0108(7)
Bi2	I12	3.0715(7)
Bi3	I13	3.0764(8)
Bi3	I14	2.9589(8)
Bi3	I15	3.3455(8)
Bi3	I16	3.0570(7)
Bi3	I17	3.2179(7)
Bi3	I18	2.9212(8)
Bi4	I19	3.1248(8)
Bi4	I20	3.0834(8)
Bi4	I21	3.2038(7)
Bi4	I22	3.0153(8)
Bi4	I23	3.0750(7)
Bi4	I24	2.9964(7)
S1	C1	1.733(12)
N1	C1	1.322(15)
N2	C1	1.296(14)
S2	C2	1.723(12)
N3	C2	1.314(14)
N4	C2	1.313(14)
S3	C3	1.746(11)
N5	C3	1.295(13)
N6	C3	1.315(14)
S4	C4	1.746(11)
N7	C4	1.325(14)
N8	C4	1.291(14)
S5	C5	1.731(12)
N9	C5	1.317(13)
N10	C5	1.308(13)
S6	C6	1.731(12)
N11	C6	1.337(14)
N12	C6	1.294(13)
S7	C7	1.681(13)
N13	C7	1.467(15)
N14	C7	1.299(15)
S8	C8	1.706(11)
N15	C8	1.316(14)
N16	C8	1.330(14)
S9	C9	1.742(11)
N17	C9	1.320(13)
N18	C9	1.313(13)
S10	C10	1.745(11)
N19	C10	1.319(14)
N20	C10	1.315(13)
S11	C11	1.716(11)
N21	C11	1.307(14)
N22	C11	1.337(14)
S12	C12	1.728(13)
N23	C12	1.305(16)
N24	C12	1.268(16)

Table A13: Bond Angles in ° for **TBI**.

Atom	Atom	Atom	Angle/°
I1	Bi1	I2	89.25(2)
I1	Bi1	I3	86.62(2)
I1	Bi1	I4	175.70(2)
I1	Bi1	I5	91.56(2)
I1	Bi1	I6	89.74(2)
I2	Bi1	I3	94.63(2)
I2	Bi1	I4	91.24(2)
I2	Bi1	I5	173.37(3)
I3	Bi1	I4	89.08(2)
I5	Bi1	I3	91.99(2)
I5	Bi1	I4	88.44(2)
I6	Bi1	I2	86.86(2)
I6	Bi1	I3	176.05(2)
I6	Bi1	I4	94.55(2)
I6	Bi1	I5	86.56(2)
I7	Bi2	I9	85.73(2)
I7	Bi2	I10	86.64(2)
I7	Bi2	I12	173.62(2)
I8	Bi2	I7	94.93(2)
I8	Bi2	I9	89.19(2)
I8	Bi2	I10	175.81(2)
I8	Bi2	I12	89.86(2)
I10	Bi2	I9	87.049(19)
I11	Bi2	I7	93.89(2)
I11	Bi2	I8	91.65(2)
I11	Bi2	I9	179.10(2)
I11	Bi2	I10	92.11(2)
I11	Bi2	I12	90.18(2)
I12	Bi2	I9	90.13(2)
I12	Bi2	I10	88.30(2)
I13	Bi3	I15	85.43(2)
I13	Bi3	I17	89.61(2)
I14	Bi3	I13	93.34(2)
I14	Bi3	I15	89.93(2)
I14	Bi3	I16	91.13(2)
I14	Bi3	I17	176.30(2)
I16	Bi3	I13	173.09(2)
I16	Bi3	I15	89.31(2)
I16	Bi3	I17	85.74(2)
I17	Bi3	I15	88.070(19)
I18	Bi3	I13	90.15(2)
I18	Bi3	I14	92.50(2)
I18	Bi3	I15	175.07(2)
I18	Bi3	I16	94.93(2)
I18	Bi3	I17	89.73(2)
I19	Bi4	I21	89.74(2)
I20	Bi4	I19	89.75(2)
I20	Bi4	I21	94.92(2)
I22	Bi4	I19	178.60(2)
I22	Bi4	I20	90.80(2)
I22	Bi4	I21	88.93(2)
I22	Bi4	I23	94.58(2)
I23	Bi4	I19	84.86(2)
I23	Bi4	I20	174.59(2)
I23	Bi4	I21	84.54(2)
I24	Bi4	I19	89.36(2)
I24	Bi4	I20	87.54(2)
I24	Bi4	I21	177.38(2)
I24	Bi4	I22	91.95(2)
I24	Bi4	I23	92.92(2)
N1	C1	S1	116.8(9)
N2	C1	S1	121.5(10)
N2	C1	N1	121.8(11)
N3	C2	S2	119.7(9)
N4	C2	S2	119.6(9)
N4	C2	N3	120.7(11)
N5	C3	S3	117.4(8)
N5	C3	N6	122.1(10)
N6	C3	S3	120.5(8)
N7	C4	S4	115.8(8)
N8	C4	S4	121.7(9)
N8	C4	N7	122.5(10)
N9	C5	S5	118.1(8)
N10	C5	S5	121.6(8)
N10	C5	N9	120.2(10)
N11	C6	S6	119.7(8)
N12	C6	S6	119.9(9)
N12	C6	N11	120.4(11)
N13	C7	S7	112.6(8)
N14	C7	S7	119.5(10)
N14	C7	N13	127.8(11)
N15	C8	S8	123.0(9)
N15	C8	N16	120.4(10)
N16	C8	S8	116.7(8)
N17	C9	S9	119.6(8)
N18	C9	S9	118.9(8)
N18	C9	N17	121.5(10)
N19	C10	S10	117.4(8)
N20	C10	S10	120.9(9)
N20	C10	N19	121.5(10)
N21	C11	S11	119.3(9)
N21	C11	N22	120.6(10)
N22	C11	S11	120.2(9)
N23	C12	S12	117.8(10)
N24	C12	S12	123.7(11)
N24	C12	N23	118.4(12)

Table A14: Hydrogen Fractional Atomic Coordinates ($\times 10^4$) and Equivalent Isotropic Displacement Parameters (Å$^2\times 10^3$) for **TBI**. U_{eq} is defined as 1/3 of the trace of the orthogonalised U_{ij}.

Atom	x	y	z	U_{eq}
H1A	8636.12	852.22	2713.82	62
H1B	8718.49	829.45	3189.52	62
H1C	8924.83	-191.76	2905.95	62
H2A	9629.53	1809.05	2680.72	52
H2B	9502.24	317.64	2744.37	52
H2C	9615.73	1211.46	3124.96	52
H3A	8344.36	-1127.45	3725.35	56
H3B	8575.38	-2403.52	3865.47	56
H3C	8168.92	-2140.62	4035.02	56
H4A	8146.91	-4401.42	3153.36	37
H4B	8314.03	-4593.19	3601.65	37
H4C	8560.68	-3903.38	3269.06	37
H5A	8518.82	4548.69	4731.24	30
H5B	8780.05	4023.4	5096.45	30
H5C	8355.4	4420.13	5171.47	30
H6A	7905.45	2015.87	4810.76	36
H6B	7961.78	2846.03	5216.85	36
H6C	8133.74	1398.67	5187	36
H7A	9656.12	-2749.38	4830.06	30
H7B	9262.66	-2605.64	5040.59	30
H7C	9545.62	-3751.25	5177.42	30
H8A	10194.95	-1977.89	5627.63	56
H8B	9989.86	-3374.59	5638.26	56
H8C	9867.83	-2225.83	5935.18	56
H9A	8203.35	-2533.3	6040.4	28
H9B	8247.88	-1427.38	6380.7	28
H9C	8102.25	-2862.97	6494.41	28
H10A	8922.36	-1340.55	6673.18	32
H10B	9075.66	-2775.61	6786.48	32
H10C	8696.9	-2253.23	6972.9	32
H11A	8951.71	2334.37	6588.1	39
H11B	8591.45	2654.99	6843	39
H11C	8718.49	3651.95	6501.42	39
H12A	7957.95	1479.7	6152.31	23
H12B	8032.82	3012.6	6083.08	23
H12C	7994.87	2452.97	6529.43	23
H13A	7394.82	7316.07	6713.73	14
H13B	7131.11	7658.3	7078.53	14
H13C	7240.12	8779.82	6766.14	14
H14A	6415.81	7881.47	6139.71	42
H14B	6700.57	9075.38	6215.54	42
H14C	6404.82	8709.65	6548.12	42
H15A	5229.74	1828.77	7003.37	39
H15B	5222.91	3025.09	7315.38	39
H15C	5337	1583.93	7468.15	39
H16A	6178.2	1377.84	7084.76	37
H16B	5905.36	799.03	7412.65	37
H16C	6169.56	2024.83	7522.82	37
H17A	6315.91	7335.76	8061.62	29
H17B	6182.84	8465.07	8359.62	29
H17C	5966.07	7089.71	8339.32	29
H18A	6962.57	7385.06	8452.41	27

Atom	**x**	**y**	**z**	U_{eq}
H18B	6944.99	7038.36	8920.62	27
H18C	6808.18	8447.29	8760.46	27
H19A	6326.54	2521.37	8224.49	28
H19B	6114.97	3158.6	8593.33	28
H19C	6027.52	1675.08	8460.84	28
H20A	6898.24	3022.98	8527.57	25
H20B	7061.07	1767.75	8764.42	25
H20C	6907.34	2998.49	9008.77	25
H21A	5390.54	6049.57	9804.71	34
H21B	5368.01	7254.83	10112.07	34
H21C	5758.78	6873.67	9923	34
H22A	5479.85	7695.6	8956.16	39
H22B	5057.37	7468.67	9083.04	39
H22C	5360.17	6325.65	9150.19	39
H23A	6217.69	10973.76	10057.02	59
H23B	5944.79	12213.51	10086.46	59
H23C	6072.07	11429.07	10484.84	59
H24A	6976.92	12025.29	10251.92	62
H24B	6730.86	11183.58	10551.56	62
H24C	6861.68	12638.44	10673.11	62

Table A15. (a) Energy density and power density calculated from cyclic voltammetry measurement; (b) Energy density and power density calculated from galvanostatic charge-discharge measurement.

a)

Scan rate / V·S^{-1}	0.5	0.2	0.1	0.05	0.02	0.01
Energy Density mWh/kg	478.07	216.6	473.3	782.84	115.74	141.78
Power Density W/kg	30.01	40.23	37.73	28.34	15.62	9.25

b)

Constant Current / mA·cm^{-1}	20	10	5	2	1
Energy Density mWh/kg	132.12	161.8	185.8	219.55	254.68
Power Density W/kg	38.67	19.04	9.43	3.76	1.87

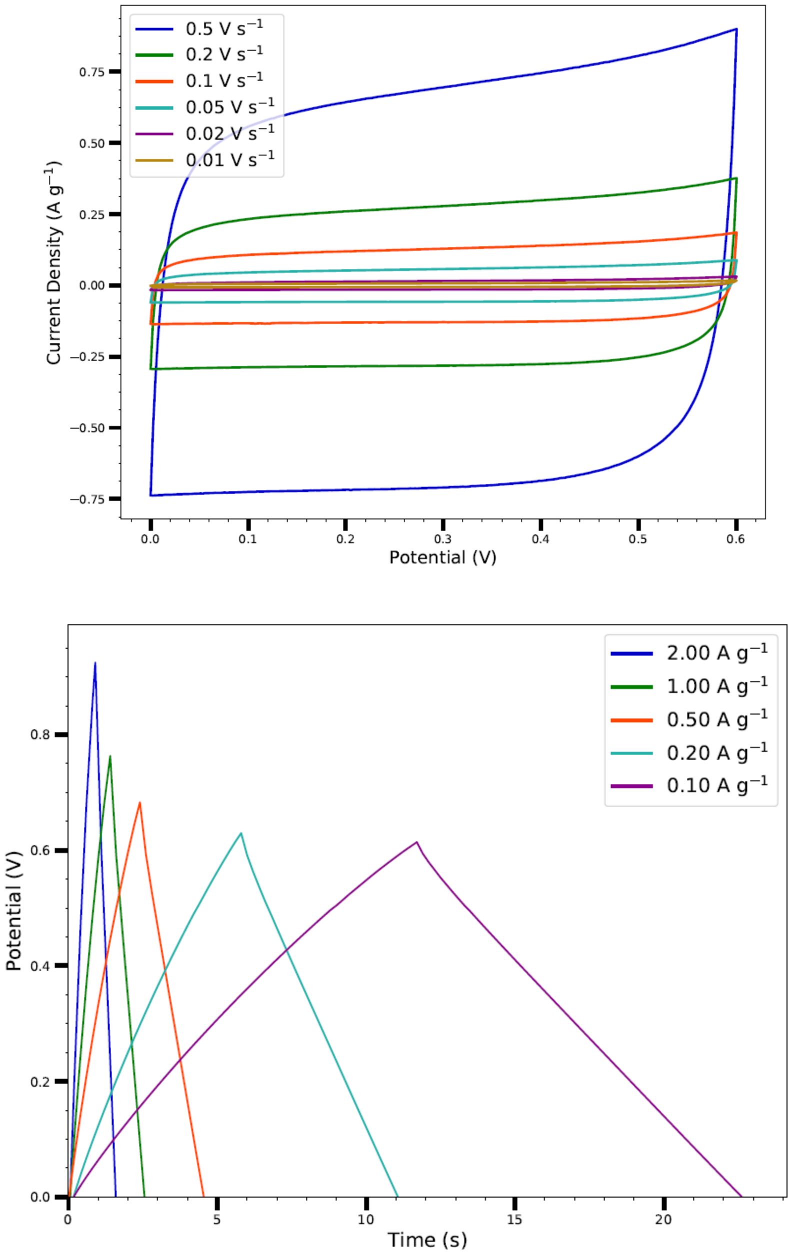

Figure A1. Cyclic voltammograms of the control blank EDLC without active material at varying scan rates. d) Galvanostatic charge−discharge curves of a control blank EDLC device.

Table A16. Areal capacitance and specific capacitance of controlled blank EDLC measured by (a) cyclic voltammetry under different scan rate and (b) galvanostatic charge−discharge under different scan rate

a)

Scan rate / $V \cdot S^{-1}$	0.5	0.2	0.1	0.05	0.02	0.01
Areal Capacitance/ $mFcm^{-2}$	1.86	1.88	1.73	1.52	0.97	0.77
Specific Capacitance /Fg^{-1}	0.66	0.67	0.62	0.54	0.34	0.27

b)

current density / $A \cdot g^{-1}$	2	1	0.5	0.2	0.1
Areal Capacitance/ $mFcm^{-2}$	2.24	2.26	2.35	2.51	2.64
Specific Capacitance /Fg^{-1}	0.8	0.8	0.84	0.89	0.94

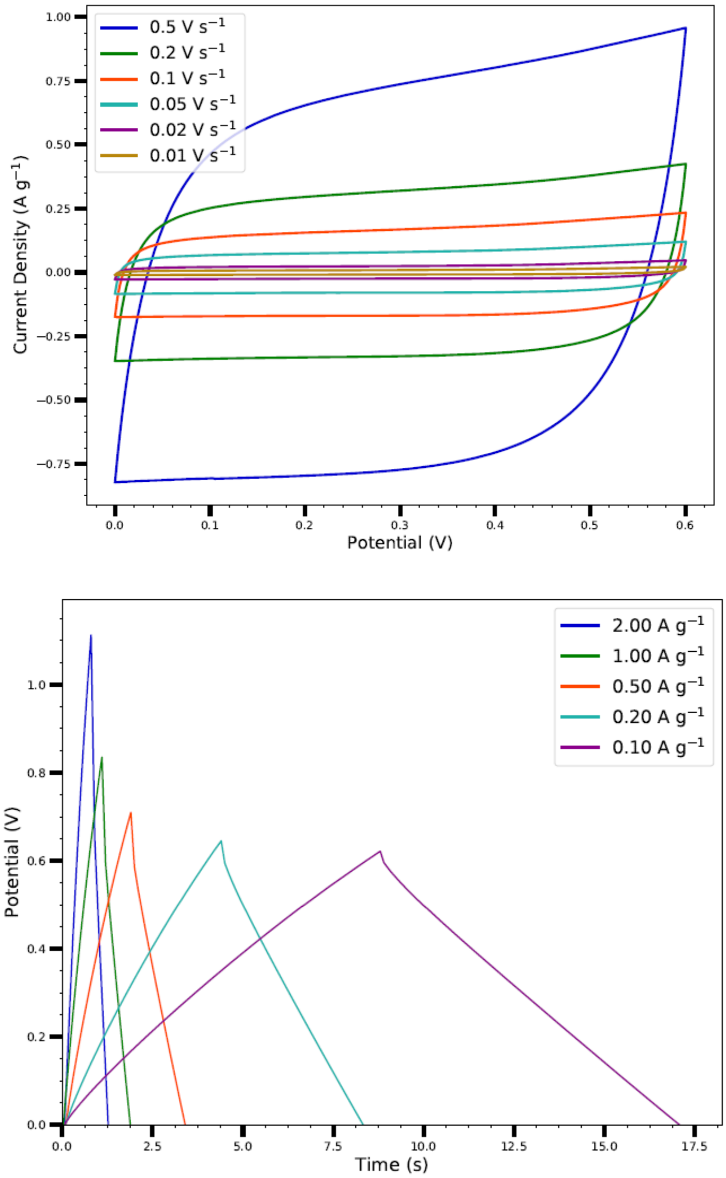

Figure A2. Cyclic voltammograms at varying scan rates (a) and Galvanostatic charge−discharge curves at different constant current (b) of the controlled suspension-deposited $Bi_{13}S_{18}I_2$-based EDLC.

Table A17 Areal capacitance and specific capacitance of controlled suspension-deposited $Bi_{13}S_{18}I_2$-based EDLC measured by (a) cyclic voltammetry under different scan rate and (b) galvanostatic charge−discharge under different scan rate

a)

Scan rate / V*S-1	0.5	0.2	0.1	0.05	0.02	0.01
Areal Capacitance/ $mFcm^{-2}$	10.33	11.28	11.67	11.07	8.51	5.97
Specific Capacitance /Fg^{-1}	0.7	0.77	0.79	0.75	0.58	0.41

b)

current density / A/g	2	1	0.5	0.2	0.1
Areal Capacitance/ $mFcm^{-2}$	8.69	9.04	9.63	10.35	10.92
Specific Capacitance /Fg^{-1}	0.59	0.61	0.65	0.7	0.74

a)

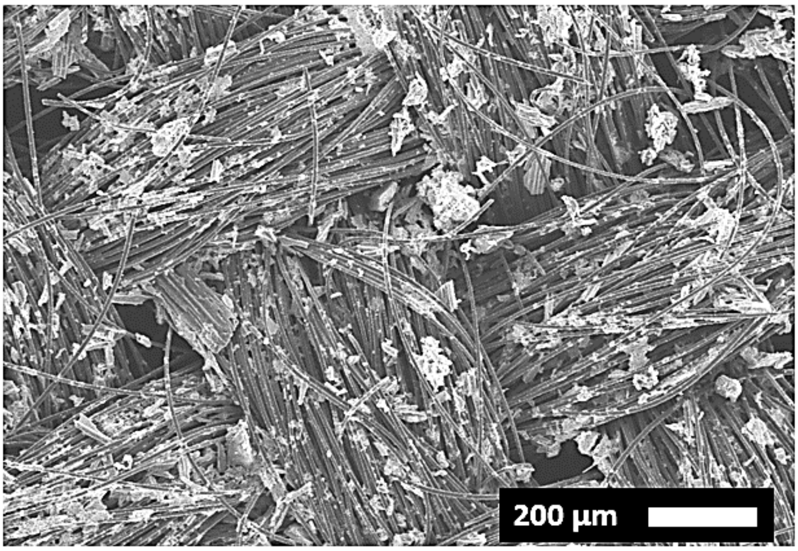

b)

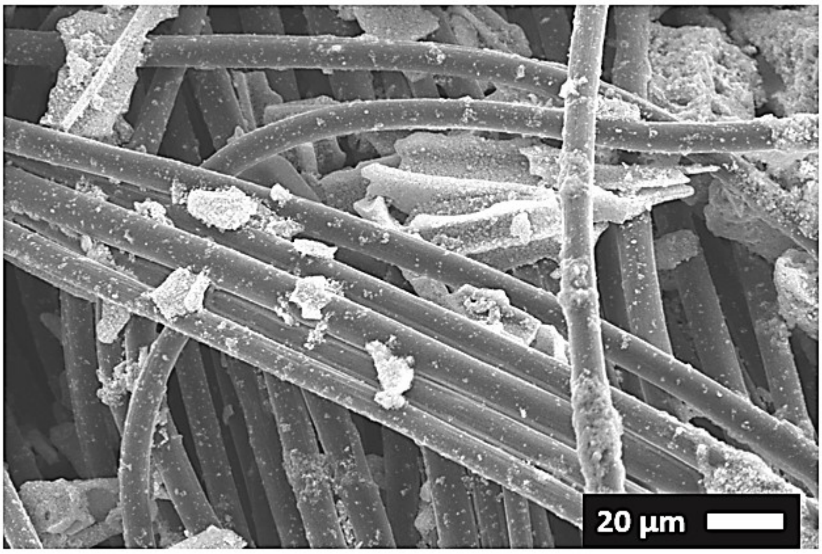

Figure A3. SEM images of $Bi_{13}S_{18}I_2$ electrode prepared from suspension-deposited method with a scale bar of 200 µm (a) and 20 µm (b).

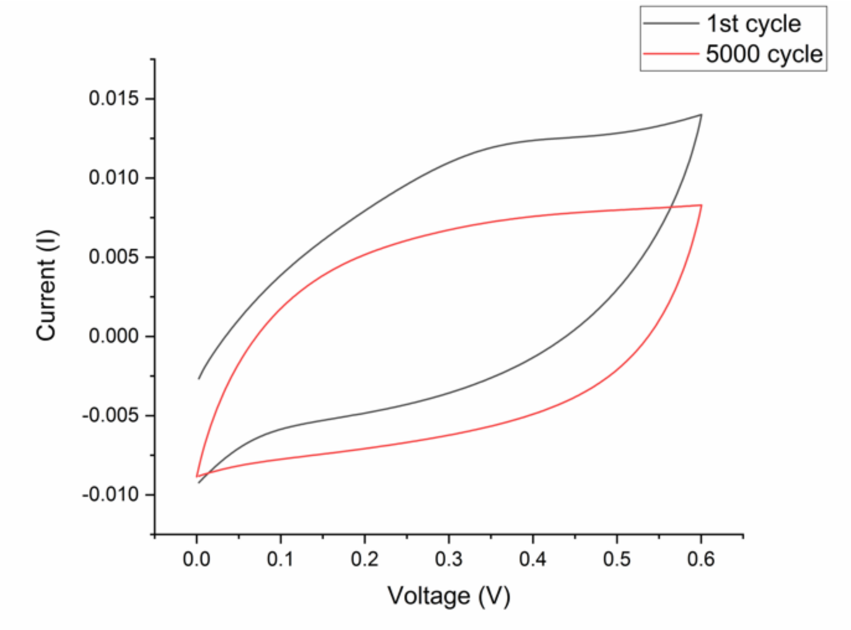

Figure A4. (a) CV curve of a TBI-based supercapacitor at its 1st cycle and 5000th cycle.

Table A18. The values for equivalent circuit elements in the simulated circuit for TBI-based supercapacitor measured after 5000 long-term cycle test

Circuit Element	Value	% Error
R_1	0.864 Ω	10.501
$Q_1 – n$	0.7496	1.503
$Q_1 – Y_0$	1.867 mF	11.023
R_2	6.27 Ω	1.634
$Q_2 – n$	1	3.272
$Q_2 – Y_0$	0.3571 F	8.072
R_3	3.58 Ω	9.135
$Q_3 – n$	0.7938	0.494
$Q_3 – Y_0$	0.1424 F	2.528
W_1	0.2087 Ω^{-1} $s^{1/2}$	6.335

Published Work

What follows are the publications prepared in the course of this work, including submitted drafts. The papers are included in chronological order.

- D-A-π-A motif quinoxaline-based sensitizers with high molar extinction coefficient for quasi-solid-state dye-sensitized solar cells

  (DOI:10.1021/acsami.6b11152)

  Y. Wang, Z. Zheng, T. Li, N. Robertson, H. Xiang, W. Wu,* J. Hua, W. Zhu and H. Tian*, *ACS Applied Materials & Interface*, 2016, **8**, 31016-31024.

  (collaborated and contributed on computational studies)

- Lead-free Pseudo-three-dimensional organic inorganic iodobismuthates for photovoltaic applications (DOI:10.1039/c6se00061d)

  T. Li, Y. Hu*, C. A. Morrison, W. Wu, H. Han and N. Robertson*, *Sustainable Energy&Fuels*, 2017, **1**, 308-316.

- High performance porphyrin-based dye-sensitized solar cells with both iodine and cobalt redox shuttles (DOI:10.1002/cssc.201601617)

  H. Xiang, W. Fan, J. Li, T. Li, N. Robertson, X. Song, W. Wu*, Z. Wang, W. Zhu and H. Tian*, *ChemSusChem*, 2017, **10**, 938-945.

  (collaborated and contributed on computational studies)

- Extending Lead-free Hybrid Photovoltaic Materials to New Structures: Thiazolium, Aminothiazolium and Imidazolium Iodobismuthates (DOI: 10.1039/c8dt00864g)

  T. Li, Q. Wang, G. S. Nichol, C. A. Morrison, H. Han, Y. Hu*, and N. Robertson*, Dalton Trans., 2018, **47**, 7050-7058.

- Facile Synthesis and Characterization of Bi13S18I2 Films as a Stable Supercapacitor Electrode Material (DOI: 10.1039/C8TA11029H)

  K. Adams, A. F. Gonzalez, J. Mallows, T. Li*, J. H. J. Thijssen and N. Robertson*, *J. Mater. Chem. A,* 2019, **7**, 1638-1646.

- Thiourea Bismuth Iodide: Crystal structure, Characterizations and Application as an Electrode Material for Supercapacitors (DOI: 10.1002/batt.201900005)

  T. Li, J. Mallows, K. Adams, G. S. Nichol, J. H. J. Thijssen and Neil Robertson*

  Batteries & Supercaps, 2019, **2,** 568 – 575.

- $Cs_3Bi_2I_9$ as high-performance electrode material achieving high capacitance and stability in an economical supercapacitor (DOI: 10.1088/2515-7655/ab22d7)

  K. Adams, J. Mallows, T. Li*, D. Kampouris, J. H. J. Thijssen and N. Robertson*

  JPhys Energy, 2019, accepted manucript

- Band Gap Engineering of 1D Iodobismuthate Photovoltaic Material with High Crystallinity Film Formation via Sulfur Doping Method (Submitted)

  T. Li, S. Monfront and N. Robertson*

- Band Gap Engineering of Iodobismuthate Materials via Dianion Substitution for Photovoltaic Applications (Submitted)

  T. Li and N. Robertson*

- Hybrid Perovskite-like Iodobismuthate as Low-cost and Stable Anode Material for Lithium-ion Battery Applications (In preparation)

  T. Li, K. Roy, S. Ogale and N. Robertson*